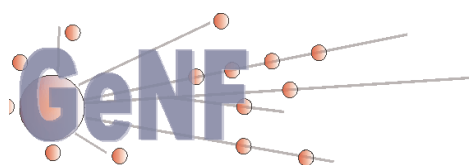


## GeNF – Experimental Report 2003



**Geesthacht Neutron Facility**



### **Editors:**

***A. Schreyer  
J. Vollbrandt  
R. Willumeit***

**GKSS 2004/1**



## **GeNF – Experimental Report 2003**

**Editors:**

***A. Schreyer***

***J. Vollbrandt***

***R. Willumeit***

**(Institute for Materials Research)**

Die Berichte der GKSS werden kostenlos abgegeben.  
The delivery of the GKSS reports is free of charge.

*Anforderungen/Requests:*

GKSS-Forschungszentrum Geesthacht GmbH  
Bibliothek/Library  
Postfach 11 60  
D-21494 Geesthacht  
Germany  
Fax.: (49) 04152/871717

Als Manuskript vervielfältigt.  
Für diesen Bericht behalten wir uns alle Rechte vor.

ISSN 0344-9629

GKSS-Forschungszentrum Geesthacht GmbH · Telefon (04152)87-0  
Max-Planck-Straße · D-21502 Geesthacht / Postfach 11 60 · D-21494 Geesthacht



## **GenF – Experimental Report 2003**

Andreas Schreyer, Jürgen Vollbrandt, Regine Willumeit (Editors)

*274 Seiten mit 243 Abbildungen und 25 Tabellen*

### **Abstract**

At the Geesthacht Neutron Facility GeNF about 210 experiments were performed in 2003 by GKSS and by or for external users, partners or contractors. In most cases the measurements were performed and analysed in cooperation by the guests and by the GKSS staff or by the permanent external user group staff. The activities, which are based on a proposal procedure and on the in house R&D program, are reported in 76 contributions in the present annual experimental report for the year 2003. The contributions may contain one or also several combined experiments.

During 2003 the GKSS research reactor FRG-1 achieved an operation time of 252 days at the full 5 MW reactor power providing a neutron flux of ca.  $1,4 \cdot 10^{14}$  thermal neutrons / cm<sup>2</sup> s. The cold neutron source was available during the complete operation time.

The focus of the in house R&D work at GeNF instruments was the characterisation of metal alloys, the analysis of stresses in welds and technical structures at ARES, FSS, DCD and SANS-2, the structural investigation of hydrogen containing substances such as polymers, colloids and biological macromolecules at SANS-1 as well as the characterisation of magnetic thin films at PNR and RÖDI. The reflectometer TOREMA was thoroughly upgraded to the instrument NeRo and now offers new measurement possibilities.

In the appendices the progress of the project REFSANS at FRM-II is reported as well as the experimental activities of the newly installed GKSS outstation HARWI-II at DESY.

## **Jahresbericht 2003 über die Experimente an GeNF**

### **Zusammenfassung**

An der Geesthachter Neutronenforschungseinrichtung GeNF wurden von GKSS und von oder für externe Nutzer, Partner oder Auftraggeber etwa 210 Experimente in 2003 durchgeführt. In den meisten Fällen wurden die Messungen gemeinschaftlich von den Gastwissenschaftlern und GKSS-Personal vorgenommen und ausgewertet. Die Experimente, die in der Regel über das Antragsverfahren und über das GKSS-eigene F&E-Programm abgewickelt wurden, werden in diesem Jahresbericht in Form von 76 Experimentierberichten dargestellt. Dabei können die Berichte einzelne Experimente oder auch mehrere zusammengefasst beschreiben.

Während 2003 erreichte der Forschungsreaktor FRG-1 252 Volllasttage bei 5 MW und bei einem Fluß von  $1,4 \cdot 10^{14}$  thermischen Neutronen je cm<sup>2</sup> und s. Die kalte Neutronenquelle war während der gesamten Betriebszeit verfügbar.

Der Schwerpunkt der GKSS-eigenen Forschungsarbeiten lag in 2003 im Bereich der Charakterisierung von Metalllegierungen, der Analyse von Eigenspannungen in Schweißverbindungen und technischen Strukturen an ARES, FSS, DCD und SANS-2, im Bereich der Strukturanalyse von wasserstoffhaltigen Substanzen wie Polymere, Kolloide und Biomolekülen an der SANS-1 sowie im Bereich der Charakterisierung magnetischer Schichtstrukturen an PNR und RÖDI. Das Reflektometer TOREMA wurde weitgehend zum neuen Instrument NeRo umgebaut und bietet nun neue Messmöglichkeiten.

In Anhängen wird auch über den Fortschritt des Projekts REFSANS am FRM-II sowie über die experimentellen Arbeiten der neuen GKSS-Außenstation HARWII bei DESY berichtet.

## CONTENTS

### Preface

- GeNF Operation
- Operation of FRG-1
- GeNF Instruments (overview)

<b>SANS-1</b>	<b>21</b>
<i>M. Andersson, J. S. Pedersen</i> Formation of silver nanoparticles with the use of a microemulsion technique studied by SANS	23
<i>M. Avdeev, L. Vekas</i> Comparative study of water-based ferrofluids by SANS	25
<i>M. Avdeev, L. Vekas</i> Application of SANS contrast variation for structural study of water-based ferrofluids	27
<i>P. M. Claesson</i> Interactions between polyethylene imine and sodium dodecyl sulfate in D <sub>2</sub> O	29
<i>H.-J. Gabius, B. Niemeyer</i> Effect of ligand and concentration on structure of <i>Viscum album</i> agglutinin in solution	31
<i>S. V. Grigoriev, G. P. Kopitsa</i> The study of the orbital part of the magnetic scattering amplitude in heavy-fermion substances by means of small angle scattering of polarized neutrons	33
<i>H. Kamusewitz</i> Shape-memory polymers by SANS	35
<i>M. Kumpugdee, C. Müller-Goymann</i> Localization of titanium dioxide in the solid lipid nanoparticles prepared from carnauba wax	37
<i>Hiroshi Maeda, J. S. Pedersen</i> Micelle growth in aqueous solutions of neutral C14DAO	39
<i>V. M. Nadutov</i> Small-angle polarized neutron scattering in Invar Fe-Ni-C alloys in magnetic field	41
<i>B. Niemeyer</i> Aggregation properties of Monosialoganglioside (GM1) in aqueous solutions measured by Small Angle Neutron Scattering (SANS)	43
<i>Hornig Der OU, V. Dötsch</i> Structural investigation of a transcription factor p63 in solution by small angle neutron scattering	45
<i>W. Richtering</i> Characterisation of hyperbranched polyglycerols with SANS	47
<i>W. Richtering</i> Contrast variation method for investigation of the polyethelenimine-amides solutions with/without silver nanoparticles	49

<i>V. Vill</i> Investigation of the supramolecular structures of ( <i>cis</i> -9-octadecenyl) glycosides	51
<i>V. Vill</i> SANS study of the phase behaviour of <i>N</i> -Hexadecanoyl-1,3-di-O- $\beta$ -D-glucopyranosyl-2-deoxy-2-amino- <i>sn</i> -glycerol	53
<i>Jinkui Zhao</i> Polarized proton target as broadband, wavelength independent neutron spin polarizer	55
<b>SANS-2</b>	<b>57</b>
<i>R. Kampmann, M. Marmotti, M. Haese-Seiller, V. Kudryashov</i> 2D-multi-wire neutron detector with a large sensitive area and high spatial resolution for SANS and reflectometry	59
<i>T. Klassen, M. Dornheim, A. Schreyer, P. K. Pranzas</i> Structural Changes of nanocrystalline Mg / MgH <sub>2</sub> during sorption and desorption of hydrogen	61
<i>D. W. Schubert, T. Rühle, A. Gruber, P. K. Pranzas, D. Bellmann, J. Vollbrandt</i> Characterisation of nanoparticles dispersed in a polymeric matrix	63
<i>A. I. Okorokov, S. V. Grigoriev, A. Schreyer</i> SANS study of the magnetic structure of Y/Dy multilayer system	65
<i>A. I. Okorokov, S. V. Grigoriev, P. Böni, R. Georgii</i> SANS study of the static magnetic structure of MnSi single crystal under applied magnetic field	67
<i>B. Jamnig</i> Nanosize precipitates in a maraging steel	71
<i>H. Leitner</i> Isochronal ageing of a maraging steel	75
<i>M. Parlog</i> Characterisation of coherent Cu precipitates in Fe-Cu model alloys	79
<i>M. Akamatsu, C. H. de Novion, P. K. Pranzas</i> SANS Round Robin for Engineering Materials Applications	81
<i>R. Wang, H. Schmiedel</i> Surface structure of negatively charged "hairy" latex	83
<i>hanse chemie AG, P. K. Pranzas, H. Eckerlebe</i> SANS investigation of SiO <sub>2</sub> nanoclusters in different solutions	85
<i>Ivan Škorvánek</i> SANS study of the early stages of crystallisation in the soft magnetic Fe-Zr-B-Cu nanocrystalline alloys	87
<i>E. Grossman, I. Gouzman, N. Eliaz, A. Schreyer, P. K. Pranzas</i> Structural Characterisation of the Erosion of Polyimides by Simulated Space Debris and Atomic Oxygen	91

<i>S. Prasetyo</i> Wide-Angle Scattering Investigations of the Phase Separation Kinetics in Cu –0.9at% Ti Using a 2-dimensional Side Detector	93
<i>G. P. Gordeev, L. A. Axelrod, S. V. Grigoriev, I. M. Lazebnik, V. N. Zabenkin, V. Wagner</i> The study of the static and dynamic spin chirality in the reentrant spin glass system (Pd <sub>0.984</sub> Fe <sub>0.016</sub> ) <sub>0.95</sub> Mn <sub>0.05</sub> by small angle scattering of polarized neutrons	95
<i>A. I. Okorokov, S. V. Grigoriev</i> Critical magnetic scattering in the isotropic ferromagnet EuS	99
<i>I. Kaban, A. Pohlers, W. Hoyer</i> Small angle scattering on liquid monotectic alloys	103
<i>M. Bischof</i> Characterisation of Particles in Dispersoid Strengthened Tantalum	105
<i>M. Bischof</i> Precipitation kinetics of a Tool Steel containing Carbides and Intermetallic Phases	107
<b>DCD</b>	<b>109</b>
<i>J. Banhart, B. Matijasevic, D. Bellmann, H. Clemens</i> Metal Foams – Structures in Unfoamed Zn Samples with 0.32% TiH <sub>2</sub>	111
<b>NeRo</b>	<b>113</b>
<b>PNR</b>	<b>115</b>
<i>R. Krastev, D. Carriere</i> Electrostatically controlled immobilized water in polyelectrolyte multilayers	117
<i>Lizhong He, R. Naumann, W. Knoll</i> Investigation of the Structure of Novel Archaea Analogue Thiolipids on Gold Surfaces for Preparation of Tethered Lipid Bilayers	119
<i>D. W. Schubert, F. Faupel, J. Kanzow</i> Initial interface formation of polystyrene/polyethylmethacrylate bilayers	121
<i>J. Fassbender</i> Characterisation of FeMn-FeNi exchange bias films using X-ray reflection and diffraction	123
<i>R. Kleinhempel</i> Mass density of MgO films determined by x-ray and neutron reflectometry	127
<b>ARES</b>	<b>129</b>
<i>W. Vaidya, M. Koçak</i> Residual stress analysis of an LBW joint of 6013 Al alloy	131
<i>O. Doerk</i> Residual stress in ferritic steel welds	133

<i>W. Marketz</i> Residual Stress in IN718 Turbine Discs	135
<i>W. Marketz</i> Residual Stress in a Ti 6Al 4V fan-shaft	139
<i>J. F. dos Santos</i> Residual stress analysis in FSW steel plates using neutron diffraction	141
<b>FSS</b>	<b>145</b>
<i>W. Stets</i> Characterisation of stress relief in a cast break disk	147
<i>D. Letzig</i> Residual stress characterization in rolled AZ 31 Mg-alloy sheets	149
<i>D. Letzig</i> Diffraction-elastic properties of AZ 31 Mg-alloy at RT and elevated temperatures	151
<i>W. Skrotzki</i> Feasibility study on DSPS specimens	155
<i>H. G. Priesmeyer</i> Elastic constants of cast iron with differing carbon content and morphology	157
<i>H. G. Priesmeyer</i> Orientation-dependent thermal expansion of anisotropic materials	159
<i>H. G. Priesmeyer</i> Orientation-dependent thermal expansion of AZ 31	163
<i>H. G. Priesmeyer</i> In-situ Investigation of Plastic Deformation by Neutrons and Positrons – a novel approach	165
<i>A. Pyzalla</i> Neutron TOF diffraction test experiments on reinforced materials	167
<b>TEX-2</b>	<b>169</b>
<i>W. Skrotzki, Guang-Hui Cao</i> Global textures of thermomechanically processed TiAl	171
<i>M. Chadima</i> Correlation between the phyllosilicate preferred orientation, low and high-field magnetic anisotropy	173
<i>S. Müller</i> Microstructure Characterization of extruded magnesium profiles	177
<i>W. Skrotzki, N. Scheerbaum</i> Global textures of ECAP deformed fcc metals	179
<i>T. Lychagina, D. Nikolayev</i> Texture Investigation and the Physical Modelling of the Graphite Texture Forming. Part 1	181

<i>J. Konrad, S. Zaefferer, D. Raabe</i> Microstructure Characterization of extruded magnesium profiles	183
<i>S.-B. Yi, H.-G. Brokmeier, K. U. Kainer</i> The texture variations of AZ31 magnesium alloy during tensile tests at different temperatures	187
<i>M. Stempniewicz, A. Pyzalla</i> Growth strategy of sauropod dinosaurs studied by pole figure analysis	189
<i>F. Cifelli, M. Mattei</i> Texture in weakly deformed mudstones: a correlation between magnetic and mineral fabrics and tectonic implications	193
<i>W. Singer, W.-H. Ye, H.-G. Brokmeier, X. Singer</i> Texture development of Nb-Cu tubes <sup>^</sup>	195
<i>H.-J. Rack, H.-G. Brokmeier</i> Texture Evolution During Severe Plastic Deformation	197
<i>M. Kocan, L. Wagner</i> Directional Properties in the Wrought Magnesium Alloy AZ80	199
<i>J. Dzwonczyk, K. U. Kainer</i> Texture measurement on as-cast form of AZ31 alloy	201
<i>J. Dzwonczyk, K. U. Kainer</i> Texture measurement on AZ31 alloy extruded via different extrusion methods	203
<i>L. Q. Chen, N. Kanetake, W.-H. Ye, H.-G. Brokmeier</i> Textures of Al-Nb Composite Sheet	207
<b>POLDI</b>	<b>209</b>
<i>R. Böttger</i> The PTB thermal neutron reference field at GeNF	211
<i>V. Wagner, J. Hesse</i> Magnetic inter-particle correlations in a system of single-domain particles	213
<i>L. A. Axelrod, G. P. Gordeev, V. N. Zabenkin, I. M. Lazebnik, V. Wagner</i> Search of chiral spin glass transition in alloy $(\text{Pd}_{0.984}\text{Fe}_{0.0016})_{0.95}\text{Mn}_{0.05}$	215
<i>D. Lott, A. Schreyer, R. Lechner</i> Neutron diffraction study on EuSe	219
<i>P. Mikula</i> Multiple reflection <i>Umweganregung</i> monochromator	221
<b>Proposal</b>	<b>223</b>

## Appendix I

227

### REFSANS Progress Report

*R. Kampmann, M. Haese-Seiller, V. Kudryashov, C. Daniel, V. Deriglazov, B. Toperverg, A. Schreyer, E. Sackmann*  
Neutron Optics of the Reflectometer REFSANS at FRM-II for Comprehensive Investigations on the Air / Liquid Interface

229

## Appendix II

233

### Reports of experiments carried out at HASYLAB/DESY by GKSS personel – GKSS outstation HARWI-II at DESY – as responsible experimenters in support of external users

*F. Beckmann, T. Lippmann, J. Metge, R. V. Martins, T. Dose, A. Schreyer*  
High-energy beamline HARWI-II

*R. Bernhardt, E. Pilling, R. Mai, D. Scharnweber, F. Beckmann, H. Worch*  
Analysis of Bony Tissue around Titanium Implants with Synchrotron Radiation Microtomography and Histology

*R. Zettler, T. Donath, F. Beckmann, J. dos Santos, D. Lohwasser, T. Lippmann, A. Schreyer*  
Investigation of Material Flow in Friction Stir Welds of Aluminium Alloys using Micro CT

*O. Brunke, S. Odenbach, F. Beckmann*  
Measurement of metallic foam structure parameters by means of synchrotron  $\mu$ CT

*S. F. Nielsen, F. Beckmann, H. F. Poulsen, J. A. Wert*  
Measurements of plastic displacement gradient components in 3D

*R. Bernhardt, K-P. Hummel, D. Scharnweber, F. Beckmann, H. Worch*  
Micro-CT Investigations of Bone Absorption caused by Rheumatoid Arthritis in an Animal Model

*H.-A. Crostack, H. Blum, J. Nellesen, F. Beckmann, T. Rauscher, G. Fischer*  
Microtomography and FE-simulation of tensile specimens of the metal-matrix-composite Al/TiN

*H.-A. Crostack, J. Nellesen, F. Beckmann, G. Fischer*  
Porosity analysis of thermally sprayed mullite utilizing synchrotron radiation based microtomography

*S.-B. Yi, H.-G. Brokmeier, B. Schwebke, T. Lippmann, W. H. Ye, J. Homeyer*  
Texture developments of extruded Mg-alloy during tensile loading

*S.-B. Yi, H.-G. Brokmeier, B. Schwebke, T. Dose, J. Homeyer*  
The evolution of internal strain during uniaxial tension of Mg-alloy, AZ31

*D. Tadic, F. Beckmann, T. Donath, M. Eppe*  
Untersuchungen an unterschiedlichen Knochenersatzmaterialien mittels Synchrotron  $\mu$ -Computertomographie

*T. Lippmann, S. Kiele, J. Geck, P. Reutler, M.v. Zimmermann, B. Büchner*  
Charge density study of  $\text{La}_{0.5}\text{Sr}_{1.5}\text{MnO}_4$  at room temperature



*A. Kirfel, T. Lippmann, W. Morgenroth*

Electron Density Distribution in Tephroite,  $\text{Mn}_2\text{S}_4$ : a High-Energy Synchrotron Radiation Study

*P.M. Cattaneo, M. Dalstra, F. Beckmann, T. Donath, B. Melsen*

Comparison of Conventional and Synchrotron-Based Microtomography of Bone around Dental Implants

*M. Dalstra, E. Karaj, T. Andersen, P. M. Cattaneo, F. Beckmann*

Comparison of Synchrotron-Based Microtomography and Scanning Acoustic Microscopy of Cortical Bone

*H. Scherf, F. Beckmann, J. Habersetzer*

Differentiation in the mineral content of trabecular bone

*R.G.J.C. Heijkants, F. Beckmann, T. Donath, R. V. van Calck, T. G. van Tienen,*

*N. Ramrattan, P. Buma, J. H. de Groot, A. J. Pennings, R.P.H. Veth, A. J. Schouten*

Micro CT of polyurethane scaffolds for meniscus replacement

*F. Beckmann, C. Hurschler, F. Witte*

Microtomography of human and animal tendons, first results

*F. Witte, H.-A. Crostack, J. Nellesen, J. Fischer, F. Beckmann*

In-vivo Degradation Kinetic of Magnesium Implants



## Preface

### GeNF Operation

The Geesthacht Neutron Facility (GeNF) is operated as an open facility for external users for about 2/3 of the available beam time and it is used for GKSS in-house research within its materials science programme for the remaining 1/3. The external users come either from national and international scientific research institutions, universities and industry, or they own and operate experiments at GeNF as permanent external partners.

The beam time allocations for GeNF instruments are established on the base of a proposal procedure which can react in a flexible and fast way on new proposals. Proposals can be submitted at any time. In 2003 about 210 experiments were performed at GeNF by or for external users, partners or contractors as well as for the in house research programmes. A part of these activities – mainly the part of external use based on proposals – is reported in the present annual experimental report for the year 2003. In many cases several experiments are concentrated in one experimental report.

### Operation of FRG-1

In 2003 the FRG-1 was operated routinely interrupted by the two planned major shut downs in January/February and in July. The total operation time was to 252 days at its full 5 MW power providing a neutron flux of ca.  $1,4 \cdot 10^{14}$  thermal neutrons/cm<sup>2</sup> s. The cold neutron source was always available during FRG operation.

### GeNF Instruments

The current set of instruments at GeNF is shown in Figure A and listed in Table A. The available sample environment is listed in table B.

In 2003 the installation of a modern hardware and software system based on LabView to control the experiments was continued for NeRo. NeRo (Neutron Reflectometer) is the result of a thorough upgrade of TOREMA by the improvement of the beam configuring system, by the complete exchange of the secondary diffractometer and by a new 2-D-position sensitive <sup>3</sup>He-detector.

The focus of the GKSS in-house research at GeNF is the investigation of metal alloys, the analysis of stresses in welds and technical structures at ARES, FSS, DCD and SANS-2, the structural investigation of hydrogen containing substances such as polymers, colloids and biological macromolecules at SANS-1 as well as the characterisation of magnetic and polymer thin films at PNR and RÖDI.

A major issue of activities concerning instrument improvements are focussed on the setup of the GKSS high-energy synchrotron beamline HARWI-II at DESY. For details see the report in appendix II.



# Geesthacht Neutron Facility (GeNF)

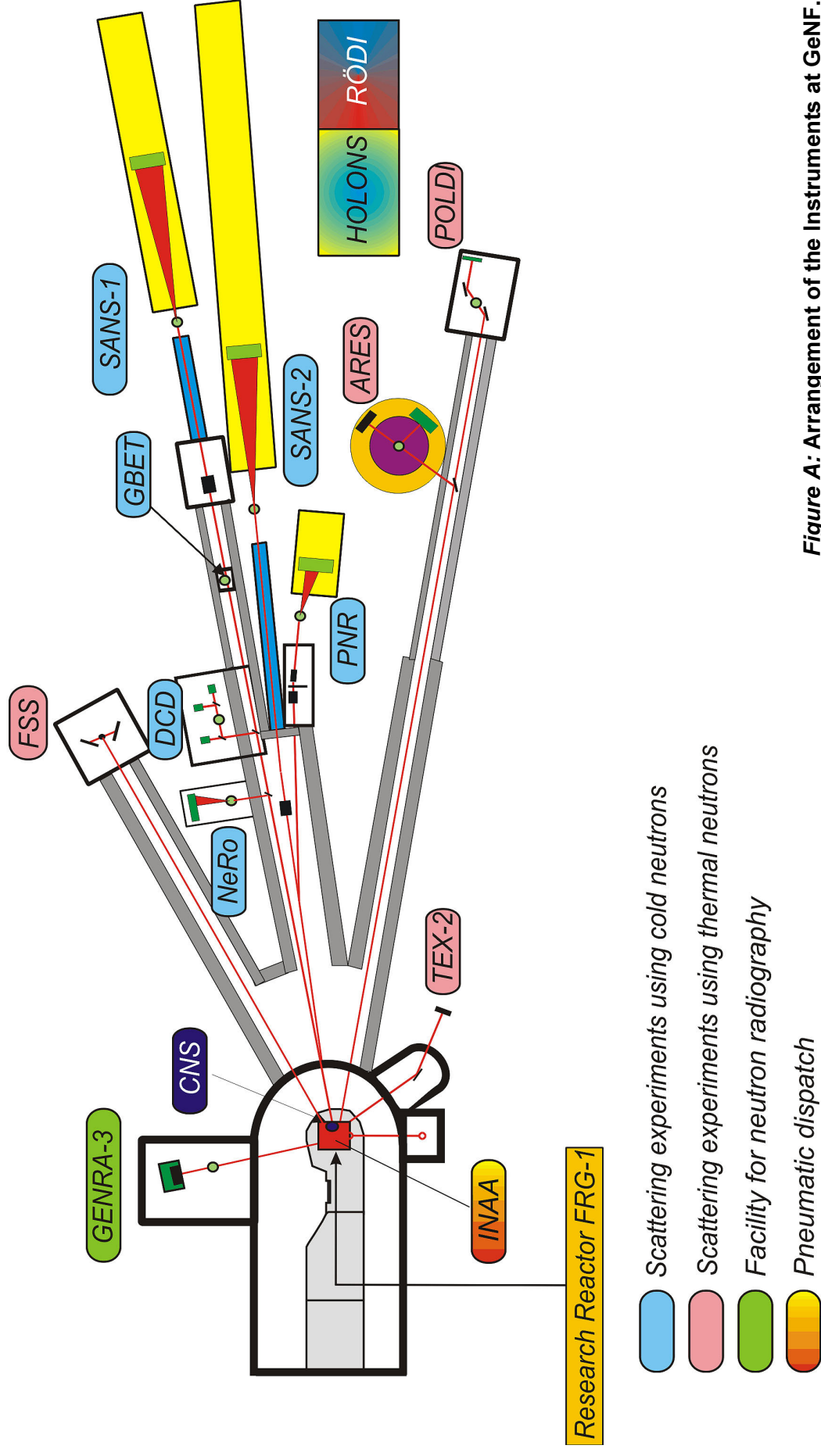


Figure A: Arrangement of the Instruments at GeNF.

**Table A:** List of GeNF Instruments.

Instrument	Short Instrument Description /Main Tasks	Characteristic Data	Operator / Local Contact
<b>SANS-1</b>	Small Angle Neutron Scattering using cold non-polarised/polarised neutrons primarily to investigate molecular biology, colloids and polymers	$\Phi_{\text{max}} = 6 \cdot 10^5 \text{ cm}^{-2} \text{ s}^{-1}$ (coll.2 m, $\lambda=0.8\text{nm}$ ) $\Delta\lambda/\lambda = 0.1$ ( $\lambda = 0.85 \text{ nm}$ ) Particle sizes: 2–80 nm 2-D position-sens. $^3\text{He}$ - detector	GKSS / Regine Willumeit Vasyil Haramus
<b>SANS-2</b>	Small Angle Neutron Scattering using cold non-polarised/polarised neutrons to characterise precipitates, clusters, interfaces, grain sizes, magnetic structures etc. in materials (metals, polymers, colloids a.o.)	$\Phi_{\text{max}} = 2 \cdot 10^7 \text{ cm}^{-2} \text{ s}^{-1}$ (coll.1 m, $\lambda=0.5\text{nm}$ ) $\Delta\lambda/\lambda = 0.1$ Particle sizes: 1–100 nm 2-D position-sens. $^3\text{He}$ - detector	GKSS / Helmut Eckerlebe P. Klaus Pranzas
<b>DCD</b>	Double Crystal Diffractometer for ultra small angle neutron scattering (USANS) using non-polarised cold neutrons to characterise large creep pores, fatigue and sintering cavities, precipitates, voids, bubbles, etc. in materials	$\Phi \approx 0.5 \cdot 10^3 \text{ cm}^{-2} \text{ s}^{-1}$ $\Delta\lambda/\lambda = 1 \cdot 10^{-5}$ ( $\lambda = 0.443 \text{ nm}$ ) Particle sizes: 30 nm–24 $\mu\text{m}$ 3 x $^3\text{He}$ - detectors	GKSS / Dieter Bellmann
<b>ARES</b>	Diffractometer for the Analysis of Residual Stresses in specimens with technical sizes (up to 100 kg) using thermal non-polarised neutrons	$\Phi \approx 3 \cdot 10^5 \text{ cm}^{-2} \text{ s}^{-1}$ (perfect Si-Monochr.) $\Delta d/d \approx 4 \cdot 10^{-3}$ take-off angle: $57^\circ$ – $120^\circ$ 2-D position-sens. $^3\text{He}$ -detector	GKSS / Peter Staron
<b>FSS</b>	Time of flight Fourier Strain Spectrometer to investigate residual stresses in specimens with technical sizes using thermal neutrons	$\Phi = 5.5 \cdot 10^6 \text{ cm}^{-2} \text{ s}^{-1}$ timing res. ca. $4 \cdot 10^{-3}$ ( $\lambda = 0.1$ – $0.4 \text{ nm}$ ) Analyser: 2 x 3072 TOF channels 2 detector banks ( $90^\circ$ & $270^\circ$ )	CAU - Universität Kiel / Hans-Georg Priesmeyer
<b>NeRo</b>	Neutronen Reflectometer to study magnetic and other surfaces, layers, thin films and membranes using cold non-polarised/polarised neutrons with high resolution	$\Phi = 5 \cdot 10^4 \text{ cm}^{-2} \text{ s}^{-1}$ (standard collimation) $\Delta\lambda/\lambda = 0.02$ ( $\lambda = 0.435 \text{ nm}$ ) 2-D position-sens. $^3\text{He}$ -detector, $^3\text{He}$ -pencil counter	GKSS / Dieter Lott
<b>PNR</b>	Polarised Neutron Reflectometer to study magnetic and other surfaces, layers, thin films and membranes using cold non-polarised/polarised neutrons at high fluxes	$\Phi_{\text{nonpol}} = 1 \cdot 10^5 \text{ cm}^{-2} \text{ s}^{-1}$ $\Phi_{\text{nonpol}} / \Phi_{\text{pol}} = 3 / 1$ $\Delta\lambda/\lambda = 0.05$ ( $\lambda \geq 0.635 \text{ nm}$ ) 2-D position-sens. $^3\text{He}$ -detector	GKSS / Danica Solina

**Table A:** List of GeNF Instruments (continued).

Instrument	Short Instrument Description /Main Tasks	Characteristic Data	Operator / Local Contact
<b>RÖDI</b>	X-ray ( <u>R</u> öntgen) <u>D</u> iffractometer to investigate residual stresses, textures and thin films	Seifert XRD 3003 PTS Heavy load goniometer	GKSS / Peter Staron
<b>TEX-2</b>	Four circle neutron <u>TEX</u> ture diffractometer to characterise textures in metallic, ceramic and geologic materials using thermal non-polarised neutrons	$\Phi = 0.3 - 2 \cdot 10^6 \text{ cm}^{-2} \text{ s}^{-1}$ take-off angle: $17^\circ - 57^\circ$ (in $10^\circ$ -steps) $\lambda$ -range: 0.08–0.27 nm $^3\text{He}$ -single detect., $38^\circ$ JULIOS-PSD, 2-D position-sens. $^3\text{He}$ -detector	TUC – Technische Universität Clausthal / Heinz-Günter Brokmeier
<b>POLDI</b>	<u>POL</u> arised <u>D</u> iffractometer; 3-D depolarisation analysis is used to investigate magnetic properties and correlations in magnetic materials; additional time of flight option in non-polarised mode	$\Phi_{\text{max}} = 0.8 \cdot 10^5 \text{ cm}^{-2} \text{ s}^{-1}$ (polarized) take-off angle: $10^\circ < 2 \Theta_{\text{M}} < 65^\circ$ $\lambda$ -range: 0.1 nm–0.36 nm $^3\text{He}$ -single detector	PTB – Physikalisch Technische Bundesanstalt / Volker Wagner
<b>HOLONS</b>	<u>HOL</u> ography and <u>Neutron Scattering</u> to investigate the properties in functional materials of photonics (e.g. photopolymers and photorefractive crystals) and to study light-induced changes simultaneously by light and neutron diffraction	holographic setup in SANS-2: angular resol. $\leq 0.01^\circ$ ; angl.setting acc = $0.001^\circ$ lasers (excitation & diffract.): $\text{Ar}^+$ -laser (single&multi line mode: 25 W /visible, 5.5 W / UV), HeNe-lasers (green, red)	Universities of Vienna and Osnabrück / Romano Rupp
<b>GENRA-3</b>	<u>GE</u> sthacht <u>Neutron R</u> adiography facility for non-destructive analysis of materials by static and dynamic imaging	$\Phi_{\text{therm}} / \Phi_{\text{epi}} = 1.4 \cdot 10^6 / 8 \cdot 10^3 [\text{cm}^{-2} \text{ s}^{-1}]$ image: $15 \times 15$ to $45 \times 45 \text{ cm}^2$ max. size of specimen: $100 \times 200 \text{ cm}^2$	GKSS / Jürgen Vollbrandt
<b>GBET</b>	<u>Ge</u> sthachter <u>Boron</u> -capture ( <u>E</u> infang) <u>T</u> herapy originally designed to study cell cultures in tumours with enriched boron; now available as a cold neutron irradiation facility	$\Phi = 1.6 \cdot 10^8 \text{ cm}^{-2} \text{ s}^{-1}$ ( $\lambda_{\text{m}} = 0.6 \text{ nm}$ ) irrad. area : $30 \times 40 \text{ mm}^2$ $E_{\text{m}} = 2.3 \text{ meV}$	GKSS / Hans-Ulrich Ruhnau
<b>ICI</b>	<u>In Core Irradiation</u> - service for industry and others, different core positions, pneumatic dispatch system available	$\Phi_{\text{therm}} = 2$ to $8 \cdot 10^{13} \text{ cm}^{-2} \text{ s}^{-1}$ $\Phi_{\text{fast}} = 0.02$ to $0.06 \Phi_{\text{therm}}$ max. sample size: $40 \text{ mm} \varnothing \times 100 \text{ mm}$	GKSS / Wolfgang Knop
<b>NAA</b>	<u>Neutron Activation Analysis</u> used as qualitative and quantitative multielement analysis of major, minor and trace elements	> 50 chem. elements can be determined sample mass: $10^{-3} - 1 \text{ g}$ LOD - range: $10^{-5}$ to $10^{-12} \text{ g}$	GKSS / Rainer Niedergesäss

**Table B: GeNF Sample Environment.**

Instrument	Cryostat	Magnets	Temp. Conditioning	Other Devices
<b>SANS-1</b>	$^3\text{He}$ / $^4\text{He}$ – Cryostat: horizontal dilution-refrigerator with NMR sample coil and microwave source; T-range: 120 mK - RT; NMR: 106 and 16 MHz; Microwave: tunable: 68 to 74 GHz sample dimension: 2,8 x 17 x 19 mm <sup>3</sup> (optimum design for NMR coil), NMR is made for $^1\text{H}$ and $^2\text{H}$ resonance in 2.5 Tesla continuous wave mode;	2.5 Tesla magnet	heater up to 80 °C	
<b>SANS-2</b>	refrigerator cryostat Model Leybold RGD 210, temp.-range: 12–475 K flexible operation in various instruments	<ul style="list-style-type: none"> <li>• <b>B-E 25</b>: up to 2 Tesla with closed cycle refrigerator (T: 8–300 K)</li> <li>• <b>B-E 15</b>: up to 1.5 Tesla with closed cycle refrigerator (T: 8–300 K)</li> <li>• <b>B-E 10</b>: up to 1 Tesla with closed cycle refrigerator (T: 8–300 K), alternative furnace (T: 300–900 K), usable for polarised neutrons,</li> <li>• <b>superconducting magnet</b>: up to 5 Tesla with closed cycle refrigerator (T: 8–300 K) usable for polarised neutrons</li> </ul>	heater (electric) / cooler (thermostat liquid circuit): T -range: -30–400 °C vacuum or inert gas atmosphere	– sample container for big samples – lasers;
<b>DCD</b>	refrigerator cryostat Model Leybold RGD 210, temp.-range: 12–475 K flexible operation in various instruments			
<b>ARES</b>	refrigerator cryostat Model Leybold RGD 210, temp.-range: 12–475 K flexible operation in various instruments			



**Table B:**    **GeNF Sample Environment** (continued).

<b>Instrument</b>	<b>Cryostat</b>	<b>Magnets</b>	<b>Temp. Conditioning</b>	<b>Other Devices</b>
<b>FSS</b>	refrigerator cryostat Model Leybold RGD 210, temp.-range: 12 –475 K flexible operation in various instruments		heater (up to 1000 °C)	–stress rig max. force: 30 t
<b>PNR</b>	refrigerator cryostat Model Leybold RGD 210, temp.-range: 12–475 K flexible operation in various instruments	<ul style="list-style-type: none"> <li>• <b>electro magnet:</b> up to 0.9 Tesla</li> <li>• <b>superconducting magnet:</b> up to 5 Tesla with closed cycle refrigerator (T: 8–300 K) usable for polarised neutrons</li> </ul>	<ul style="list-style-type: none"> <li>• heater / cooler (thermostat liquid circuit): T-range: -30–250 °C</li> </ul>	
<b>NeRo</b>	refrigerator cryostat Model Leybold RGD 210, temp.-range: 12–475 K flexible operation in various instruments	<ul style="list-style-type: none"> <li>• <b>electro magnet:</b> up to 0.9 Tesla</li> </ul>	<ul style="list-style-type: none"> <li>• 2 x vacuum furnaces: T-range: RT - 200 °C - one especially. for annealing purposes under PC control</li> <li>• heater / cooler (thermostat liquid circuit): T-range: -30–250 °C</li> </ul>	
<b>TEX-2</b>			mirror furnace up to 2000 °C	<ul style="list-style-type: none"> <li>– loading device: tension up to 1.5 t, compression up to 2.0 t</li> <li>– sophisticated set of sample holders</li> </ul>
<b>POLDI</b>	<ul style="list-style-type: none"> <li>– refrigerator T &gt; 10 K</li> <li>– Orange cryostat T &gt; 1.5 K</li> </ul>	DC magnetic field < 160 A/cm pulsed field < 6.5 kA/cm		



**Small-angle scattering instrument SANS-1**

**Short Instrument Description:**

The small angle neutron scattering instrument SANS-1 using cold non-polarised/polarised neutrons serves primarily to investigate molecular biology, colloids and polymers.

**Local Contact:**

Dr. Regine Willumeit

Phone/Fax : +49 (0)4152 87 – 1291 / +49 (0)4152 87–1356

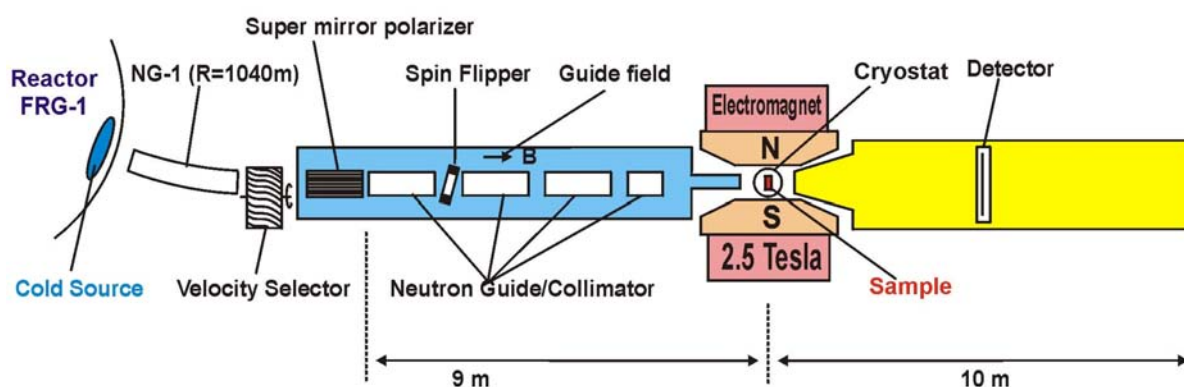
e-mail: [regine.willumeit@gkss.de](mailto:regine.willumeit@gkss.de)

Dr. Vasyl Haramus

Phone/Fax : +49 (0)4152 87 – 1290 / +49 (0)4152 87 – 1356

e-mail: [vasyl.haramus@gkss.de](mailto:vasyl.haramus@gkss.de)

**Schematic View of SANS-1:**



**Instrument Details:**


<u>Beamline:</u>	Beamline 8 - NG-1, radius of curvature $R = 1040$ m, cross section $3 \times 4 \text{ cm}^2$ , cold neutrons
Monochromator	helical slot selector
Wavelength range behind polariser and selector:	$\geq 0.45 \text{ nm}$ ;
Wavelength resolution	$\Delta\lambda / \lambda = 0.1$ ( $\lambda = 0.85 \text{ nm}$ )
Length L of collimation:	1 m, 3 m, 5 m, 7 m, 9 m
Flux at specimen:	$\Phi = 0.04 - 6 \cdot 10^5 \text{ cm}^{-2} \text{ s}^{-1}$ see table

**Instrument Details** (continued):

Range of momentum transfer:	$0.05 \leq Q \leq 3 \text{ nm}^{-1}$
Distance sample to detector:	$0.7 \text{ m} \leq d \leq 9 \text{ m}$
<u>Detector:</u> active area: effective pixel size: background:	2-dim position-sensitive $^3\text{He}$ -counter $55 \times 55 \text{ cm}^2$ $0.7 \times 0.7 \text{ cm}^2$ 1 cps
<u>Polarized target station:</u>	dilution refrigerator (120 mK) 2.5 T C-shaped electro-magnet microwave emitter (68–74 GHz) NMR circuit for protons and deuterons selective nuclear spin depolarisation
<u>Other sample environment</u>	thermostat (5 °C to +200 °C) automatic sample change

**Flux of polarized cold neutrons at the sample position:**

<b>length of collimator [m]</b>	<b>1</b>	<b>3</b>	<b>5</b>	<b>7</b>	<b>9</b>
$\Phi [10^3 \text{ n cm}^{-2} \text{ s}^{-1}]$ ( $\lambda = 0.85 \text{ nm}$ )	<b>600</b>	<b>360</b>	<b>120</b>	<b>72</b>	<b>40</b>

	<b>EXPERIMENTAL REPORT</b>	<b>GeNF SANS-1</b>
<b>Formation of silver nanoparticles with the use of a microemulsion technique studied by SANS</b>		
<b>Principal Proposer:</b>	<b>Martin Andersson<sup>1</sup>, Jan Skov Pedersen<sup>2</sup></b> <sup>1</sup> Department of Material and Surface Chemistry, Chalmers University of Technology SE-412 96 Göteborg, Sweden, <sup>2</sup> Department of Chemistry, University of Aarhus, DK-8000 Aarhus Denmark	
<b>Experimental Team:</b>	<b>Anders Palmqvist<sup>1,3</sup></b> <sup>3</sup> Competence Centre for Catalysis , Chalmers University of Technology SE-412 96 Göteborg, Sweden	
<b>Date(s) of Experiment:</b>	June 2003	

In this work we are studying the formation of silver nanoparticles with the use of a microemulsion technique. A microemulsion is a macroscopically homogeneous mixture of oil, water and surfactant, but microscopically it consists of individual domains of oil and water separated by a monolayer of surfactant. The microemulsion is thermodynamically stable and will never separate into its different components. It has been shown that water-in-oil microemulsions consisting of nanometer size range water droplets can be used as microreactors to produce nanoparticles. The normal way of doing the synthesis is to mix two equal microemulsions in respect of oil, water-phase and surfactant, but containing different types of salts. When they are mixed a reaction occur due to the coalescence of the droplets forming particles which are in the same size-range as the water droplets. The dynamics in the microemulsion is very rapid so the reaction occurs in the order of milleseconds. This makes it hard to study the kinetics of the particle formation. Many groups have used the microemulsions to produce silver particles and self organized nanoclusters of these. They show that the particle radii are dependent on the size of the microemulsion droplets, which in turn is dependent on the molar ratio of water to surfactant ( $W = [H_2O]/[Surfactant]$ ). Liz-Marzán et al. showed that  $Ag^+$  ions could be reduced in ethanol when certain surfactants were present. They showed that the most successful surfactants for the reduction are the non-ionic ethoxylated surfactants. This is due to the hydrophilic oxyethylene groups are oxidised (mainly into aldehydes). They show that the reduction is dependent of the silver concentration in a first order fashion. In this work we work with a novel method for the formation of silver nanoparticles, were we utilise the duality of the surfactants as both template and reduction agents (Figure 1). This method, due to its slow kinetics to form the nanoparticles (approximately 24 hours) makes it a good candidate for studying the particle formation inside the water droplet. We have shown how the kinetics is dependent on the surfactant and silver concentration and how it influences the size and size distribution of the formed particles. By using different ratios of non-ionic surfactant and the ionic surfactant AOT (which don't give rise to silver reduction), the influence of the surfactant concentration could be examined. SAXS studies show how the droplets size and size distribution are dependent on the surfactant ratios as well as how this influences the formed particles. The growth of the particles inside the water droplets was studied in-situ by UV-vis absorption spectroscopy, which gives both the kinetics as well as an indirect measure of the size and size distribution.

TEM (Transmission Electron Microscopy) was used to study the size, morphology and size distribution of the particles. We have tried to study the formation directly by SAXS but the silver concentration (0.1 %) seems to be too low to be able to do so. For SAXS we cannot do the contrast matching of the droplet scattering, however, according to some calculations, it should be possible with SANS.

## Ag formation in microemulsions

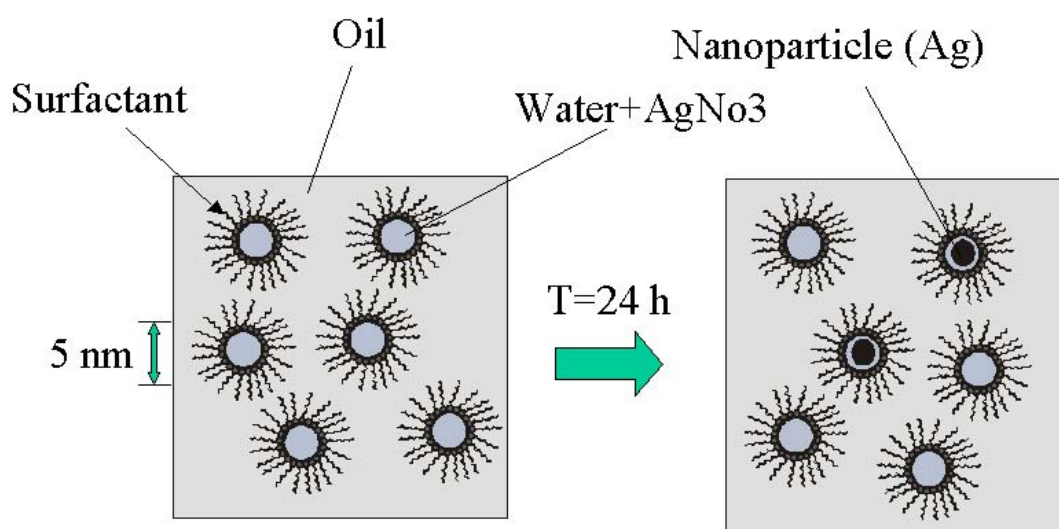



Figure 1.

To be able to study the silver nanoparticles formation within the microemulsion SANS experiments were carried out on SANS-1 instrument. Microemulsions consisting of mixtures heptan (protonated and deuterated), water ( $\text{H}_2\text{O}/\text{D}_2\text{O}$ ), Brij30 surfactant and  $\text{AgNO}_3$  were prepared. The ratios of protonated to deuterated water and heptan were contrast matched to be able to “only” see the silver and its formation. Solutions consisting of different amounts of  $\text{AgNO}_3$  were prepared to be able to study its impact on the formation.

No SANS signal from the silver formation could be detected. According to TEM data ( $r = 5 \text{ nm}$ ) the SANS signal should be in order of  $0.15 \text{ cm}^{-1}$ . In present studies we have got that scattering from silver nanoparticles should be less than  $0.05 \text{ cm}^{-1}$  which points that TEM data do not reflect the average parameters of system such as radius.

	<b>EXPERIMENTAL REPORT</b>	<b>GeNF SANS-1</b>
<b>Comparative study of water-based ferrofluids by SANS</b>		
<b>Principal Proposer:</b>	<b>Mikhail Avdeev<sup>1</sup>, Ladislau Vekas<sup>2</sup></b> <sup>1</sup> Joint Institute for Nuclear Research, Dubna, Russia <sup>2</sup> Center for Fundamental and Advanced Technical Research, Timisoara, Romania	
<b>Experimental Team:</b>	<b>Maria Balasoiu<sup>1,3</sup>, Viktor Aksenov<sup>1</sup>, Doina Bica<sup>2</sup></b> <sup>3</sup> Institute of Space Sciences, Bucharest, Romania	
<b>Date(s) of Experiment:</b>	July 2003	

Ferrofluids, fine stable dispersions of magnetic materials in liquids, find a wide range of applications in many technical and industrial fields [1]. Much promise is connected with the development of their applications in medicine [2]. This explains a great interest to the structure of water-based ferrofluids in last years. In contrast to ferrofluids based on non-polar liquids such as benzene, where the structure can be described well by the common concept of the spherical core-shell model (magnetic particles covered by single surfactant layer) [3–5], the structure of water-based ferrofluids is more complicated. In this case the so-called double stabilization is used, when the first surfactant layer due to hemisorption is followed by the next layer due to physical absorption. In these fluids specific aggregation and agglomerates are found [5–8] before the fluids are set under magnetic field. The aim of the current experiments is to clarify the structure of the aggregates by means of small-angle neutron scattering for a number of water-based ferrofluids and see how this structure changes with the temperature.

Ferrofluids (Table 1) with magnetite dispersed in water and stabilized by different surfactants were synthesized [3] at the CFATR, Timisoara, Romania. The radius of the magnetite particles in the fluids lies within interval of about 311 nm with the mean value of 6.6 nm. SANS experiments were performed at temperature values of 25, 50 and 70 °C, and, then, measurements were repeated with the same samples at the initial temperature of 25 °C.

*Table 1.* Investigated ferrofluids with double stabilization by oleic acid (OA), dodecylbenzenesulphonic acid (DBS) and lauric acid (LA).

sample	carrier	stabilizers	Magnetite
1	H <sub>2</sub> O	LA + LA	2.1 vol. %
2	H <sub>2</sub> O	LA + DBS	2.2 vol. %
3	H <sub>2</sub> O	DBS + DBS	2.1 vol. %
4	sap	OA + OA	2.2 vol. %

Figure 1 shows the SANS curves corresponding to the room temperature. One can see that they reflect quite different structures for different fluids. The SANS signal from sample 1 is significantly smaller in comparison with other samples. The reason for this is required additional analysis of all steps of sample preparation and of the stability of the ferrofluid. Such an analysis is in progress. Nevertheless, the character of the scattering curves from samples 1 and 3 are quite similar, despite the large difference in the magnitude of the mean scattering. In particular, the scattering at small  $q$ -values within interval of 0.05–0.26 nm<sup>-1</sup>

satisfies well to the power-low behavior, which can correspond to the fractal clusters in the fluids. The fractal dimension of such clusters is determined from the slope of the fitting line in the double logarithmic plot (Figure 2) and is found to be 1.47 for both samples. So, at once one can see that the stabilization by lauric and dodecylbenzenesulphonic acids results in very close types of the structure of aggregation in the ferrofluids. The scattering for samples 2 and 4 reflects more complex structures of aggregates, which are to be clarified.

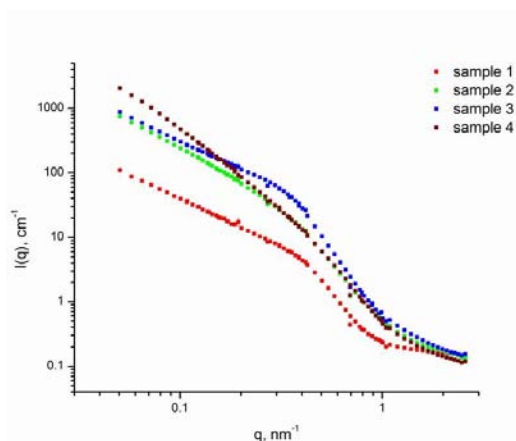


Figure 1: Experimental scattering curves for studied samples.

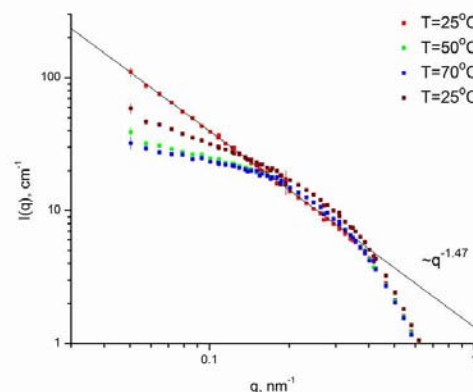


Figure 2: Experimental scattering curves for sample 2 at different temperature values.

Changes in the scattering curves with the temperature give evidence that the structure of the ferrofluids with respect to the aggregation is temperature-dependent. The most pronounced changes are observed for samples 1 and 3 (Figure 2), which are quite similar again. They concern only the scattering over above-mentioned  $q$ -interval of the power-low behavior (Fig. 2), which approximately corresponds to the size-interval of 25–120 nm in the real space. From Fig. 2 one can conclude that the temperature increase from RT (25 °C) to 50 °C is followed by the degradation of the aggregates and change in the characteristic aggregate size from the value of more 120 nm (it is not observable in the curve) to that of about 36 nm. The further increase in the temperature does not affect the last size significantly. When the temperature is decreased back to the first value, the aggregation starts again, but does not achieve for the initial state during first hours. For samples 2, 4 changes in the scattering with the temperature are not so significant, nevertheless, the same tendencies as for samples 1, 3 repeat. The development of the appropriate model for detailed treatment of all curves is in progress.

## References

- [1] Magnetic fluids and Applications Handbook, Ed. B. Berkovski (Beggel House, New York, 1996).
- [2] Scientific and Clinical Applications of Magnetic Carriers, Eds. W. Schutt, et al. (Plenum, New York, 1997).
- [3] L. Vékás, D. Bica, M. Raşa, O. Balau, I. Potencz, D. Gheorghe, In Micro and nanostructures, Eds. D. Dascalu, et al. (Ed. Academiei Romane, 2001) 127.
- [4] V. Aksenov, M. Avdeev, M. Balasoiu, L. Rosta, Gy. Torok, L. Vekas, D. Bica, V. Garamus, J. Kohlbrecher, *Applied Physics A* [Suppl.] (2002) 943.
- [5] M. Avdeev, M. Balasoiu, V. Aksenov, V. Garamus, J. Kohlbrecher, D. Bica and L. Vekas, *J. Mag. Mater.*, in press (2003).
- [6] D. Bica, L. Vékás, M.V. Avdeev, M. Balasoiu, O. Marinică, F.D. Stoian, D. Susan-Resiga, Gy. Török, L. Rosta, *Prog. Colloids Polymer Sci.*, in press (2003).
- [7] M. Kammel, A. Wiedenmann, A. Hoell, *J. Mag. Mater.* 252 (2002) 89.



 <b>GKSS</b> FORSCHUNGSZENTRUM in der HELMHOLTZ GEMEINSCHAFT	<b>EXPERIMENTAL REPORT</b>	<b>GeNF SANS-1</b>
<b>Application of SANS contrast variation for structural study of water-based ferrofluids</b>		
<b>Principal Proposer:</b>	<b>Mikhail Avdeev<sup>1</sup>, Ladislau Vekas<sup>2</sup></b> <sup>1</sup> Joint Institute for Nuclear Research, Dubna, Russia <sup>2</sup> Center for Fundamental and Advanced Technical Research, Timisoara, Romania	
<b>Experimental Team:</b>	<b>Maria Balasoiu<sup>1,3</sup>, Viktor Aksenov<sup>1</sup>, Doina Bica<sup>2</sup></b> <sup>3</sup> Institute of Space Sciences, Bucharest, Romania	
<b>Date(s) of Experiment:</b>	July 2003	

To clarify structural features of the water-based ferrofluids the SANS contrast variation was performed for a ferrofluid, which is the water dispersion of magnetite stabilized by double layered surfactant shell (lauric acid (LA) plus dodecylbenzenesulphonic acid (DBS)). The ferrofluid was synthesized at the CFATR, Timisoara, Romania. The volume fraction of magnetite in the fluid, 4.4 vol.%, was found from the magnetization saturation measurements. The radius of the magnetite particles in the fluids was determined from the electron microscopy images and lies within interval of about 3–11 nm with the mean value of about 6.6 nm. The initial H<sub>2</sub>O-based sample was dissolved with the ratio 1:4 by different mixtures of D<sub>2</sub>O/H<sub>2</sub>O so that the content of D<sub>2</sub>O in the final fluids (magnetite fraction 0.88 vol.%) was equal to 0, 20, 40, 60 and 80 %. SANS experiments were performed at temperature of 25 °C. Scattering curves were obtained with the standard corrections in a  $q$ -interval 0.05–2.67 nm<sup>-1</sup>. The corresponding mixtures D<sub>2</sub>O/H<sub>2</sub>O were used as buffers for correction on the scattering from the carrier.

Obtained scattering curves for different contrasts are presented in Figure 1 and show significant difference.

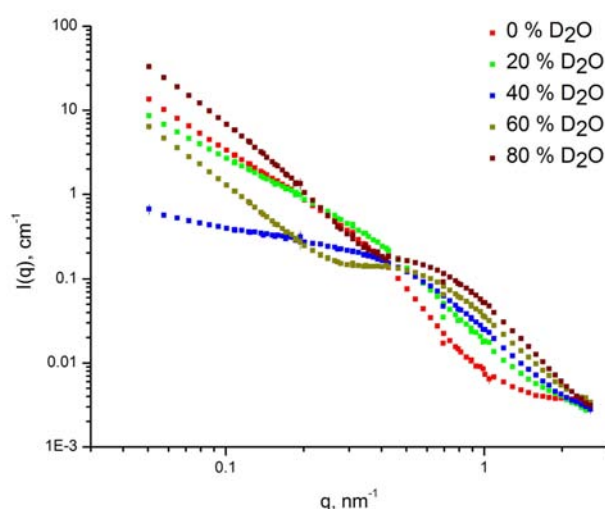


Figure 1: Experimental scattering curves for different content of D<sub>2</sub>O in the studied ferrofluid.

The preliminary treatment of the curves was made in terms of basic functions [1] using the expression for the scattering intensity:

$$I(q) = I_c(q) + \Delta\rho I_{cs}(q) + (\Delta\rho)^2 I_s(q), \quad (1)$$

where the basic functions  $I_c(q)$ ,  $I_s(q)$ ,  $I_{cs}(q)$  describe the scattering from the shape of the particles ( $I_c(q)$ ), the scattering from inhomogeneities inside the particles ( $I_s(q)$ ) and interference between these two contributions ( $I_{cs}(q)$ ). The contrast,  $\Delta\rho$ , is determined as the difference between mean values of the scattering length density of the particles and the solvent (carrier). Measurements of the scattering intensity (1) with different values of the contrast (minimum three) makes it possible to find out the basic functions. Functions  $I_c(q)$ ,  $I_s(q)$  obtained from experimental curves (Fig. 1) are presented in Figure 2. The dependence of the mean scattering length density of the particles on their size is neglected in the calculations.

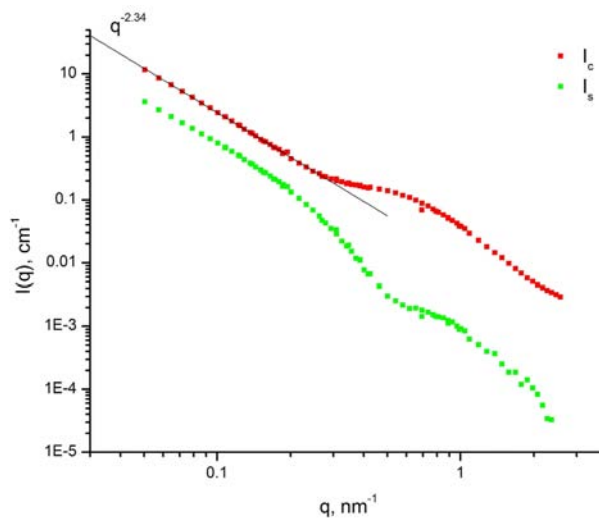



Figure 2: Basic functions  $I_c$  and  $I_s$  obtained from experimental scattering curves.

The obtained functions point to a complex structure of the studied ferrofluid. In contrast to the whole scattering curve (red points in Fig. 1) two characteristic scales can be clearly seen in the  $I_c(q)$  and  $I_s(q)$  curves (Fig. 2). The first one ( $q > 0.4 \text{ nm}^{-1}$ ) corresponds to particles with the size of about 10 nm, which is in good agreement with the mean size of the magnetic particles of the fluid. The second scale ( $q < 0.4 \text{ nm}^{-1}$ ) reflects the formation in the fluid of fractal aggregates with the size more than at least 120 nm. The fractal dimension of the aggregates was estimated from the slope of the fitting line in the double logarithmic plot (Fig. 2) and is found to be 2.34. Whether all the magnetic particles of the fluids are involved in these aggregates or one deals with the mixture of single particles and aggregates is to be clarified.

## Reference

- [1] Feigin, L. A.; Svergun, D. I. Structure Analysis by Small-Angle X-Ray and Neutron Scattering. NY: Plenum Press, 1987

	<b>EXPERIMENTAL REPORT</b>	<b>GeNF SANS-1</b>
<b>Interactions between polyethylene imine and sodium dodecyl sulfate in D<sub>2</sub>O</b>		
<b>Principal Proposer:</b>	<b>P. M. Claesson<sup>1</sup></b> <sup>1</sup> Department of Chemistry, Surface Chemistry, Royal Institute of Technology (KTH), Stockholm, Sweden, and Institute for Surface Chemistry, Stockholm, Sweden.	
<b>Experimental Team:</b>	<b>L. A. Bastardo-Zambrano<sup>1</sup></b>	
<b>Date(s) of Experiment:</b>	March–May 2003	

We have studied the interactions between sodium dodecyl sulfate and polyethylene imine, which are relevant to different processes. The aim here was to characterize the surfactant – polyelectrolyte system in solution.

- Polyethylene imine (PEI) is a hyperbranched polyelectrolyte that has been extensively used in a diversity of applications. These applications include cosmetics (like in anti-perspirants and hair conditioners), as a wet strength agent in the paper industry, a flocculating agent of silicate soils in mining and in gene delivery therapy, among others. This polyelectrolyte is highly charge at low pH, but it behaves as a weak polyelectrolyte in high pH solutions.
- The interactions between PEI and sodium dodecyl sulfate (SDS) has been investigated in some details. Some of these studies report unusual pH behaviour on the SDS/PEI systems. Studies in this area using PEI and SDS have been performed in the past in our group.
- In order to understand the nature of the interactions of these molecules in solution light scattering and small angle neutron scattering (SANS) measurements were performed.

SANS measurements in solutions containing highly charged PEI and SDS (Figure 1) indicate, at low surfactant concentration the presence of disk-like aggregates. As the surfactant concentration was increased the aggregates changed to a more complex three dimensional structure. Another interesting feature is the occurrence of a Bragg peak at high  $Q$  values and relatively low surfactant concentration (up to the charge neutralization point). This kind of peak has been attributed to the formation of polyelectrolyte/surfactant structures in similar polyelectrolyte surfactants systems.

At charge neutralization point there was precipitation of the sample. X-ray diffraction measurements on the precipitate confirmed the existence of a lamellar phase structure. The formation of a peak at intermediate  $Q$  values, at concentrations above the charge neutralization point, corresponds to the presence of free surfactant micellar aggregates. These data are going to be further analyzed by IFT and different modelling.

Measurements at high pH (low polyelectrolyte charge) reveal that when SDS is added to PEI, the aggregates size start to decrease. The minimum size of the aggregates is reached at the charge neutralization point. The decrease on the polyelectrolyte aggregates size may be due to the neutralization of the small charge still present on the aggregates at high pH.

After the charge neutralization point the aggregates size starts to increase again. The increment on the surfactant–polymer aggregates size may be due to recharging and expansion due to inter chain electrostatic repulsion.

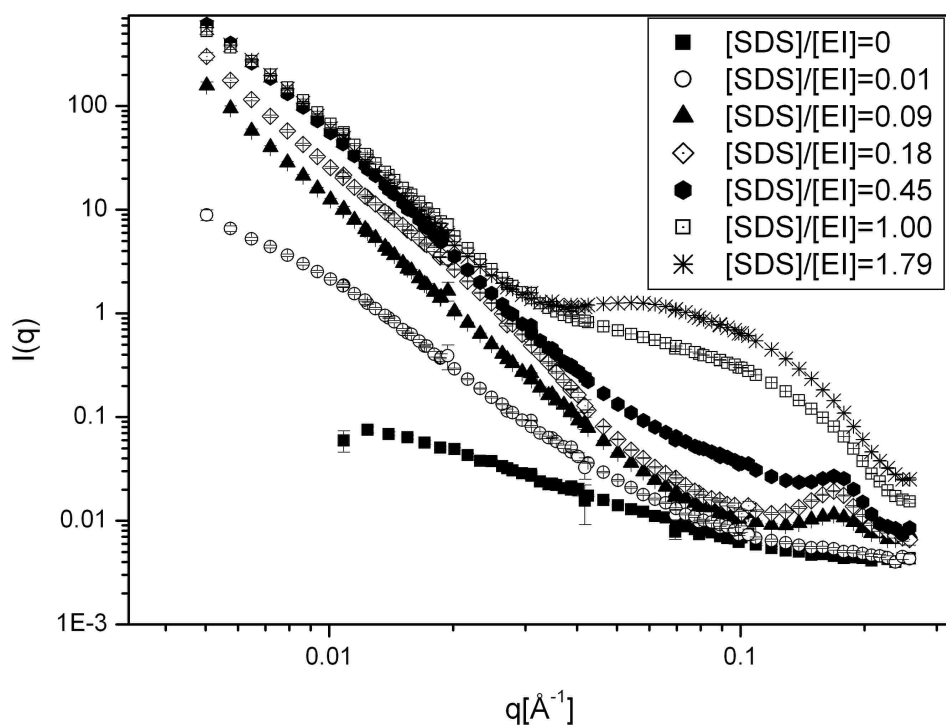



Figure 1: SANS data of PEI samples (2000 ppm) at low pH ( $\sim 5.2$ , high charge) and different h-SDS concentrations in  $\text{D}_2\text{O}$  (different SDS/PEI ratio).

	<b>EXPERIMENTAL REPORT</b>	<b>GeNF SANS-1</b>
<b>Effect of ligand and concentration on structure of <i>Viscum album</i> agglutinin in solution</b>		
<b>Principal Proposer:</b>	<b>H.-J. Gabius<sup>1</sup>, B. Niemeyer<sup>2</sup></b> <sup>1</sup> Institute for Physiological Chemistry, Faculty of Veterinary Medicine, Ludwig- Maximilians-University of Munich, Veterinärstr. 13 D-80539 Munich, Germany, <sup>2</sup> GKSS Research Centre	
<b>Experimental Team:</b>	<b>L.-Z. He<sup>2,3</sup>, Sabine André<sup>1</sup></b> <sup>3</sup> Max Planck Institute for Polymer Research, Ackermannweg 10, D-55128 Mainz, Germany	
<b>Date(s) of Experiment:</b>	June–July 2003	

Lectins are defined as carbohydrate-binding proteins which are distinct from immunoglobulins, do not enzymatically alter the structure of their ligands and do not act as sensor/transport proteins for free mono- or disaccharides. Besides their various physiological function such as mediating crucial cell activities (e.g. fertilization, cell growth and apoptosis, cell adhesion and migration, endocytosis, and immune mediator production/release), lectins can be employed as versatile tools to isolate and characterize diverse glycans of medical or technological interest [1]. *Viscum album* agglutinin (VAA) is a lectin purified from mistletoe, which is a strong immunomodulatory effector. In the present work, the conformation of VAA at different concentrations was investigated in the presence and absence of ligand by small angle neutron scattering.

D<sub>2</sub>O was obtained from Merck (Darmstadt, Germany). The purification of VAA started from aqueous extracts of dried mistletoe leaves and used affinity chromatography on lactosylated Sepharose as the crucial step as previously described [2]. Before SANS measurement, the samples were extensively dialyzed against phosphate buffer (pD 7.2, 20 mM) prepared from D<sub>2</sub>O.

The SANS experiments were performed on the instrument SANS-1 at the Geesthacht Neutron Facility GeNF, Germany. The range of scattering vectors  $q$  ( $q = 4\pi \sin \theta / \lambda$ , where  $2\theta$  is scattering angle and  $\lambda$  is wavelength) from 0.007 to 0.25 Å<sup>-1</sup> was covered by four sample-to-detector distances (from 0.7 to 7 m). For isothermal conditions, a thermostatic sample holder was used. For each sample, the scattering spectra from the corresponding dialysis buffer were also measured, and they were subtracted from the sample data.

The scattering behaviors of VAA at different concentrations are shown in Figure 1. At low angle, the normalized intensities at the concentration of 3.6 mg/ml and 5.9 mg/ml are close to each other. The IFT method gave the radius of gyration with a value of  $51.5 \pm 0.5$  Å at the concentration of 3.6 mg/ml. In contrast, the radius of gyration is  $53 \pm 0.8$  Å at the concentration of 5.9 mg/ml. At a high concentration of 15.6 mg/ml, the normalized intensity at low angle is slightly higher than those at low concentration. This indicates that a high concentration induces further oligomerization of the protein. Indeed, the radius of gyration at this concentration is  $57 \pm 0.9$  Å.

In Figure 2, the effect of ligand on the scattering spectra is presented. In the presence of ligand, the intensities at low angle are significantly lower than those in the absence of ligand. This results in a decrease of radius of gyration from  $53 \pm 0.8 \text{ \AA}$  to  $49 \pm 0.7 \text{ \AA}$ . The data suggest that ligand binding induces a compact conformation of the protein.

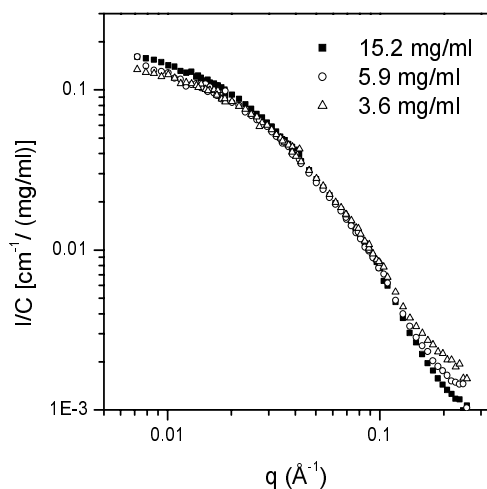



*Figure 1:* Comparison of scattering spectra at different concentrations. The scattering data were normalized by dividing intensities with the concentration.

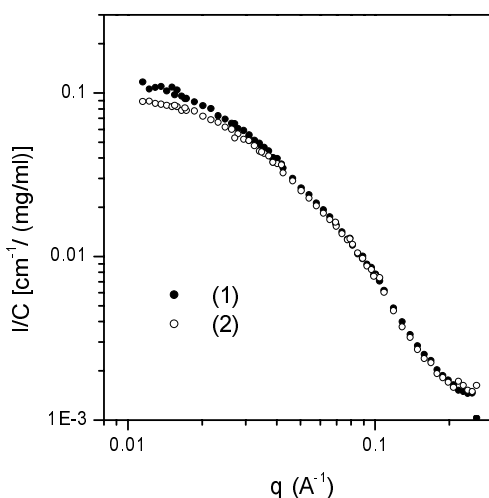


*Figure 2:* Effect of the ligand on the scattering behavior of VAA at the concentration of 5.9 mg/ml. (1) in the absence of the ligand, and (2) in the presence of the ligand (20 mM lactose).

## References

- [1] H.-J. Gabius, *Biochimie* 83 (2001) 659.
- [2] H.-J. Gabius, *Anal. Biochem.* 189(1990) 91.

	<b>EXPERIMENTAL REPORT</b>	<b>GeNF SANS-1</b>
<b>The study of the orbital part of the magnetic scattering amplitude in heavy-fermion substances by means of small angle scattering of polarized neutrons</b>		
<b>Principal Proposer:</b>	<b>S. V. Grigoriev, G. P. Kopitsa</b> Petersburg Nuclear Physics Institute, Gatchina, Russia	
<b>Experimental Team:</b>	<b>S. V. Grigoriev, G. P. Kopitsa</b>	
<b>Date(s) of Experiment:</b>	August 2003	

### Scientific Objective

The proposal was aimed to observe and to investigate the orbital part of the magnetic scattering amplitude in heavy-fermion substances at low temperatures (1 K) by means of small angle polarized neutron scattering (SAPNS). A good example of such systems is a family of compounds  $\text{CeRu}_2(\text{Si}_{1-x}\text{Ge}_x)_2$  [1]. The single crystal  $\text{CeRu}_2\text{Si}_2$  was used in this experiment.

### Theoretical background

The theoretical studies have shown that the magnetic scattering amplitude contains also the contribution of the orbital part of the spin with the singularity near  $Q = 0$  [2]:  $F_{\text{SING}} = -ir (\sigma [\mathbf{Q}\mathbf{x}\mathbf{p}])/Q^2$ , where  $\mathbf{p}$  is the electron momentum. It is also shown that the scattering cross section is proportional to  $(m/M)^2$ , where  $m$  is the effective mass of the carriers. For ordinary metals this factor is of order  $10^{-5}$ - $10^{-6}$  and the neutron-electron scattering is negligibly small. However for some heavy-fermion substances  $m \sim 100 m_e$  [1] and  $(m/M)^2 \sim 10^{-2}$ . In such cases the neutron-carrier scattering could be observed if one takes into account that the static cross section is proportional to  $\theta^{-1}$  for  $2E\theta \gg T$  and  $T/(\theta^2 E)$  for  $T \gg 2E\theta$ , where  $\theta \ll 1$  is the scattering angle and  $E$  is the neutron energy. The crossover from one regime to another is observed at  $q_c = k \sin(T/2E)$ . As a rule the heavy-fermion compounds are strongly disordered and the electron-carrier scattering could be determined as it gives contribution to the spin-flip channel.

### Experimental Technique

The SAPNS experiments were carried out at the SANS-1. A neutron beam with the wavelength  $\lambda = 8.1 \text{ \AA}$  ( $\Delta\lambda/\lambda=0.1$ ) was used. The scattered neutrons were detected by a position sensitive detector with  $64 \times 64$  pixels. The scattering intensity was measured at two different temperatures: room temperature ( $T = 290 \text{ K}$ ) and  $T = 0.14 \text{ K}$  using dilution  $^3\text{He}/^4\text{He}$  cryostat. The external magnetic field was varied from 0 to 2.5 T. The single crystal was oriented in such a way that (001) axis was set perpendicular to the incident beam and parallel to the magnetic field. The scattering intensity and the transmission through the empty cryostat ( $I^{\text{cryo}}(q)$ ,  $T^{\text{cryo}}$ ) and those of the cryostat with the sample ( $I^{\text{cryo+sam}}(q)$ ,  $T^{\text{cryo+sam}}$ ) were studied. We obtained the intensity scattered by the sample only as:  $I^{\text{sam}}(q) = [I^{\text{cryo+sam}}(q) - I^{\text{cryo}}(q) \cdot T^{\text{cryo+sam}}/T^{\text{cryo}}]$ .

### Results

The scattering intensity  $I^{\text{sam}}(q)$  at  $T = 290 \text{ K}$  and  $H = 0$ , at  $T = 0.14 \text{ K}$  and  $H = 0$ , and at  $T = 0.14 \text{ K}$  and  $H = 2.5 \text{ T}$  are shown in Figure 1. Firstly, Fig. 1 demonstrates that the scattering at

low temperatures are higher than that at high temperatures. Secondly, the applied magnetic field influences the scattering, namely, it suppresses the scattering. The additional scattering at low temperatures may be attributed to the orbital part of the magnetic scattering amplitude in the heavy-fermion system under study. We denoted this part of the scattering as an orbital one  $I^{\text{orb}}(q)$  and extracted it from the other scattering processes subtracting  $I^{\text{sam}}(q, T = 290 \text{ K})$  from  $I^{\text{sam}}(q, T = 0.14 \text{ K})$  at  $H = 0$ , i.e.  $I^{\text{orb}}(q) = I^{\text{sam}}(q, T = 0.14 \text{ K}) - I^{\text{sam}}(q, T = 290 \text{ K})$ .

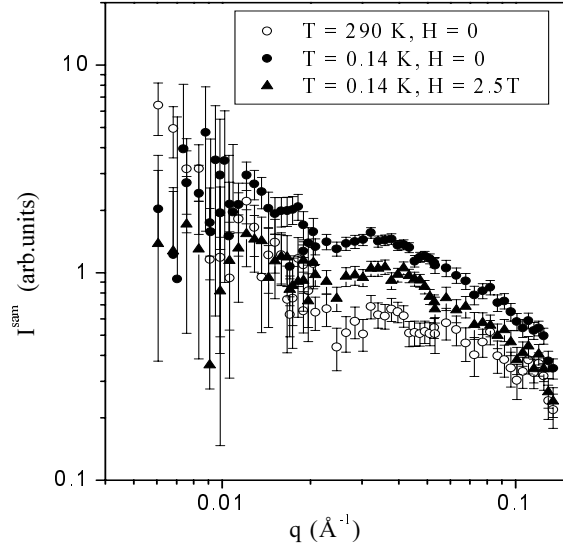


Figure 1.

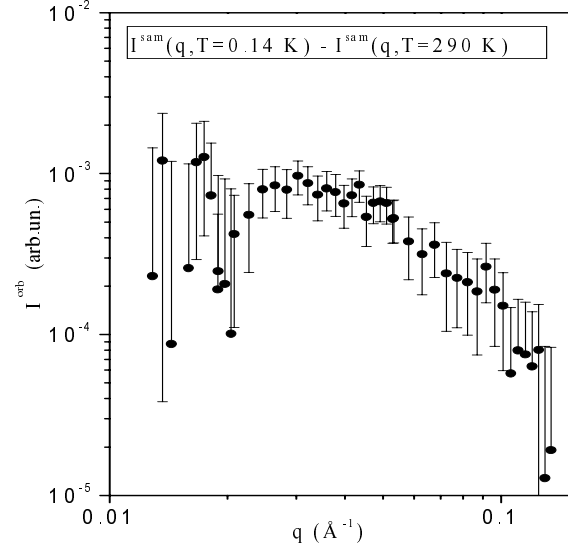
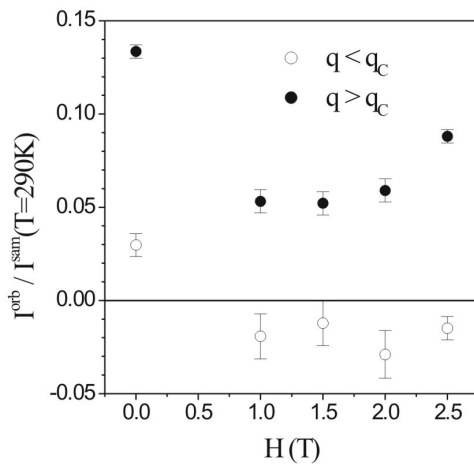


Figure 2.

The  $q$ -dependence of  $I^{\text{orb}}(q)$  is presented in Fig.2. It is well seen in Fig.2 that the scattering is constant with  $q$  at  $q < 0.04 \text{ Å}^{-1}$  and it decreases with  $q$  at  $q > 0.04 \text{ Å}^{-1}$  submitted to the low  $I^{\text{orb}}(q) \sim q^{-1}$ . The crossover point  $q = 0.04 \text{ Å}^{-1}$  well corresponds to the theoretically predicted quantity  $q_c = k(T/2E) = 0.035 \text{ Å}^{-1}$ . The behaviour of the scattering at large  $q$  also corresponds to that predicted theoretically [2].

As was mentioned above the magnetic field effects the scattering intensity at low temperatures. Fig.3 shows the integral scattering intensity as a function of the magnetic field for small- $q$  and large- $q$  limits, i.e. for  $q < q_c$  and for  $q > q_c$ . The integral intensity is suppressed with the field in the intermediate field range at  $H = 1 - 2 \text{ T}$ .



## Conclusion


The experiment shows presence of the additional scattering at low temperatures of order of 1 K. The scattering is affected by the magnetic field of order of 1 T. The theoretical interpretation of the experiment is very desirable.

Figure 3.

## References

- [1] S. Raymont et. al., Physica B, 259-261 (1999) 48-53
- [2] S.L.Ginzburg, S.V. Maleyev, Fiz.Tv.Tela 7, 3065(1965); 8, 2320 (1966).



	<b>EXPERIMENTAL REPORT</b>	<b>GeNF SANS-1</b>
<b>Shape-memory polymers by SANS</b>		
<b>Principal Proposer:</b>	<b>Helmut Kamusewitz<sup>1</sup></b> <sup>1</sup> GKSS Research Centre	
<b>Experimental Team:</b>	<b>Nico Scharnagl<sup>1</sup>, Regine Willumeit<sup>1</sup>, Vasyl Haramus<sup>1</sup></b>	
<b>Date(s) of Experiment:</b>	July, November 2003	

Shape-memory polymers are stimuli-responsive materials. They belong to the group of intelligent respectively smart polymers. Upon application of an external stimulus they have the capability of changing their shape. A change in shape caused by a change in temperature is called thermally induced shape-memory effect. By exceeding the switching temperature  $T_{\text{trans}}$ , the polymer switches from its actual, temporary shape to its memorized, permanent shape. If the shape-memory effect is related to a specific material property of single polymer molecules or rather results from a combination of the polymer structure respectively the polymer morphology together with the applied processing and programming technology is not clear at all. To find an answer to this question SANS-experiments at different temperatures are necessary. For the understanding of the basis of the shape-memory effect, it is important to look at the nano-scale in order to understand how polymer structure, mol weight or phase segregation influence the behaviour of the whole material. The investigation will result in a better view on the molecular movements during the switching and programming steps of the shape-memory effect.

### Synthesis of the shape-memory polymer systems

To evaluate the thermo-mechanical properties of a shape-memory polymer for initial experiments, a stable polymer system (PPDL-co-PCI) was chosen. Afterwards degradable macrodiols like oligo-para-dioxanone (PPDO), oligo- $\epsilon$ -caprolactone (PCI) or Diorez have to be synthesized as well as the relevant combinations of the macrodiol building blocks to polymer systems.

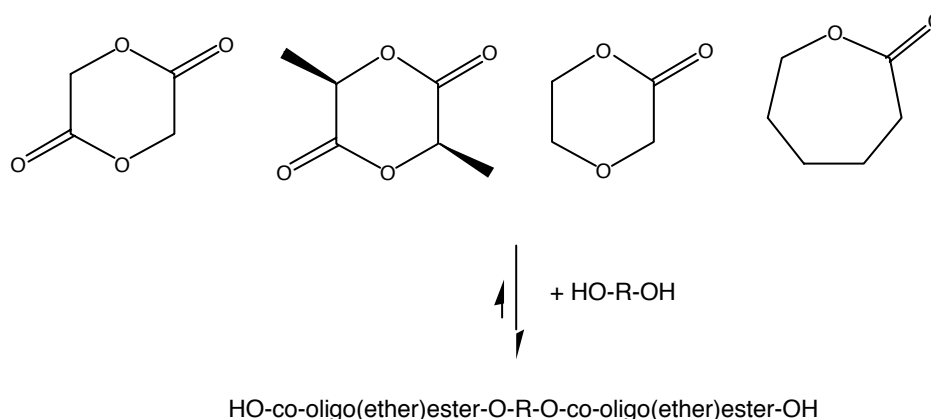


Figure 1: Synthesis of the macrodiols via ring opening polymerization.

SANS measurements were performed in the way of heating-cooling cycles there  $T_{\min} < T_{\text{trans}}$  and  $T_{\max} > T_{\text{trans}}$ . In Figure 2 the scattering data measured on sample (mixture of PPDO and PCI in the ratio 40:60) at temperature below and above  $T_{\text{trans}}$  are shown ( $T_{\text{trans}} = 42^\circ\text{C}$ ). It is clear to see that heating of the sample gives an additional scattering in the intermediate  $q$  region (length scale of about 100–300 Å). The scattering at lower  $q$  (length scale  $> 500$  Å) does not change. Further data analysis will take into account the hierarchy of the complex structure of the shape-memory polymer.

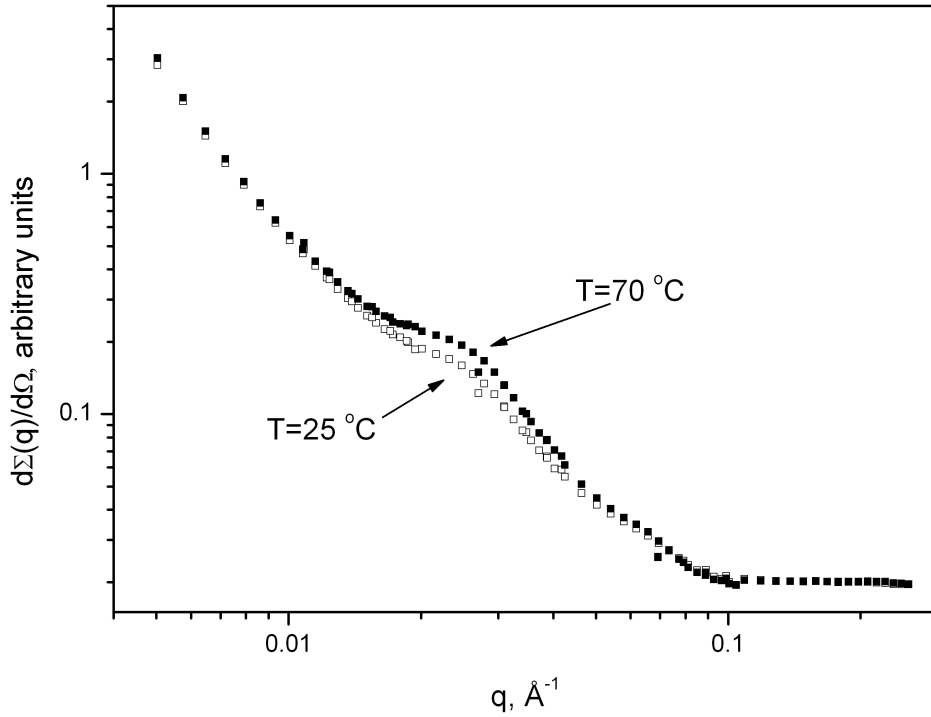



Figure 2: An example of scattering data measured at different temperatures.

	<b>EXPERIMENTAL REPORT</b>	<b>GeNF SANS-1</b>
<b>Localization of titanium dioxide in the solid lipid nanoparticles prepared from carnauba wax</b>		
<b>Principal Proposer:</b>	<b>M. Kumpugdee<sup>1</sup>, C. Müller-Goymann<sup>2</sup></b> <sup>1</sup> GKSS Research Centre <sup>2</sup> Institute of Pharmaceutical Technology, Technical University of Braunschweig, Mendelssohnstr. 1, 38106 Braunschweig, Germany	
<b>Experimental Team:</b>	<b>J. R. V. Hernandez<sup>2</sup></b>	
<b>Date(s) of Experiment:</b>	October–November 2003	

Solid lipid nanoparticles (SLN) are a new generation of drug carriers consisting of an internal solid lipid phase dispersed in an external aqueous phase. The particle sizes of those delivery systems are found in submicron scale<sup>1</sup>. Coated titanium dioxide (TiO<sub>2</sub>) is a commonly used inorganic sunscreen in the cosmetic industry. Conventional sunscreen preparations of that compound are based on the dispersion of the crystals either alone or in combination with organic sunscreens in different media to obtain products with a desired sun protection factor (SPF)<sup>2</sup>. However, the SPF of inorganic pigments encapsulated by substances possessing high crystalline components, such as carnauba wax (CW) has not been reported. The solid lipid nanoparticles composed by the triple combination: carnauba wax – TiO<sub>2</sub> – and excipient has proven to exhibit higher SPFs than those of non encapsulated pigment preparations, particularly, when high concentrations of carnauba wax and TiO<sub>2</sub> are applied<sup>3</sup>. By means of small angle neutron scattering (SANS), the characterization of the solid lipid nanoparticles (SLN) containing encapsulated TiO<sub>2</sub> should be performed. A comparison with TiO<sub>2</sub> free SLN as well as with TiO<sub>2</sub> itself in aqueous dispersion is of particular interest.

This present work was performed by using SANS-1, Geesthacht Neutron Facility (GeNF), Germany, in order to localize the titanium dioxide whether they are only inside the matrix of the nanoparticles or they are also on the surface of the nanoparticles. Figure 1 shows the schematic description of the expected nanoparticles prepared from carnauba wax and TiO<sub>2</sub>. Table 1 shows formulations composition of the two samples that are measured with SANS. Before SANS measurement, the initial concentrated ~ 10 % mixture of particles in H<sub>2</sub>O was diluted with D<sub>2</sub>O to have a concentration of about 1 % w/w. The samples were measured at 15 °C which was controlled by a thermostatic sample holder. For each sample, the scattering spectra from the corresponding blank containing H<sub>2</sub>O and D<sub>2</sub>O at the same ratio as samples were also measured and subtracted from the sample data.

The scattering data were fitted with the power law<sup>4</sup> and the values of slope are obtained. These values can give an answer about the roughness of the surface. If the value is near to -4 it means that the surface is smooth and if it is between -3 and -4 it means that the surface is rough.

Figure 2 shows the scattering data from sample without TiO<sub>2</sub> (formulation a) which suggest the smooth surface because of the slope value ( $\alpha = -4$ ). The scattering from sample composed of TiO<sub>2</sub> (formulation b) follow the power with  $\alpha = -3.5$  which corresponds to rough surface. Therefore we can summarize that TiO<sub>2</sub> are located at the surface of nanoparticles

because the addition of  $\text{TiO}_2$  to solid lipid nanoparticles has changed the properties of surface from smooth to rough one.

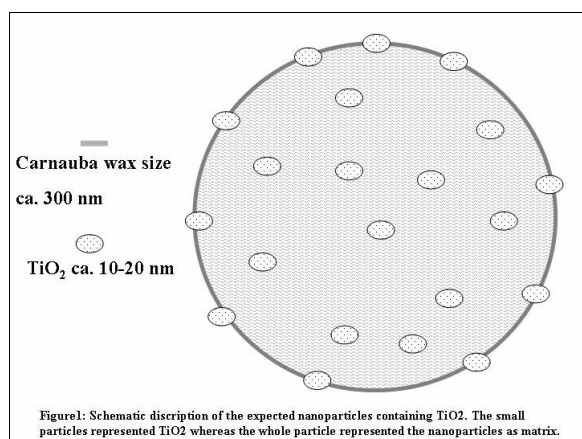


**Table 1: Formulations composition of nanoparticles prepared from carnauba wax free of  $\text{TiO}_2$  (a) and composed of  $\text{TiO}_2$  (b)**

(a) Carnauba wax 10% w/w

Substances	w/w (%)
<b>Lipid phase</b>	
Carnauba wax	10
excipient	5
<b>Aqueous Phase</b>	
excipient	1.04
dd water	q.s. 100%

(b) Carnauba wax 10% w/w and  $\text{TiO}_2$  6% w/w

Substances	w/w (%)
<b>Lipid phase</b>	
Carnauba wax	10
Pigment: $\text{TiO}_2$	6
excipient	5
<b>Aqueous Phase</b>	
excipient	1.04
dd water	q.s. 100%

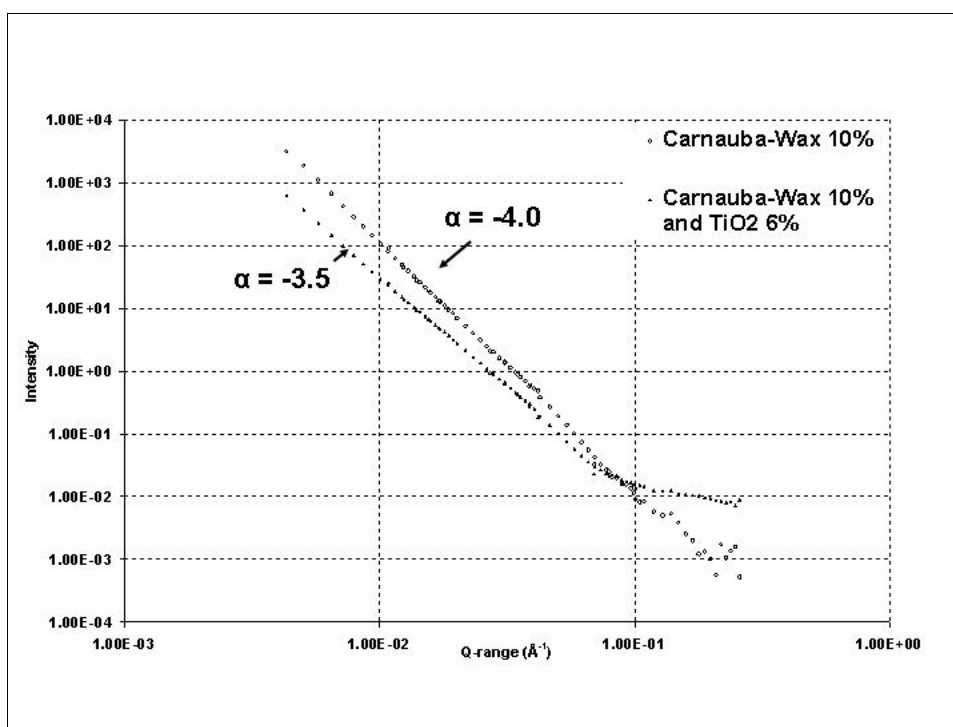



Figure 2: SANS data on sample with and without  $\text{TiO}_2$ .

## References

- [1] K. Tabatt. Pharmazeutische-biotechnologische Anwendungen von Festen Lipidnano-partikel: Vakzinadjuvantien und Gentransfervehikel. Dissertation. FU-Berlin (2002)
- [2] G. P. Dransfield. Inorganic sunscreens. Radiat. Prot. Dosim. 91(1-3), pp 271-273 (2000)
- [3] J. R. Villalobos and C. C. Müller-Goymann. Evaluation of a novel nanoparticle carrier system for inorganic sunscreens based on carnauba wax and decyl oleate. Poster Pub. Pend. (2003)
- [4] P. W. Schmidt: Use of scattering to determine the fractal dimension. in D. Avnir (Ed.), The fractal approach to Heterogeneous Chemistry, Wiley, New York, 67-79 (1989)

	<b>EXPERIMENTAL REPORT</b>	<b>GeNF SANS-1</b>
<b>Micelle growth in aqueous solutions of neutral C14DAO</b>		
<b>Principal Proposer:</b>	<b>Hiroshi Maeda<sup>1</sup>, Jan Skov Pedersen<sup>2</sup></b> <sup>1</sup> Department of Chemistry, Faculty of Science, Kyushu University, Fukuoka, Japan, <sup>2</sup> Department of Chemistry, University of Aarhus, DK-8000 Aarhus Denmark	
<b>Experimental Team:</b>	<b>Hideya Kawasaki<sup>1</sup></b>	
<b>Date(s) of Experiment:</b>	<b>March 2003</b>	

The formation of micelles is specific feature of surfactant molecules which depends on many factors: molecular architecture, nature of solvent, additives, T and P. Interaction and its variation between headgroup of surfactant molecules plays dominant role in the formation of large aggregates (worm-like micelles). The process is induced by increasing of T (non-ionic surfactants), addition of salt (ionic surfactants) or mixing of opposed charged surfactants.

One of alternative method to change headgroup interaction is the charging of initially neutral surfactant (amino oxide head group) by variation of solution pH. It was shown that critical micelle concentration of solution of amino oxide surfactants achieves the minimum at degree of ionization of headgroup  $\alpha = 0.5$  and in opposite the “zero shear” viscosity is at maximum value at  $\alpha = 0.5$ . Formation of hydrogen bonds between headgroups seems to be responsible for these phenomena. It makes studies of amino oxide surfactants quite important for life science there hydrogen bond formation is main driving force of supermolecular structures.

Present studies are the continue of systematic SANS investigations on structure of aggregates – degree of headgroup ionization relationship. It was already observed the formation of long flexible micelles in solutions of tetradecyldimethylamine oxide (C14DAO) at  $\alpha = 0.5$  [1] and the short stiff cylindrical micelles at  $\alpha = 1.0$  [2] at same external conditions.

Here we report results of systematic studies of micelle growth in solution of neutral C14DAO ( $\alpha = 0$ ) with variation of concentration.

The concentration of C14DAO in 0.1 M NaCl/heavy water was varied from  $6.17 \times 10^{-5}$  to  $5.28 \times 10^{-2}$  g/mL (CMC =  $4.63 \times 10^{-5}$  g/mL). Data were analysed by approach developed for growing worm-like micelles [3]. This method consists of separate analysis different q intervals as first step and second step is full q range fitting.

In Figure 1 one can see the dependence the apparent mass of micelles formed by C14DAO with neutral ( $\alpha = 0$ ), half ionized ( $\alpha = 0.5$ ) and full ionized  $\alpha = 1.0$ ) amino oxide head groups versus concentration of surfactant. The micelles of neutral C14DAO are the smaller and do not grow at low and intermediate concentration which points, one more time, on role of hydrogen bond formation in micelle behaviour. The further analysis will take into account interaction among micelles.

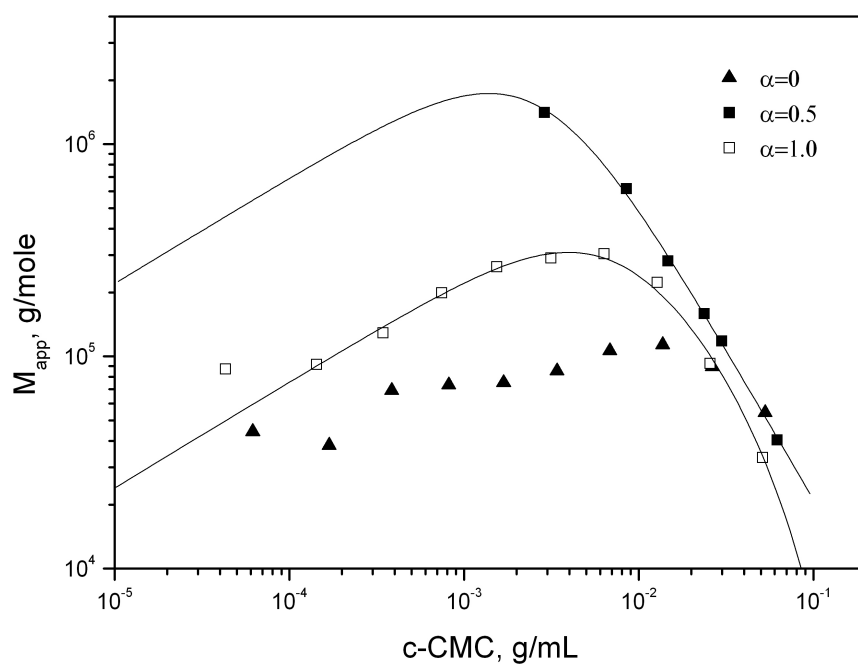



Figure 1: Dependence of apparent mass of micelles ( $M_{app}$ ) versus concentration (c-CMC) at different degree of surfactant ionization ( $\alpha = 0$ , present studies).

## References

- [1] Garamus, V. M.; Pedersen, J. S.; Kawasaki, H.; Maeda, H. *Langmuir* 2000, 16, 6431.
- [2] Garamus, V. M.; Pedersen, J. S.; Maeda, H.; Schurtenberger, P. *Langmuir* 2003, 19, 3656.
- [3] Pedersen, J. S.; Schurtenberger, P. *Macromolecules* 1996, 29, 7602.

	<b>EXPERIMENTAL REPORT</b>	<b>GeNF SANS-1</b>
<b>Small-angle polarized neutron scattering in Invar Fe-Ni-C alloys in magnetic field</b>		
<b>Principal Proposer:</b>	<b>Volodymyr M. Nadutov<sup>1</sup></b> <sup>1</sup> G.V. Kurdyumov Institute for Metal Physics of the N.A.S. of Ukraine, Kyiv, Ukraine	
<b>Experimental Team:</b>	<b>Denys V. Semenov<sup>1</sup></b>	
<b>Date(s) of Experiment:</b>	February 2003	

### Scientific Objective

The small-angle neutron scattering (SANS) in Invar alloys containing 30-35%Ni has magnetic nature [1]. As shown, in Mössbauer studies, carbon varies the hyperfine magnetic fields in the f.c.c. Fe-Ni-based alloys in a wide range and this effect depends on composition [2]. SANS experiment in the Fe–30.5 % Ni–1.5 % C (wt.%) and Fe–30.3 % Ni alloys has shown the growing scattering intensity and two-slope curve of scattering with addition of carbon [3]. We assumed that carbon results in formation of magnetic inhomogeneities possibly originate from inhomogeneous atomic order in the Invar alloys.

In this work the SANS experiment was performed on the Invar type Fe-Ni and Fe-Ni-C alloys using polarized neutrons beam and applied magnetic field in order to excluded magnetic component from the nuclear one in SANS.

### Experimental Technique

The Fe-29.2 % Ni, Fe-30.3 % Ni, Fe-30.5 % Ni-0.4 %C, Fe-30.5 % Ni-1.5 % C, (wt.%) alloys were melted in a vacuum induction furnace in protective argon atmosphere. The ingots were aged at 1000 °C for 3 hours. The carbon concentration was determined by chemical analysis and the content of Ni was obtained by means of X-ray fluorescence analysis. The samples were 2–2.5 mm thick plates, which were solution treated at 1100 °C in vacuum and subsequently quenched in water.

Small-angle neutron scattering experiments were performed at room temperature at the SANS1 instrument at the FRG1 research reactor of GKSS [4]. The neutron wavelength was 8.5 Å and the wavelength resolution was 10 %. The range of scattering vectors  $0.005 < q < 0.25 \text{ Å}^{-1}$  was obtained using four sample-to-detector distances, 0.7–9.7 m. The polarized neutron beam and applied magnetic field of 2.5 T at the samples perpendicular to the neutron beam were used. The initial polarization of the neutrons (parallel to direction of the magnetic field) was close to 1, while the efficiency of the spin flipper to realize the inverse polarization state was 0.9.

### Results

In Figure 1 the  $\varphi$ -averaged scattering intensities in the Fe–30.5 % Ni–1.5 % C (wt.%) alloy for  $H = 0$  and  $H = 2.5 \text{ T}$  are presented. We have observed the dramatically decreasing (from 5 to 20 times) of intensities when magnetic field is applied that points to significant changes in magnetic structure of alloys.

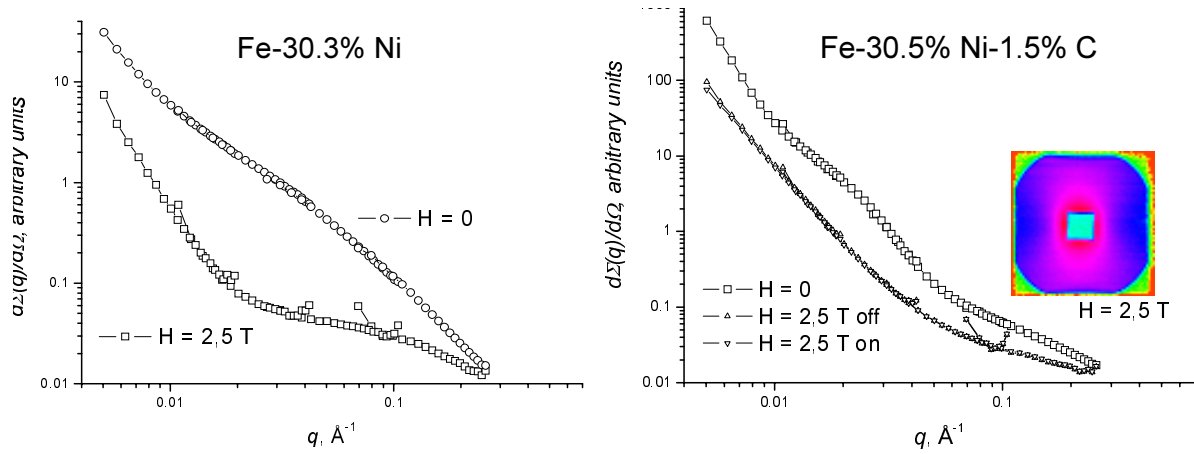


**Figure 1:** Polarized neutrons SAS (averaged by  $\varphi$ -angle and summarized by spin direction) in the Fe–30.3 % Ni and Fe–30.5 % Ni-1.5 % C (wt.%) alloys for  $H = 0$  and  $H = 2,5$  T. Insert is the example of 2D scattering pattern in logarithmic scale obtained at sample detector distance of 1.1 m (large  $q$ ).

The obtained decreasing of scattering intensities of about one order of magnitude under magnetic field gives us possibility to assume this scattering as almost scattering from nuclear structure of alloys  $F_N(q)$ . We can support our suggestion by negligible difference between curves which represent different spin direction  $I(q, H)$  and  $I^+(q, H)$ .

However, the anisotropy of 2D scattering pattern (Fig 1, insert) points to the fact that magnetic scattering is still present even at  $H = 2.5$  T. This effect was observed in all alloys for large  $q$  corresponding to small length-scale inhomogeneities. The mathematical formalism connected with data treatment of SANS patterns from magnetic materials described in Ref. [5] shows that the scattering intensity in the magnetic field comprises the nuclear  $F_N(q)$  contribution and the reduced magnetic  $F_M(q)$  component in the proportion:  $I(q, H = 2.5) = F_N^2(q) + (1/2)F_M^2(q)$ .

To characterize the structures the power-law was applied for approximation of the SANS curves,  $I(q) = Aq^{-\alpha} + B$ . The size of aggregates (for  $q > 0.05 \text{ \AA}^{-1}$ ) was estimated using the Indirect Fourier Transformation method. The analysis of the power-law exponent  $\alpha$  has shown that we observed scattering from the volume and surface fractal-like inhomogeneities. The sizes of aggregates lie in the interval of 16–300 Å. Further experiments with Invar Fe-Ni-C alloys at low temperature are required.


## Acknowledgments

This study was carried out under support of GKSS Research Centre and the Science and Technology Center in Ukraine (the project #2412).

## References

- [1] V. I. Gomankov, I. M. Puzej, V. N. Sigaev, et al., JETP Lett., 13 (1971) pp. 600–603.
- [2] V. M. Nadutov, Ye. O. Svystunov, T. V. Efimova, A. V. Gorbatov. NATO Science Series, II. Mathematics, Physics and Chemistry, 94, Material Research in Atomic Scale by Mössbauer Spectroscopy, M. Mashlan, M. Migliorini and P. Schaaf (eds.) (2003) p. 105.
- [3] V. M. Nadutov, V. M. Garamus, R. Willumeit, Ye. O. Svystunov: Metallofizika i noveishie tekhnologii, 24(5), 717 (2002).
- [4] H. B. Stuhmann, N. Burkhardt, G. Dietrich, R. Jünemann, W. Meerwinck, M. Schmitt, J. Wadzack, R. Willumeit, J. Zhao, K. H. Nierhaus: Nucl. Instr. Meth. A356 (1995), p.133.
- [5] W. Wagner, A. Wiedenmann, W. Petry, A. Geibel, and H. Gleiter, J. Mater. Res. 6 (1991) 2305.; A. Wiedenmann, J. Met. Nanocryst. Mater. 2–6 (1999) 315.



	<b>EXPERIMENTAL REPORT</b>	<b>GeNF SANS-1</b>
<b>Aggregation properties of Monosialoganglioside (GM1) in aqueous solutions measured by Small Angle Neutron Scattering (SANS)</b>		
<b>Principal Proposer:</b>	<b>Bernd Niemeyer<sup>1,2</sup></b> <sup>1</sup> GKSS Research Centre; <sup>2</sup> University of Federal Armed Forces, Institute of Thermodynamics, Hamburg, Germany	
<b>Experimental Team:</b>	<b>Henning Rosenfeld<sup>1</sup></b>	
<b>Date(s) of Experiment:</b>	November 2003	

Gangliosides are components of the external lipid layer of cell plasma membranes of vertebrates and are abundant in nervous system. It is assumed that Gangliosides play a crucial role in the regulation of differentiation and proliferation processes and participate in the process of signal transduction of membrane mediated information. The increasing evidence of these implications has focused attention on the chemical and physicochemical features of Gangliosides. One of most characteristic properties is their amphiphilic character. To accomplish the purification of Gangliosides from natural tissue by means of affinity chromatography using immobilised lectin columns, it is absolute essential to elucidate the adsorption behaviour of monomers, micelles and higher aggregates.

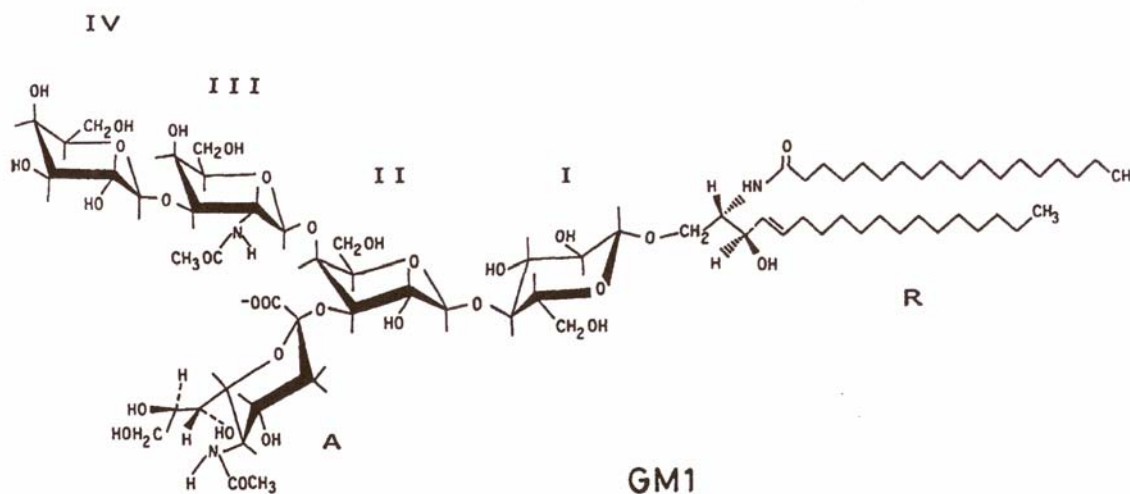


*Figure 1:* I-IV displays the saccharide chain: Glu-Gal-NacGal-Gal respectively (I-IV). The sialic acid that is connected to the Galactose (II) is named A. The bulky head is linked to a double tailed Ceramide moiety.

Micellar properties like molecular weight, size and shape are investigated of Monosialoganglioside (GM1) in the concentration 457 µg/ml dissolved in D<sub>2</sub>O. The molecular weight is 1545 g/mol and the length of the molecule is calculated by Corti et al to be 3.2 nm [1]. The CMC for the Gangliosides GM1 differs in literature in a range about 10<sup>-5</sup> M to 10<sup>-9</sup> M depending on the used method and available purity of the compound. The result of thermodynamic calculations provides a CMC of 2 · 10<sup>-8</sup> M [2]. The specific volume of GM1 is 0.7976 cm<sup>3</sup>/g [1].

Figure 2 shows the neutron scattering cross section  $d\Sigma(q) / d\Omega$  versus the scattering vectors  $q$ . The data are in good agreement with the spherical model. Thus the form of the micelles is spherical.

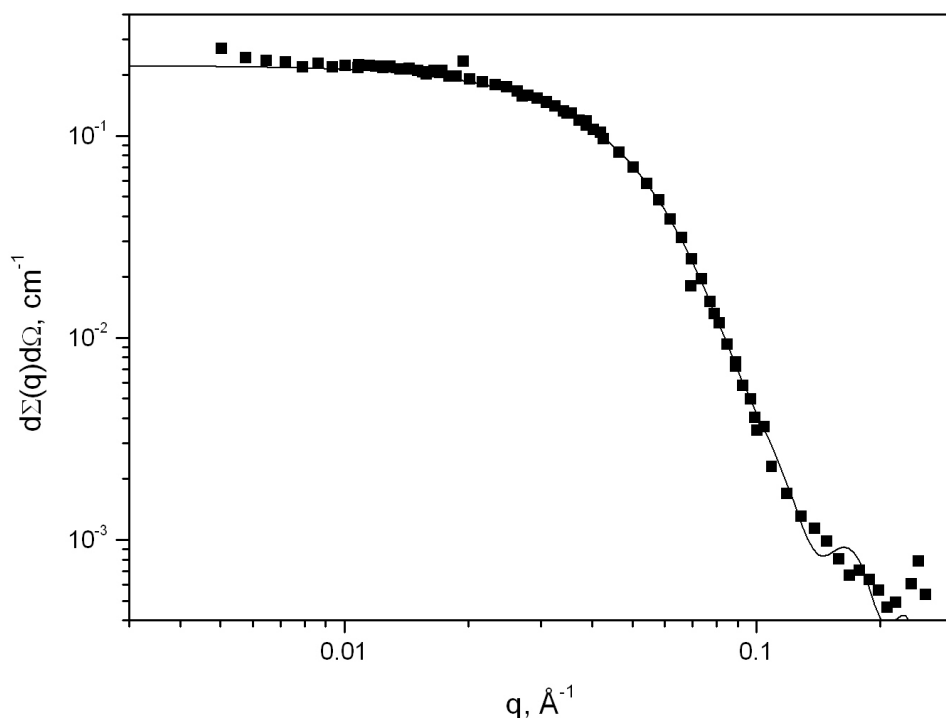



Figure 2: Experimental SANS data (457  $\mu\text{g/ml}$  of GM1) and Fited curves by IFT method (continuous line).

The radius of gyration is obtained via analysis of the SANS data by IFT method.  $R_g = 36.4 \pm 0.5 \text{ \AA}$ . With an approximated  $D_{\text{max}}$  of 100  $\text{\AA}$  for the upper limit for the particle size. The radius of the corresponding homogeneous sphere is calculated to be 47  $\text{\AA}$ .

## References

- [1] Corti, M., L. Cantu and P. Salina. Aggregation Properties of Biological Amphiphiles. *Advances in Colloid and Interface Science*, 36 (1991), pp.153–171.
- [2] Sonnino, S., L. Cantu, M. Corti, D. Acquotti and B. Venerando. Aggregative Properties of gangliosides in solution. *Chemistry and Physics of Lipids*, 71 (1994), pp. 21–45.

	<b>EXPERIMENTAL REPORT</b>	<b>GeNF SANS-1</b>
<b>Structural investigation of a transcription factor p63 in solution by small angle neutron scattering</b>		
<b>Principal Proposer:</b>	<b>Horng Der OU<sup>1,2</sup>, Volker Dötsch<sup>2</sup></b> <sup>1</sup> Graduate Group in Biophysics, University of California San Francisco, San Francisco, California 94143, USA <sup>2</sup> Institute of Biophysical Chemistry, Biocenter, Johann Wolfgang Goethe-Universität Frankfurt am Main, Marie Curie Straße 9, D-60439 Frankfurt, Germany	
<b>Experimental Team:</b>	<b>Horng Der OU<sup>1,2</sup>, Volker Dötsch<sup>2</sup></b>	
<b>Date(s) of Experiment:</b>	September 2003	

p63 is an essential transcription factor in gene regulation during development. Knock-out mice of p63 exhibits abnormal limb development and the absence of differentiated epidermal cells (Mills et. al. 1999; Yang et.al. 1999). This protein is expressed in the cell in six different spliced forms, which depend on the composition of three different C-terminus domains and the presence or the lack of the transactivation domain (TA) at the N-terminus. In previous work (Serber et al., 2002), we found that the TID domain can interact with the TA domain of p63 and inhibiting its transcriptional activity. Thus, a deletion of this domain can restore the activity of this protein. It is suggested that the TID-TA interaction can adopt a compact structure, while a disruption of this interaction results in a loose conformation. However, there is no experimental evidence to address this issue. In this work, we aim to investigate the conformation of this protein in solution using small angle neutron scattering (SANS).

p63 $\alpha$  is purified from *E. Coli* and exchanged into D2O buffer (20mM Bis-Tris Propane, 150mM NaCl, 3mM TCEP) before SANS measurement. The SANS experiments were performed on the instrument SANS-1. The range of scattering vectors  $q$  from 0.007 to 0.25 Å<sup>-1</sup> was covered using four sample-to-detector distances (from 0.7 to 7 m).

## Results and Discussion

Figure 1 shows the scattering curve of p63 at 8 °C. Fitting the curves using the Glatter method gave the radius of gyration with a value of 90 Å and Dmax = 260 Å for the maximum size of the protein. This indicates that the protein has an elongated shape (e.g. cylinder or ellipsoid). Furthermore, using BSA as a standard solution, the molecular weight of the protein calculated from SANS data was 350 kD, which was slightly higher than the value (280 kD) from its sequence. The high experimental value of the molecular weight might be caused by a small amount of aggregates in the sample. Further experiment using highly purified protein is planned for the next round of SANS experiment, which will allow us to obtain the low resolution structure of the protein.

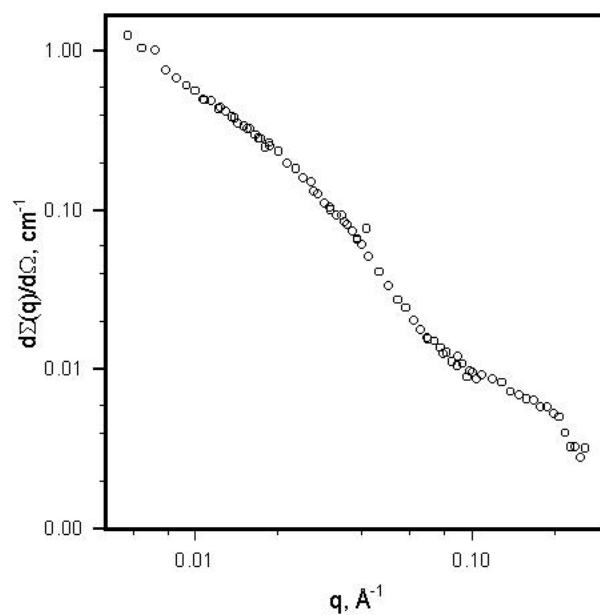



Figure 1: Scattering spectra of p63 with a concentration of 2.9 mg/ml at 8 °C.

## References

- Mills A. A, Zheng B., Wang X. J., Vogel H., Roop D. R., Bradley A. *Nature*, 1999, 398, pp. 708–713.
- Serber Z, Lai H. C., Yang A, Ou H. D., Sigal MS, Kelly A. E., Darimont B. D., Duijf PH, Van Bokhoven H., McKeon F, Dotsch V.. *Mol. Cell. Biol.* 2002, 22, pp. 8601–8611
- Yang A., Schweitzer R., Sun D., Kaghad M., Walker N., Bronson R. T., Tabin C., Sharpe A., Caput D., Crum C., McKeon F. *Nature*, 1999, 398, pp. 714–718.

	<b>EXPERIMENTAL REPORT</b>	<b>GeNF SANS-1</b>
<b>Characterisation of hyperbranched polyglycerols with SANS</b>		
<b>Principal Proposer:</b>	<b>Walter Richtering<sup>1</sup></b> <sup>1</sup> RWTH Aachen, Physikalische Chemie II, Aachen, Germany	
<b>Experimental Team:</b>	<b>Tatiana Maksimova<sup>2</sup>, Stefan Mecking<sup>3</sup>, Ulf Schlitterbeck<sup>3</sup></b> <sup>2</sup> University of Kiel, Institute of Physical Chemistry, Kiel, Germany <sup>3</sup> Institute for Macromolecular Chemistry, Albert-Ludwigs-University Freiburg, Germany	
<b>Date(s) of Experiment:</b>	April–June, September 2003	

Hyperbranched polymers (HPs) are a relatively new type of highly branched macromolecules with a treelike topology and a large number of functional groups. These kinds of polymer structures are known from polysaccharides such as glycogen, dextran, and amylopectin since the 1930s. Unlike dendrimers, HPs with similar properties can be easily synthesized via one-step reactions<sup>1</sup> and therefore represent economically promising products for large-scale industrial applications. Their molecular architecture is not as well-defined as for dendrimers and their molecular mass distribution is not monodisperse, giving rise to different properties. For example, dendrimers display a maximum in the relationship between their intrinsic viscosity and molecular mass, while in general HPs do not.<sup>1</sup>

We investigated Polyglycerols core of different averaged molecular weight. The samples were synthesized in Institute for Macromolecular Chemistry, Albert-Ludwigs-University Freiburg. As solvent we used D<sub>2</sub>O and deuteriomethanol (CD<sub>3</sub>OD). The samples were measured at 25 °C in quartz cuvettes with a path length of 1 and 2 mm.

All curves show at low  $q$  a typical Guinier behavior originating from the overall size of polymers. The sizes (radius of gyration ( $R_g$ )) of polymers and the mass of polymer aggregates  $M_w$  in solution (scattering intensity at zero angle ( $d\Sigma(0)/d\Omega$ )) were obtained from the Guinier approximation, the Zimm approximation of the inverse of the scattering intensity and indirect Fourier transformation methods (IFT). Different approaches give the consistent values of parameters.

For solution in D<sub>2</sub>O appears the problem of deuterium exchange. A part of hydrogen atoms in a particle can be substituted by deuterium atoms that reduce to exchange of scattering length density of particle. The upper value of deuteration is achieved when all atoms of hydrogen in polar groups of polymer are substituted. We have calculated  $M_w$  with/without deuterium exchange for hyperbranched polyglycerols in D<sub>2</sub>O. The scattering length density of polymer increases by taking into account the deuterium exchange. In the result of that we have got the small increasing of  $M_w$ .

Dependence of the size of HPs ( $R_g$ ) on molecular mass of HPs ( $M_w$ ) for different solvents taking into account substitution of H atoms by D atoms in heavy water is shown in figure 1.

$R_g$  increases with the increase of  $M_w$  of polymer and is larger for HPs in CD<sub>3</sub>OD than in D<sub>2</sub>O. Also the value of parameter  $\alpha$  is larger for HPs in D<sub>2</sub>O which show the more non-compact or non-spherical structure of HPs in D<sub>2</sub>O than CD<sub>3</sub>OD. For CD<sub>3</sub>OD the parameter  $\alpha$  is equal to 1/3 which points on compact 3D structures.

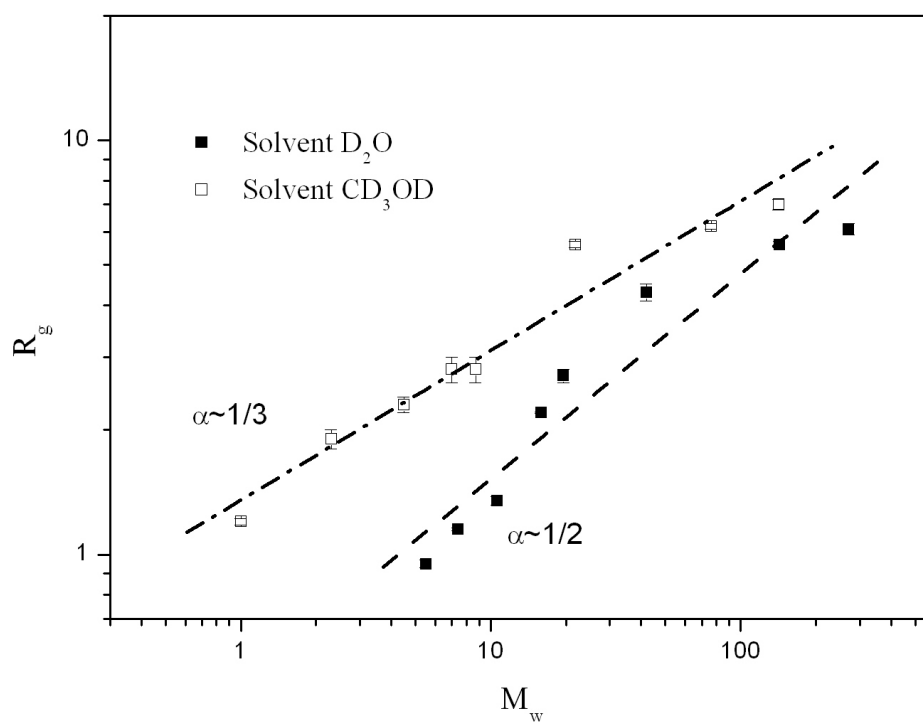


Figure 1. Dependence of  $R_g$  of HPs on the mass  $M_w$  of polymer obtained from SANS in different solvents. Straight lines are the fit  $R_g \sim M_w^\alpha$ .

## Reference

Frechet, J. M. J.; Hawker, C. J.; Gitsov, I.; Leon, J. W. *Pure Appl. Chem.* 1996. A33, 1399

	<b>EXPERIMENTAL REPORT</b>	<b>GeNF SANS-1</b>
<b>Contrast variation method for investigation of the polyethelenimine-amides solutions with/without silver nanoparticles</b>		
<b>Principal Proposer:</b>	<b>Walter Richtering<sup>1</sup></b> <sup>1</sup> RWTH Aachen, Physikalische Chemie II, Aachen, Germany	
<b>Experimental Team:</b>	<b>Tatiana Maksimova<sup>2</sup>, Stefan Mecking<sup>3</sup>, Lydie Antonietti<sup>3</sup></b> <sup>2</sup> University of Kiel, Institute of Physical Chemistry, Kiel, Germany <sup>3</sup> Institute for Macromolecular Chemistry, Albert-Ludwigs-University Freiburg, Germany	
<b>Date(s) of Experiment:</b>	September, November, December 2003	

Recent approaches of the controlled preparation of metal or semiconductor nanoparticles have utilized surfactants or the self-assembled nanostructures of block copolymer micelles [1]. However, template structures from a larger number of individual molecules are very dynamic in solution. Thus, their size and aggregation numbers are subject of fluctuations, and such structures can be shear-sensitive. Therefore, the concept of particle preparation in macromolecular compartments has been explored. Polymerized micelles [2], and very recently dendrimers [3] have been employed.

The high selectivity and activity of homogeneous catalysts based on soluble metal complexes are opposed by a usually tedious separation from the products, often involving thermal strain on the reactants. In most cases, the development of materials combining the advantages of classical homogeneous and heterogeneous catalysts remains an exclusive goal. Soluble nanoparticles might bridge this gap. Different reactions of model substrates, catalysed by metal particles prepared by some of the above routes have been reported recently [4]. However, the fundamental issue of catalyst recycling has virtually not been addressed utilizing well defined systems.

As a different approach, we have used hyperbranched polymers for the synthesis of stable silver nanoparticles. We investigated the Polyethyleneimines Amides (PEI5k/AmC16<sup>lin</sup> 45% and PEI25k/AmC16<sup>lin</sup> 34%) solutions with/without silver nanoparticles contrast variation method of SANS. Wide range of contrast was covered varying the solvent (C<sub>6</sub>H<sub>6</sub>/C<sub>6</sub>D<sub>6</sub> mixture).

The samples were synthesized in Institute for Makromolekular Chemistry, Albert-Ludwigs-University Freiburg. The concentration of polymer in solutions was kept constant 0.5 wt.% and content of C<sub>6</sub>H<sub>6</sub> (C<sub>6</sub>H<sub>6</sub>/C<sub>6</sub>D<sub>6</sub> mixture) was varied from 0 to 0.5. The samples were measured at 25 °C in quartz cells with a path length of 1 mm.

The scattering data were analyzed by Indirect Fourier Transformation analysis and such parameters of system as scattering at “zero angle” ( $d\Sigma(0)/d\Omega$ ) and radius of gyration ( $R_g$ ) vs scattering length density of solvent were obtained.

Figure 1 shows the square root of zero-angle scattering as a linear function of the scattering-length density of the solvent for PEI25k/AmC16<sup>lin</sup> 34% solutions with/without silver nanoparticles.

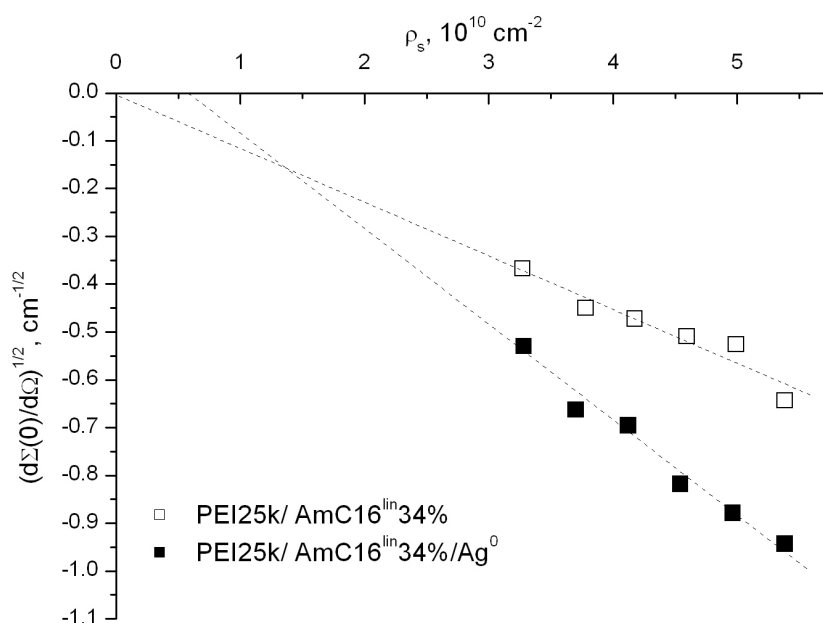


Figure 1: The square root of zero-angle scattering as linear function of the scattering-length density of the solvent.


Important characteristic of studied aggregates is “compensation point” by that  $\Delta\rho = 0$  ( $d\Sigma(0)/d\Omega = 0$ ). In this point is  $\bar{\rho} = \rho_s$  i.e., the value of  $\rho_s$  is equal to average value of scattering length density of a particle.

For PEI5k/Am<sup>lin</sup>C<sub>16</sub>45% + Ag nanoparticles we have obtained  $\bar{\rho} = 1.05 \cdot 10^{10} \text{ cm}^{-2}$  and without silver -  $\bar{\rho} = 0.093 \cdot 10^{10} \text{ cm}^{-2}$ . Average scattering length density for pure PEI25k/AmC16<sup>lin</sup> 34% -  $\bar{\rho} = (-0.034 \pm 0.093) \cdot 10^{10} \text{ cm}^{-2}$  is lower than for PEI25k/AmC16<sup>lin</sup> 34%/Ag<sup>0</sup> ( $\bar{\rho} = (0.58 \pm 0.07) \cdot 10^{10} \text{ cm}^{-2}$ ). Volume fraction of Ag<sup>0</sup> can be obtained from values of scattering length density of pure Ag<sup>0</sup>. The calculated radii of gyration for hyperbranched polyethyleneimines PEI5k/Am<sup>lin</sup>C<sub>16</sub>45% and PEI25k/AmC16<sup>lin</sup> 34% with/without silver in C<sub>6</sub>D<sub>6</sub>/C<sub>6</sub>H<sub>6</sub> are analysed by Stuhrmann approach [5]. The main conclusion is that Ag<sup>0</sup> particles locate more at periphery of aggregates but its enrichment is quite small in PEI25k/AmC16<sup>lin</sup> 34%/Ag<sup>0</sup> complexes.

## References

- [1] Spatz, J.P.; Roescher, A.; Moeller, M. *Adv. Mater.* 1996, 8, 337–340
- [2] Kurihara, K.; Fendler, J.H. *J. Am. Chem. Soc.* 1983, 105, 6152
- [3] Zhao, M.; Sun, L.; Crooks, R. M. *J. Am. Chem. Soc.* 1998, 120, 4877
- [4] Boennemann, H.; Brijoux, W.; Brinkmann, R.; Dinjus, E.; Jousen, T.; Korall, B. *Angew. Chem., Int. Ed. Engl.* 1991, 30, 1312
- [5] Stuhrmann, H.B.; Kirste, R. *G. Z. Phys. Chem.* 1967, vol. 56, 334–341



	<b>EXPERIMENTAL REPORT</b>	<b>GeNF SANS-1</b>
<b>Investigation of the supramolecular structures of (<i>cis</i>-9-octadecenyl) glycosides</b>		
<b>Principal Proposer:</b>	<b>Volkmar Vill<sup>1</sup></b> <sup>1</sup> Universität Hamburg, Inst. f. Organische Chemie, Martin-Luther-King-Platz 6, 20146 Hamburg	
<b>Experimental Team:</b>	<b>Götz Milkereit<sup>1</sup>, Koen Veermans<sup>1</sup></b>	
<b>Date(s) of Experiment:</b>	May, September-November 2003	

The unique properties of the solutions of amphiphilic molecules in polar (e.g. water) and non-polar (e.g. paraffin) solvents are well-known. The molecular structure of amphiphilic compounds has a great influence on the formation of specific structures like spherical micelles, rod-like and wormlike aggregates, vesicles and lamellar aggregates. Although other properties of solutions like the CMC, solubility of non-dissolved substances or phase borders are depending on the molecular shape of the amphiphile [1]. The delicate balance between opposite forces associated with the hydrophobic and the hydrophilic parts of the molecule plays an key role, especially in the case of long chain surfactants.

We have investigated a set of synthetic alkylglycosides in dilute solutions (Figure 1). To derive structure property relationship the alkyl chain type was kept constant and the polar head group was changed systematically. This gives the possibility to separate the influence of the head group size from the chemical nature of the aggregation properties of solutions. All substances have long unsaturated oleyl alkyl chains – (*cis*-9-octadecenyl) and different head groups: disaccharide – 4-*O*-( $\alpha$ -D-glucopyranosyl)- $\beta$ -D-glucopyranoside (**1**); trisaccharide – 4-*O*-[4'-*O*-( $\alpha$ -D-glucopyranosyl)- $\alpha$ -D-glucopyranosyl]- $\beta$ -D-glucopyranoside (**2**) and modified by an ethylamino spacer between the alkyl chain and the headgroup (2''-aminoethyl) 4-*O*-( $\alpha$ -D-glucopyranosyl)- $\beta$ -D-glucopyranoside (**3**).

The surfactants were synthesized using standard procedures [2,3,4]. Size and shape of the aggregates in dilute solutions (micellar L<sub>1</sub> phase) were studied by small angle neutron scattering (SANS) methods.

The results from the SANS data analysis are shown in Table 1. It is observed that the micellar structure changes from large worm-like aggregates to smaller mostly stiff rod-like objects and further to relatively small nearly spherical micelles with increasing size of the surfactant head group. The first interesting observation is that the normal alkyl glycoside **1** forms large micelles. This has not been reported yet for long chain alkyl glycosides in their pure state. Furthermore it can be seen, that even small changes in the polar/alkyl chain balance of the molecule leads to drastic changes in the structure of the aggregates of the aggregates. In case of compound **1** and **3** the introduction of a small polar spacer increases the size of the headgroup only a little but this change leads to the formation of shorter cylindrical micelles. Although the flexibility if the micelles decreases, possible due to the strong influence of hydrogen bonding networks normally built up by amidic groups.

In case of compound **2** the disaccharide headgroup is exchanged by a trisaccharide headgroup. As observed by polarizing microscopy the micellar  $L_1$  phase disappears, and a texture, similar to the discontinuous cubic phase is observed. Further x-ray diffraction experiments were carried but results are not available at the moment.

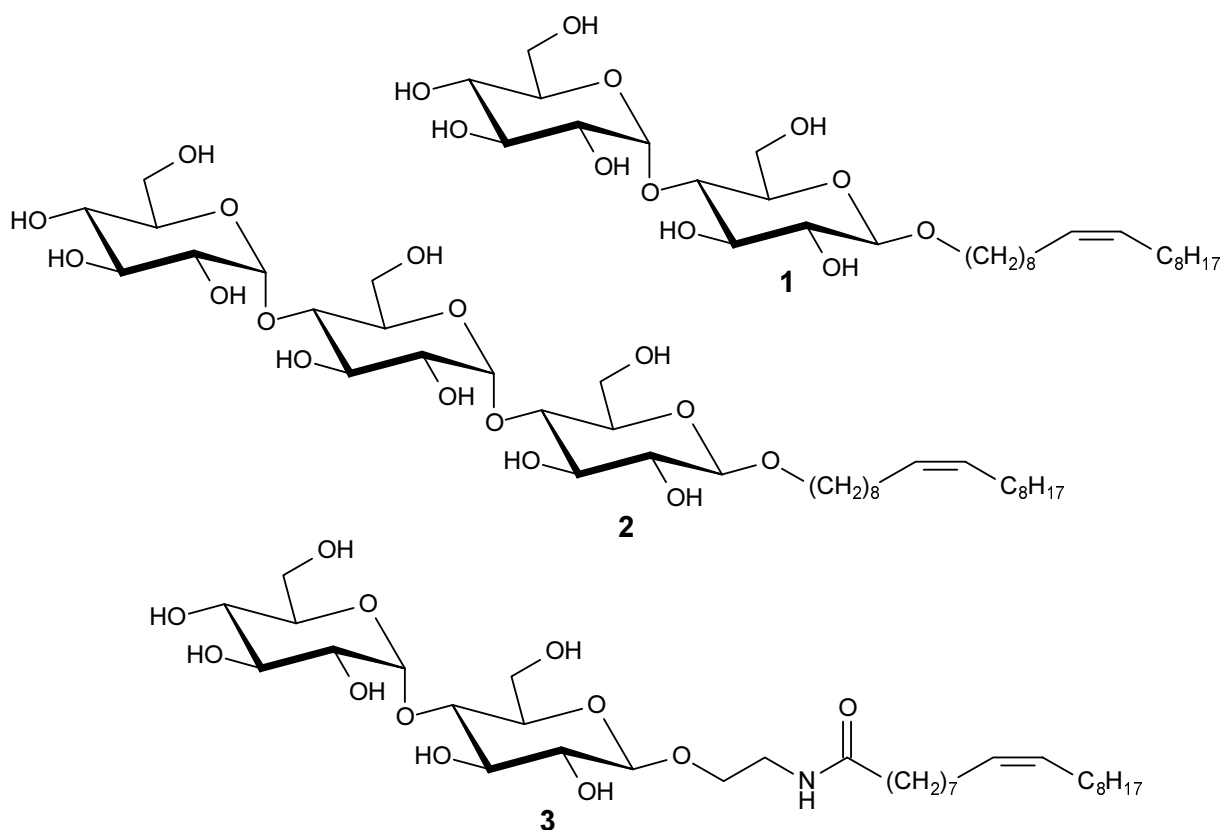



Figure 1: Chemical structures of the investigated glycolipids.

Table 1: Results of SANS data analysis by model independent approach.

Compounds	<b>1</b>	<b>2</b>	<b>3</b>
Type of micelles	Worm-like	Spheres	Stiff cylinders
Radius or cross-section radius, Å	24.7	32.7	24.2
Length, Å	> 1300	-/-	542
Persistent length	~ 190	-/-	-/-
$N_{agg}$	> 2400	155	926

## References

- [1] B. Jönsson, B. Lindman, K. Holmberg and B. Kronberg, *Surfactants and Polymers in Aqueous Solution*, John Wiley & Sons, New York, 1998, 423
- [2] H. M. von Minden, K. Brandenburg, U. Seydel, M. H.J. Koch, V. M. Garamus, R. Willumeit, V. Vill, *Chem. Phys. Lipids*, 2000, 106, 157–179.
- [3] G. Milkereit, V. M. Garamus, K. Veermans, R. Willumeit, V. Vill, *Langmuir*, submitted.
- [4] G. Milkereit, K. Veermans, V. Vill, *Chem. Phys. Lipids*, submitted.

	<b>EXPERIMENTAL REPORT</b>	<b>GeNF SANS-1</b>
<b>SANS study of the phase behaviour of <i>N</i>-Hexadecanoyl-1,3-di-O-<math>\beta</math>-D-glucopyranosyl-2-deoxy-2-amino-<i>sn</i>-glycerol</b>		
<b>Principal Proposer:</b>	<b>Volkmar Vill<sup>1</sup></b> <sup>1</sup> Universität Hamburg, Inst. f. Organische Chemie, Martin-Luther-King-Platz 6, 20146 Hamburg	
<b>Experimental Team:</b>	<b>Götz Milkereit<sup>1</sup>, Koen Veermans<sup>1</sup></b> <sup>1</sup> Universität Hamburg, Inst. f. Organische Chemie, Martin-Luther-King-Platz 6, 20146 Hamburg	
<b>Date(s) of Experiment:</b>	July, October 2003	

We have measured solutions of the synthetic glycolipid *N*-Hexadecanoyl-1,3-di-O- $\beta$ -D-glucopyranosyl-2-deoxy-2-amino-*sn*-glycerol (**1**) (figure 1). Glycolipids as well as other amphotropic molecules form both thermotropic liquid crystalline phases in their pure state upon heating and lyotropic liquid crystalline phases upon the addition of solvent. The principal phase behaviour is described in the literature [2–5]. Between the micellar solution and the hexagonal phase discontinuous cubic phases may occur.

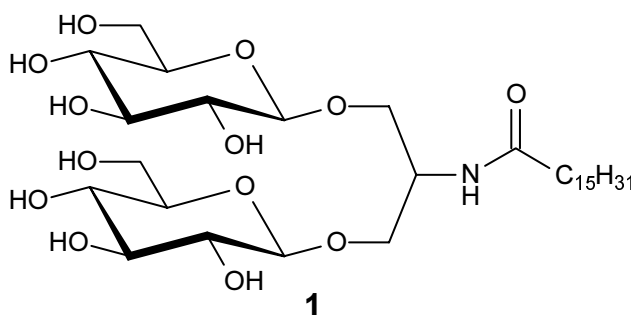


*Figure 1:* Structure of *N*-Hexadecanoyl-1,3-di-O- $\beta$ -D-glucopyranosyl-2-deoxy-2-amino-*sn*-glycerol

The lyotropism was measured using the contact preparation technique. Compound **1** displayed in the contact with water the phase sequence:



The cubic phase can have two possible shapes, discontinuous and bicontinuous phases. Whereas the discontinuous cubic phases are based upon various packing of spherical or slightly anisotropic micelles, the bicontinuous cubic phases with interwoven fluid structures are based upon underlying infinite periodic minimal surfaces [6].

The fitting results of obtained SANS data are shown in Figure 2, showing the model fit for spherical micelles and the data. The fitting of the data shows another interesting result of the experiments. It can be seen, that the fitted curve is close to the experimental data. But it is remarkable that at low  $q$  values, the curves of the model fit and the experimental data diverge, and this discrepancy is cannot be explained as an experimental error. We assume that in this experiment we observed the formation of an non micellar aggregate besides the

spherical micelles. The lowest part of experimental data ( $q < 0.01 \text{ \AA}^{-1}$ ) was analysed by power law

$$d\Sigma(q)/d\Omega \sim q^{-\alpha}.$$

The obtained value of  $\alpha$  is equal to  $2.7 \pm 0.1$  which points on the formation of aggregates with a relation between the mass ( $M$ ) and linear sizes ( $r$ ) as  $M \sim r^{2.7}$  for an length scale of  $r > 300 \text{ \AA}$ .

Looking at the phase sequence obtained by the contact preparation, this should be the begin of the phase transition from the cubic/micellar phase to the hexagonal phase. However from the neutron scattering data it was not possible to obtain information about the space group of this cubic phase, this information can be provided by x-ray diffraction experiments.

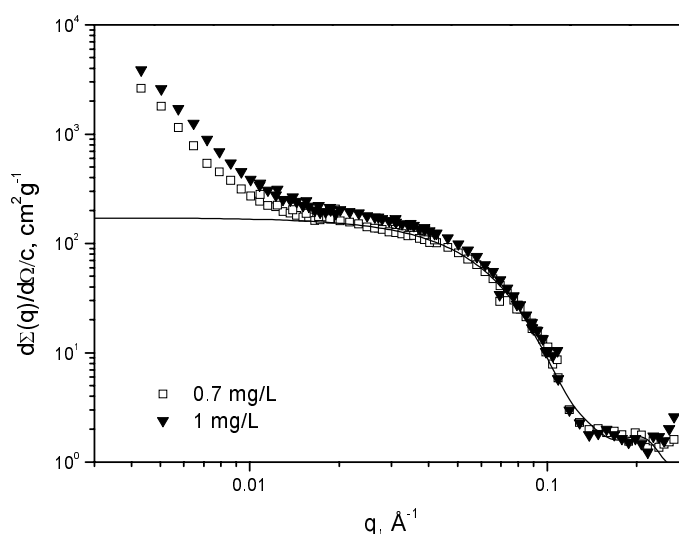



Figure 2. Scattering data for  $c = 7.0 \times 10^{-4} \text{ g/mL}$  (empty squares) and  $c = 10.0 \times 10^{-4} \text{ g/mL}$  (solid triangles) together with the model fit for spherical micelles (solid line).

## References

- [1] G. Milkereit, V. M. Garamus, K. Veermans, R. Willumeit, V. Vill, *Chem. Phys. Lipids*, *submitted*.
- [2] Curatolo, W., *Biochim. Biophys. Acta*, 1987, 779, 381–401.
- [3] Prade, H., Miethchen, R., Vill, V., *J. Prakt. Chem.*, 1995, 337, 427–440.
- [4] Blunk, D., Praefke, K., Vill, V., Amphotropic liquid crystals. In: Demus, D., Goodby, J., Gray, G. W., Spiess, H.-W., Vill, V. (Eds.), *Handbook of Liquid Crystals*, Vol. 3, 1998 Wiley-VCH, Weinheim, pp. 305–340.
- [5] Jeffrey, G. A., Wingert, L. M., *Liq. Cryst.*, 1992, 12, 179–202.
- [6] Fairhurst, C. E., Fuller, S., Gray, J., Holmes, M. C., Tiddy, G. J., Lyotropic surfactant liquid crystals. In: Demus, D., Goodby, J., Gray, G. W., Spiess, H.-W., Vill, V. (Eds.), *Handbook of Liquid Crystals*, Vol. 3, 1998, Wiley-VCH, Weinheim, pp. 341–392.

	<b>EXPERIMENTAL REPORT</b>	<b>GeNF SANS-1</b>
<b>Polarized proton target as broadband, wavelength independent neutron spin polarizer</b>		
<b>Principal Proposer:</b>	<b>Jinkui Zhao</b> Spallation Neutron Source, Oak Ridge National Lab. Oak Ridge, TN, USA	
<b>Experimental Team:</b>	<b>Jinkui Zhao</b>	
<b>Date(s) of Experiment:</b>	April–May 2003	

With the construction of the Spallation Neutron Source at the Oak Ridge National Laboratory, USA, accelerator-based next generation neutron sources are going to play a key role in many areas of scientific research. One of neutron's unique features is that its scattering is spin-dependent, which offers a unique way to study many materials that are otherwise difficult or impossible. On reactor sources, polarized neutron beams are typically obtained using crystals or super mirrors. At pulsed neutron sources, where broadband polarizers are required, these polarizing techniques are difficult to apply, especially for neutrons with shorter wavelength. A polarized  $^3\text{He}$  filter provides a good broadband polarizer. However, it also has its practical and intrinsic limitations. Obtaining very high  $^3\text{He}$  polarization is difficult at the present, and the neutron polarization thus obtained is wavelength dependent.

Dynamically polarized hydrogen (DNP) target offers a new way to achieve broadband neutron polarizations. The scattering cross section of protons strongly depends on the spin states of the protons and of the neutrons. This property can be exploited to build a broadband neutron polarizer. Such a polarizer has the intrinsic advantage of wavelength independence. The current experiment is intended to test the feasibility of using the dynamically polarized hydrogen target as a neutron polarizer.

The experimental setup uses the DNP target at the SANS-1 instrument with modified beam geometry: the polarizer and guide field on the instrument is turned off. The standard 1mm thick glycerol/water mix solvent sample was used. The size of the neutron beam at the sample is about  $14 \times 14 \text{ mm}^2$ . A 2 mm pinhole slit was put in front of the flipper and is 1 m away from the sample. Neutron polarization was analyzed after the neutrons passed the DNP-sample using a supermirror analyzer. The wavelength of the neutrons is 8.1 Å.

Proton polarization of ~70 % was achieved. No further effort was invested to achieve even higher proton polarization due to time constraints. The time constraint also limited our ability to optimize the experimental setup. As a consequence, neutron depolarization seems to occur at the transition between the electromagnetic field for the DNP and the guide field for the neutron flipper. To account for this depolarization, a calibration run was done using a 100 % polarized incident neutron beam. The supermirror polarizer and the guide field on the SANS-1 instrument were turned on while the proton spins in the sample were totally depolarized. The ratio of between the expected neutron polarization (100 %) and the actually measured one (36.6 %) was then used as the correction factor in the final polarization

calculations. Figure 1 shows the measured neutron polarization. They agree nicely with the theoretical calculation. In conclusion, we have shown that dynamically polarized hydrogen samples can provide a real alternative for broadband neutron polarization.

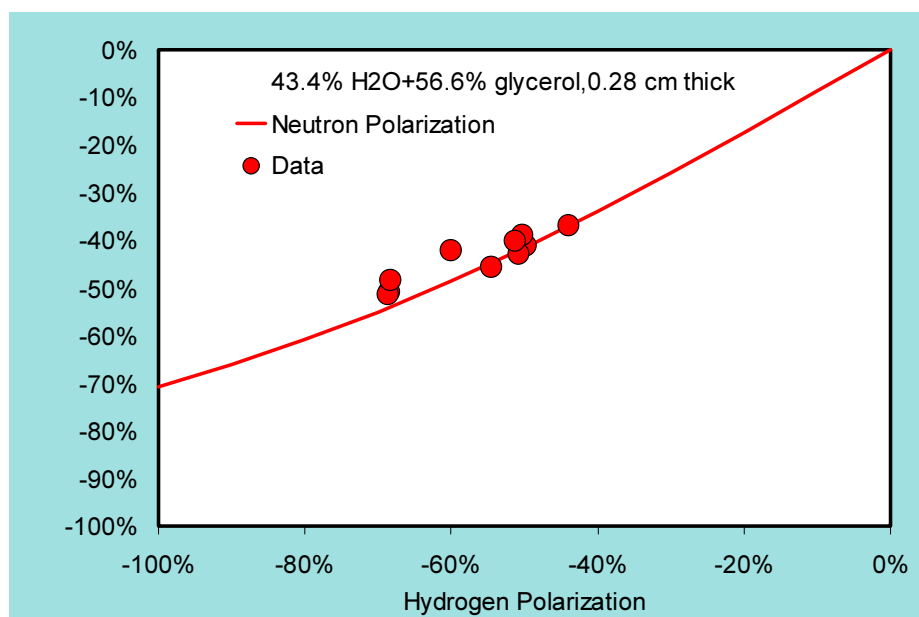


*Figure 1:* Neutron polarization after passing through the polarized DNP sample as a function of proton polarization (circle). The solid line is the theoretical calculation for the neutron polarization with the used sample.

**Small-angle scattering instrument SANS-2**

**Short Instrument Description:**

Small angle neutron scattering using cold non-polarised/polarised neutrons is a powerful tool for investigating the structure of matter in the range between 1 and 100 nm. It is a non destructive method for a wide range of application in:

- Metal physics (precipitates, clusters, interfaces, grain boundaries,...)
- Materials science (defects, porosity,...)
- Nanocrystalline materials (grain size, magnetic structures,...)
- Polymers and polymer systems (blends, mixtures, structure and morphology,...)
- Biology (viruses, proteins,...)
- Complex liquids (microemulsions, colloids, liquid crystals,...).

**Local Contacts:**

Helmut Eckerlebe

Phone/Fax : +49 (0)4152 87-1202 / +49 (0)4152 87-1338

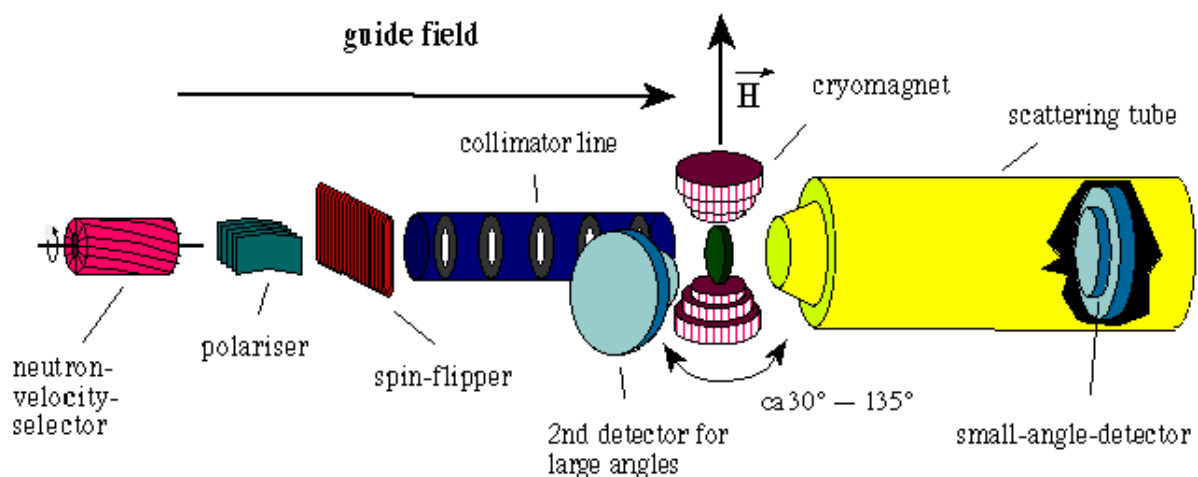
e-mail: [helmut.eckerlebe@gkss.de](mailto:helmut.eckerlebe@gkss.de)

Dr. P. Klaus Pranzas

Phone/Fax : +49 (0)4152 87-1326 / +49 (0)4152 87-1338

e-mail: [pranzas@gkss.de](mailto:pranzas@gkss.de)


**Schematic View of SANS-2:**



**Instrument Details:**

Beamline:	beamline 8 – cold neutron guide NG-2, radius of curvature $R = 900\text{ m}$ , cross section $3 \times 4\text{ cm}^2$
Monochromator:	helical slot velocity selector (Dornier)
Wavelength range at sample position:	0.3 to 2.0 nm
Wavelength resolution:	$\Delta\lambda/\lambda = 0.1$ (2 additional velocity selectors with $\Delta\lambda/\lambda = 0.05$ and $0.2$ available)
Length of collimation:	max. 16 m (2 m elements)
Flux at sample position:	$\Phi_{\text{max}} = 2 \cdot 10^7\text{ cm}^{-2}\text{ s}^{-1}$ (1 m collimation, $\lambda = 0.5\text{ nm}$ )
Range of momentum transfer:	$0.01 \leq q \leq 3\text{ nm}^{-1}$ (small-angle scattering) $q \leq 25\text{ nm}^{-1}$ (wide-angle scattering with 2. detector)
Distance sample to detector:	$1.0\text{ m} \leq d \leq 22\text{ m}$ optional 2. detector for wide angles: $d = 1\text{ m}$
Detector: active area: resolution: background:	2-dim position-sensitive $^3\text{He}$ -counter $50 \times 50\text{ cm}^2$ $0.25 \times 0.25\text{ cm}^2$ $< 0.5\text{ cps}$
Supplementary equipment:	<ul style="list-style-type: none"> <li>– several electro-magnets up to 2.0 T (horizontal and vertical fields)</li> <li>– superconducting magnet up to 5.0 T</li> <li>– cryostats (8–300 K)</li> <li>– furnace (<math>-30\text{ }^\circ\text{C}</math> to <math>+400\text{ }^\circ\text{C}</math>, atmospheric condition, inert gas and vacuum)</li> <li>– linear translation, rotary, tilting and lift tables (freely programmable sample position)</li> <li>– “HOLONS”: holographic combined with SANS setup (see table A)</li> </ul>
Special features:	<ul style="list-style-type: none"> <li>– Sample environment space is variable from a few mm up to 2500 mm</li> <li>– User-friendly software for data reduction and evaluation running on PC (SANDRA a. o.)</li> </ul>



	<b>EXPERIMENTAL REPORT</b>	<b>GeNF SANS-2</b>
<b>2D-multi-wire neutron detector with a large sensitive area and high spatial resolution for SANS and reflectometry</b>		
<b>Principal Proposer:</b>	<b>R. Kampmann<sup>1,2</sup>, M. Marmotti<sup>2</sup>, M. Haese-Seiller<sup>1</sup>, V. Kudryashov<sup>1,3</sup></b> <sup>1</sup> GKSS-Forschungszentrum, Institut für Werkstofforschung, D-21502 Geesthacht, <sup>2</sup> DENEX Detektoren für Neutronen und Röntgenstrahlung GmbH, D-21339 Lüneburg, <sup>3</sup> Petersburg Nuclear Physics Institute, Gatchina, 188350, Russian Federation	
<b>Experimental Team:</b>	<b>R. Kampmann, M. Haese-Seiller, V. Kudryashov</b>	
<b>Date(s) of Experiment:</b>	February 2003	

## Introduction

A two-dimensional position-sensitive multi-wire gaseous detector for small-angle neutron scattering (SANS), reflectometry and high-resolution diffractometry has been developed at the GKSS research centre in co-operation with DENEX GmbH. The counter with a sensitive area of  $500 \times 500 \text{ mm}^2$  has been designed to be used in the reflectometer REFSANS being built at the new high flux reactor FRM-II [1].

## Design and performance of the detector

The REFSANS detector is a  $^3\text{He}$  and  $\text{CF}_4$  filled multi-wire proportional counter (MWPC) with delay line read-out, its design is based on that of detectors with smaller active areas developed previously at GKSS [2,3]. REFSANS needs a detector which meets requirements both of reflectometers and SANS instruments [1]:

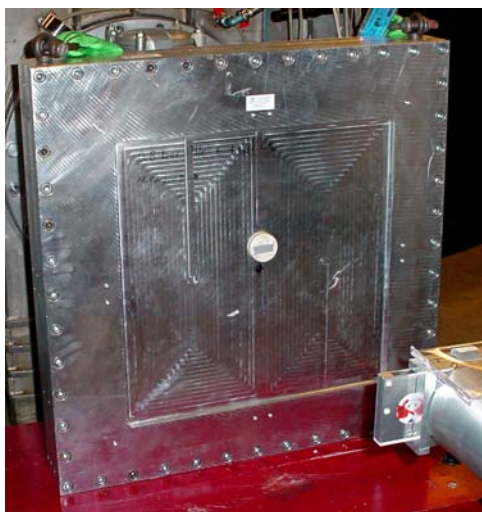


*Figure 1: REFSANS detector being tested at SANS-2 at GKSS.*

- i) Sensitive area:  $500 \times 500 \text{ mm}^2$ ;
- ii) Spatial resolution:  $\approx 2 \text{ mm} \times 2 \text{ mm}$ ;
- iii) Wavelength range:  $0.3 \text{ nm} < \lambda < 3 \text{ nm}$ ;
- iv) Read-out: fast, ToF-application;
- v) Background: very low;
- vi)  $\gamma$ -sensitivity  $\varepsilon_\gamma$ : extremely low ( $\varepsilon_\gamma \ll 10^{-6}$ ).

All electrodes are made of tungsten wires with a distance of 2 mm. Drift electrodes limit the detection volume which has a depth of 3 cm to achieve a high detection probability  $p$  at rather low  $^3\text{He}$  partial pressure. The anode is located in the centre of the detection volume. Its distance to the pick-up electrodes is only 5 mm to achieve high capabilities for both good position resolution and high local count rates.

One prototype of REFSANS detector has been manufactured and characterised with neutrons. It has been filled with only 0.8 bar  $^3\text{He}$  and 1 bar  $\text{CF}_4$  for use in the SANS-2 at the GKSS Research Centre (Figure 1).

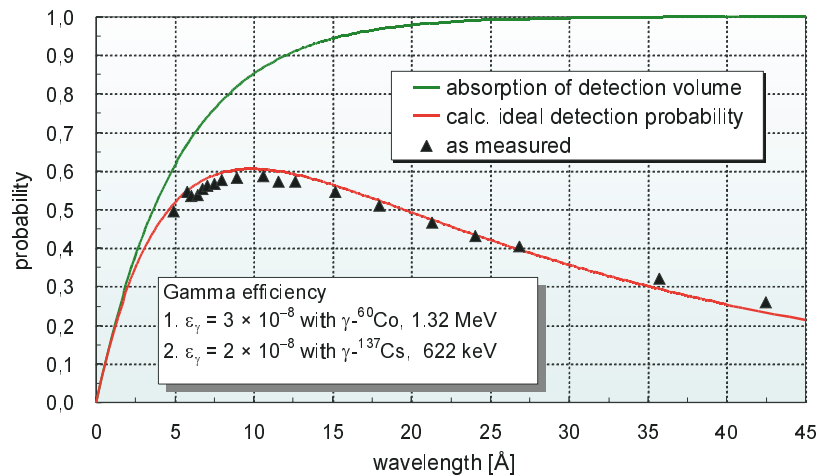


Figure 2: Neutron detection probability and  $\gamma$ -efficiency of the prototype REFSANS detector.

The detection probability was measured with a well collimated neutron beam at SANS-2 in comparison with an almost black  $^3\text{He}$  counter tube. A detection probability larger than 50% over the range for  $0.5 \text{ nm} < \lambda < 1.8 \text{ nm}$  with a maximum of  $\approx 58\%$  at  $\lambda = 1.0 \text{ nm}$  was found (Fig. 2). This detection probability is close to the ideal one which is calculated by accounting for the losses

in the detector window (20 mm thick Al-alloy) and the dead volume between the window and the first drift electrode (thickness:  $\approx 2 \text{ mm}$ ).

The  $\gamma$ -efficiency was measured without changing the setting of the analogue electronics. Radioactive sources were positioned at short distance ( $\approx 10 \text{ cm}$ ) in front of the detector. Extremely low  $\gamma$ -sensitivities of  $\varepsilon_\gamma \ll 10^{-7}$  were measured (Fig. 2).

After these tests the detector was mounted in the evacuated scattering tube of SANS-2/ GKSS. An isotropic scatterer was set in the beam at a distance of  $\approx 3 \text{ m}$  from the detector which was covered by a Cd-mask ( $\approx 20 \text{ cm}$  in front of its window) with a grid of holes with distances of  $50 \text{ mm}$ . A spatial resolution of  $\approx 3 \text{ mm} \times 3 \text{ mm}$  together with an excellent linearity was found [3].

## Summary


Due to its large sensitive area ( $500 \times 500 \text{ mm}^2$ ), its spatial resolution of  $\approx 3 \text{ mm} \times 3 \text{ mm}$  and its low  $\gamma$ -sensitivity ( $\varepsilon_\gamma \ll 10^{-7}$ ) the prototype detector meets already central requirements of the REFSANS detector and it is an excellent detector for a SANS at a monochromatic beam. For the use in REFSANS the detection probability will be further increased by changing the electrode design to avoid any dead volume behind the detector window. Furthermore, the spatial resolution will be improved to  $\approx 2 \text{ mm} \times 2 \text{ mm}$  by increasing the partial pressure of  $\text{CF}_4$ . The REFSANS detector has been licensed by GKSS to DENEX.

## Acknowledgements

The support of M. Pauls, H. Eckerlebe and K. P. Pranzas during tests of the REFSANS detector at SANS-2 / GKSS is gratefully acknowledged. The development of REFSANS has been supported by the German Federal Ministry of Education, Research, and Technology (BMBF) under Contracts 03-KA5FRM-1 and 03-KAE8X-3.

## References

- [1] Kampmann, R., Haese-Seiller, M., Marmotti, M., Burmester, J., Deriglazov, V., Syromiatnikov, V., Okorokov, A., Frisius, F., Tristl, M., Sackmann, E. *Applied Physics A*, 74, (2002), 249–251.
- [2] Marmotti, M., Burmester, J., Haese-Seiller, M., Kampmann, R. *Nuclear Instruments and Methods A*, 477, (2002), 347.
- [3] Kampmann, R., Haese-Seiller, M., Marmotti, M., Burmester, J., Deriglazov, V., Syromiatnikov, V., Okorokov, A., Frisius, F., Tristl, M., Sackmann, E. *Applied Physics A*, 74, (2002), 252–254.

	<b>EXPERIMENTAL REPORT</b>	<b>GeNF SANS-2</b>
<b>Structural Changes of nanocrystalline Mg/MgH<sub>2</sub> during sorption and desorption of hydrogen</b>		
<b>Principal Proposer:</b>	<b>T. Klassen, M. Dornheim, A. Schreyer, P. K. Pranzas</b> GKSS Research Centre	
<b>Experimental Team:</b>	<b>P. K. Pranzas, M. Dornheim</b>	
<b>Date(s) of Experiment:</b>	<b>May 2003</b>	

### Scientific Objective

Nanostructured magnesium hydride is considered to be one of the most interesting alternatives for the reversible storage of hydrogen. MgH<sub>2</sub> offers a safe alternative to the storage of hydrogen in compressed or liquid form. It has a very high storage capacity by volume and by weight and is therefore favoured for mobile applications. In the framework of the R&D program of GKSS, Mg-based hydrogen storage materials together with metal-oxide catalysts with improved hydrogen sorption properties were developed in view of a technical application [1–6]. In this work it is planned to study structural changes as well as the hydride formation and the precipitation process of MgH<sub>2</sub> with grain sizes in the nm-range with small-angle scattering during sorption and desorption of hydrogen.

### Experimental Techniques

As first step two samples – nanocrystalline Mg and nanocrystalline MgH<sub>2</sub> which was fully loaded with Hydrogen – were measured at the SANS-2 instrument at room temperature in quartz cuvettes with a thickness of 1 mm. A wavelength of 0.4 nm ( $\Delta\lambda/\lambda = 0.1$ ) and distances between sample and detector of 1, 3, 9 and 21 m were used to cover the range of scattering vector  $q$  from 0.03 nm<sup>-1</sup> to 3.5 nm<sup>-1</sup>.

After normalisation of the scattering data by a monitor, the detector response was corrected using the isotropic scattering of a polyethylene reference sample. The scattering pattern of 1 mm Vanadium, corrected for sample transmission, background and detector response was used to obtain the scattering cross section in absolute units. Furthermore, the scattering of the empty cuvette was subtracted.

### Results

The scattering curve of nanocrystalline Mg showed a small incoherent background as if there was still some hydrogen left in the sorption material. In contrast the curve of MgH<sub>2</sub> had a quite large incoherent background due to the incoherent scattering of hydrogen.

The scattering curves after subtraction of the incoherent background are shown in figure 1.

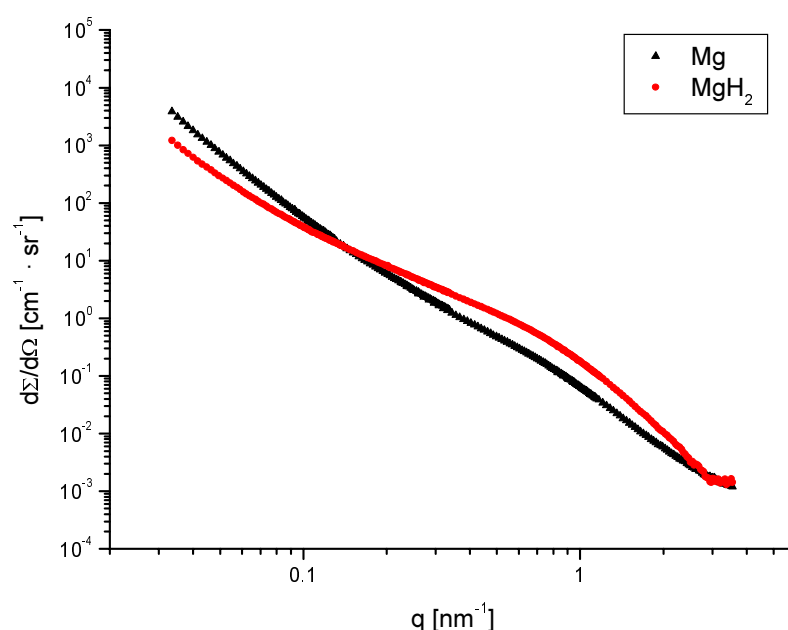



*Figure 1:* Scattering curves of nanocrystalline Mg and of nanocrystalline MgH<sub>2</sub> with maximal sorption of hydrogen after subtraction of the incoherent background.

At larger  $q$  values a shoulder can be observed in both scattering curves – a small one in the Mg curve and a larger one in the MgH<sub>2</sub> curve. The enlargement of the signal is caused by a formation of inhomogeneities with sizes of about 6 nm during the hydrogen sorption process. At smaller  $q$  values a  $q^{-4}$ -decay is visible which indicates the presence of larger structures in the samples, e. g. pores, clusters and/or grains.

With SANS it is not possible to distinguish between changes in the grain size of the magnesium hydride and a cluster formation of hydrogen. Therefore additional information and measurements are necessary for the interpretation of the scattering curves. Hence SAXS/USAXS experiments with synchrotron radiation at HASYLAB are planned to get information about the structure of MgH<sub>2</sub> without the scattering contribution of hydrogen. As next step ASAXS measurements at HASYLAB are planned to analyse the distribution of metal-oxide catalysts, e.g. Cr<sub>2</sub>O<sub>3</sub>, Mn<sub>2</sub>O<sub>3</sub>, Fe<sub>3</sub>O<sub>4</sub> or CuO, in magnesium hydride, measuring at the absorption edges of the different metals. The combined use of neutrons and X-rays gives complementary results which are necessary for a better understanding of such a complex system.

## References

- [1] G. Barkhordarian, T. Klassen, R. Bormann; Effect of Nb<sub>2</sub>O<sub>5</sub> content on hydrogen reaction kinetics of Mg. *J. Alloy Compd* 364 (2004) 242
- [2] G. Barkhordarian, T. Klassen, R. Bormann; Fast hydrogen sorption kinetics of nanocrystalline Mg using Nb<sub>2</sub>O<sub>5</sub> as catalyst. *Scripta Materialia* 49 (2003) 213
- [3] Z. Dehouche, T. Klassen, W. Oelerich, J. Goyette, T.K. Bose, R. Schulz; Cycling and thermal stability of nanostructured MgH<sub>2</sub>-Cr<sub>2</sub>O<sub>3</sub> composite for hydrogen storage. *J. Alloy Compd* 347 (2002) 319
- [4] W. Oelerich, T. Klassen, R. Bormann; Metal oxides as catalysts for improved hydrogen sorption in nanocrystalline Mg-based materials. *J. Alloy Compd* 315 (2001) 237
- [5] W. Oelerich, T. Klassen, R. Bormann; Hydrogen sorption of nanocrystalline Mg at reduced temperatures by metal-oxide catalysts. *Adv. Eng. Mat.* 3 (2001) 487
- [6] W. Oelerich, T. Klassen, R. Bormann; Mg-based hydrogen storage materials with improved hydrogen sorption. *Materials Transactions* 42 (2001) 1588

	<b>EXPERIMENTAL REPORT</b>	<b>GeNF SANS-2/DCD</b>
<b>Characterisation of nanoparticles dispersed in a polymeric matrix</b>		
<b>Principal Proposer:</b>	<b>D. W. Schubert<sup>1</sup>, T. Rühle<sup>1</sup>, A. Gruber<sup>1</sup>, P. K. Pranzas<sup>2</sup>, D. Bellmann<sup>2</sup>, J. Vollbrandt<sup>2</sup></b> <sup>1</sup> Freudenberg Forschungsdienste KG, <sup>2</sup> GKSS Research Centre	
<b>Experimental Team:</b>	<b>D. Bellmann<sup>2</sup>, P. K. Pranzas<sup>2</sup></b> <sup>2</sup> GKSS Research Centre	
<b>Date(s) of Experiment:</b>	April, May, June 2003	

### Scientific Objective

TiO<sub>2</sub> nanoparticles are used in a wide range of applications, e.g. in photocatalysis and photovoltaic engineering as well as in sunscreens, cosmetics and paints. The most important impact factor augmenting the material is related to the degree of dispersion of the nanoparticles. Our focus is the characterisation of TiO<sub>2</sub> nanoparticles dispersed in a Polyamide matrix using a combination of conventional Small- (SANS) and Ultra Small-Angle Neutron Scattering (USANS) to estimate the degree of dispersion of nanoparticles in the matrix. With the help of the neutron scattering techniques information on the fractions of dispersed and aggregated nanoparticles can be obtained covering length scales from one nanometer up to more than 20 micrometers.

### Experimental Techniques

1,6 % by weight TiO<sub>2</sub> nanoparticles were dispersed in a PA matrix. This sample and the Polyamide itself were investigated at the small-angle neutron scattering instrument SANS-2 and at the double-crystal diffractometer DCD.

At SANS-2 neutrons with a wavelength of 0.4 nm (resolution  $\Delta\lambda/\lambda = 0.1$ ) and distances between sample and detector of 1, 3, 9 and 21 m were used to cover the range of scattering vector  $q$  from 0.03 to 4 nm<sup>-1</sup>. The samples pieces were measured at room temperature stacked in quartz cuvettes with a thickness of 3 mm using an aperture in front of the sample with a diameter of 9 mm. After normalisation of the scattering data by a monitor, the detector response was corrected using the isotropic scattering of a polyethylene reference sample. The scattering pattern of 1 mm Vanadium, corrected for sample transmission, background and detector response was used to obtain the scattering cross section in absolute units.

Ultra small-angle neutron scattering (USANS) measurements were carried out at DCD with a wavelength of 0.44 nm resulting in an accessible range of scattering vector  $q$  from 10<sup>-5</sup> to 10<sup>-3</sup> nm<sup>-1</sup>. The gap between the range of DCD and SANS data had to be interpolated (see figure 1).

### Results

In figure 1 the results of the combined DCD and SANS scattering data are shown. In figure 2 the corresponding size distribution is demonstrated which was calculated from the scattering curves shown in figure 1 using the hard sphere model.

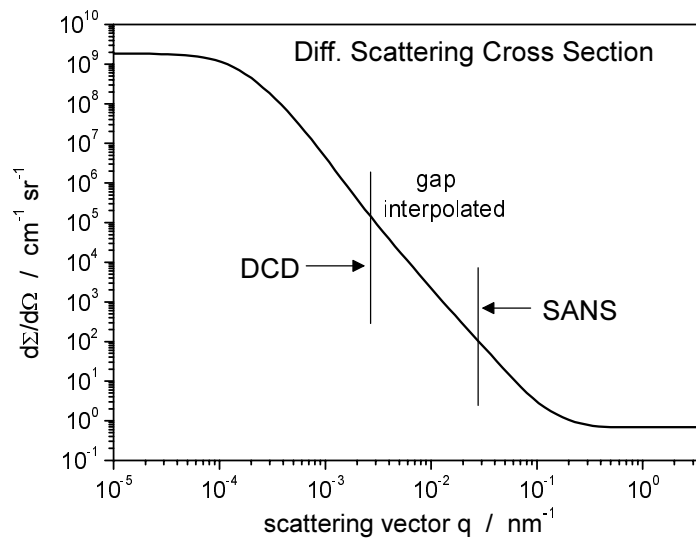


Figure 1: SANS and DCD scattering curves of 1.6 wt.-% TiO<sub>2</sub> nanoparticles dispersed in a PA matrix. The differential scattering cross section is plotted against the scattering vector.

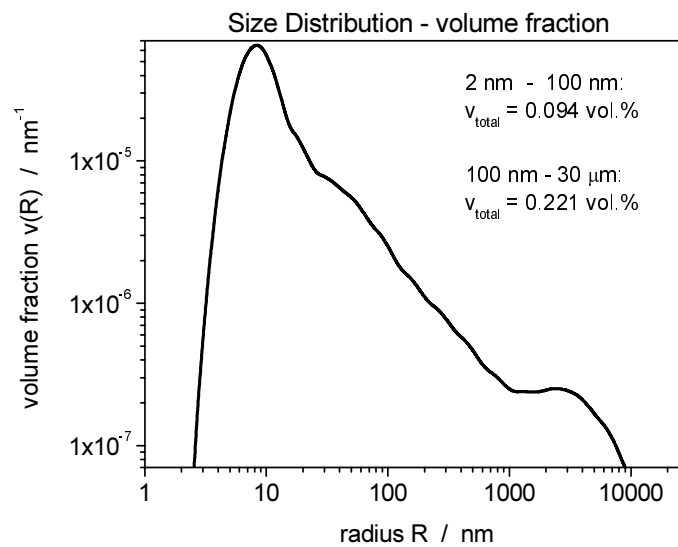



Figure 2: Sizes distribution calculated from the data shown in figure 1 assuming that the particles have a spherical shape. The relative volume fraction is plotted against the sphere radius.

The size distribution shows that only 30 % of the TiO<sub>2</sub> nanoparticles are "dispersed" in aggregates smaller than 100 nm, the rest forms larger aggregates. The volume fraction of 0.3 vol.% calculated from the scattering curves differ from the "true" total volume fraction which is about 0.4 vol.%. This indicates that the TiO<sub>2</sub> aggregations include also interstitial volume filled by PA or air.

Neutron scattering, in particular the combination of conventional SANS and Ultra Small-Angle Neutron Scattering reveals degree of dispersion and information on the type of packaging of nanoparticles, where the accuracy is highly statistical significant due to the large probed sample volume.



 <b>GKSS</b> FORSCHUNGSZENTRUM in der HELMHOLTZ GEMEINSCHAFT	<b>EXPERIMENTAL REPORT</b>	<b>GeNF SANS-2</b>
<b>SANS study of the magnetic structure of Y/Dy multilayer system</b>		
<b>Principal Proposer:</b>	<b>A. I. Okorokov<sup>1</sup>, S. V. Grigoriev<sup>1</sup>, A. Schreyer<sup>2</sup></b> <sup>1</sup> Petersburg Nuclear Physics Institute, <sup>2</sup> GKSS Research Centre	
<b>Experimental Team:</b>	<b>H. Eckerlebe<sup>2</sup>, P. K. Pranzas<sup>2</sup>, A. I. Okorokov<sup>1</sup>, S. V. Grigoriev<sup>1</sup>, Yu. O. Chetverikov<sup>1</sup></b>	
<b>Date(s) of Experiment:</b>	June 2003	

### Scientific Objective

The proposal was aimed to investigate of the magnetic structure in the film samples made of rare-earth materials in a wide temperature range by means of small angle polarized neutron scattering (SAPNS). The sample is a superlattice of the layer sequence

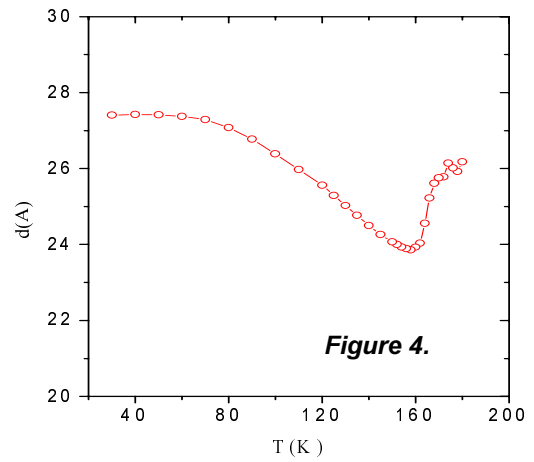
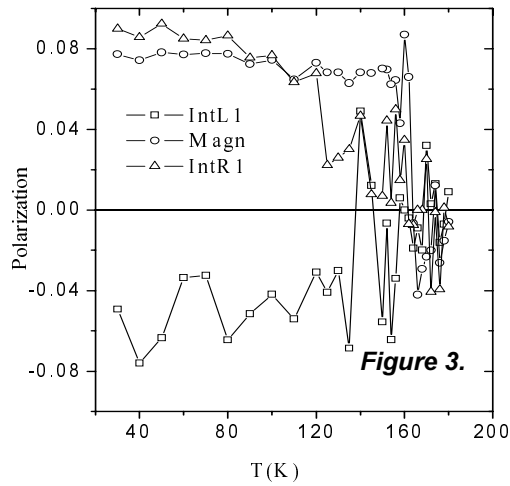
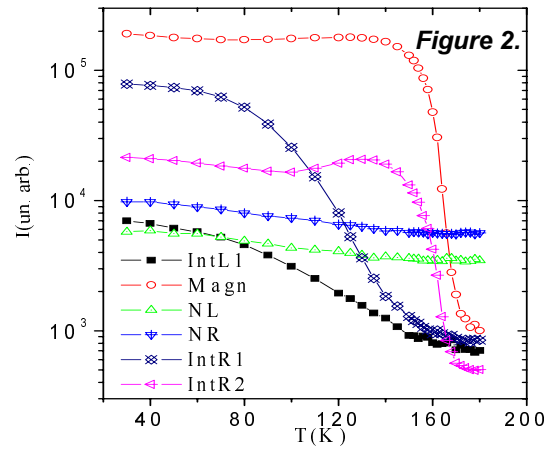
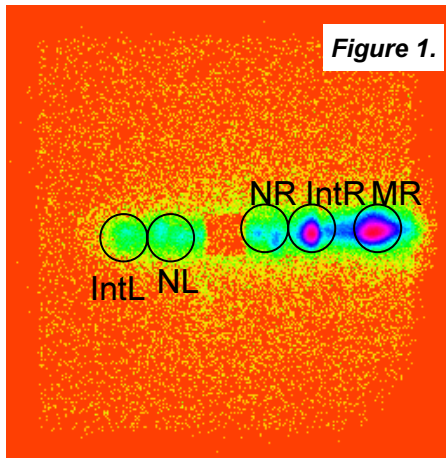
$Y_{50 \text{ nm}}[Dy_{4.3 \text{ nm}}/Y_{2.8 \text{ nm}}]_{350}/Y_{234 \text{ nm}}/Nb_{200 \text{ nm}}Al_2O_3(\text{substrate})$ , which was grown along the c-axis of the hcp-structure of Dy and Y, the same as used in [1]. Below its bulk Neel temperature of 179 K, Dy exhibits a helical phase, which transform into a ferromagnetic structure below 89 K. In Dy/Y superlattices, a coherent helical phase occurs, which extends over many bilayers, whereas the ferromagnetic transition is suppressed due to magnetoelastic effect [2]. It is supposed that the coherent helical phase propagates through the paramagnetic Y interlayers via RKKY exchange coupling. This RKKY interaction is anisotropic, i.e. it is ferromagnetic within ab-plane and antiferromagnetic along c-axis. Thus anisotropy of the crystal fixes the direction of the magnetic spirals  $\mathbf{m} = [\mathbf{S}_1 \times \mathbf{S}_2]/S^2$  along the axes [001]. It is an axial vector and therefore the presence of RKKY interaction leads to appearance of the polarization dependent contribution into the neutron scattering cross-section [3]. According to Ref. [3] the elastic chiral magnetic cross section has the form:

$$\sigma_{el}(\mathbf{q}) = [r S F(\mathbf{q})/2]^2 \{ (1 + (\mathbf{q}\mathbf{m})^2 + 2(\mathbf{q}, \mathbf{P}_0)(\mathbf{q}, \mathbf{m}))\Delta_{\mathbf{q}+\mathbf{Q}} N_R + (1 + (\mathbf{q}\mathbf{m})^2 - 2(\mathbf{q}, \mathbf{P}_0)(\mathbf{q}, \mathbf{m}))\Delta_{\mathbf{q}-\mathbf{Q}} N_L \}, \quad (1)$$

where  $r = 0.54 \times 10^{-12}$  cm,  $\mathbf{q}$  is a momentum transfer and  $\Delta_{\mathbf{q} \pm \mathbf{Q}} = [(2\pi)^3/V] \delta(\mathbf{q} \pm \mathbf{Q})$ , where  $V$  is the volume of the low-level cell. The cross section depends on the mutual orientation of the  $\mathbf{P}_0$  and  $\mathbf{m}$  (Eq.1). It follows from Eq.(1) that polarised neutron scattering allows one to determine the handedness of the magnetic spiral. In the real samples there are always the domains with the two different directions of the spiral. In this case polarization-dependent part of the scattering is proportional to the difference of the population numbers:  $(N_R - N_L)$ .

### Experimental Technique

The SAPNS experiments were carried out at the SANS-2 scattering facility of FRG-1 research reactor in Geesthacht (Germany). A polarized beam of neutrons with an initial polarization of  $P_0 = 0.94$ , the neutron wavelength  $\lambda = 4.8 \text{ \AA}$  ( $\Delta\lambda/\lambda = 0.1$ ) and a divergence of 2.5 mrad was used. The scattered neutrons were detected by a position sensitive detector with  $(256 \times 256)$  pixels. The scattering intensity was measured in the temperature range from  $T = 30$  to 190 K. The external magnetic field  $\mathbf{H}$  from 1 to 800 mT was applied to the sample perpendicularly to the incident beam and the polarization followed the direction of the magnetic field. The multilayer was oriented in such a way that the c-axis was set almost perpendicular to the incident beam. The direction of the magnetic spirals, or the chiral vectors  $\mathbf{m}$  expected to be parallel to this axis. This geometry allows one to observe diffraction peaks in a range of small-angle scattering that originates from the interaction of the neutron with the spin helices and/or structural periodicity of the superlattice, provided that the Bragg condition is fulfilled:  $2d \sin(\theta/2) = \lambda$ , or  $q = 2\pi/d$ .




## Results

Figure 1 gives the contour map of the diffraction peaks in a logarithmic scale at  $H = 0$  and  $T = 100$  K. There are two peaks (closest to the center), which are reflections from the nuclear periodical structure. We denote these two peaks as NL and NR on the left and right side of the direct beam. The peak on the right side of the map originates from the scattering on the spin spiral. It is denoted as MR. Two peaks between NR and MR appear due to interference of the magnetic and nuclear scattering, they are named as IntR1 and IntR2. There is the only interference peak on the left side of the map IntL. We investigate experimentally the intensities with the polarization directed along  $[I(q, \mathbf{P}_0)]$  and opposite  $[I(q, -\mathbf{P}_0)]$  to the magnetic field. As for experimental quantities we have extracted for different peaks: 1)  $I_P = (I_q(P) + I_q(-P))$  (the intensity of the peak); 2)  $P_P = (I_q(P) - I_q(-P)) / I_P$  (the polarization of the peak); 3)  $q_p$  (the position of the peak). The integral intensity for NL and NR, for IntL, IntR1 and IntR2, for MR peaks is shown in Figure 2 as a function of the temperature. The polarization of the magnetic MR and Interference peaks is presented in Figure 3. The polarization of the magnetic peak M1 is constant for the temperature range below  $T_N$  and is equal to 0.08. The polarization of the Interference peaks is equal to -0.06 for IntL peak and +0.06 for IntR1 peak. The opposite sign of the polarization for these two peaks shows that the difference of the population numbers:  $(N_R - N_L) \neq 0$ . The period of spin density wave  $d$  is obtained from the Bragg law  $\lambda = 2d \sin(\theta/2)$ , or,  $d = 2\pi/Q$ . The temperature dependence of the period  $d$  is shown in Figure 4. The period increases with decreasing the temperature what may be interpreted as interplay between RKKY interaction and the temperature.

## References

- [1] A. Schreyer, et. al, J.Appl.Phys. 87 (2000), 5443
- [2] M. B.Solomon, et al., Phys. Rev. Lett. 56 (1986) 259.
- [3] S. V.Maleyev, V. G. Bar'jakhtar, R. A. Suris, Fiz.Tv.Tela 4 (1962) 3461; M. Blume, Phys. Rev. 130 (1963) 1670.



 <b>GKSS</b> FORSCHUNGSZENTRUM in der HELMHOLTZ GEMEINSCHAFT	<b>EXPERIMENTAL REPORT</b>	<b>GeNF SANS-2</b>
<b>SANS study of the static magnetic structure of MnSi single crystal under applied magnetic field</b>		
<b>Principal Proposer:</b>	<b>A. I. Okorokov<sup>1</sup>, S. V. Grigoriev<sup>1</sup>, P. Böni<sup>2</sup>, R. Georgii<sup>2</sup></b> <sup>1</sup> Petersburg Nuclear Physics Institute (PNPI), <sup>2</sup> TU-München	
<b>Experimental Team:</b>	<b>H. Eckerlebe<sup>3</sup>, P. K. Pranzas<sup>3</sup>, A. I. Okorokov<sup>1</sup>, S. V. Grigoriev<sup>1</sup>, Yu. O. Chetverikov<sup>1</sup>, D. Lamago<sup>2</sup>,</b> <sup>3</sup> GKSS Research Centre	
<b>Date(s) of Experiment:</b>	June 2003	

### Scientific Objective

The proposal was aimed to continue investigation of the spin chirality in a single crystal MnSi below  $T_C$  under the applied magnetic field by means of small angle polarized neutron scattering (SAPNS). The magnetic structure of MnSi is a helical spin density wave below 29 K with a propagation vector  $(2\pi/a)(\zeta, \zeta, \zeta)$  with  $\zeta = 0.017$  and  $a = 0.4558$  nm [1,2]. The helicity is realized by an antisymmetric Dzyaloshinski-Moriya (DM) exchange interaction caused by the lack of a center of symmetry in Mn atomic arrangement [3-5]. This DM interaction itself is isotropic but another weak pseudodipolar interaction, connected to anisotropy of the crystal, fixes the direction of the magnetic spirals  $\mathbf{m} = [\mathbf{S}_1 \times \mathbf{S}_2]/S^2$  along the axes [111]. When an external magnetic field  $\mathbf{H}$  is applied, the direction of the magnetic spiral  $\mathbf{m}$  follows that of the magnetic field. The period does not depend on the direction of  $\mathbf{m}$ . The  $\mathbf{m}$ -rotation effect was theoretically considered by Plumer and Walker [6,7]. DM vector is an axial vector and therefore the presence of DM interaction leads to appearance of the polarization dependent contribution into the neutron scattering cross-section [8,9]. According to Ref. [8] the elastic chiral magnetic cross section has the form:

$$\sigma_{el}(\mathbf{q}) = [r S F(\mathbf{q})/2]^2 \{ (1 + (\mathbf{q}\mathbf{m})^2 + 2(\mathbf{q}, \mathbf{P}_0)(\mathbf{q}, \mathbf{m}))\Delta_{\mathbf{q}+\mathbf{Q}} + (1 + (\mathbf{q}\mathbf{m})^2 - 2(\mathbf{q}, \mathbf{P}_0)(\mathbf{q}, \mathbf{m}))\Delta_{\mathbf{q}-\mathbf{Q}} \},$$

where  $r = 0.54 \times 10^{-12}$  cm,  $\mathbf{q}$  is a momentum transfer and  $\Delta_{\mathbf{q} \pm \mathbf{Q}} = [(2\pi)^3/V] \delta(\mathbf{q} \pm \mathbf{Q})$ , where  $V$  is the volume of the low-level cell. The cross section depends on the mutual orientation of the  $\mathbf{P}_0$  and  $\mathbf{m}$  (Eq.1). When  $\mathbf{P}_0 \parallel \mathbf{m}$ , then the scattering is fully polarized at  $\mathbf{q} = \pm \mathbf{Q}$ . When  $\mathbf{P}_0 \perp \mathbf{m}$ , then the scattering is fully depolarized at  $\mathbf{q} = \pm \mathbf{Q}$ .

### Experimental Technique

The SAPNS experiments were carried out at the SANS-2 scattering facility of FRG-1 research reactor in Geesthacht (Germany). A polarized beam of neutrons with an initial polarization of  $P_0 = 0.94$ , the neutron wavelength  $\lambda = 5.8$  Å ( $\Delta\lambda/\lambda = 0.1$ ) and a divergence of 2.5 mrad was used. The scattered neutrons were detected by a position sensitive detector with (128x128) pixels. The scattering intensity was measured in the temperature range from  $T = 10$  K to  $T_C = 28.7$  K. The external magnetic field  $\mathbf{H}$  from 1 to 800 mT was applied perpendicularly to the incident beam and the polarization followed the direction of the magnetic field. The single crystal was oriented in such a way that two axes [111] were set in a plane perpendicular to the incident beam. According to the geometry of the crystal, these two axes are inclined at about 71° with respect to each other. The direction of the magnetic spirals, or the chiral vectors  $\mathbf{m}$  expected to be parallel to the axes [111]. This geometry allows one to observe diffraction peaks in a range of small-angle scattering that originates from the interaction of the neutron with the spin helices, provided that the Bragg condition is fulfilled:  $2d \sin(\theta/2) = \theta$ , or  $q = 2\pi/d$ . The magnetic field with the polarization vector  $\mathbf{P}_0$  along it had being set in the plane (110) (perpendicular to the incident beam) in four different directions of interest: a)  $\mathbf{H} \parallel [110]$ ; b)  $\mathbf{H} \parallel [001]$ ; c)  $\mathbf{H} \parallel [111]$ ; d)  $\mathbf{H} \perp [111]$ .

We investigate experimentally the intensities with the polarization directed along  $[l(q, \mathbf{P}_0)]$  and opposite  $[l(q, -\mathbf{P}_0)]$  to the magnetic field. As for experimental quantities we have extracted for 4 different peaks:

- 1)  $I_P = (I_q(P) + I_q(-P))$  (the intensity of the peak);
- 2)  $P_P = (I_q(P) - I_q(-P)) / I_P$  ( the polarization of the peak);
- 3)  $q_p$  (the position of the peak).

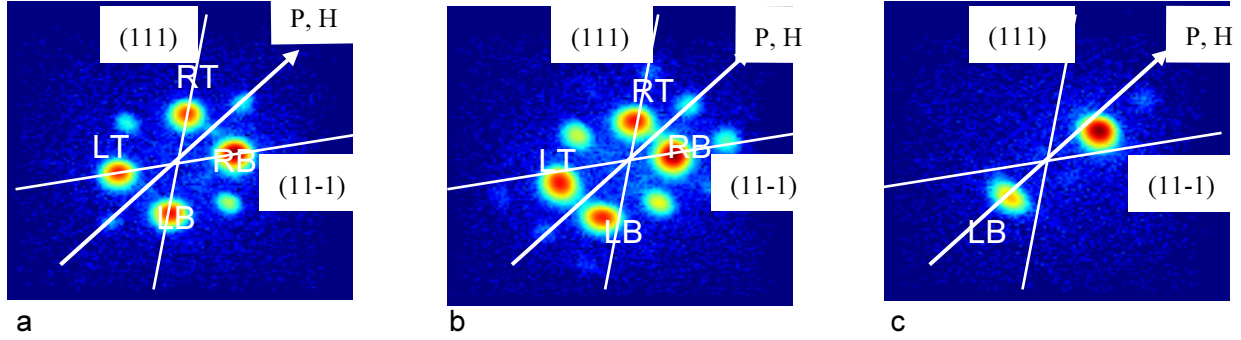
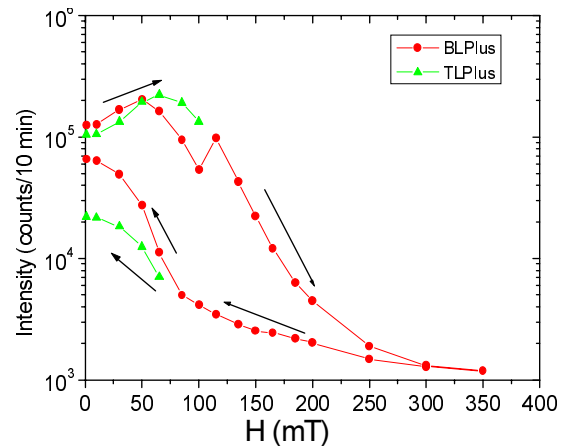
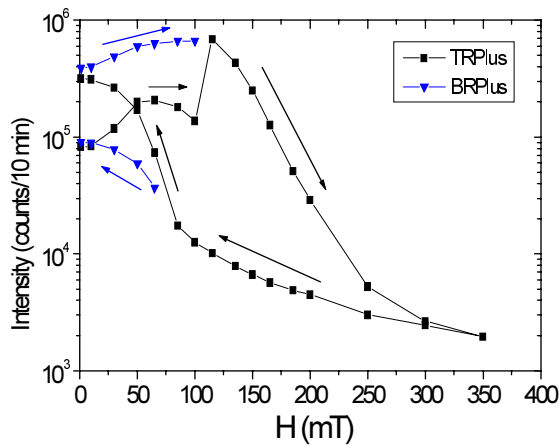


Figure 1: Maps of diffraction peaks with changing magnetic field.

## Results

A typical behavior of the magnetic spirals is shown in Figure 1 for the geometry when the field is applied along  $[110]$  direction. Fig. 1 gives the maps of the diffraction peaks in a logarithmic scale and how it changes with the magnetic field. The contour map at  $H = 0$  and  $T = 10$  K shows the four major and four minor peaks (Fig. 1a). Four major peaks (closest to the center) are reflections for two chiral vectors  $\mathbf{m}_{1,2}$ , which are collinear to the axes  $[111]$  and  $[11-1]$  visible in this geometry of the experiment. The coexistence of two peaks both at  $\mathbf{q} = (\mathbf{Q})$  may be explained by the mosaicity of the magnetic or crystallographic structure of MnSi. We denote these four peaks as Left-Top (LT), Left-Bottom (LB), Right-Top (RT) and Right-Bottom (RB) ones. Additional small peaks at  $\mathbf{q} = \mathbf{q}_{LB} + \mathbf{q}_{RB}$ ,  $\mathbf{q} = \mathbf{q}_{RB} + \mathbf{q}_{RT}$ ,  $\mathbf{q} = \mathbf{q}_{RT} + \mathbf{q}_{LT}$  and  $\mathbf{q} = \mathbf{q}_{LT} + \mathbf{q}_{LB}$  appear as a result of a double scattering process. When a relatively small magnetic field is applied ( $H < 120$  mT), the peaks move toward the direction of the magnetic field, so that a direction of the scattering vector  $\mathbf{q}$  changes but its value  $|\mathbf{q}|$  is constant (Fig. 1 b). When the field exceeds the certain value  $H_{C1} = 130$  mT, the peaks collapse to the direction of the magnetic field  $\mathbf{q} \parallel \mathbf{H}$ , so that only two peaks are left on the contour map (Fig. 1c).



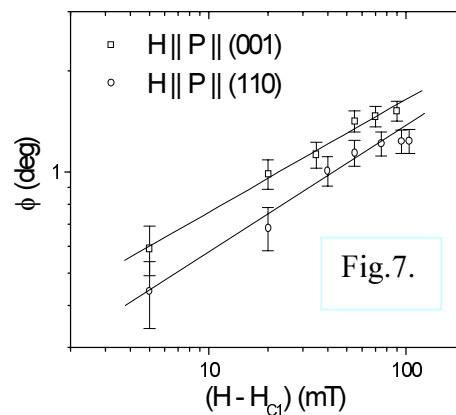
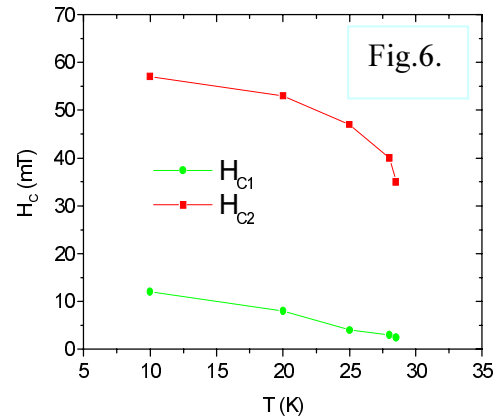
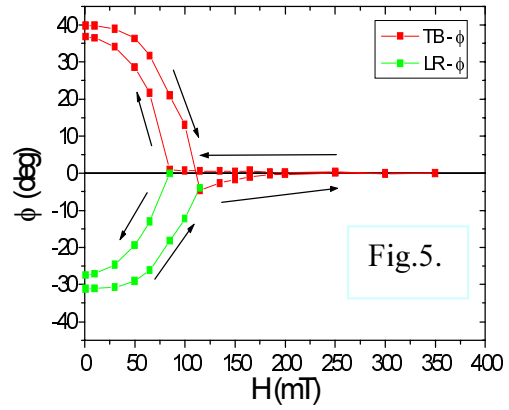
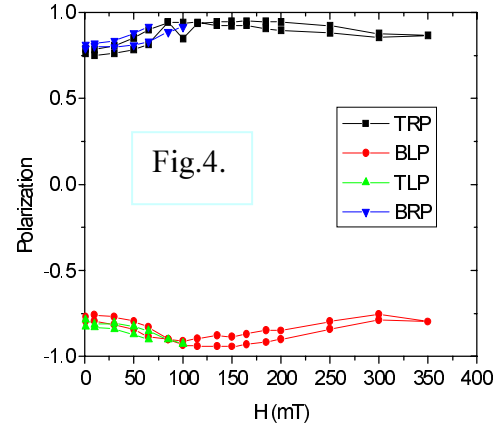
Figures 2 and 3: Intensity for LT and LB as well as RT and RB peaks as function of magnetic field.

The integral intensities for the LT and LB, and RT and RB peaks are shown in Figure 2 and Figure 3, respectively, as a function of the magnetic field. The polarization of the peaks is presented in Figure 4. The position of the peaks is determined by the angle between the direction of spiral and that of the magnetic field. This angle for four peaks is shown in Figure 5. As is seen from Figures 2–5, upon increasing magnetic field in the range from 0 to 700 G,

1) intensity of the peaks increases; 2) all peaks rotate toward the field direction; and 3) the polarization of the peaks increases to the saturation value. In the field range  $H \sim 120$  mT peaks collapse to the direction of the magnetic field. The two united peaks make the single peak.

The intensity of this united peak decreases strongly with further increase of the magnetic field. The polarization as well as the position of the united peaks remains unchanged. The consequent decrease of the magnetic field shows large hysteresis loop in the intensity. Peaks become separated again at the point  $H_{c2} = 70$  mT. The intensity of the peaks after manipulation with magnetic fields differs from the intensity before the manipulation.

The results are interpreted as follows. The magnetic field applied to the direction [110] rotates the direction of the spirals competing with another intrinsic anisotropy force of the magnetic structure. The magnetic field suppresses this anisotropy force at the strength of 120 mT. Thus we determine the critical field characterizing the weakest interaction of the system. Further increase of the magnetic field results in decrease of the intensity and is interpreted as an inclination of the spin of Mn from the plane perpendicular to the field toward the field thus making a cone instead of a spiral structure. The change in polarization of the peaks is related to the movement of the peaks toward the field direction. It is well described by the expression  $P_P = (\mathbf{q}_p \cdot \mathbf{P}_0) / (|\mathbf{q}_p| |\mathbf{P}_0|) = P_0 \cos(\varphi_{exp})$ . Thus the calculated value of the polarization with  $\varphi_{exp}$ , shown in Figure 5, follows, if not coincides with, the experimentally measured value of the polarization (Fig. 4). Further increase of the field strength results in the transformation of



the spiral to the conical structure and finally to the ferromagnet at  $H = 550$  mT. The similar sets of the data were taken for this geometry at different temperatures  $T = 10, 20, 25, 28, 28.5$  K. The data shows qualitatively the same behavior. The temperature dependence of both critical fields  $H_{C1}$  and  $H_{C2}$  is shown in Figure 6. To show the properties of the first magnetic field transition at  $H_{C1}$  the field dependence  $\langle h \rangle$  with where  $h = (H - H_C)/H_C$  is shown in Figure 7. The value of the angle  $\phi$  is scaled with  $h$  as:  $\phi \sim h^\beta$  with  $\beta = 0.34$  for  $H \parallel [001]$  axis and with  $\beta = 0.39$  for  $H \parallel [110]$  axis, what corresponds to the critical exponents of the second order phase transition.

## References

- [1] Y. Ishikawa, K. Tajima, D. Bloch, M. Roth, Solid State Commun. 19 (1976) 525.
- [2] Y. Ishikawa, G. Shirane, J. A. Tarvin, M. Kohgi, Phys. Rev. B 16 (1977) 4956.
- [3] I. E. Dzyaloshinskii, Zh. Eksp. Teor. Fiz. 46 (1964) 1420
- [4] P. Bak, M. H. Jensen, J. Phys. C 13 (1980) L881.
- [5] D. Nakamishi, A. Janase, A. Hasejawa, M. Kitaoka, Solid State Commun. 35 (1980) 995.
- [6] M. L. Plumer, M. B. Walker, J. Phys. C 14 (1981) 4689.
- [7] M. B. Walker, Phys. Rev. B 40 (1989) 9315
- [8] S. V. Maleyev, V. G. Bar'jakhtar, R. A. Suris, Fiz. Tv. Tela 4 (1962) 3461; M. Blume, Phys. Rev. 130 (1963) 1670.
- [9] S. V. Maleyev, Phys. Rev. Lett. 75 (1995) 4682; D. N. Aristov, S. V. Maleyev, Phys. Rev. B 62 (2000) R751.

	<b>EXPERIMENTAL REPORT</b>	<b>GeNF SANS-2</b>
<b>Nanosize precipitates in a maraging steel</b>		
<b>Principal Proposer:</b>	<b>B. Jamnig<sup>1</sup></b> <sup>1</sup> Materials Center Leoben, Leoben, Austria	
<b>Experimental Team:</b>	<b>H. Eckerlebe<sup>1</sup>, P. Staron<sup>1</sup></b> <sup>1</sup> GKSS Research Centre	
<b>Date(s) of Experiment:</b>	July 2003	

Maraging steels are widely used in many technological sectors such as aerospace and military as well as for tools and dies because of their high strength and toughness. For further improvement of these mechanical properties, which are mainly controlled by intermetallic precipitates in the nanometer size range, fundamental understanding of the influence of composition and heat treatment on the microstructural development is necessary. Quantitative characterisation of the precipitate dispersion based on transmission electron microscopy (TEM) is complicated and time-consuming because of the small size of the precipitates and the small observable sample volume. Therefore, small-angle neutron scattering (SANS) can be used in addition to determine precipitate size distributions and volume fractions [1]. SANS measurements were carried out on a cobalt-free corrosion resistant maraging steel (Table 1) after different ageing treatments at 475 °C and 525 °C.

Selector-monochromated neutrons with a mean wavelength of  $\lambda = 0.57$  nm and a wavelength spread of  $\Delta\lambda/\lambda = 10$  % were used. The neutron beam impinging on the 1 mm thick samples had a diameter of approximately 8 mm. The samples were magnetized to saturation in a field of 2 T. Four detector distances (1 m, 3 m, 9 m, 21 m) were used together with appropriate collimations to cover scattering vectors  $q$  from  $0.02 \text{ nm}^{-1}$  to  $2.5 \text{ nm}^{-1}$ . Scattered neutrons were recorded with a  $50 \times 50 \text{ cm}^2$  area detector using  $256 \times 256$  pixels. Measured intensities were corrected for the sample transmission, background intensity and detector response. Macroscopic differential scattering cross sections were obtained by calibration against a Vanadium standard.

The scattering curves after short heat treatments showed an interference maximum caused by a high particle number density (Figures 1, 3). For a treatment of interparticle interference we have adopted the local monodisperse approximation as described by Pedersen [2]. A normal distribution function was used for the particle size distribution  $n(R)$ . In case of magnetic scattering there is a magnetic scattering contrast  $\Delta\eta_{\text{mag}}$  in addition to the nuclear one  $\Delta\eta_{\text{nuc}}$ . The magnetic scattering cross section depends on the angle  $\alpha$  between the scattering vector and the magnetic field. The precipitates are assumed to be non-magnetic and are thus magnetic holes in the ferromagnetic matrix. Volume fractions of precipitates that are non-magnetic (magnetic holes) can be obtained from the magnetic cross section by supplying information only about the magnetic scattering length density of the matrix, without knowledge about the chemical composition of the precipitates. The resulting size distributions are shown in Figures 2 and 4.

After the shortest aging time of 0.25 h, there is already a significant precipitate volume fraction of about 4 % with a mean radius of 0.62 nm (475 °C) or 1.1 nm (525 °C). After 2 h,

there are  $2.5 \cdot 10^{19} \text{ cm}^{-3}$  with a mean radius of 0.94 nm and a volume fraction of 7.2 % (475 °C) or  $2.2 \cdot 10^{18} \text{ cm}^{-3}$  with a mean radius of 1.92 nm and a volume fraction of 4.9 % (525 °C). During the heat treatment there is still a slight increase of the volume fraction, but the particle number density decreases, i.e. coarsening takes place.

The ratio  $A$  of magnetic to nuclear scattering intensity depends on the chemical composition of the precipitates. In the case of non-magnetic precipitates, this can be used for estimating the nuclear scattering length density of the precipitates from measured scattering curves. Therefore, an assumed chemical composition of the precipitates can be tested by comparing the nuclear scattering length density obtained from the measurement to calculated nuclear scattering length densities. An analysis of the  $A$ -ratios determined from the SANS data (Figures 5, 6) will be subject of further investigations.

The present data will contribute to the understanding of the precipitation mechanism in technologically relevant maraging steels.

Table 1: Chemical composition of the steel.

	Fe	Cr	Ni	Al	Mo	Mn	Si	C
Wt. %	74.97	12.12	9.14	1.67	1.38	0.39	0.30	0.025

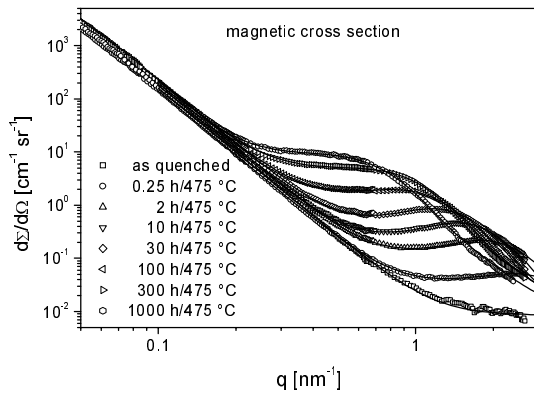


Figure 1: Fit of magnetic cross section, aged at 475 °C.

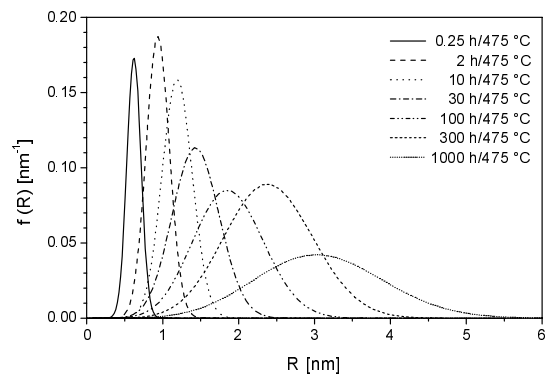


Figure 2: Particle size distributions obtained from the fit of the magnetic SANS curves shown in Fig. 1 (volume fraction).

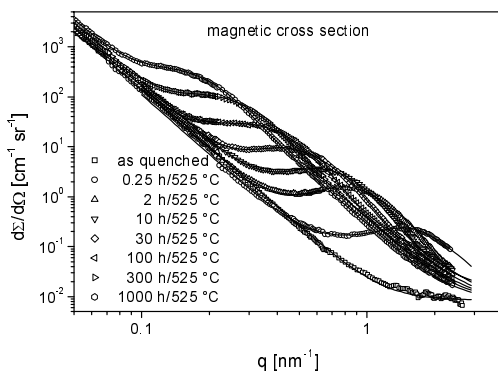


Figure 3: Fit of magnetic cross section, aged at 525 °C.

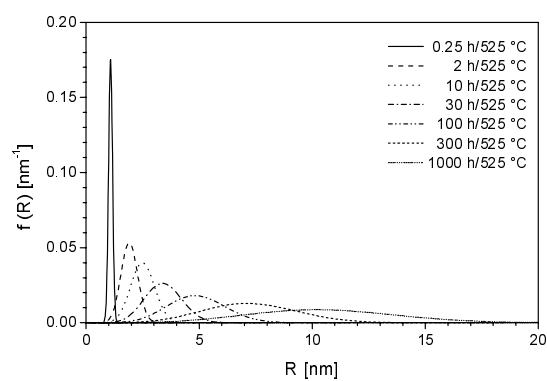
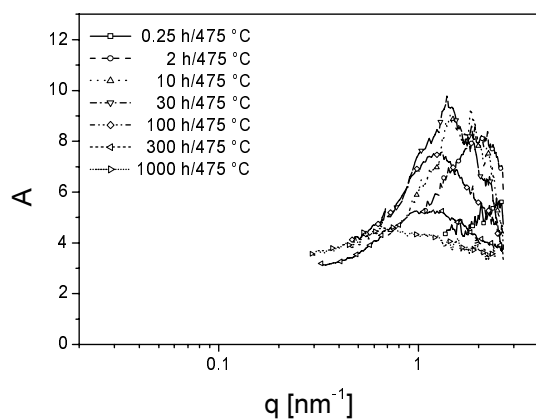
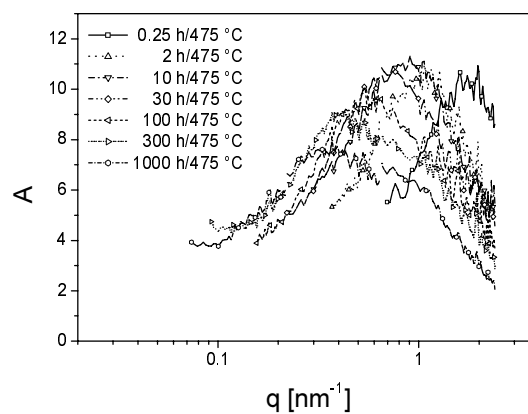


Figure 4: Particle size distributions obtained from the fit of the magnetic SANS curves shown in Fig. 3 (volume fraction).



*Figure 5:* Ratio A obtained from measured scattering curves, aged at 475 °C.




*Figure 6:* Ratio A obtained from measured scattering curves, aged at 525 °C.

## Preferences

- [1] P. Staron, B. Jamnig, H. Leitner, R. Ebner, H. Clemens, J. Appl. Cryst. 36 (2003) 415–419
- [2] J. S. Pedersen, J. Applied Crystallography 27 (1994), 595





	<b>EXPERIMENTAL REPORT</b>	<b>GeNF SANS-2</b>
<b>Isochronal ageing of a maraging steel</b>		
<b>Principal Proposer:</b>	<b>H. Leitner<sup>1</sup></b> <sup>1</sup> University of Leoben, Leoben, Austria	
<b>Experimental Team:</b>	<b>H. Eckerlebe<sup>1</sup>, P. Staron<sup>1</sup></b> <sup>1</sup> GKSS Research Centre	
<b>Date(s) of Experiment:</b>	July 2003	

Maraging steels are widely used in many technological sectors such as aerospace and military as well as for tools and dies because of their high strength and toughness. For further improvement of these mechanical properties, which are mainly controlled by intermetallic precipitates in the nanometer size range, fundamental understanding of the influence of composition and heat treatment on the microstructural development is necessary. Quantitative characterisation of the precipitate dispersion based on transmission electron microscopy (TEM) is complicated because of the small size of the precipitates. Therefore, small-angle neutron scattering (SANS) had been used to determine precipitate size distributions and volume fractions [1]. In this work, SANS measurements were carried out on a cobalt-free corrosion resistant maraging steel (Table 1) after continuous heating the samples up to temperatures of 450 °C, 500 °C, 600 °C, and 700 °C. The SANS results have been compared to results obtained by differential scanning calorimetry (DSC).

Selector-monochromated neutrons with a mean wavelength of  $\lambda = 0.57$  nm and a wavelength spread of  $\Delta\lambda/\lambda = 10$  % were used. The neutron beam impinging on the 1 mm thick samples had a diameter of 8 mm. The samples were magnetized to saturation in a field of 2 T. Four detector distances (1 m, 3 m, 9 m, 21 m) were used together with appropriate collimations to cover scattering vectors  $q$  from  $0.02 \text{ nm}^{-1}$  to  $2.5 \text{ nm}^{-1}$ . Scattered neutrons were recorded with a  $50 \times 50 \text{ cm}^2$  area detector using  $256 \times 256$  pixels. Measured intensities were corrected for the sample transmission, background intensity and detector response. Macroscopic differential scattering cross sections were obtained by calibration against a Vanadium standard.

Some of the scattering curves of heat treated samples showed an interference maximum caused by a high particle number density. For a treatment of interparticle interference we have adopted the local monodisperse approximation as described by Pedersen [2]. A normal distribution function was used for the particle size distribution  $n(R)$ . In case of magnetic scattering there is a magnetic scattering contrast  $\Delta\eta_{\text{mag}}$  in addition to the nuclear one  $\Delta\eta_{\text{nuc}}$ . The magnetic scattering cross section depends on the angle  $\alpha$  between the scattering vector and the magnetic field. The precipitates are assumed to be non-magnetic and are thus magnetic holes in the ferromagnetic matrix. Volume fractions of precipitates that are non-magnetic (magnetic holes) can be obtained from the magnetic cross section by supplying information only about the magnetic scattering length density of the matrix, without knowledge about the chemical composition of the precipitates. The resulting size distributions are shown in Figure 4.

From Figures 1 and 2 it can be seen that heating up to 450 °C has no effect on the scattering intensity, which means that no particles have been formed. After heating to 500 °C, a small

scattering signal at large  $q$  due to a large number of small particles with a mean radius of 0.6 nm and a volume fraction of 1.7 % is observed. After heating to 600 °C the scattering intensity has increased; the mean radius of the particles is 1.2 nm, the volume fraction is 3.2 %. An interference maximum is observed in the scattering curves for 500 °C and 600 °C indicating that the precipitates are surrounded by a depletion zone where the formation of other precipitates is suppressed by a low concentration of the corresponding solute atoms in the matrix. Heating up to 600 °C has no effect on the small and medium- $q$  part of the scattering curve. Thus the heating does not change the larger and medium-size particles that are also present in the steel. Heating up to 700 °C leads to dramatic changes in the scattering curve: the maximum at large  $q$  has vanished, the volume fraction of medium-size particles is increased (mean radius 8.6 nm), and also the small- $q$  part of the scattering curve exhibits a strong intensity increase. Thus, upon heating to 700 °C, also the volume fraction of large particles is increased. The small particles seem to have grown to medium size.

The DSC results had shown that in the temperature range investigated one exothermic and two endothermic heat effects can be observed, which are related to precipitation reactions. The exothermic peak, being a result of the formation of precipitates, occurs in the temperature range of about 400 to 550 °C. This exothermic peak is directly followed by an endothermic peak. The second endothermic peak occurs after  $\alpha$ - $\gamma$  transformation and has its beginning at about 680 °C.

SANS results showed that heating up to 600 °C still leads to an increase of the volume fraction of the precipitates compared to 500 °C. On the other hand the particle number density decreases if the final temperature is increased from 500 to 600 °C. Comparing DSC and SANS results it is evident that the endothermic peak is associated to the dissolution of precipitates. After heating up to 700 °C the scattering curve showed a dramatical change indicating a growth or dissolution of the smallest particles. This observation match well with the second endothermic peak in the DSC.

In summary it can be said that SANS is a suitable technique to interpret the DSC results.

Table 1: Chemical composition of the maraging steel.

	Fe	Cr	Ni	Mo	Ti	Al	Si	Mn	C
wt. %	75.8	12.3	8.89	0.98	0.83	0.57	0.55	0.11	0.01

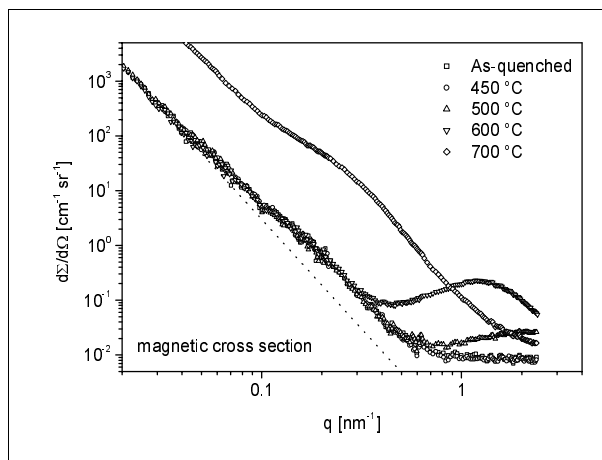


Figure 1: SANS scattering curves, magnetic cross section. The dotted line gives the  $q^{-4}$ -slope.

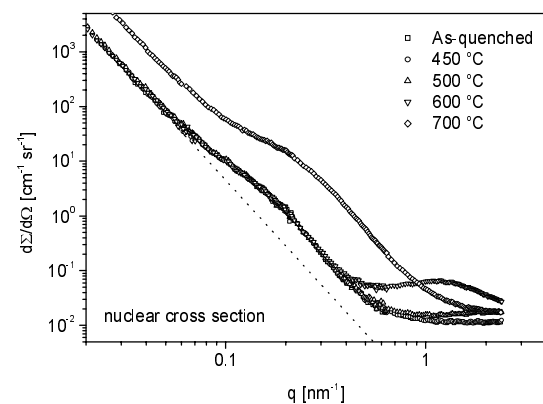
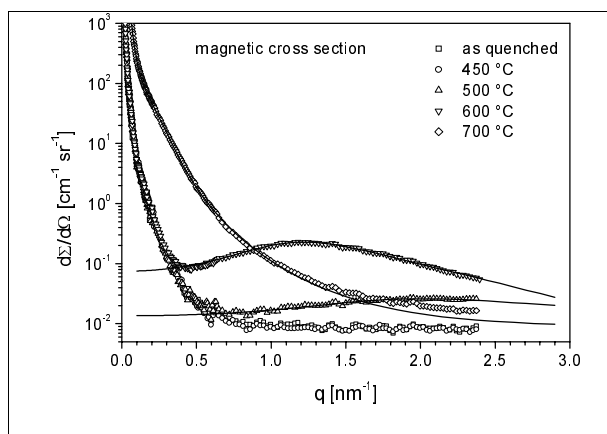
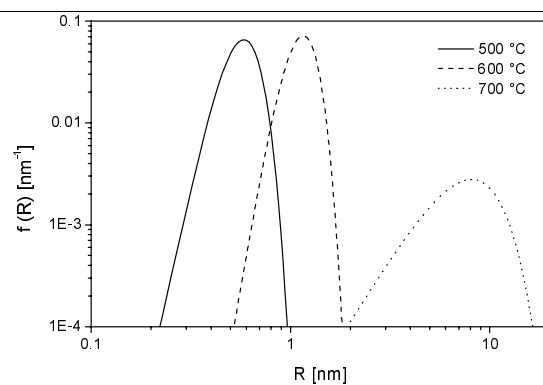


Figure 2: SANS scattering curves, nuclear cross section. The dotted line gives the  $q^{-4}$ -slope.



*Figure 3: Fit of magnetic cross section.*




*Figure 4: Particle size distributions obtained from the fit of the SANS curves (volume fraction).*

## References

- [1] P. Staron, B. Jamnig, H. Leitner, R. Ebner, H. Clemens, J. Appl. Cryst. 36 (2003) 415–419
- [2] J. S. Pedersen, J. Applied Crystallography 27 (1994) 595



	<b>EXPERIMENTAL REPORT</b>	<b>GeNF SANS-2</b>
<b>Characterisation of coherent Cu precipitates in Fe-Cu model alloys</b>		
<b>Principal Proposer:</b>	<b>M. Parlog<sup>1</sup></b> <sup>1</sup> Fraunhofer-Institut für zersörungsfreie Prüfverfahren, IZFP	
<b>Experimental Team:</b>	<b>M. Parlog<sup>1</sup>, P. K. Pranzas<sup>2</sup>, G. Kozik<sup>2</sup></b> <sup>2</sup> GKSS Research Centre	
<b>Date(s) of Experiment:</b>	July 2003	

### Scientific Objectives

The precipitation hardening of binary Fe-Cu alloys by thermal aging at 550 °C was investigated by using Small Angle Neutron Scattering (SANS). Cu precipitates are coherent with the Fe-matrix if they are smaller than 5 nm. In this size range all Cu particles are spherical. TEM investigations didn't detect any precipitates. SANS is an ideal tool to investigate structures in nanometer range. The aim of the present experiment was the determination of size, coherency, number density and volume fraction of coherent Cu precipitates in Fe-Cu alloys.

### Experimental technique

For the present study Fe-Cu samples with Cu content between 0.65 and 2.1 wt.% were manufactured. In order to get Fe-Cu alloys containing small and coherent copper precipitates, the specimens were solution treated at 1000 °C for 2 hours, quenched into water and thermally aged at 550 °C using the following conditions:

10 minutes, samples with Cu content between 0.65 and 1.4 wt. %

5 minutes, samples with Cu content between 1.5 and 2.1 wt. % [1].

SANS measurements were carried out with the instrument SANS-2 at the Geesthacht Neutron Facility (GeNF) by using selector-monochromated neutrons with a mean wavelength of  $\lambda = 0.58$  nm and a wavelength spread of  $\Delta\lambda/\lambda = 10$  %. The samples were magnetized to saturation in a field of 2 T. Four detector distances (1 m, 3 m, 9 m, 21 m) were used together with appropriate collimation to cover scattering vectors of magnitude  $q$  from  $0.02 \text{ nm}^{-1}$  to  $2.5 \text{ nm}^{-1}$ .

### Results

SANS measurements showed that the Fe-Cu samples contain Cu precipitates with a mean radius of 1.6–2.1 nm. It can be also observed that the maximum radius of the Cu particles is about 4 nm. In this size range all Cu precipitates are spherical and coherent with the  $\alpha$ -Fe-matrix. In this way the coherency of Cu particles with the  $\alpha$ -Fe-matrix was demonstrated.

Figure 1 shows that the Cu number density increases with rising Cu content. Figure 2 shows that also the volume fraction of coherent Cu particles increases with growing Cu content. This behaviour is caused by an increasing possibility of nucleation with rising Cu content, because the diffusion ways, which have to be crossed by the Cu atoms for Cu precipitates' nucleation, are shorter.

These measurements demonstrate that nucleation processes of Cu particles take place already during the early stage of ageing (5–10 min).

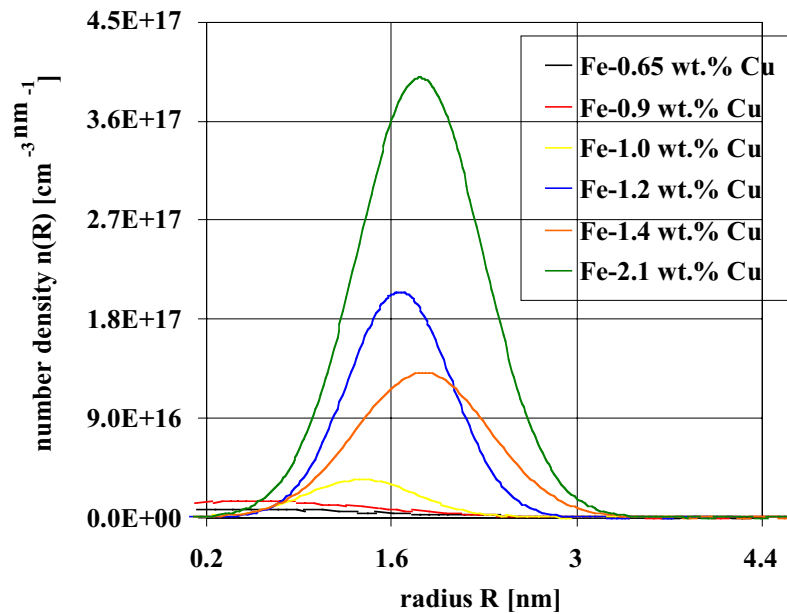


Figure 1: Number density distribution in Fe-Cu alloys assuming spherical precipitates.

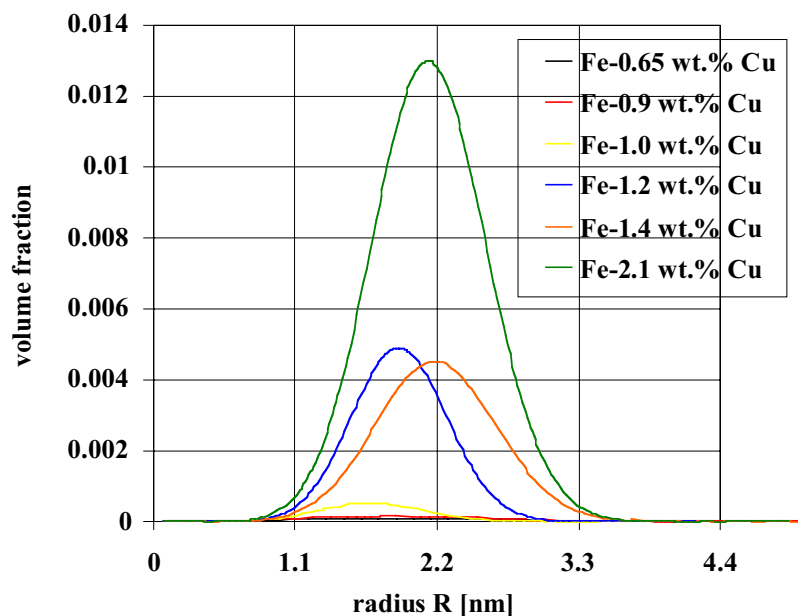



Figure 2: Volume fractions of Cu precipitates assuming spherical particles.

## References

- [1] M. Parlog, I. Altpeter, J. Breme, G. Dobmann: "Characterization of Copper Precipitates in Fe-Cu Alloys Using Micromagnetic NDE Techniques", eNDE2002, Saarbrücken, Germany, 12–14.07.2002
- [2] Williams, C., May, R.P. and Guinier, A. (1994) "Small-Angle Scattering of X-rays and Neutrons" in "Characterisation of Materials", E. Lifshin ed., Vol. 2B of "Materials Science and Technology", Weinheim: VCH Verlagsgesellschaft, pp. 611–656.

 <b>GKSS</b> FORSCHUNGSZENTRUM in der HELMHOLTZ GEMEINSCHAFT	<b>EXPERIMENTAL REPORT</b>	<b>GeNF SANS-2</b>
<b>SANS Round Robin for Engineering Materials Applications</b>		
<b>Principal Proposer:</b>	<b>M. Akamatsu<sup>1</sup>, C. H. de Novion<sup>2</sup>, P. K. Pranzas<sup>3</sup></b> <sup>1</sup> Electricité de France, Materials and Mechanics of Components Department, <sup>2</sup> CEA LLB, <sup>3</sup> GKSS Research Centre	
<b>Experimental Team:</b>	<b>P. K. Pranzas<sup>3</sup></b> <sup>3</sup> GKSS Research Centre	
<b>Date(s) of Experiment:</b>	July/August 2003	

### Scientific Objective

In the framework of the NET European Network on “Neutron Techniques Standardization for Structural Integrity” of the European Commission a Task Group (TG3) has been established with the aim to contribute towards a standardization of SANS for engineering materials applications. In a first step experimental procedures used at various SANS instruments at different neutron sources are compared to check that same scattering curves in absolute units are obtained. For this round-robin thermally-aged austeno-ferritic steels which are used e. g. in the primary loop of Pressurized Water Reactors have been chosen. These industrial samples – extensively characterized by Electricité de France [1] – have been measured on several SANS instruments at different neutron sources in Europe. The composition of the steel samples is listed in table 1. In table 2 ageing treatment, sample name, ferrite content and thickness are listed for each sample.

Table 1: Chemical composition of the studied steels (wt. %).

	<b>C</b>	<b>Si</b>	<b>Mn</b>	<b>Cr</b>	<b>Mo</b>	<b>Ni</b>
steel A10	0.039	1.22	0.60	20.0	2.56	10.0
steel P100	0.030	0.98	0.85	21.7	2.46	10.3

Table 2: Ageing treatments and ferrite contents of the studied samples.

<b>Heat</b>	<b>Ageing treatment</b>	<b>Sample</b>	<b>Ferrite content (%)</b>	<b>Thickness (mm)</b>
A10	homogenized	BOER	22.7	1.08
	2 500 h 350°C	BOC3.2	23.3	1.12
	10 000 h 350°C	BOC4	23.1	1.20
	30 000 h 350°C	BOC5	24.3	1.00
	30 000 h 400°C	BOD5A	24.5	0.58
		BOD5B	24.5	0.94
P100	homogenized	1208SZC2	28.1	1.40
	30 000 h 350°C	1208S3CM1	29.5	1.37

### Experimental Techniques

The experiments were carried out at the SANS-2 scattering facility of FRG-1 research reactor in Geesthacht (Germany). Neutrons with a wavelength of 0.58 nm with a resolution of  $\Delta\lambda/\lambda = 0.1$  and distances between sample and detector of 1, 3, 9 and 21 m were used to cover the range of scattering vector  $q$  from  $0.02 \text{ nm}^{-1}$  to  $2.4 \text{ nm}^{-1}$ . The scattered neutrons were detected by a position sensitive detector with  $256 \times 256$  pixels. The samples ( $10 \times 8 \times 1 \text{ mm}$ ) were magnetized to saturation in a horizontal magnetic field of 2 T and measured at room temperature. The aperture in front of the sample had a diameter of 5 mm.

The scattering data collected were normalized by a monitor. The detector response was determined using the isotropic scattering of a polyethylene reference sample. The scattering pattern of 1 mm Vanadium, corrected for sample transmission, background and detector response was used to obtain the scattering cross section in absolute units. In the 2-D scattering patterns of the steel samples the nuclear scattering is isotropic whereas the magnetic scattering can be observed only in vertical direction with an angle of 90° to the magnetic field. The scattering curves were calculated by azimuthal integration using sectors with a width of 15° in vertical (nuclear and magnetic scattering) and horizontal (nuclear scattering only) direction. The two scattering curves were subtracted from each other to obtain the structure information of the precipitates in the steel samples which appear as “magnetic holes”.

## Results

The obtained difference scattering curves are shown in figure 1.

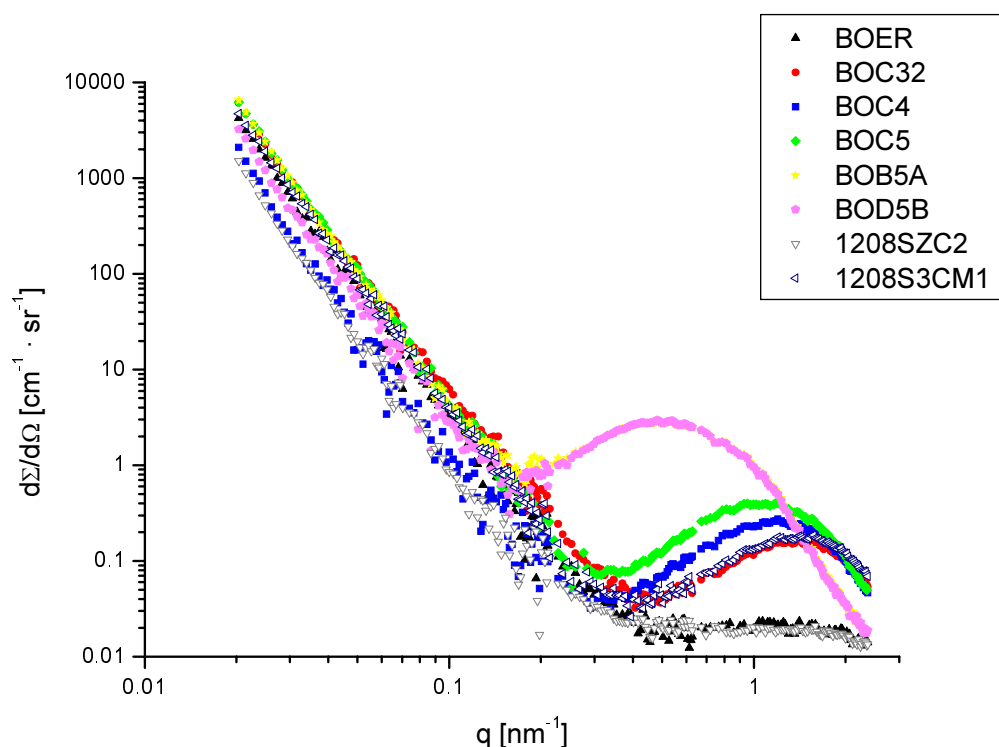



*Figure 1: Difference scattering curves showing the scattering of non-magnetic heterogeneities in the thermally-aged duplex stainless steel samples.*

At large  $q$  values a maximum can be observed in the scattering curves which is growing and at the same time moving to smaller  $q$  values with increasing ageing time and temperature. This signal is obviously caused by the formation and growth of non-magnetic heterogeneities in the steel samples. At smaller  $q$  values a  $q^{-4}$  decay is visible.

## Reference

- [1] J. P. Massoud, P. Auger, P. Danoix, R. Rezakhanlou, J. C. Van Duysen; Evaluation of the thermal ageing of duplex stainless steels, in R. E. Gold and E.P. Simonen (eds.); 6<sup>th</sup> Int. Symp. On Environmental Degradation of Materials in Nuclear Power Systems-Water Reactors; The Minerals, Metals & Materials Society (1993), 399–407.



	<b>EXPERIMENTAL REPORT</b>	<b>GeNF SANS-2</b>
<b>Surface structure of negatively charged “hairy” latex</b>		
<b>Principal Proposer:</b>	<b>R. Wang<sup>1</sup>, H. Schmiedel<sup>1</sup></b> <sup>1</sup> University of Leipzig, Institute of experimental Physics	
<b>Experimental Team:</b>	<b>R. Wang<sup>1</sup>, P. K. Pranzas<sup>2</sup>, H. Eckerlebe<sup>2</sup>, G. Kozik<sup>2</sup></b> <sup>2</sup> GKSS Research Centre	
<b>Dates of Experiment:</b>	August 17 <sup>th</sup> 2003 – September 6 <sup>th</sup> 2003	

### Scientific Objective

Negatively charged, hydrophilic copolymer latex nanoparticles (poly-(2, 3-epoxypropyl-methacrylate-co-methacrylic acid) in different ratio) possess hairy layers. The interaction between the hairy carboxylated layer of the latex and ionic detergents as well as non-ionic detergents was studied by isothermal titration calorimetry (ITC) and dynamic light scattering (DLS) where we found a monomer adsorption mechanism of CTAB on the carboxylated latex surface by Coulombic force<sup>0</sup>. In this report we carried out SANS measurements of latex nanoparticles in excess H<sub>2</sub>O/D<sub>2</sub>O mixtures. These measurements gave evidence and physical characterization of the core and the hairy layer of the particles.

### Experimental Technique

Copolymer latices EPS5, EPS3 and EPS1 of charge density 37, 22 and 8.5  $\mu\text{C}/\text{cm}^2$  were synthesized by a semi-batch emulsion polymerization and purified by ultrafiltration and ion exchange in Fraunhofer Institute for applied Polymer Research, Golm. Latices were dispersed in 7 H<sub>2</sub>O/D<sub>2</sub>O mixtures with mole ratio D<sub>2</sub>O of 0.9, 0.8, 0.7, 0.5, 0.3, 0.1 and 0.0. In all samples the latex concentration is 2 mg/mL. 1 mm quartz cuvettes were used for all measurements at room temperature.

Wavelengths were 5.8 and 11.58 Å with a resolution of  $\Delta\lambda/\lambda = 0.1$  and distances between sample and detector were 970, 2970, 8970 and 20970 mm with proper collimations and therefore the range of the scattering vector  $0.01 \text{ nm}^{-1} < q < 2.5 \text{ nm}^{-1}$  was used in the SANS experiments.

### Results

The neutron scattering curves change slightly with charge density on latex surface (Figure 1 right) indicating different core radii of the particles. More significant changes are observed for EPS5, EPS1 (Figure 1, left and middle) and EPS3 (not shown) in contrast variation.

As example, in a dispersion of EPS5 in H<sub>2</sub>O/D<sub>2</sub>O with  $X_{\text{D}_2\text{O}} = 0.7$  (Figure 2) we found striking difference between SANS and DLS radii. While DLS determined a hydrodynamic radius  $R_{\text{H}}$  of 72 nm for this sample<sup>1</sup>, SANS measurements brought out only 55.2 nm by GIFT program from Glatter<sup>2</sup> or 53 nm by SANSFIT program from GKSS. This can be interpreted as a core-hair structure with core of 55 nm and hair shell of 17 nm, which stretches into H<sub>2</sub>O/D<sub>2</sub>O mixtures. This supposition seems to be supported by the behaviour of the mean scattering length density profile (Figure 2, right) of the particles obtained by preliminary evaluation of the SANS data.

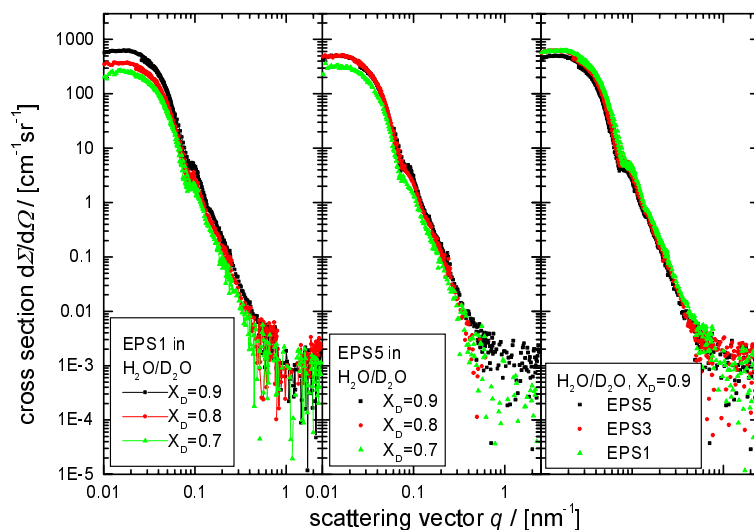


Figure 1: Scattering curves after subtraction of solvent. Latices (EPS5, EPS3 and EPS1) in H<sub>2</sub>O/D<sub>2</sub>O mixtures with  $X_{D_{2O}} = 0.9$  (right), EPS5 in H<sub>2</sub>O/D<sub>2</sub>O with  $X_{D_{2O}} = 0.9, 0.8$  and  $0.7$  (middle) and EPS1 in H<sub>2</sub>O/D<sub>2</sub>O with  $X_{D_{2O}} = 0.9, 0.8$  and  $0.7$  (left), all latex concentrations account to 2 mg/mL.

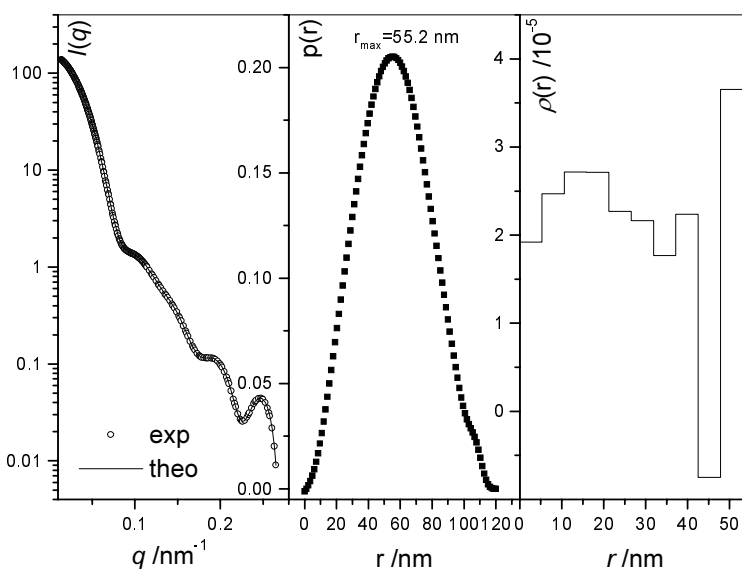



Figure 2: Scattering curve (left) for 2 mg/mL latex EPS5 in H<sub>2</sub>O/D<sub>2</sub>O mixture with  $X_{D_{2O}} = 0.7$ . These data were fitted with GIFT program and the resulting pair distance distribution was calculated (middle). The scattering length density versus radius  $r$  (right) was obtained from DECON program, Glatter<sup>2</sup>, taking 5 % polydispersity into account.

## References

- [1] Isothermal titration calorimetric (ITC) studies of surfactant interactions with negatively charged “hairy” latex nanoparticles, R. Wang, H. Schmiedel, B-R. Paulke, *Colloid and Polymer Science*, 2003, *submitted*.
- [2] Evaluation of small-angle scattering data of charged particles using the generalized indirect fourier transformation technique, G. Fritz, A. Bergmann, O. Glatter, *J. Chem. Phys.* 113, 2000, 9733–9740

	<b>EXPERIMENTAL REPORT</b>	<b>GeNF SANS-2/DCD</b>
<b>SANS investigation of SiO<sub>2</sub> nanoclusters in different solutions</b>		
<b>Principal Proposer:</b>	<b>hanse chemie AG</b> , Geesthacht, Germany <b>P. K. Pranzas<sup>1</sup>, H. Eckerlebe<sup>1</sup></b> <sup>1</sup> GKSS Research Centre	
<b>Experimental Team:</b>	<b>P. K. Pranzas<sup>1</sup></b>	
<b>Date(s) of Experiment:</b>	September 2003	

### Scientific Objective

Nanoscaled particles play an important role in various fields, e. g. as pigments and filler material in paints, coatings, castings, pottery or insulating materials.

Hanse Chemie develops the technology to synthesize oxide nanoparticles in an aqueous environment and to transform the particles into organic reactive polymers retaining their monodispersed structure. The particle surface should be tailored to the specific matrices. Small-angle neutron scattering (SANS) and Ultra small-angle neutron scattering (USANS) measurements aimed to investigate structure and size of a new class of nanocomposites.

### Experimental Techniques

Samples with different concentrations of SiO<sub>2</sub> in different organic solutions filled in quartz cells (Suprasil from Hellma, 1 mm flight path) were measured at the SANS-2 facility. The mean neutron wavelength was  $\lambda = 0.58$  nm and  $\lambda = 1.16$  nm ( $\Delta\lambda/\lambda = 0.1$ ). The range of the scattering vector ( $8 \cdot 10^{-3} \text{ nm}^{-1} < q < 1 \text{ nm}^{-1}$ ) was covered by 4 detector-sample distances (1 m, 3 m, 9 m, 21 m) at a wavelength  $\lambda = 0.58$  nm and by the detector-sample distance 21 m at  $\lambda = 1.16$  nm with appropriate collimations. The scattered neutrons were detected by a position sensitive detector with 256 x 256 pixels. Measured intensity was corrected for sample transmissions, background and detector efficiency. The absolute cross section was calculated by comparison with the incoherent scattering of vanadium.

Ultra small-angle neutron scattering (USANS) measurements were carried out at the double-crystal diffractometer DCD with a wavelength of 0.44 nm resulting in an accessible range of scattering vector  $q$  from  $10^{-5}$  to  $2 \cdot 10^{-2} \text{ nm}^{-1}$ .

### Results

The scattering behaviour of the samples is compared in figures 1 and 2. All SANS scattering spectra show an isotropic scattering pattern, thus the data were averaged over the azimuthal scattering angle. As it can be seen in Fig. 2 the cross section of the samples 12 and 13 are nearly equal, that means the size of the smaller particles are all about the same. The USANS data (Fig. 1) clearly indicates a difference in the particle size distribution of both samples for structures greater than 200 nm, which may be a result of the production process.

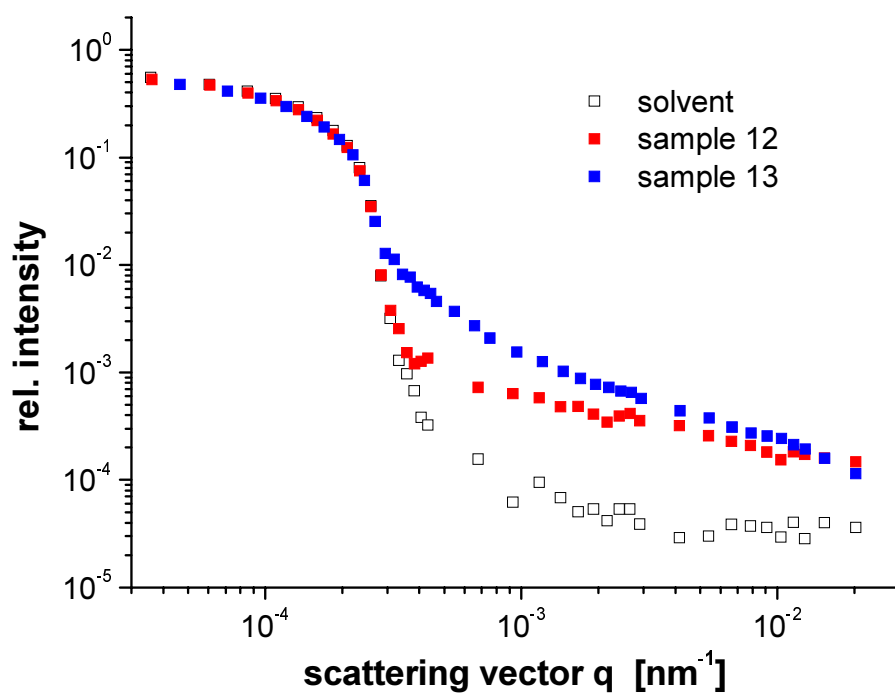


Figure 1: DCD scattering curves of solvent and samples 12 and 13. The relative intensity is plotted against the scattering vector  $q$ .

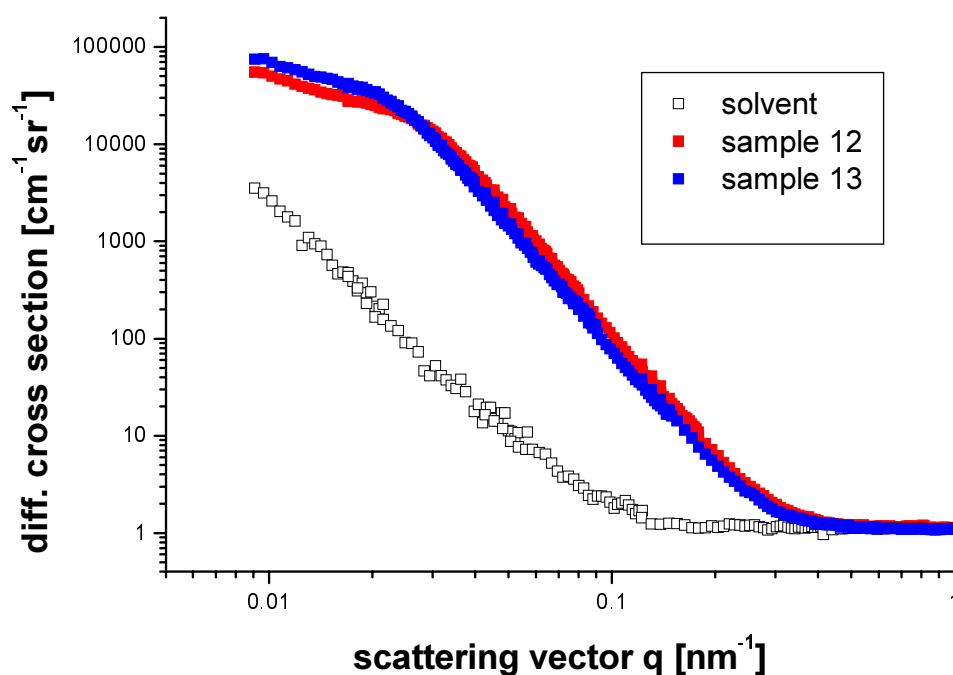



Figure 2: SANS scattering curves of solvent and samples 12 and 13. The differential cross section is plotted against the scattering vector  $q$ .

These initial results demonstrate that SANS and USANS are adequate methods to characterise  $\text{SiO}_2$  nanoclusters in solution and to distinguish between different  $\text{SiO}_2$  samples.

	<b>EXPERIMENTAL REPORT</b>	<b>GeNF SANS-2</b>
<b>SANS study of the early stages of crystallization in the soft magnetic Fe-Zr-B-Cu nanocrystalline alloys</b>		
<b>Principal Proposer:</b>	<b>Ivan Škorvánek</b> Institute of Experimental Physics SAS, Košice, Slovakia,	
<b>Experimental Team:</b>	<b>Jozef Marcin<sup>1</sup>, Helmut Eckerlebe<sup>2</sup>, Gerhard Kozik<sup>2</sup>, Ivan Škorvánek<sup>1</sup></b> <sup>1</sup> Institute of Experimental Physics SAS, Košice, Slovakia <sup>2</sup> GKSS Research Centre	
<b>Date(s) of Experiment:</b>	September 15–26, 2003	

### Scientific objective

Much attention has been devoted to the study of the mechanism of the evolution of nanocrystalline structures during the heat treatment process in soft magnetic FeZrB(Cu) alloys. The recent investigations performed by APFIM-technique provided some insight into the early stages of nanocrystallisation, revealing the significant role of the microscopic inhomogeneities (such as Cu-rich clusters), which are present in the thermally treated amorphous precursor alloy [1]. However, the nature of such inhomogeneities in different pre-crystallisation structural stages is not fully understood yet. In order to throw light on this topic, the local microstructural changes of amorphous  $\text{Fe}_{86}\text{Zr}_7\text{B}_6\text{Cu}_1$  alloy annealed up to the primary crystallisation were investigated in our study by using SAPNS technique.

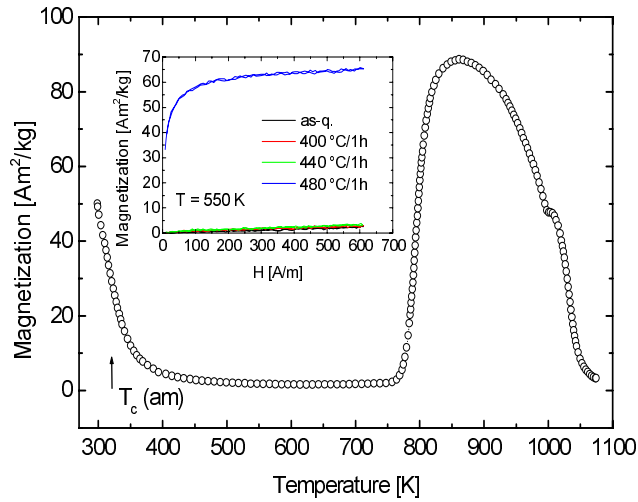
### Experimental Techniques

Amorphous ribbons of  $\text{Fe}_{86}\text{Zr}_7\text{B}_6\text{Cu}_1$  alloy were prepared by the method of planar flow casting. Pieces of these ribbons were annealed for 1 hour under high vacuum (better than  $10^{-6}$  mbar) at the temperatures 400, 440 and 480 °C to prepare the series of samples characterised by different microstructure. Changes in microstructure upon annealing were studied using the SANS-2 facility at the FRG-1 reactor at GeNF. A polarised neutron beam with a wavelength of  $\lambda = 0.58$  nm was used. The magnetic field of 1 T was applied perpendicular to the n-beam direction in order to saturate the ferromagnetic samples. All measurements were performed with polarisation of the primary neutron beam parallel and antiparallel to the sample magnetisation.

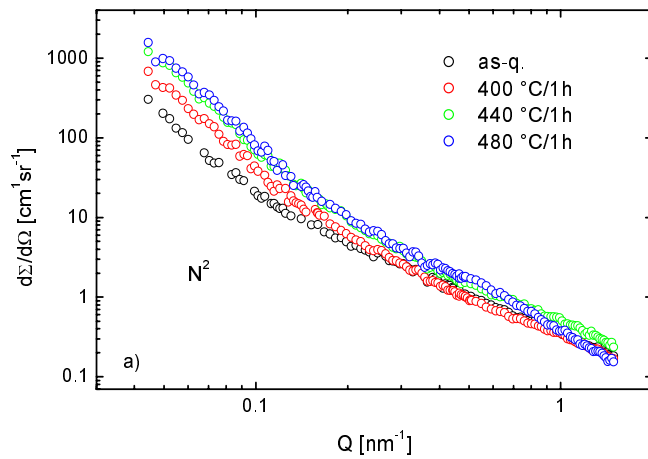
### Main Results

Fig. 1 shows the temperature dependence of magnetisation for the as-quenched amorphous sample as determined by VSM magnetometry. The first fall of magnetisation after heating of material corresponds to the ferro-paramagnetic transition of the amorphous material ( $T_C(\text{am}) \sim 320$  K). The increase of magnetisation at temperatures above 760 K is associated with the formation of the ferromagnetic bcc-Fe grains with a Curie temperature higher than the measuring temperature. The inset in Fig. 1 shows the field dependence of magnetisation taken at 550 K for the samples annealed for 1 hour at indicated temperatures. Since the amorphous phase is paramagnetic at this temperature, the saturation magnetisation can be used as a direct measure of the corresponding fraction of ferromagnetic crystalline phase that has been formed due to amorphous-crystalline transformation. It is evident that only the sample annealed at 480°C for 1 hour exhibits a presence of the ferromagnetic bcc-Fe nanograins (as confirmed also by XRD).

Figures 2(a) and (b) show the nuclear and nuclear + magnetic SANS components for the investigated samples. The SANS intensity evolution after heat treatment at different annealing temperatures, both below and above the crystallisation temperature of the alloy, clearly indicates the formation of nano-sized structural and magnetic inhomogeneities.



*Figure 1: Temperature dependence of magnetisation for the as-quenched amorphous samples determined by VSM magnetometry. The inset shows the field dependence of magnetisation taken at 550 K for the samples annealed for 1 hour at indicated temperatures.*



*Figure 2a: Nuclear cross section for the investigated samples.*

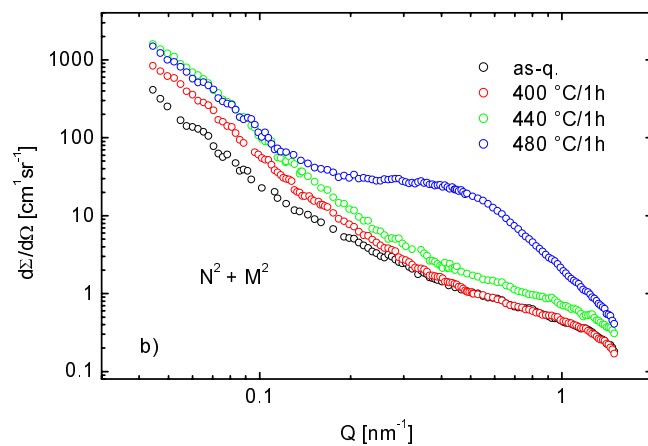


*Figure 2b: Nuclear cross section for the investigated samples.*

The presence of small scattering centers before crystallisation is indicated from the observed difference between the as-quenched sample and the samples annealed for 1 hour at 400 °C and 440 °C. The estimated size corresponds to that of Cu-rich clusters (~1 nm) observed for the alloy of similar composition by using APFIM and HRTEM [1]. On the other hand, a

marked difference between the nuclear and magnetic SANS components for the sample annealed at 480 °C for 1 hour clearly shows the presence of magnetic inhomogeneities of bigger dimensions which are associated with the ferromagnetic bcc-Fe nanocrystalline grains (10–20 nm) embedded in weak magnetic amorphous residual phase.


Since the extremely fine structure of the precipitates are formed before crystallisation, an angle of scattering larger than that of conventional small-angle scattering should be used to cover the corresponding range of scattering vectors. It is clear that such wider q-range data are essential for the reliable determination of the respective size distribution function. For this purpose it is necessary to use an additional wide-angle 2-dimensional side detector in future experiments.

## **Reference**

[1] T. Okubo et al., Scripta Mater. 44 (2001), 971





	<b>EXPERIMENTAL REPORT</b>	<b>GeNF SANS-2/DCD</b>
<b>Structural Characterisation of the Erosion of Polyimides by Simulated Space Debris and Atomic Oxygen</b>		
<b>Principal Proposer:</b>	<b>E. Grossman<sup>1</sup>, I. Gouzman<sup>1</sup>, N. Eliaz<sup>2</sup>, A. Schreyer<sup>3</sup>, P. K. Pranzas<sup>3</sup></b> <sup>1</sup> Soreq NRC, Space Environment Division, <sup>2</sup> Tel Aviv University, Dept. Solid Mechanics, Materials and Systems, <sup>3</sup> GKSS	
<b>Experimental Team:</b>	<b>D. Bellmann<sup>3</sup>, P. K. Pranzas<sup>3</sup>, H. Eckerlebe<sup>3</sup></b>	
<b>Date(s) of Experiment:</b>	October 2003	

### Scientific Objective

Kapton and other polyimides are ubiquitous on spacecraft. However, like all hydrocarbon-based polymers, polyimides erode in the highly oxidative environment of low-Earth orbit (LEO), thus, requiring an Atomic-Oxygen (AO) protective layer. A specifically promising approach to the production of space-survivable polymers (which do not need an AO protective layer) is to incorporate polyhedral oligomeric silsesquioxanes (POSS<sup>TM</sup>) into the polymer structure, thereby creating an inorganic/organic hybrid polymer. The exposure of POSS-polymer material to AO forms an oxide protective layer preventing further degradation of the material. However, micrometeoroids or space debris impacts, resulting in holes or cracks, could expose the bulk material beneath the protective layer to atomic oxygen attack. In addition to conventional characterization techniques such as light microscopy, SEM, XRD and tensile testing, small and ultra-small angle scattering experiments were performed to study the synergistic effect of debris impact and atomic oxygen attack on the POSS<sup>TM</sup> polyimides erosion.

### Experimental Techniques

In a first approach 50 and 125  $\mu\text{m}$  thick Kapton (polyimide) foils which had been exposed to space-simulating environment were investigated at the two instruments SANS-2 and DCD.

At the small-angle neutron scattering instrument SANS-2 neutrons with a wavelength of 0.58 nm (resolution  $\Delta\lambda/\lambda = 0.1$ ) and distances between sample and detector of 1, 3, 9 and 21 m were used to cover the range of scattering vector  $q$  from 0.023 to 2.6  $\text{nm}^{-1}$ . The samples were measured at the area surrounding a penetrating hole using an aperture in front of the sample with a diameter of 4 mm. The scattering data collected were normalized by a monitor. The detector response was determined using the isotropic scattering of a polyethylene reference sample. The scattering pattern of 1 mm Vanadium, corrected for sample transmission, background and detector response was used to obtain the scattering cross section in absolute units.

Ultra small-angle neutron scattering (USANS) measurements were carried out at the double-crystal diffractometer DCD with a wavelength of 0.44 nm resulting in an accessible range of scattering vector  $q$  from  $10^{-5}$  to  $10^{-3} \text{ nm}^{-1}$ . With this techniques particle sizes up to 24  $\mu\text{m}$  are still detectable. The gap between the range of DCD and SANS data had to be interpolated (see figure 2), because of the low scattering power and high background in case of DCD measurements the  $q$ -range was limited to  $4 \times 10^{-3} \text{ nm}^{-1}$ .

### Results

In figure 1 the DCD scattering curves of two Kapton foils are shown – one after the impact of high-velocity debris and one reference foil without impact. The region with the strongest signal is marked.

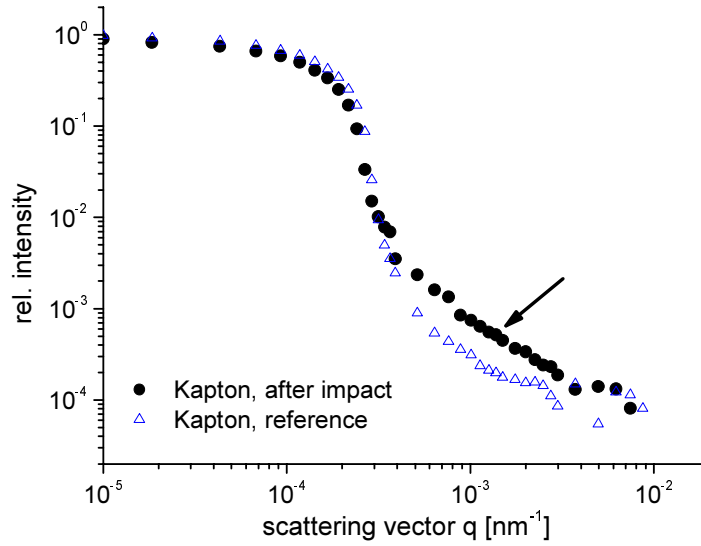


Figure 1: DCD scattering patterns of a 125  $\mu\text{m}$ -thick Kapton film after impact of high-velocity debris and of a reference foil. The relative intensity is plotted against the scattering vector  $q$ .

In figure 2 the results of the combined DCD and SANS scattering data are shown together with the fit of the model calculation. In figure 3 the corresponding size distribution is demonstrated which was calculated from the scattering curves using the hard sphere model.

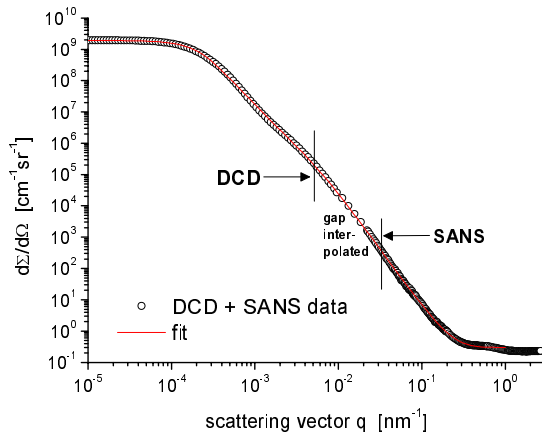


Figure 2: Results of combined SANS and DCD scattering curves of a 125  $\mu\text{m}$ -thick Kapton film following the impact of high-velocity debris. The scattering cross section is plotted against the scattering vector.

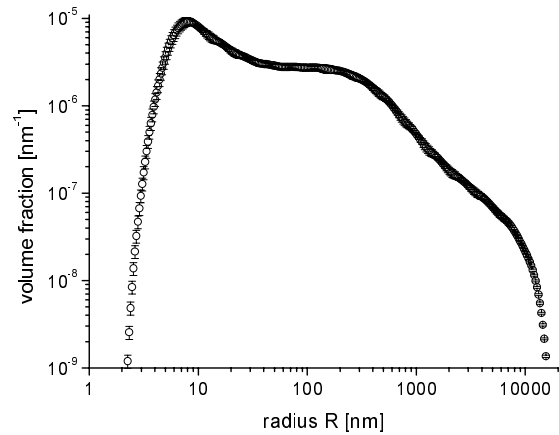



Figure 3: Corresponding sizes distribution calculated from the data shown in fig. 2. The relative volume fraction of the scatter centres is plotted against the sphere radius.

The maximum of the distribution at approx. 10 nm results from the Kapton itself. The two shoulders at larger radius are from the structures surrounding the penetration hole in the impact samples. Structures with maximum radii up to 12  $\mu\text{m}$  were found. Equal results – of course with a loss in the statistics – were obtained for a 50  $\mu\text{m}$  thick Kapton foil.

These initial results clearly demonstrate that neutron scattering methods are ideally suited to provide information on structural changes due to the destruction of the Kapton samples.

	<b>EXPERIMENTAL REPORT</b>	<b>GeNF SANS-2</b>
<b>Wide-Angle Scattering Investigations of the Phase Separation Kinetics in Cu-0.9 at.% Ti Using a 2-dimensional Side Detector</b>		
<b>Principal Proposer:</b>	<b>S. Prasetyo</b> GKSS Research Centre	
<b>Experimental Team:</b>	<b>S. Prasetyo, H. Eckerlebe</b> GKSS Research Centre	
<b>Date(s) of Experiment:</b>	October 2003	

### Scientific Objective

A fine scale dispersion of second phase within a metallic matrix in a copper-titanium alloy can lead to significant strengthening. The most important methods of introducing a second phase in a metallic matrix are precipitation hardening or age hardening. The formation of a second phase commonly results from the decomposition of the solid solution during cooling. The small sizes of the precipitates during nucleation and at short ageing times as well as the fine scale of the precipitate distribution make it difficult to obtain detailed and unambiguous information concerning the initial stages of the process.

Wide Angle Neutron Scattering (WANS) is used in this work because of its ability to provide access to structural analysis of unmixed alloy in the very early stages where the composition fluctuations are extremely small in spatial extension and in amplitude. To determine the end of the nucleation process, the Ti concentration in the Cu matrix is calculated from the diffuse Laue scattering. Furthermore, the composition of the precipitates in the alloy is investigated.

### Experimental Technique

Cu-0.9 at.%Ti single crystals were solution annealed at the three different homogenisation temperatures 700 °C, 750 °C and 850 °C and aged at 300 °C for 20 seconds and 1, 2, 5, 10, 20, 60 minutes as well as 2, 5, 10 and 135 hours.

The neutron scattering measurements were carried out at the small-angle scattering instrument SANS-2 at GKSS, using a 2-dimensional side detector for wide angles.

The used neutron wavelength was 0.58 nm. The range of the scattering vector ( $0.6 \text{ nm}^{-1} < q < 8 \text{ nm}^{-1}$ ) was covered by moving the detector around the sample for  $27^\circ$  referring to the beam direction. A pure copper sample was used as a reference, and it has been measured together with the Cu-Ti sample in each step during measurement. Measured intensity was corrected for sample transmission, background and detector efficiency.

### Results

The small maximum of the as-quenched sample between  $1 \text{ nm}^{-1} < q < 3 \text{ nm}^{-1}$  indicates that a phase separation has occurred during the quench process (Fig. 1). This is in agreement with the concentration of Ti in the Cu matrix, which is smaller than 0.9 at.% (Fig. 3), calculated from the diffuse Laue scattering at  $q > 6 \text{ nm}^{-1}$  (Fig. 2). After annealing for  $t_A = 5$  minutes only, the decrease of the diffuse Laue scattering can clearly be seen. With increasing aging time,

the volume fraction (Fig. 4) of the formed particles grow rapidly. This indicates that the nucleation process is in progress. After aging for  $\sim 6$  h the Ti concentration in the matrix is nearly 0.2 at.%, hence the nucleation process is completed and the coarsening process has become dominant. The theoretical maximum volume fractions of  $\text{Cu}_3\text{-Ti}$  and  $\text{Cu}_4\text{-Ti}$  clusters are  $2.82 \times 10^{-2}$  and  $3.93 \times 10^{-2}$  respectively, and these measurements clearly match with the maximum value for  $\text{Cu}_3\text{-Ti}$  clusters (Fig. 4).

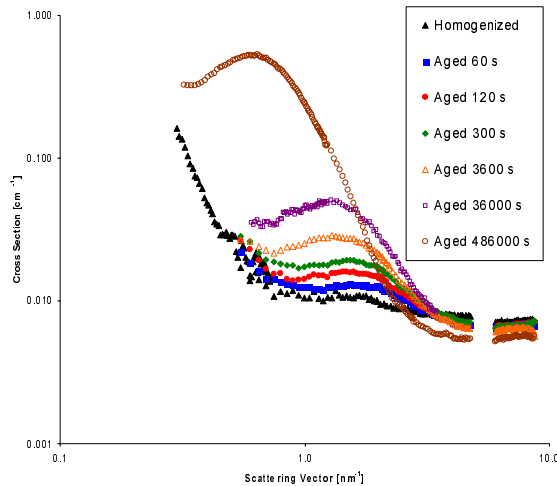


Figure 1: Scattering curves of annealed Cu-0.9 at.%Ti samples.

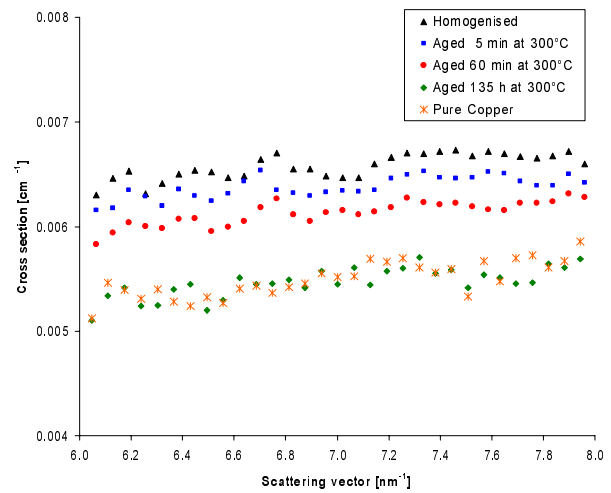


Figure 2: Enlargement of Fig. 1 in the range  $6 \text{ nm}^{-1} < q < 8 \text{ nm}^{-1}$  for better view of the diffuse Laue scattering.

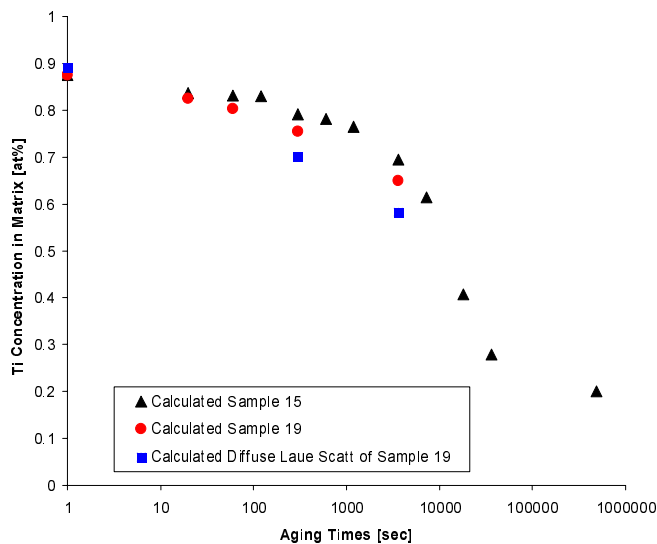


Figure 3: Decrease of the Ti concentration in the Cu matrix with aging time.

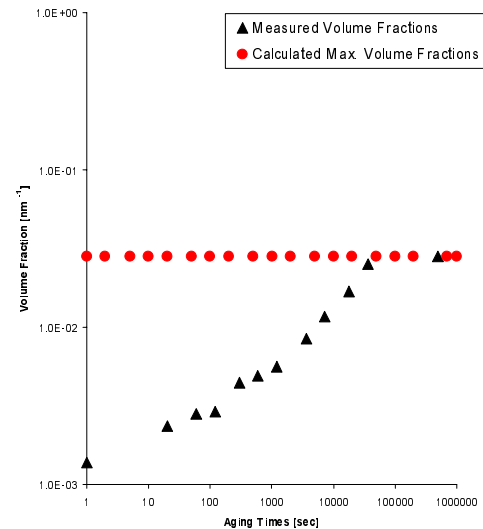



Figure 4: Volume fraction of precipitations assuming spherical particles. The dotted line shows the max. volume fraction assuming  $\text{Cu}_3\text{Ti}$  clusters.

	<b>EXPERIMENTAL REPORT</b>	<b>GeNF SANS-2</b>
<b>The study of the static and dynamic spin chirality in the reentrant spin glass system <math>(\text{Pd}_{0.984}\text{Fe}_{0.016})_{0.95}\text{Mn}_{0.05}</math> by small angle scattering of polarized neutrons</b>		
<b>Principal Proposer:</b>	<b>G. P. Gordeev<sup>1</sup>, L. A. Axelrod<sup>1</sup>, S. V. Grigoriev<sup>1</sup>, I. M. Lazebnik<sup>1</sup>, V. N. Zabenkin<sup>1</sup>, V. Wagner<sup>2</sup></b> <sup>1</sup> Petersburg Nuclear Physics Institute (PNPI), Russia <sup>2</sup> Physik.Tech.Bundesanstalt (PTB), Braunschweig, Germany	
<b>Experimental Team:</b>	<b>G. P. Gordeev<sup>1</sup>, L. A. Axelrod<sup>1</sup>, S. V. Grigoriev<sup>1</sup>, H. Eckerlebe<sup>3</sup>, G. Kozik<sup>3</sup></b> <sup>3</sup> GKSS Research Centre	
<b>Date(s) of Experiment:</b>	<b>Oktober 2003</b>	

### Scientific Objective

This experiment is a part of a long-term project and is aimed to investigate the static and dynamic properties of the spin system in dilute alloy  $(\text{Pd}_{0.984}\text{Fe}_{0.016})_{0.95}\text{Mn}_{0.05}$ . Due to competition of exchange spin interactions this alloy has a nontrivial magnetic mesostructure [1] with the ferromagnetic transition at  $T_C = 40$  K and the reentrant spin-glass transition at  $T_{SG} = 30$  K. Recently, Kawamura proposed the chiral mechanism for explanation of the spin-glass phase transition [2]. He suggested that not pair correlation of the Ising's spins, but the chiral three-spin fluctuation is the key object of such a transition. Kawamura supposed that experimentally observed effects at such transitions in Heisenberg magnetics should be referred to a chiral rather than an ordinary spin glass. This approach requires reconsideration of the spin glass transition both from theoretical and experimental point of view. In this connection it was interesting to perform a thorough study of the polarised neutron scattering in the spin (chiral) glass systems in an external magnetic field. The use of Polarised Neutrons allows one, first, to separate chiral contribution in the scattering from that of the ordinary pair spin correlation extracting the asymmetrical part of the Small-Angle Polarised Neutron Scattering (SAPNS). Second, the inclined and/or perpendicular experimental geometry of the magnetic field [3] makes it possible to separate the dynamic and static contributions in the chiral scattering in the spin glass system. We tried to observe these different contributions using SANS2 setup of FRG-1 research reactor.

### Experimental Techniques

A polarized neutron beam with the initial polarization  $P_0 = 0.95$  and the wavelength  $\lambda = 0.58$  nm ( $\Delta\lambda/\lambda = 0.1$ ) was used. The scattered neutrons were detected by an area detector with  $256 \times 256$  pixels of  $2.2 \times 2.2$  mm<sup>2</sup>. The thermostat with the sample was settled in the magnet producing the horizontal magnetic field along the largest dimension (25 mm) of the sample. The scattered intensity was measured in the wide temperature range from  $T = 120$  K down to  $T = 9$  K for two states of a spin flipper, i.e. with the in beam polarization  $\pm P_0$ . The magnet allowed to change angle  $\varphi$  between the magnetic field  $\mathbf{H}$  and the beam direction  $\mathbf{k}_0$  from  $45^\circ$  to  $90^\circ$ . The external magnetic field  $\mathbf{H}$  from 6.25 mT to 100 mT was applied at the angles  $\varphi = 45^\circ$ ,  $\varphi = 60^\circ$ ,  $\varphi = 75^\circ$  (inclined geometry) and  $\varphi = 90^\circ$  (perpendicular geometry). The differences  $\Delta I = I(P_0) - I(-P_0)$  were analyzed at different angles  $\varphi$  for each temperature and magnetic field. At the preliminary data processing the simple averaging on  $90^\circ$  sector along horizontal axis X of the detector was used to get the dependences  $\Delta I(T)$  and  $\Delta I(H)$  for left and right side of the detector, i.e. for  $-q$  and  $+q$ .

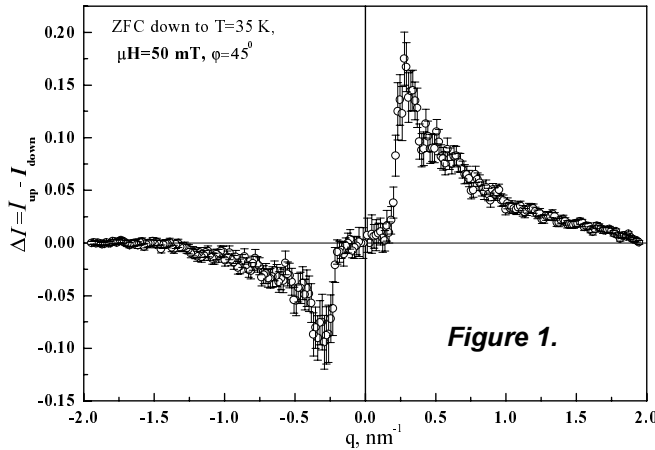
The inclined geometry allows observation of the left-right asymmetry in SAPNS pattern that originates from the interaction of the neutron spin with the chiral spin excitations. At the same time the contribution from the static chirality may also take place, originating from the peculiarities of magnetic structure in spin glass state [2]. Generally, the cross section of polarized neutron is described by a sum of two items: one of them does not depends on initial polarization  $P_0$  and another is proportional to  $P_0$ . The later is given by [3]:

$$\frac{\partial^2 \sigma}{\partial \Omega \partial \omega} = \frac{1}{2\pi} A_m^2 \frac{k'}{k} |F(\mathbf{q})|^2 S(\mathbf{q}, \omega, P_0) \quad (1)$$

where  $A_m$  is magnetic scattering length of the atom,  $F(\mathbf{q})$  is magnetic form factor (for small angle scattering one can put  $F(\mathbf{q}) = 1$ ). For  $\mathbf{P} \parallel \mathbf{m}$  ( $\mathbf{m} = \mathbf{M}/M$ ) the scattering law can be written as  $S = S_s + S_{as}$ , where  $S_s$  and  $S_{as}$  are symmetrical (magnetic-nuclear interference) and asymmetrical (chiral) contributions, which are maximal for momentum transferred  $q$  perpendicular and parallel to  $\mathbf{m}$ , respectively. The  $\omega$ -integrated cross section (1) is given by

$$\frac{\partial \sigma}{\partial \Omega} = 2P_0 A_m^2 \int d\omega (\mathbf{e} \cdot \mathbf{m})^2 S_{as}(\mathbf{q}, \omega) \quad (2)$$

where  $\mathbf{e} = \mathbf{q}/q$ . The  $\omega$ -dependent cross section has a maximum at  $\varphi = 45^\circ$  and it changes sign with changing sign of  $q$  due to the factor  $(\mathbf{e} \cdot \mathbf{m})^2$ . But in the case of  $\varphi = 90^\circ$  ( $\mathbf{k}_0 \perp \mathbf{H}$ )  $\omega$ -dependent contribution disappears and the static chiral contribution  $S_{as}(q)$  will be observed.



## Results

The existence of the typical asymmetry in a difference  $\Delta I(q)$  attributing to the chiral scattering cross section is demonstrated in Figure 1. From this  $q$ -dependence the angle  $\theta_c$  (the spin wave cut off angle) and its behavior with the magnetic field ( $\theta_c^2 = \theta_0^2 - g\mu H\theta_0/E_n$ ) are evaluated. The angle  $\theta_0$  is inversely proportional to the spin wave stiffness  $D = h/(4\pi m_n \theta_0)$  ( $m_n$  is the neutron mass).

The evaluation gives a value of  $D \approx 20 \text{ meV} \cdot \text{\AA}^2$ . It is smaller than that of the FeNi alloy, where  $D = 140 \text{ meV} \cdot \text{\AA}^2$ . Both temperature and magnetic field dependence of the difference  $\Delta I$ , integrated over  $q$ , are shown in Figures 2 and 3 respectively.

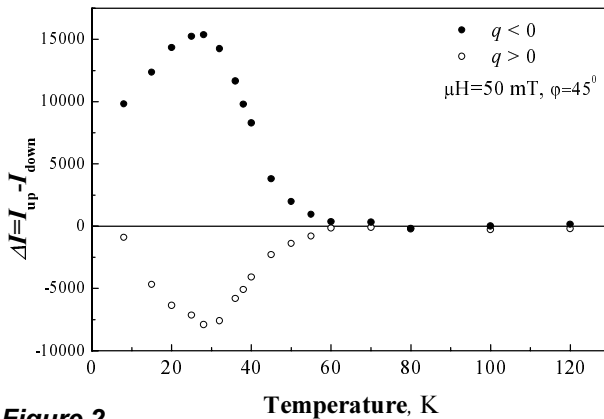


Figure 2.

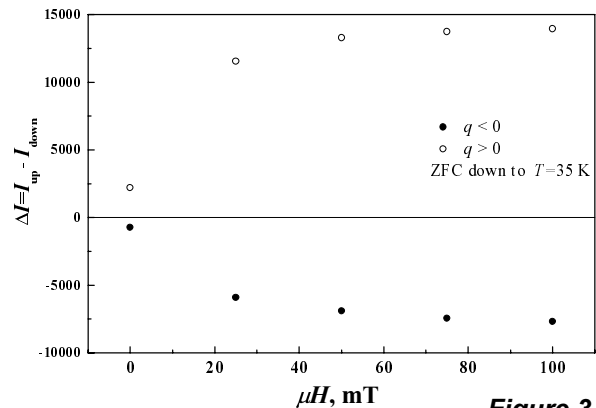


Figure 3.

Figure 2 shows the maximum in the asymmetric scattering at  $T = 25\text{--}28\text{ K}$ . The contribution of symmetric part is also well seen. Figure 3 shows  $\Delta I(H)$  linearly increasing at the low field. It tends to saturate at the field  $H \approx 40\text{ mT}$ . A weak influence of  $\Delta I$  on the cooling regimes was also observed.

More interesting results were observed at  $\varphi = 90^\circ$  (Figure 4). The asymmetry is also present in this case. However, it is by factor of 10 smaller than that observed at  $\varphi = 45^\circ$ . Perhaps, this may be ascribed to the sum of the symmetric (magnetic-nuclear interference) and asymmetric contributions. The asymmetric part in this case is attributed to the pure static chirality in spin glass region of alloy under investigation. The presence of the spin chirality is also demonstrated in Figure 5, where the temperature dependence of  $\Delta I$  in a very low field (0.4 mT) shows the increase of the asymmetric scattering at  $T = 37\text{ K}$ . The detailed analysis of the data currently goes on.

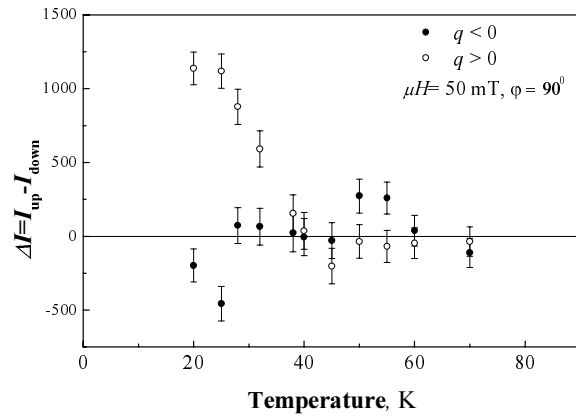


Figure 4.

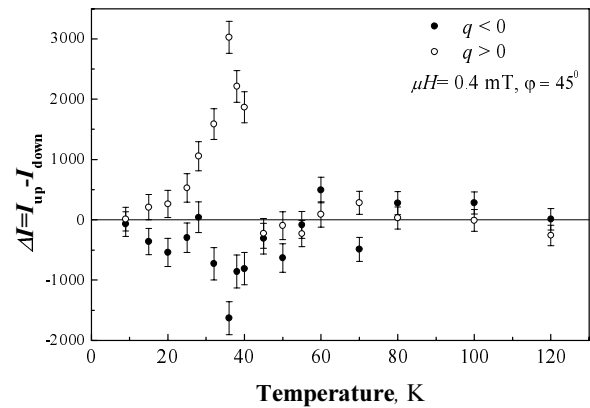


Figure 5.

## Conclusion


The results of experiment show undoubtedly an urgency to search the chiral ordering in spin glass system by using such setups as SANS-2.

## References

- [1] G. P. Gordeev, L. A. Axelrod, V. N. Zabenkin, I. M. Lazebnik, V. Wagner, H. Eckerlebe, Physica B 335 (2003) 127–129.
- [2] G. P. Gordeev, L. A. Axelrod, I. M. Lazebnik, S. V. Grigoriev, V. N. Zabenkin, V. Wagner, H. Eckerlebe, Physica B (in press).
- [3] H. Kawamura, M. Suan Li, Phys. Rev. Lett. 87 (2001) 187204 (1–4).
- [4] A. V. Lazuta, S.V. Maleyev, B.P. Toperverg, Sov. Phys. JETP 54, 113 (1981).





 <b>GKSS</b> FORSCHUNGSZENTRUM in der HELMHOLTZ GEMEINSCHAFT	<b>EXPERIMENTAL REPORT</b>	<b>GeNF SANS-2</b>
<b>Critical magnetic scattering in the isotropic ferromagnet EuS</b>		
<b>Principal Proposer:</b>	<b>A. I. Okorokov<sup>1</sup>, S. V. Grigoriev<sup>1</sup></b> <sup>1</sup> Petersburg Nuclear Physics Institute	
<b>Experimental Team:</b>	<b>H. Eckerlebe<sup>2</sup>, P. K. Pranzas<sup>2</sup>, D. Lamago<sup>3</sup>, A. I. Okorokov<sup>1</sup>, S. V. Grigoriev<sup>1</sup>, S. V. Metelev<sup>1</sup>, Yu. O. Chetverikov<sup>1</sup></b> <sup>1</sup> PNPI, <sup>2</sup> GKSS, <sup>3</sup> TU-München	
<b>Date(s) of Experiment:</b>	November 2003	

### Scientific Objective

This experiment was aimed to investigate the spin dynamics of the isotropic ferromagnet EuS near the magnetic phase transition by means of small angle polarized neutron scattering (SAPNS). EuS is interesting for its large magnetic moment and for the effect, which the dipole forced may have on the critical behavior of the system. SAPNS experiments were performed using the special "inclined" magnetic field geometry [1–4].

### Experimental Techniques

The SAPNS experiments were carried out at the SANS-2 scattering facility of FRG-1 research reactor in Geesthacht (Germany). A polarized beam of neutrons with an initial polarization of  $P_0=0.95$ , the neutron wavelength  $\lambda = 5.8 \text{ \AA}$  ( $\Delta\lambda/\lambda=0.1$ ) and a divergence of 10 mrad was used. The scattered neutrons were detected (in the  $q$ -range from 0.25 to 2.5  $\text{nm}^{-1}$ ) by a position sensitive detector with 256×256 pixels. The scattering intensity was measured in the temperature range from  $T = 14 \text{ K}$  to  $T = 50 \text{ K}$ . The external magnetic field  $H$  from 1 to 200 mT was applied at the angle  $\varphi = 45^\circ$ , with respect to the incident beam  $\mathbf{k}$ , providing, so-called, "inclined" geometry. This geometry allows one to observe the left-right asymmetry in SAPNS pattern that originate from the interaction of the neutron spin with the chiral dynamical excitations. According to Ref. [2] in a magnetized sample the magnetic cross section has the form:

$$\sigma(\mathbf{q}, \omega) = \sigma_0(\mathbf{q}, \omega) + (\mathbf{q}, \mathbf{P}_0)(\mathbf{q}, \mathbf{H})\sigma_{\text{ch}}(\mathbf{q}, \omega)/q^2,$$

where the second term is determined by chiral dynamical spin fluctuations and  $\mathbf{P}_0$  and  $\mathbf{H}$  are the neutron polarization and the magnetic field, respectively.

$$\sigma(\mathbf{q}, \omega) = \sigma_0(\mathbf{q}, \omega) + (\mathbf{q}, \mathbf{P}_0)(\mathbf{q}, \mathbf{H})\sigma_{\text{ch}}(\mathbf{q}, \omega)/q^2,$$

where the second term is determined by chiral dynamical spin fluctuations and  $\mathbf{P}_0$  and  $\mathbf{H}$  are the neutron polarization and the magnetic field, respectively.

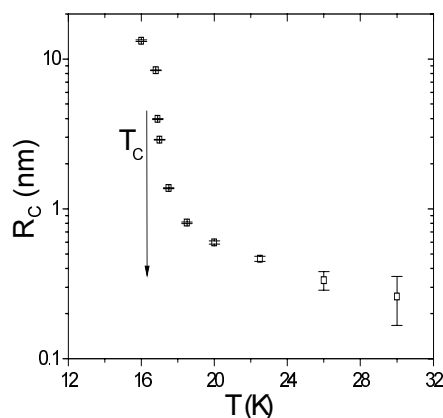


Figure 1: Temperature dependence of correlation radius  $R_C$ .

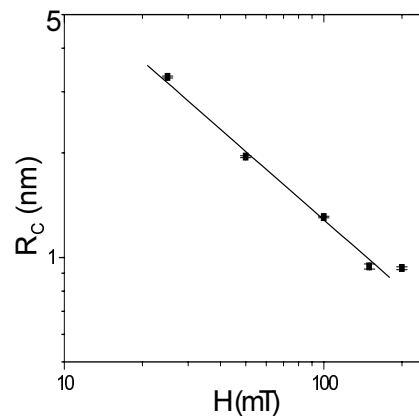


Figure 2: Effect of magnetic field on  $R_C$  at  $T = 16.6 \text{ K}$ .

In the case of small-angle scattering  $\omega$  integrated chiral contribution to the cross section changes sign with  $\theta$  and may be easily extracted from the total scattering intensity. These two contributions to the critical magnetic scattering were studied in the temperature range around  $T_C = 16.6$  K. First, the intensity of the magnetic scattering,  $I_m(q) = I(q, T) - I(q, T \gg T_C)$ , is attributed to the pair spin correlation function. Another contribution caused by the three-spin chiral fluctuations. It is separated from other contributions as the asymmetric part of the polarization dependent scattering [1–4]:  $\Delta I(\theta) = [I_+(\theta) + I_-(-\theta) - I_+(-\theta) - I_-(\theta)]$  where  $I_+(\theta)$  and  $I_-(\theta)$  are  $\omega$  integrated intensities with the polarization directed along and opposite to the field.

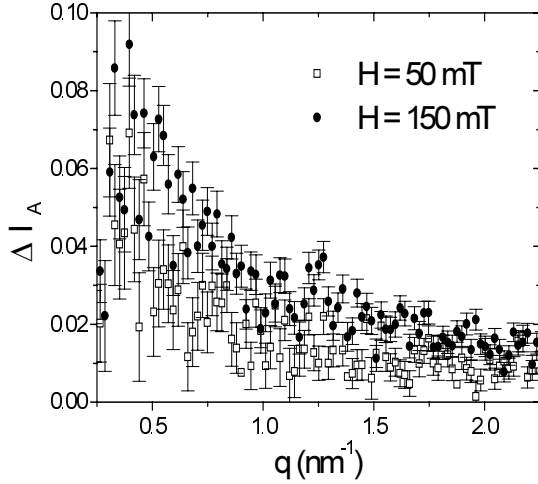


Fig. 3: Asymmetric scattering  $\Delta I_A(q)$  at magnetic field of  $H = 50$  and  $150$  mT at  $T = 16.6$  K.

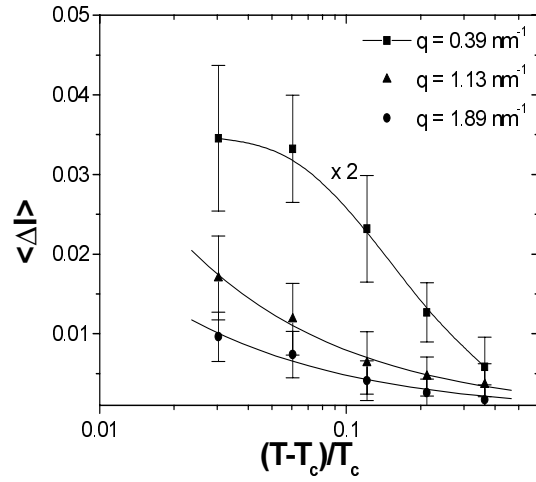


Fig. 4: Averaged values  $\langle \Delta I_A \rangle$  as function of reduced temperature  $\tau$ .

## Results

The measured SAPNS intensity is well described by the Ornstein-Zernike expression:  $I(q) = A/(q^2 + \kappa^2)$ , where  $A$  and  $\kappa$  are the scattering amplitude and the inverse correlation length, respectively. As shown in Fig. 1, the correlation radius  $R_C = \kappa^{-1}$  increases while temperature approaches  $T_C = 16.6$  K from above and decreases with further lowering of  $T$ . The value of  $A$  demonstrates a similar behavior.

The effect of the magnetic field on the correlation length  $R_C$  at  $T = 16.6$  K is shown in Fig. 2. The value of  $R_C$  decreases with increasing field. This behavior of  $R_C$  is a result of a crossover to the strong field regime, which is determined by the condition  $T_C(\kappa_C a_0)^Z = g\mu H$ , where  $Z$  is the critical field exponent and  $a_0$  is a constant of order of  $1\text{\AA}$  (see for example [5]). The fit gives value of the parameter  $1/Z = 0.65 \pm 0.02$ , that is different from the theoretical value of  $1/Z = 2/5$  for classical ferromagnets.

Figure 3 shows typical examples of the asymmetric scattering  $\Delta I_A(q)$  at the magnetic field of  $H = 50$  and  $150$  mT and at  $T = 16.6$  K.  $\Delta I_A(q)$  depends on  $q$  as  $(1/q^2)$  while it increases linearly with  $H$ . We have averaged the value of  $\Delta I_A(q)$  over the ranges of  $q$  (i) from  $0.25$  to  $0.75$   $\text{nm}^{-1}$ ; (ii) from  $0.75$  to  $1.50$   $\text{nm}^{-1}$ ; (iii) from  $1.50$  to  $2.25$   $\text{nm}^{-1}$ . These averaged values  $\langle \Delta I_A \rangle$  are shown as a function of the reduced temperature  $\tau = (T - T_C)/T_C$  at  $H = 50$  mT (Fig.4).  $\langle \Delta I_A \rangle$  depends on the temperature as  $(\tau)^\nu$  with  $\nu = 0.62 \pm 0.05$  for  $q = 1.89$   $\text{nm}^{-1}$  and with  $\nu = 0.65 \pm 0.03$  for  $q = 1.13$   $\text{nm}^{-1}$ , i.e. for  $q < (R_C)^{-1}$ . This dependence  $\Delta I_A(q) \times 2$  is broken for  $q = 0.39$   $\text{nm}^{-1}$ , i.e. for  $q \sim (R_C)^{-1}$ . The observed difference in temperature dependence for different  $q$  may be related with the crossover to the strong field regime.


## Conclusion

The experimental data confirm the principle of the critical factorization [5], which is known as Polyakov – Kadanoff – Wilson operator algebra.

## References

- [1] A. I. Okorokov, A. G. Gukasov, V. V. Runov, M. Roth, Sol. St. Comm. 38 (1981) 583
- [2] A. V. Lazuta, S. V. Maleyev, B. P. Toperverg, Sol. St. Comm. 38 (1981) 589
- [3] A. I. Okorokov, V. V. Runov, B. P. Toperverg, A. D. Tret'yakov, E. I. Mal'tsev, I. M. Puzeii, V. E. Mikhailova, JETP Lett. 43 (1986) 503
- [4] V. Deriglazov, A. Okorokov, V. Runov, B. Toperverg, R. Kampmann, H. Eckerlebe, W. Schmidt, W. Lobner, Physica B 181-182 (1992) 262
- [5] S. V. Maleyev, in Physics Review, edited by I. M. Khalatnikov (Harwood Academic, Chur, 1987) Vol. 8, p. 323



	<b>EXPERIMENTAL REPORT</b>	<b>GeNF SANS-2</b>
<b>Small angle scattering on liquid monotectic alloys</b>		
<b>Principal Proposer:</b>	<b>I. Kaban<sup>1</sup>, A. Pohlers<sup>1</sup>, W. Hoyer<sup>1</sup></b> <sup>1</sup> Institut für Physik, Technische Universität Chemnitz	
<b>Experimental Team:</b>	<b>I. Kaban<sup>1</sup>, A. Pohlers<sup>1</sup>, H. Eckerlebe<sup>2</sup></b> <sup>2</sup> GKSS Research Centre	
<b>Date(s) of Experiment:</b>	December 2003	

### Scientific Objective

Ga-Pb system is characterised by a miscibility gap in a wide concentration as well as temperature range. Although a number of experimental investigations of the Ga-Pb system have been performed so far, the results obtained in the high-temperature region, especially in the vicinity of the critical point, are rather contradictory [1].

The aim of present work are the high-temperature investigations of the immiscible Ga-Pb system with the help of small-angle neutron scattering (SANS) and study of the structural behaviour of the Ga-Pb alloys at the beginning of demixing process. This could help to determine the demixing temperatures for investigated alloys as well as the values of the critical point exponents.

### Experimental Technique

Three Ga-Pb alloys have been investigated at the SANS-2 instrument. The scattered neutrons were detected by a two-dimensional position-sensitive <sup>3</sup>He detector. The measurements were performed with the neutron wavelength  $\lambda = 5.8 \text{ \AA}$  ( $\Delta\lambda/\lambda = 0.1$ ) at two sample-detector distances (1 m and 3 m). The magnitude of the diffraction vector  $Q = 4\pi \sin\theta/\lambda$ , where  $\theta$  is half the scattering angle, ranged from  $\sim 0.1$  to  $\sim 3.2 \text{ nm}^{-1}$ . The proper amounts of high pure Ga and Pb (99.999%) were put in flat quartz glass containers, which were evacuated and sealed. The temperature was determined with an accuracy of  $\pm 5 \text{ }^\circ\text{C}$  by a thermo-element mounted below the sample container. The samples first were heated up to  $750 \text{ }^\circ\text{C}$  and held at this temperature for several hours. Then the temperature was reduced step by step and the scattering intensity was recorded.

The experimental data were treated with the SANDRA program [2]. Measured intensity was corrected for sample transmission, background, detector efficiency and geometry. The scattering data were averaged over azimuthal scattering angle and absolute cross sections were calculated by comparison with the incoherent scattering from vanadium.

### Experimental Results

Figure 1 shows the semi-logarithmic plots of the coherently scattered intensity for the investigated Ga-Pb liquid alloys. As it was expected, the highest small-angle scattering signal is observed for the  $\text{Ga}_{60}\text{Pb}_{40}$  alloy, which is very close to the critical composition. A temperature-dependent behaviour of the SANS intensity for  $\text{Ga}_{60}\text{Pb}_{40}$  and  $\text{Ga}_{80}\text{Pb}_{20}$  alloys is found. The scattering intensity first is increasing with the temperature decrease, and then it is vanishing if the temperature is further reduced. The strongest small-angle scattering signal is observed at  $640 \text{ }^\circ\text{C}$  for the  $\text{Ga}_{60}\text{Pb}_{40}$  alloy and at  $620 \text{ }^\circ\text{C}$  for the  $\text{Ga}_{80}\text{Pb}_{20}$  alloy.

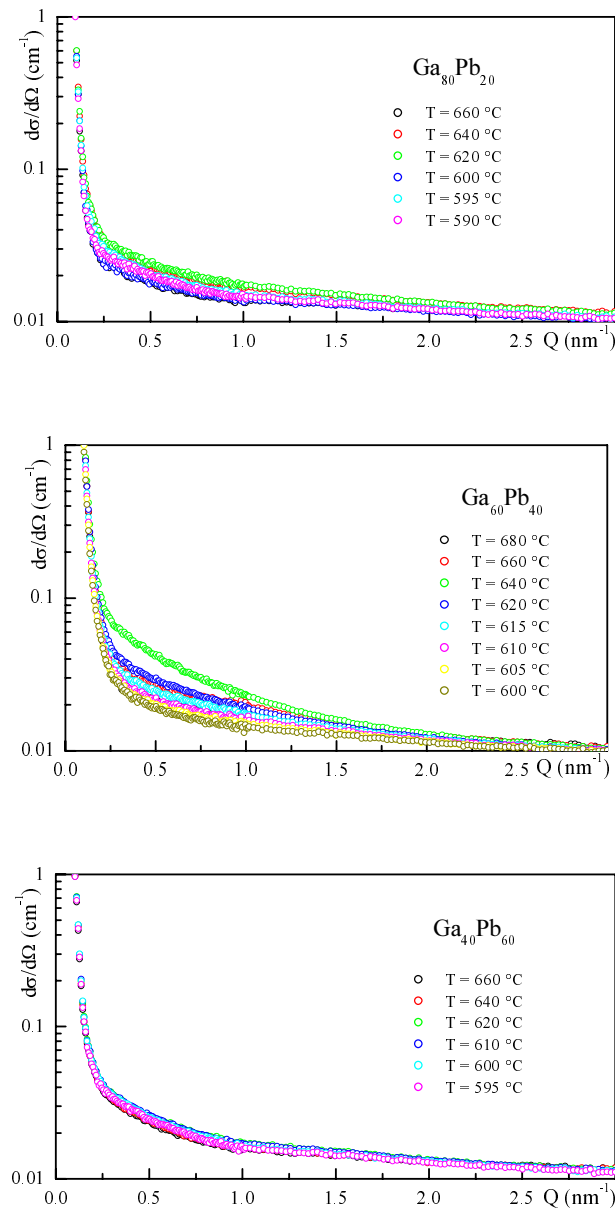



Figure 1: Experimental SANS scattering patterns for the Ga-Pb liquid alloys.

## Acknowledgements

Two of us (I. Kaban and A. Pohlers) acknowledge GKSS Research Centre for hospitality and financial support.

## References

- [1] Yu. Plevachuk, V. Filippov, V. Kononenko, P. Popel, A. Rjabina, V. Sidorov, V. Sklyarchuk. Z. Metallkd. 94 (2003). 1034
- [2] P. Biemann, M. Haese-Sailler, P. Staron, SANDRA (SANS Data Reduction and Analysis); [http://www.gkss.de/pages.php?page=w\\_abt\\_genesys\\_downloads.html&language=d&version=g](http://www.gkss.de/pages.php?page=w_abt_genesys_downloads.html&language=d&version=g)

	<b>EXPERIMENTAL REPORT</b>	<b>GeNF SANS-2</b>
<b>Characterisation of Particles in Dispersoids Strengthened Tantalum</b>		
<b>Principal Proposer:</b>	<b>M. Bischof<sup>1</sup></b> <sup>1</sup> University of Leoben, Department of Physical Metallurgie and Materials Testing, Leoben, Austria	
<b>Experimental Team:</b>	<b>H. Eckerlebe<sup>2</sup>, G. Kozik<sup>2</sup>, K. Pranzas<sup>2</sup>, P. Staron<sup>2</sup></b> <sup>2</sup> GKSS Research Centre	
<b>Date of Experiment:</b>	December 2003	

## Introduction

Tantalum shows some interesting properties like its high melting point (2996°C), good workability and very good corrosion resistance [1]. But its limited strength at high temperatures prevents it from usage in some technically interesting applications. Small particles (precipitations or dispersoids) should prevent the Ta-grains from growing and thereby ensure both a sufficient high-temperature strength and ductility. But the particles have to be thermodynamically stable and of the right size to do so. The following experiment should reveal the presence of such particles and their sizes in some selected dispersion strengthened Ta-samples.

## Experiment

To determine differences in particle-distribution between different doping, annealing, and drawing conditions, four samples were measured: two differently doped Ta-wires with a diameter of 0.2 mm and two bars with a size of 6 x 6 mm and a thickness of about 2 mm, one in the cold-swaged state and one recrystallised by annealing at 1350 °C. These bars represent a preliminary product for the wire production. The doping of both discs was equal to the doping of one of the measured wires. The wires were cut in pieces of about 15 mm length and arranged to form a grid with spacings being as small as possible. These spacings were controlled in a stereomicroscope and found to be negligible. An “effective thickness” of these samples was calculated using the equation  $t = A / d$ , where A is the cross section of the wires and d is their diameter.

*Table 1: Summary of measured samples.*

Sample	Shape	Doping-condition	Working-condition
1	Wire Ø 0.2 mm	Mod. 1	cold-rolled
2	Wire Ø 0.2 mm	Mod. 2	cold-rolled
3	Bar 6x6x2 mm	Mod. 1	cold-rolled
4	Bar 6x6x2 mm	Mod. 1	annealed at 1350 °C

The experiments were carried out at the SANS-2 scattering facility. Scattered neutrons were detected by a position-sensitive detector with a resolution of 256 x 256 pixels. The range of the scattering vector ( $0.025 \text{ nm}^{-1} - 2.5 \text{ nm}^{-1}$ ) was covered by 4 different distances between detector and sample (1 m, 3 m, 9 m, and 21 m). Appropriate apertures and collimators were used. The measurements were performed using neutrons at a wavelength of  $\lambda = 5.8 \text{ nm}$ . Measured intensity was corrected for sample transmission, background and detector

efficiency. The scattering data were averaged over azimuthal scattering angle and absolute cross sections were calculated by comparison with the incoherent scattering of vanadium.

## Results

Figure 1 shows that there are no significant amounts of precipitates in the wire-shaped samples, at least within the experimentally covered range of size. The slope of both scattering curves shows almost the theoretical value of -4. It can therefore be assumed that large dispersoids ( $> 200$  nm) are present, but further investigations, for example with Double Crystal Diffraction (DCD), must be performed to determine their size. The scattering curves of both wires are largely identical except for scatterings vectors  $> 1 \text{ nm}^{-1}$ . This difference can be caused by very small inhomogenities like small precipitates of a size  $< 3$  nm, small clusters or maybe scattering of dislocations. But most likely there is a difference in monotonic Laue-scattering and incoherent scattering of doping elements due to the use of different doping-elements and a varying matrix solubility of the used elements. But this conclusion has to be proved by further investigation, too.

Figure 2 displays the scattering curves of the bars. The black line is the same linear fit as in Figure 1 and can be used for comparisons. As it can be seen, the curves are not linear in the viewed Q-range. Therefore, particles with sizes of up to about 100 nm are present in the plates while the amount of larger particles ( $> 200$  nm) seems to be smaller than in the wires. This result agrees well with preliminary investigations in the same material. The scattered intensity of the annealed specimen is about 10 times lower than those of the cold-rolled one, indicating a coarsening or dissolution of particles during annealing at  $1350^\circ\text{C}$ . Again, the DCD could be used to investigate the observed changes in more detail.

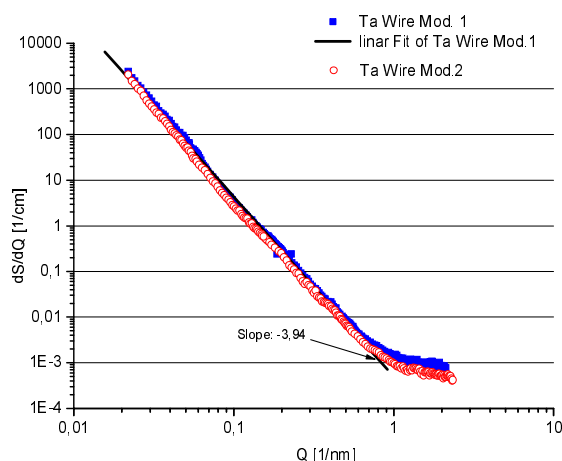


Figure 1: Scattering curves of Ta-wires.

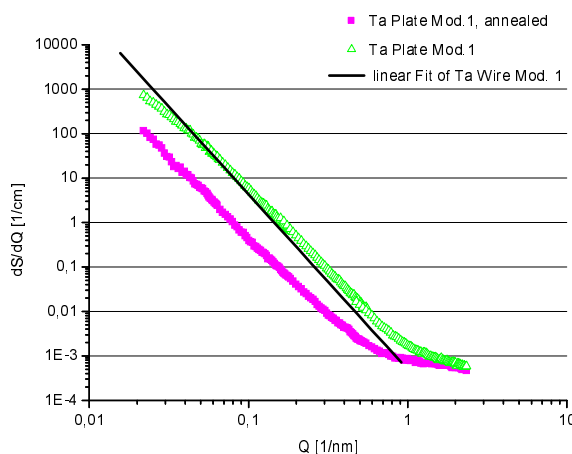


Figure 2: Scattering curves of Ta-plates.


## Conclusions

The size distribution of particles in the investigated Ta-wires could not be determined due to a limited Q-range of the experiment. Referring to the obtained scattering curves, there seem to be some big particles ( $> 200$  nm) and maybe some very small ones ( $< 3$  nm). The preliminary products (bars) show varying scattering properties. Obviously, there are smaller particles present than in the wires. Subsequent annealing of the rolled material has a great influence on the particles. They seem to dissolve or coarsen, even during moderate heating to  $1350^\circ\text{C}$ . The additional production steps from the annealed bar to the wire lead to additional changes in the particle size distribution that could be characterised in more detail by using a DCD.

## Reference

- [1] K. Andersson, K. Reichert, R. Wolf, H.C., Ullmann's Encyclopedia of Industrial Chemistry, Vol. A 26 (1995), 71ff.



	<b>EXPERIMENTAL REPORT</b>	<b>GeNF SANS-2</b>
<b>Precipitation kinetics of a Tool Steel containing Carbides and Intermetallic Phases</b>		
<b>Principal Proposer:</b>	<b>M. Bischof<sup>1</sup></b> <sup>1</sup> University of Leoben, Department of Physical Metallurgie and Materials Testing, Leoben, Austria	
<b>Experimental Team:</b>	<b>H. Eckerlebe<sup>2</sup>, G. Kozik<sup>2</sup>, P. K. Pranzas<sup>2</sup>, P. Staron<sup>2</sup></b> <sup>2</sup> GKSS Research Centre	
<b>Date of Experiment:</b>	December 2003	

## Experiment

Tool steels have to feature high toughness and strength, even when exposed to relatively high working temperatures. Precipitates contribute a lot to the properties of these steels and therefore knowledge of their formation kinetics is fundamental for optimizing these properties. The size distribution of precipitates under different annealing conditions shall be revealed by SANS measurements.

The investigations were performed on three samples with identical chemical composition: 0.3 % C, 2.4 % Cr, 2.5 % Mo, 6.5 % Ni, 0.26 % V, 1.18 % Co, 2.6 % Al, 1.18 % Si, 0.23 % Mn, Fe to balance. All samples had been solution annealed at 990 °C for 30 minutes and quenched in oil. Sample “A” represents this state. Sample “B” had additionally been annealed at 690 °C for 30 minutes and cooled in air, Sample “G” had been annealed for 1000 min at the same temperature. The samples had a diameter of 25 mm and a thickness of 1 mm.

**Table 1:** Summary of measured samples.

Sample	Heat Treatment
K011 A	990 °C, 30 min, Oil (“as quenched”)
K011 D	990 °C, 30 min, Oil / 690 °C, 30 min, Air
K011 G	990 °C, 30 min, Oil / 690 °C, 1000 min, Air

Measurements were carried out at the SANS-2 facility. Scattered neutrons were detected by a position-sensitive detector with a resolution of 256 x 256 pixels. Four detector distances (1 m, 3 m, 9 m and 21 m) were used with appropriate apertures and collimators to cover scattering vectors  $Q$  from 0.025 nm<sup>-1</sup> to 2.5 nm<sup>-1</sup>. The measurements were performed using neutrons at a wavelength of  $\lambda = 5.8$  nm and a wavelength spread of  $\Delta\lambda/\lambda = 10$  %. The neutron beam impinging on the samples had a diameter of 4 mm. The samples were magnetized to saturation in a field of 2 T. Measured intensities were corrected for sample

transmission, background and detector efficiency. The nuclear cross sections were measured at azimuthal detector angles of  $\alpha = 0^\circ$  and  $180^\circ$ , while the sum of nuclear and magnetic cross section was measured at angles of  $\alpha = 90^\circ$  and  $270^\circ$ , where  $\alpha$  is the angle between the scattering vector and the magnetization. The scattered intensity was averaged over sectors of  $12^\circ$  around the given mean angles. Absolute cross sections were calculated by comparison with the incoherent scattering of vanadium.

## Results

Figure 1 shows scattering curves for the solution annealed steel specimen. The sample contains primary carbides, which have not been completely dissolved. The magnetic scattering intensity, which can be calculated by subtracting the nuclear scattering curve from the sum curve of magnetic and nuclear scattering, is about 10 times higher than the nuclear scattering intensity. This information is going to be used to determine the so called “A-Ratio”, the ratio of magnetic and nuclear scattering intensity. This ratio provides, under certain assumptions, information on the chemical composition of the precipitates and other particles.

As it can be seen in Figure 2, the scattering curves have changed after additional heat treatments. A significant volume fraction of small precipitates with a size of a few nm has formed after annealing at  $690^\circ\text{C}$  for 30 minutes. These particles are growing by a factor of about 2 during further annealing at the same temperature up to 1000 minutes. A detailed inspection of the A-ratio will help to clarify if the particles remain chemically equal or if there is a significant change in the particle composition.

Further investigations using SANS will be performed on additional samples to cover a wider range of heat treatment conditions. Existing and future results will be combined with information from Atom Probe Field Ion Microscopy to provide a wide knowledge about the precipitation reactions taking place in the researched steel.

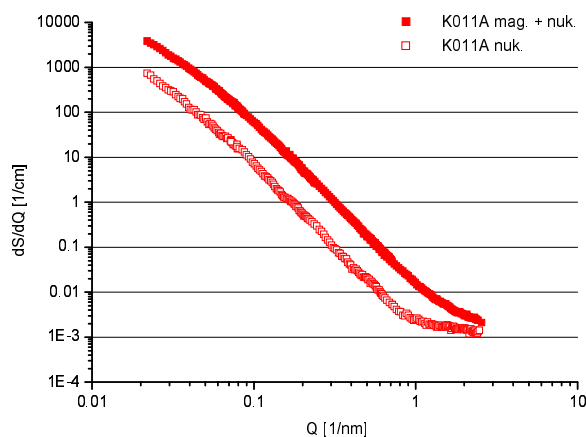


Figure 1: Scattering curves of the as-quenched sample A; open symbols:  $\alpha = 0^\circ$ , full symbols:  $\alpha = 90^\circ$  (see text).

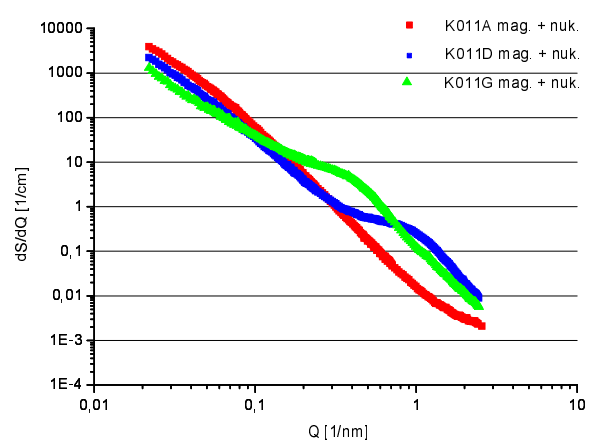


Figure 2: Scattering curves of samples A, D, and G ( $\alpha = 90^\circ$ ).

**Double crystal diffractometer DCD**

**Short Instrument Description:**

The double crystal diffractometer for ultra small angle neutron scattering (USANS) uses non-polarised cold neutrons to characterise in materials large creep pores, fatigue and sintering cavities, precipitates, voids, bubbles, etc. with particle sizes with about 100 nm to 40  $\mu\text{m}$  in diameter.

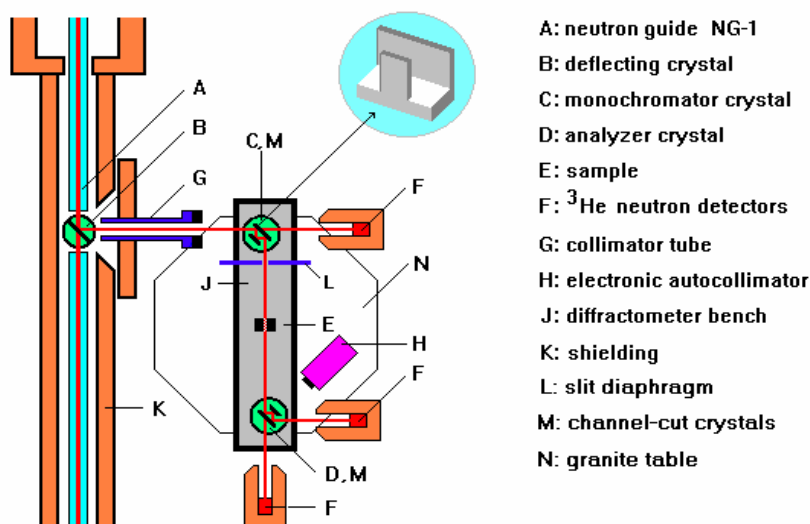
**Local Contact:**

Dieter Bellmann

Phone/Fax : +49 (0)4152 87-2803 / +49 (0)4152 87-2840

e-mail: [dieter.bellmann@gkss.de](mailto:dieter.bellmann@gkss.de)


**Schematic View of DCD:**



**Instrument Details:**

Beamline:	beamline 8 – cold neutron guide NG-1, max. beam cross section 30 x 40 mm <sup>2</sup>
Deflecting crystal:	Si(111), Si(311), mosaic spread 0.1 mrad
Monochromator / analyser:	channel-cut perfect Si crystals
Wavelength resolution	$\Delta\lambda/\lambda = 1 \cdot 10^{-5}$ ( $\lambda = 0.443$ nm)
Max. flux at deflecting crystal	$\Phi = 2.3 \times 10^8 \text{ cm}^{-2} \text{ s}^{-1}$
Flux at sample position:	$\Phi \approx 500 \text{ cm}^{-2} \text{ s}^{-1}$ (Si(111), $\lambda = 0.443$ nm) $\Phi \approx 180 \text{ cm}^{-2} \text{ s}^{-1}$ (Si(311), $\lambda = 0.232$ nm)
Range of momentum transfer:	$1 \cdot 10^{-5} \text{ nm}^{-1} \leq Q \leq 5 \cdot 10^{-2} \text{ nm}^{-1}$
Detectors:	three $^3\text{He}$ -detectors
Control of crystal alignment:	electronic autocollimator, angular resolution < 0.05 $\mu\text{rad}$

A major part of the beam time at DCD was used for experiments in combination with SANS-2 measurements.

 <b>GKSS</b> FORSCHUNGSZENTRUM in der HELMHOLTZ GEMEINSCHAFT	<b>EXPERIMENTAL REPORT</b>	<b>GeNF DCD SANS-2</b>
<b>Metal Foams – Structures in Unfoamed Zn Samples with 0.32 % TiH<sub>2</sub></b>		
<b>Principal Proposer:</b>	<b>J. Banhart<sup>1</sup>, B. Matijasevic<sup>1</sup>, D. Bellmann<sup>2</sup>, H. Clemens<sup>3</sup></b> <sup>1</sup> Technische Universität Berlin, <sup>2</sup> GKSS Research Centre, <sup>3</sup> Montanuniversität Leoben	
<b>Experimental Team:</b>	<b>D. Bellmann<sup>2</sup>, H. Eckerlebe<sup>2</sup></b>	
<b>Date(s) of Experiment:</b>	February, April and July 2003	

## Motivation

The aim of this work is to continue investigations of early stages of metal foam formation [1, 2]. Some important parameters which affected the foaming process are the type of the used blowing agent and the homogeneity of the blowing agent. For a better reproduction the manufacture process for the samples has been optimized.

The influence of the roughness of the surface of two unfoamed Zn samples, one polished, was studied with small-angle neutron scattering techniques. The samples have a content of 0.32 wt.% TiH<sub>2</sub>, acting as blowing agent.

This work is supported by DFG, grant no. Ba 1170/4-2.

## Experimental Technique

Ultra small-angle neutron scattering (USANS) is a useful technique for detecting particles in a wide size range from about 100 nm to 50 µm, when using DCD at a neutron wavelength of 0.232 nm and 0.443 nm, respectively. In combination with the traditional pinhole SANS instrument a wide size range from about 1 nm to 50 µm is detectable.

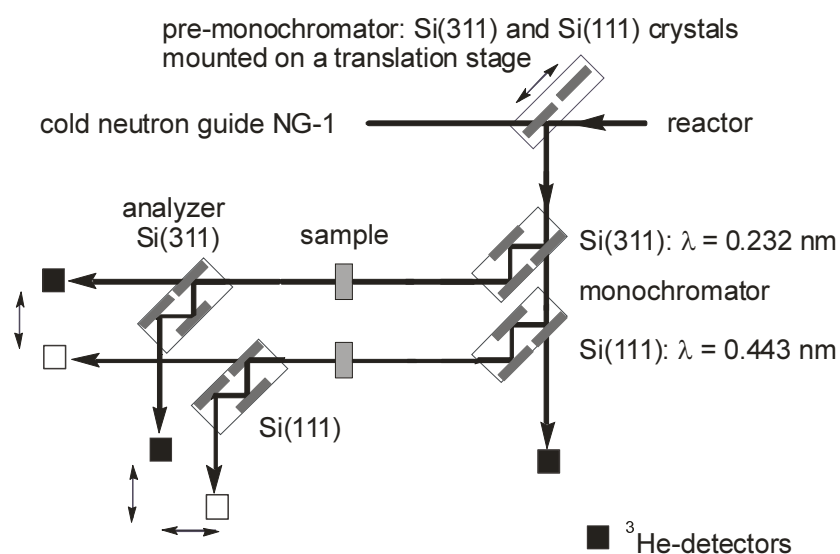


Figure 1: The layout of DCD at GeNF with triple-bounce channel-cut perfect silicon crystals.

In order to detect all blowing agent particles sieved loose powder with particle sizes  $< 28 \mu\text{m}$  was used. Unfoamed zinc samples were prepared by applying the powder compaction method which comprising mixing zinc powder with a small fraction of blowing agent ( $\text{TiH}_2$ ) powder and compacting this mix (110 MPa at  $350^\circ\text{C}$ ).

## Results

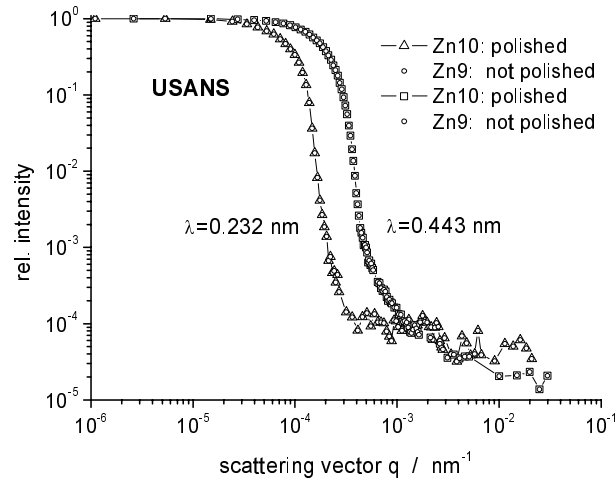


Figure 2: The scattering curves obtained by DCD measurements at two wavelengths. The difference of the scattering power between both samples is extremely small.

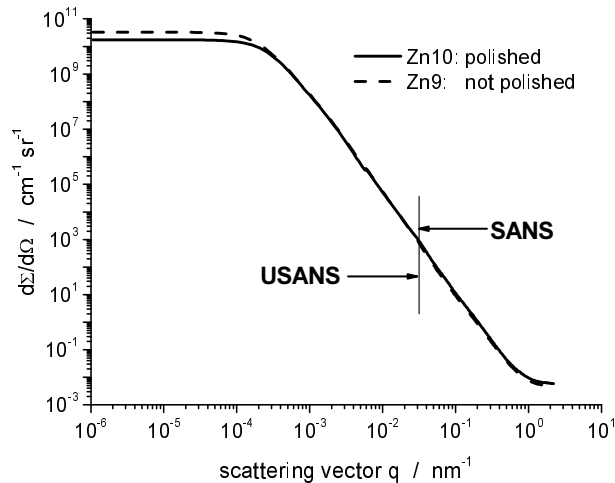


Figure 3: The diff. scattering cross section is shown as a result of USANS and SANS measurements. Only a small drop of the cross section at low  $q$ -values can be seen resulting from a decrease of the roughness of the surface by polishing one sample.

## References

- [1] Banhart, J., Bellmann, D., Clemens, H.: Investigation of metal foam formation by microscopy and ultra small-angle neutron scattering, *Acta Mater.* 49 (2001) 3409–3420
- [2] Bellmann, D., Banhart, J., Clemens, H.: Investigation of metal foam formation by small-angle neutron scattering techniques (Metfoa 2003, Berlin), to be published in: "Metal Foams and Porous Metal Structures", Ed. J. Banhart, M. F. Ashby, N. A. Fleck, MIT-Verlag, Bremen (2003)

**New neutron reflectometer NeRo**

**Short Instrument Description**

The new Neutron Reflectometer NeRo has been built at the former location of TOREMA 2. The instrument is designed for measurements of thin film systems including polymer and magnetic systems using cold non-polarised/polarised neutrons with high resolution.

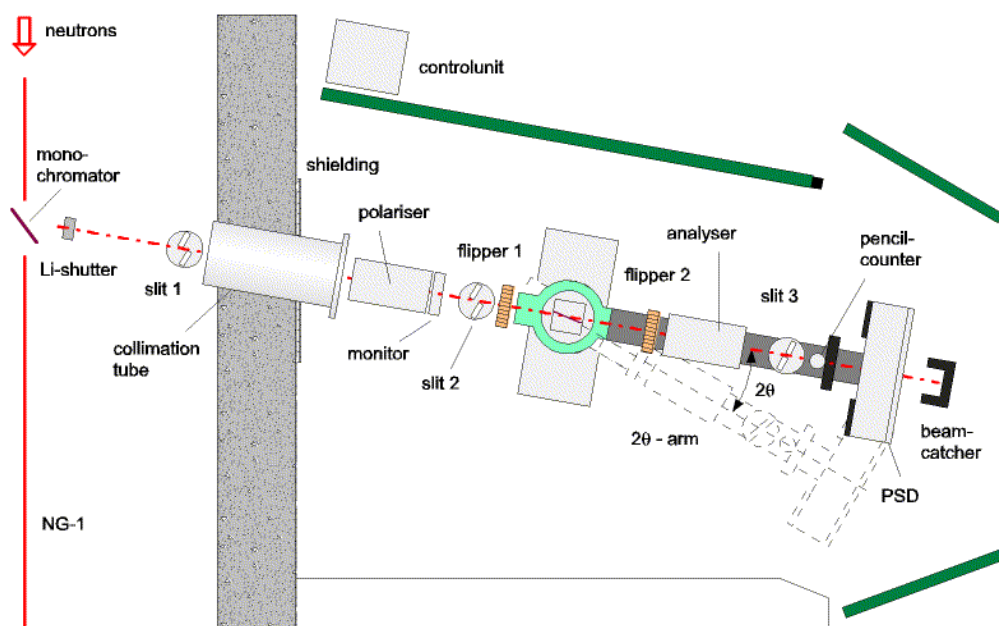
**Local Contact:**

Dr. Dieter Lott

Phone/Fax : +49 (0)4152 87 – 1372 / +49 (0)4152 87 – 1338

e-mail: [dieter.lott@gkss.de](mailto:dieter.lott@gkss.de)

**Schematic View of NeRo:**



**Instrument Details:**

Beamline:	beamline 8 (NG-1)
Wavelength:	$\lambda = 0.435 \text{ nm}$ ;
Wavelength resolution	$\Delta\lambda/\lambda = 0.02$
Angular range	$0 \leq \theta \leq 10^\circ$
Flux at sample position:	$\Phi = 5 \cdot 10^4 \text{ cm}^{-2} \text{ s}^{-1}$ (unpolarised, standard collimation)
Detectors:	2-dim position-sensitive $^3\text{He}$ -counter $^3\text{He}$ pencil counter
Ancillary equipment:	refrigerator cryostat – temp.-range: 12 - 475 K electro magnet with field up to 0.9 T





**Reflectometer for polarised neutrons PNR**

**Short Instrument Description:**

The polarised neutron reflectometer is used to study magnetic and other surfaces, layers, thin films and membranes applying cold non-polarised/polarised neutrons at high fluxes.

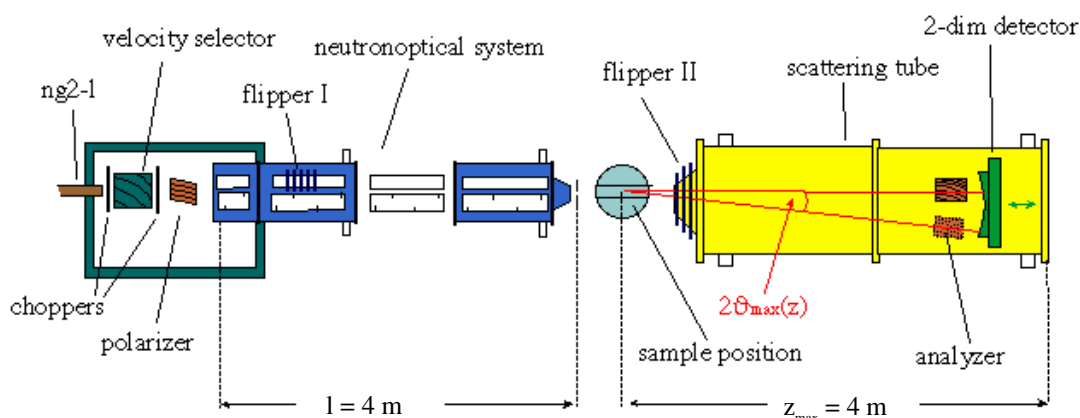
**Local Contact:**

Dr. Danica Solina

Phone/Fax : +49 (0)4152 87–1373 / +49 (0)4152 87–1338

e-mail: [danica.solina@gkss.de](mailto:danica.solina@gkss.de)


**Schematic View of PNR:**



**Instrument Details:**

Beamline:	beamline 8 (NG-2I), cross section 30 x 40 mm <sup>2</sup>
Monochromator:	helical slot selector
Wavelength:	$\lambda \geq 0.635$ nm
Wavelength resolution:	$\Delta\lambda/\lambda = 0.05$
TOF equipment:	2 choppers, to be used if a resolution better than 0.05 is required
Polariser and analyser:	set of bent supermirrors
Spin flipper:	hf-flipper or Mezei-coil-flipper
Collimation lengths:	4 m
Flux at sample position: (beamsize: 0.5 x 40 mm <sup>2</sup> )	$\Phi_{\text{nonpol}} = 1 \cdot 10^5 \text{ cm}^{-2} \text{ s}^{-1}$ (unpolarised) $\Phi_{\text{pol}} = 3 \cdot 10^4 \text{ cm}^{-2} \text{ s}^{-1}$ (polarised neutrons)
distance sample-detector:	3 m to 4 m
angular range:	$0^\circ \leq \theta \leq 4^\circ$
Detector:	2-dim position-sensitive <sup>3</sup> He-counter
Ancillary equipment:	– refrigerator cryostat – temp.-range: 12 – 475 K – electro magnet up to 0.9 T – superconducting magnet up to 5 T



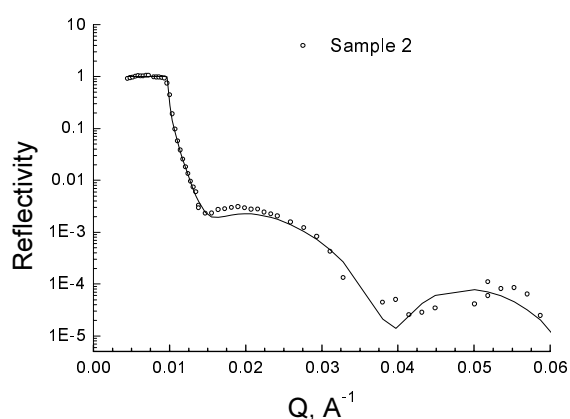
	<b>EXPERIMENTAL REPORT</b>	<b>GeNF PNR</b>
<b>Electrostatically controlled immobilized water in polyelectrolyte multilayers</b>		
<b>Principal Proposer:</b>	<b>R. Krastev<sup>1</sup>, D. Carriere<sup>2</sup></b> <sup>1</sup> Hahn-Meitner-Institute (HMI), Berlin <sup>2</sup> Max-Planck-Institute (MPI-KGF), Golm	
<b>Experimental Team:</b>	<b>R. Krastev<sup>1</sup>, D. Lott<sup>3</sup></b> <sup>3</sup> GKSS Research Centre	
<b>Date(s) of Experiment:</b>	31.03. – 6.04.2003	

The layer-by-layer self-assembly (LbL) of polyelectrolytes has been extensively studied for the preparation of ultrathin films due to the versatility of the build-up process [1]. These multilayers are prepared by alternate adsorption of positively charged and negatively charged polyelectrolytes on a charged surface. The method was applied successfully to fabricate various films incorporating biopolymers, enzymes, conjugated polymers, inorganic particles for potential applications in biosensors, microelectronics, optics, etc. The most extensively studied system is prepared by alternative adsorption of poly(styrene sulfonate) (PSS) and poly(allylamine hydrochloride) (PAH) on top of Si surfaces treated with polyethylene imine (PEI) [2]. However, the films produced by this method are soft materials very sensitive to atmosphere humidity and other environmental conditions (pH, ionic strength). This environment-sensitive behaviour can be prejudicial for some applications like the development of protective coatings or optical devices requiring the high stability of the internal structure of the film.

Recent NMR studies [3] showed that the hydration of the multilayers seems to be dramatically affected by the terminating layer (PSS or PAH). The effect is currently interpreted as a reversible swelling and deswelling of the polymer matrix in dependence of the electric potential of the outermost layer. A positive surface charge causes a swelling of the polymer matrix, while due to the negative surface charge a deswelling of the matrix occurs. The reversible surface potential controlled swelling and deswelling is attributed to the non-compensated polycation charges within the matrix, which respond to the electric field. In addition, the dissociation equilibrium of the weak polyelectrolyte PAH was shown to have an effect on the swelling amplitude, since it changes the number of excess polycation charges, which are responsible for the surface potential driven swelling.

Since the reversible swelling is a completely new and interesting property found for polyelectrolyte multilayers, it is essential to confirm it with additional structural data. Neutron reflectivity is best suited here, since it is not only sensitive to the overall layer thickness, but also to the water content distribution in the layers. The aim of the proposed experiment was to measure the neutron reflectivity from PE multilayers in dry atmosphere and to obtain the Scattering Length Density (SLD) of the dry material. These data are important as reference data for further studies.

The experiments were performed at the PNR reflectometer at Research Centre GKSS, Geesthacht. The PE layers were deposited onto Si wafers with dimensions of 20x20 mm<sup>2</sup>. Two samples were studied: Sample 1 (Si/PEI/(PSS/PAH)<sub>6</sub>PSS) – PSS(-) terminated; Sample 2 (Si/PEI(PSS/PAH)<sub>7</sub>) – PAH(+) terminated. The samples were prepared from H<sub>2</sub>O solutions of the polyelectrolytes. After the deposition of the last layer they were placed into pure D<sub>2</sub>O and then dried. The last step was necessary in order to assure equilibrium exchange of H to D atoms in the PE layers. This is a process which takes place in the NR studies when the behavior of the layers in aqueous surrounding is studied. In order to get better contrast usually D<sub>2</sub>O is used in such studies. The samples were placed into a specially designed Al chamber [4] which allows measurements at controlled conditions to be performed. The experiments were conducted at decreased air pressure and elevated temperature (60 °C). These conditions were necessary preposition to assure dry atmosphere. The PSS/PAH multilayers are very hygroscopic and even small amounts of water vapors in the atmosphere are absorbed into the film.




The obtained neutron reflectivity curves are shown on the Figure. The reflectivity spectra were analyzed by applying the standard fitting routine Parratt 32 [5]. The program calculates the optical reflectivity of neutrons from flat surfaces. The calculation is based on the Parratt's recursion scheme for stratified media. The film was modeled as consisting of layers of specific thickness and scattering length density. The reflectivities were calculated using the dynamic iterative model.

The model reflectivity profile was calculated and compared to the measured one. Then the model was adjusted to the best chi-square fit to the data. From the fits the layer thickness (244 Å), SLD ( $0.75 \times 10^{-6} \text{\AA}^{-2}$ ) and the roughness (10 Å) of the layer were obtained. These data are very useful and will be used as starting reference point in the further studies which will study the amount of absorbed water in the PSS/PAH PE multilayers and especially its dependence on the charge of the last adsorbed during the preparation layer.

## References

- [1] Decher G., *Science* 277 (1997), 1232
- [2] Lösche M; Schmitt J; Decher G; Bouwman W; Kjaer K, *Macromolecules* 31 (1998) 8893.
- [3] Schwarz B; Schonhoff M, *Langmuir* 18 (2002), 2964.
- [4] Krasteva N., Krustev R., Yasuda A., and Vossmeier T., *Langmuir* (2003), ASAP article.
- [5] Braun, C. *Parratt32 Fitting routine for reflectivity data*; HMI: Berlin, 1997–1999

	<b>EXPERIMENTAL REPORT</b>	<b>GeNF PNR</b>
<b>Investigation of the Structure of Novel Archaea Analogue Thiolipids on Gold Surfaces for Preparation of Tethered Lipid Bilayers</b>		
<b>Principal Proposer:</b>	<b>Lizhong He<sup>1</sup>, Renate Naumann<sup>1</sup>, Wolfgang Knoll<sup>1</sup></b> <sup>1</sup> Max-Planck-Institute for Polymer Research, Ackermannweg 10, D-55128 Mainz, Germany	
<b>Experimental Team:</b>	<b>Lizhong He<sup>1</sup>, Dieter Lott<sup>2</sup>, Ursula Tietze<sup>2</sup>, Danica Solina<sup>2</sup></b> <sup>2</sup> GKSSResearch Centre, Institute for Material Science, Max-Planck Str. 1, D-21502 Geesthacht, Germany	
<b>Date(s) of Experiment:</b>	June 2003	

## Introduction

Tethered bilayer lipid membranes (tBLM's) on solids are promising model systems to investigate functions (e.g. recognition, transport) of membrane proteins and receptors [1]. To avoid non-physiological interactions of integral membrane proteins with the solid support, tethered membranes using soft polymers as cushions are often used. For such a model system, stability and fluidity of tethered membrane are crucial for their scientific and practical application, which strongly depend on the chemical structure of lipid and support material. Recently, we have developed a novel archaea analogue thiolipids, 2,3-di-O-phytanyl-*sn*-glycerol-1-tetraethylene glycol-D,L- $\alpha$ -lipoic acid ester lipid (DPTL) for the preparation of tethered bilayer lipid membranes [2]. Via a thiol-modified tether as spacer, the molecules can be immobilized on gold substrate by self-assembly. The polar tethered group of the molecule also provides a hydrophilic layer with functional properties of the cytosol/cytoskeleton. It thus reduces the hydrophobic influence of the metal surface. Consequently, this molecule enables the functional incorporation of membrane proteins.

Our previous investigation by impedance spectroscopy and surface plasmon resonance (SPR) has shown that DPTL is promising to serve as a model membrane system [2]. In this work, we aimed to investigate the conformation of DPTL monolayer and the lipid bilayer based on DPTL. For this purpose, neutron reflectivity experiments were performed.

## Experiments

The gold substrate for reflection experiments were prepared by thermal evaporation of ~20 Å chromium, then ~50 Å gold onto silicon wafers. The DPTL monolayer was deposited on gold substrate by self-assembly in ethanol solution, followed by vesicle fusion to form a lipid bilayer. Neutron reflectometry experiments were performed on the instrument PNR at the Geesthacht Neutron Facility GeNF, Germany. All experiments were carried out in PBS buffer (D<sub>2</sub>O) using a solution cell at room temperature. To facilitate detailed analysis of thin films structure at surface, a serial of experiments using bare silicon, gold-coated silicon, DPTL monolayer, and lipid bilayer were performed. The raw data were treated by program Panorama and further data analysis was carried out using the program Parratt.

## Results and discussion

The neutron reflectivity curve (Figure 1) from the bare silicon substrate shows that its surface has a silicon oxide layer with a thickness of 3.9 nm. The reflectivity data from gold-coated

silicon indicates that chromium film has a thickness of 2.4 nm while the thickness of gold film is around 4.6 nm. Note that the gold surface is not a discrete interface and it has a roughness around 0.4 nm. From the scattering data, the scattering length density (SLD) of gold was calculated to be  $4.8 \times 10^{10} \text{ cm}^{-2}$ , which is slightly higher than the theoretical value ( $4 \times 10^{10} \text{ cm}^{-2}$ ). This might be explained by possibly porous structure of evaporated gold and that  $\text{D}_2\text{O}$  may exist in pores of gold. Indeed, x-ray reflectivity experiment in air also indicates that the gold might be porous (data not shown). The surface structure parameters of the gold-coated silicon were used without adjustment for later analysis of reflectivity data of DPTL layer.

DPTL molecule consists of a tetraethylene glycol spacer and a di-O-phytanyl chain, which have different SLD value. Indeed, the SLD profile from the reflectivity data shows that ethylene oxide region (thickness of 1.9 nm) has a SLD value of  $0.67 \times 10^{10} \text{ cm}^{-2}$  while the hydrocarbon chain (thickness of 2.3 nm) has an average SLD value of  $-0.40 \times 10^{10} \text{ cm}^{-2}$ . It should be noted that the experimental SLD value of ethylene oxide region is only slightly higher than the theoretical SLD value ( $0.67 \times 10^{10} \text{ cm}^{-2}$  calculated from its chemical composition and mass density) for a homogeneous ethylene oxide layer without hydration. If there were strong hydration of ethylene oxide, a higher SLD value would have been observed since the DPTL monolayer was contacted with  $\text{D}_2\text{O}$  buffer. Thus, the data suggests that the ethylene oxide region was only weakly hydrated. Further neutron reflectivity experiment was performed after vesicle fusion on DPTL monolayer. A thickness increase of 2 nm was observed at the surface, indicating the formation of lipid bilayer. Future experiments are planned to investigate structure of DPTL monolayer diluted by small molecules, which will enable us to incorporate membrane proteins for their function analysis.

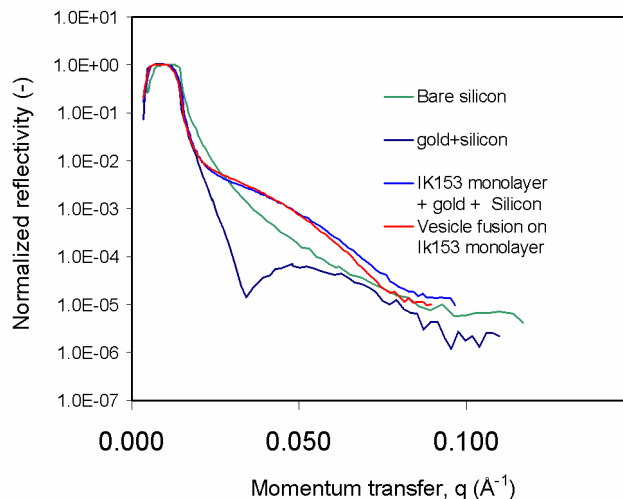



Figure 1: Neutron reflectivity data from bare silicon, gold-coated silicon, DPTL monolayer and lipid bilayer.

## References

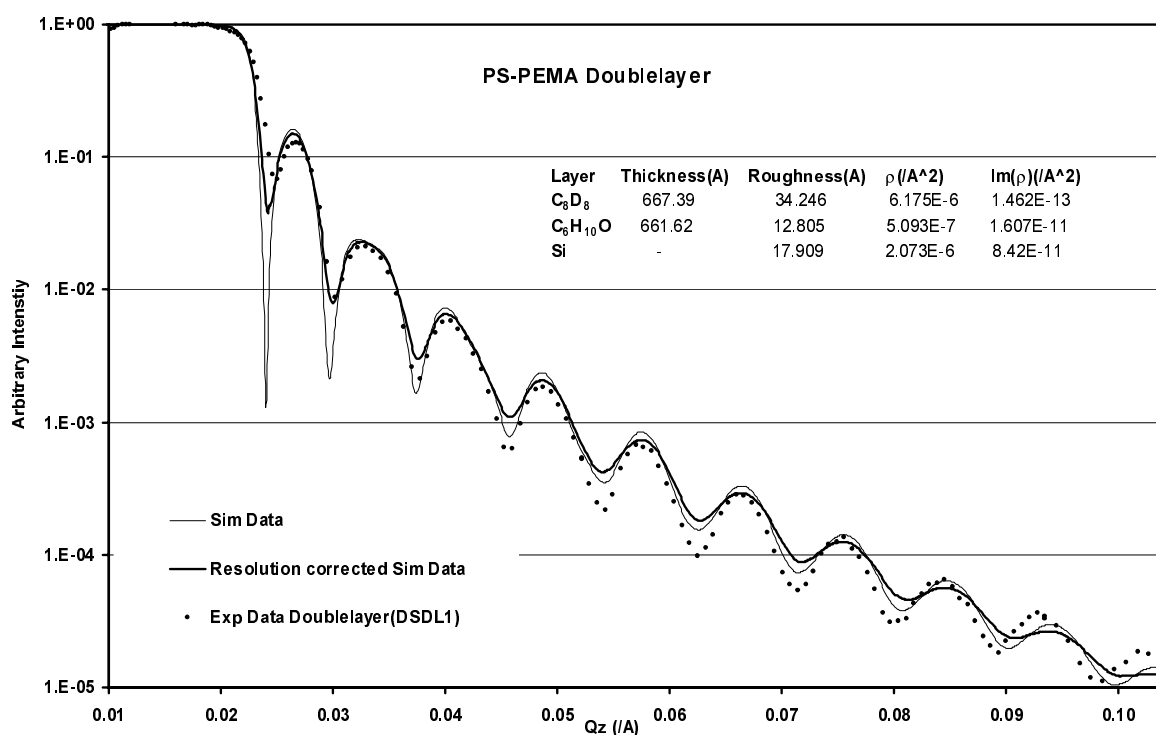
- [1] E. Sackmann, Supported membranes: Scientific and practical applications, *Science*. 271 (1996), pp. 43–48.
- [2] S. M. Schiller, R. Naumann, K. Lovejoy, H. Kunz, W. Knoll, Archaea analogue thiolipids for tethered bilayer lipid membranes on ultrasmooth gold surfaces. *Angew. Chem. Int. Ed.* 42 (2003), pp. 208–211.

 <b>GKSS</b> FORSCHUNGSZENTRUM in der HELMHOLTZ GEMEINSCHAFT	<b>EXPERIMENTAL REPORT</b>	<b>GeNF PNR</b>
<b>Initial interface formation of polystyrene/polyethylmethacrylate bilayers</b>		
<b>Principal Proposer:</b>	<b>Dirk W. Schubert<sup>1</sup>, F. Faupel<sup>2</sup>, J. Kanzow<sup>2</sup></b> <sup>1</sup> Freudenberg Forschungsdienste KG, 69465 Weinheim, <sup>2</sup> Technische Fakultät der CAU, Kaiserstr.2, 24143 Kiel	
<b>Experimental Team:</b>	<b>Danica Solina<sup>1</sup>, Dirk W. Schubert<sup>2</sup>, T. Dunkel<sup>3</sup>, U. Tietze<sup>3</sup></b> <sup>1</sup> WFN, GKSS-Forschungszentrum <sup>2</sup> Freudenberg Forschungsdienste KG, 69465 Weinheim <sup>3</sup> SST, GKSS-Forschungszentrum	
<b>Date(s) of Experiment:</b>	August 2003	

A bilayer sample consisting of weak incompatible polymers, deuterated polystyrene (PS(D)) and polyethylmethacrylate (PEMA) was chosen as a large interface polymeric model system. The initial state with a sharp polymer/polymer interface before annealing is characterized using neutron reflectometry (NR). The large interface profile after annealing is however beyond the resolution of NR experiments. Therefore, a novel technique of positron annihilation lifetime spectroscopy (PALS) for interface characterization will be used. These measurements will be done at the positron beam facility of the university of the Bundeswehr, Munich.


The goal of this work is to evaluate the complementary application of NR and PALS techniques for interface investigation.

As a first step the following experiment was carried out at PNR and analysed which yields accurate film thicknesses and demonstrate that no interdiffusion occurred between the PS(D) and PEMA before annealing. Thus one has a well defined bilayer sample for envisaged PALS experiments.







	<b>EXPERIMENTAL REPORT</b>	<b>GeNF PNR &amp; RÖDI</b>
<b>Characterisation of FeMn-FeNi exchange bias films using X-ray reflection and diffraction</b>		
<b>Principal Proposer:</b>	<b>J. Fassbender</b> Universität Kaiserslautern	
<b>Experimental Team:</b>	<b>D. M. Solina, U. Tietze, A. Schreyer</b> GKSS Research Centre	
<b>Date(s) of Experiment:</b>	February, April and July 2003	

### Scientific Objective

FeMn, a strong anti-ferromagnetic (AFM) material, establishes a large exchange bias field ( $H_E$ ) with low coercivity ( $H_C$ ) when coupled with NiFe. The exchange bias characteristics of this system can be influenced by ion irradiation [1] whereby a shift of the hysteresis loop occurs allowing the tailoring of the exchange bias effect. It is unclear as to how ion irradiation affects the system although it has been suggested that the ions fractionally displace atoms when traversing through the layers which can modify the magnetic structure. In an ongoing study, in co-operation with the Universität Kaiserslautern, the structural and magnetic characteristics of this system are being investigated using both x-ray and neutron scattering techniques in order to better understand the mechanism of the exchange bias process. In this report a number of results using x-ray and neutron reflectivity are given which was used to determine the scattering length density profile of an FeMn/NiFe exchange bias system before and after ion irradiation.

### Experimental Technique

The films, supplied and irradiated by the Universität Kaiserslautern, were prepared using electron beam evaporation. The layer structure for the two samples discussed here are oxidised silicon crystal/Cu(100 Å)/FeMn(10 Å)/FeNi(5 Å)/Cr(2 Å) (sample 304) and oxidised silicon crystal/ Cu(100 Å)/FeNi(5 Å)/ FeMn(10 Å)/Cr(2 Å) (sample 214). Ion irradiation was made using helium with a dosage of  $4 \times 10^{15}$  ions.cm<sup>-2</sup>. The acceleration voltage (~5 keV) has been chosen so that imbedding of the ions is in the substrate rather than the metallic layers.

The films were characterised using both x-ray and neutron reflection. In this way a layer model with greater reliability and higher degree of uniqueness can be obtained.

RÖDI, a  $\theta$ -2 $\theta$  diffractometer, was employed to make the x-ray reflectivity measurements. It was configured with a Göbel mirror for a parallel beam set-up giving an angular resolution better than 0.03°  $\theta$  FWHM and a CuK $\alpha$  source ( $\lambda = 1.5406$  Å). PNR, used for the neutron reflectivity measurements, was operated with an angular divergence of 0.02° and wavelength resolution of  $\frac{\Delta\lambda}{\lambda} = 5\%$  for a selected wavelength of 6.37 Å.

Both data sets were modelled using the program Parratt3.2, v.1.5, available through the Berlin Neutron Scattering Centre. Parratt3.2 does not allow the simultaneous modelling of both neutron and x-ray data therefore it was necessary to model the data manually. This was done via an iterative process whereby one data set (x-ray or neutron) was modelled and the other used to confirm the validity. The program also allows the application of a smearing function to be applied to the data in order to simulate the resolution function.

## Results and Preliminary Conclusions

Figures 1 and 2 give the experimental data and the models obtained for the two samples before and after irradiation. In all cases T and R are the thickness and roughness respectively.  $\rho$  and  $\text{Im}(\rho)$  are the real and imaginary components of the scattering cross section.

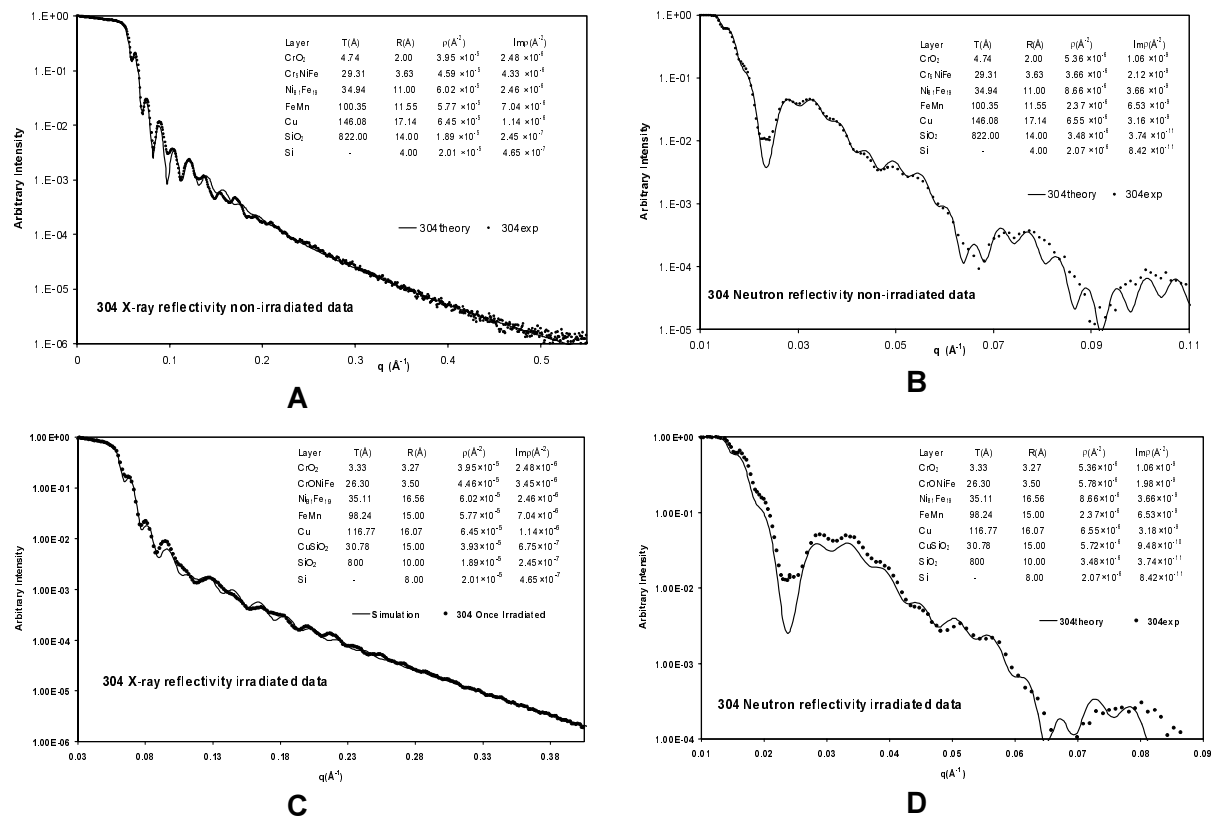


Figure 1: A & C are x-ray reflectivity data and simulation curves before and after irradiation for sample 304. B & D are neutron reflectivity data and simulation curves before and after irradiation for the sample 304.

It should be noted that only rough values for stoichiometry can be determined from reflectivity data. The layer formulae are based on expected layer composition and interpolation from modelled scattering length densities.

The modelling process, although an iterative one, is weighted for some layers with regards to technique thus allowing better refinement. For the neutron data, the fine oscillations observed are directly related to the silicon oxide layer whereas the large oscillations of the x-ray data to the upper metallic layers. This allows the setting of some 'boundary conditions' simplifying the design procedure.

It can be inferred from the model that the as deposited samples have layer thicknesses approaching the nominated thickness. The layers also deposit with some mixing and/or some diffusion at the layer interface. This is suggested by the large values obtained for interface roughness which in some cases is 30 % of the layer thickness.

Ion irradiation results in a smearing effect on the reflectivity data which is more pronounced in the x-ray data.

Preliminary modelling of the irradiated data indicate that there is increased roughness at the interfaces with minor changes in layer thickness for the surface layers. The increased

roughnesses suggest that ion irradiation encourages interfacial mixing. At the copper/silicon-oxide interface it was necessary to include a composite layer in order to improve the model for both samples after irradiation. The silicon-dioxide and copper layers are modelled with a significant thickness decrease.

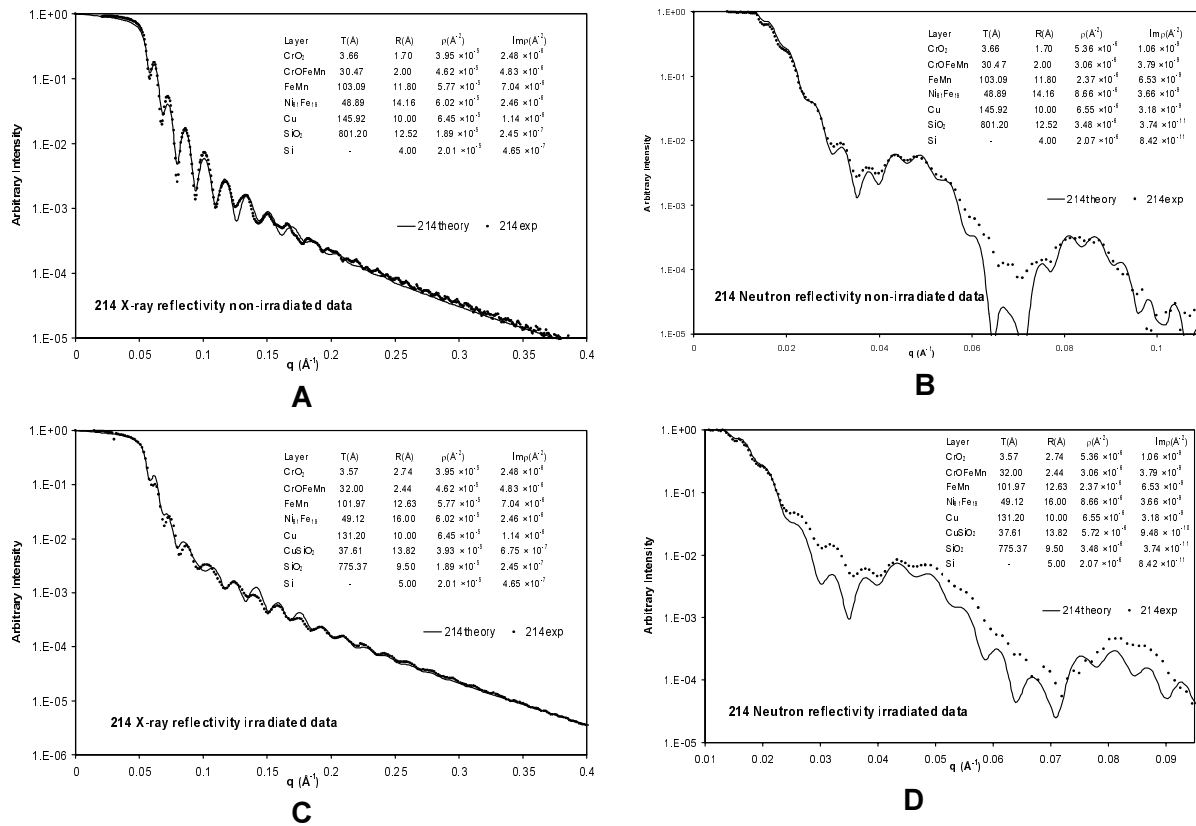


Figure 2: A & C are x-ray reflectivity data and simulation curves before and after irradiation for sample 214. B & D are neutron reflectivity data and simulation curves before and after irradiation for the sample 214.


Magnetic hysteresis measurements made before and after irradiation show a decrease in the exchange bias field with irradiation [1]. Our reflectivity models of the irradiated films suggest this fall is in part related to increased interfacial mixing between layers however Li et al. [2] showed that a reduction in buffer layer thickness can have a similar effect on the exchange bias. As the model indicates that the effective copper buffer layer is reduced by a significant amount (30 Å and 15 Å for samples 304 and 214 respectively) this may also be a contributing factor.

Although this study answers some questions concerning the influence of irradiation on the exchange bias it does not determine whether small perturbations of the atoms as the ions pass do affect the anti-ferromagnetic domain structure and thus the exchange bias. This is the next step in this study and will use epitaxially deposited films. The films will be studied using polarised neutron reflectivity on PNR as well as high angle neutron diffraction measurements on POLDI.

## References

- [1] T. Mewes, R. Lopusnik, J. Fassbender, B. Hillebrands, M. Jung, D. Engel, A. Ehresmann, and H. Schmoranzner, Appl. Phys. Lett. 76, 1057 (2000)
- [2] H.Y. li, J. Li, S. J. Yuan, L. Wang, S. M. Zhou, J. T. Song, J. Magn. Magn. Mater. 1 (2002)



	<b>EXPERIMENTAL REPORT</b>	<b>GeNF PNR &amp; RÖDI</b>
<b>Mass density of MgO films determined by x-ray and neutron reflectometry</b>		
<b>Principal Proposer:</b>	<b>R. Kleinhempel</b> TU Chemnitz, Institut für Physik, 09107 Chemnitz	
<b>Experimental Team:</b>	<b>R. Kleinhempel<sup>1</sup>, D. Solina<sup>2</sup>, U. Tietze<sup>2</sup>, D. Lott<sup>2</sup></b> <sup>1</sup> TU Chemnitz, Institut für Physik, 09107 Chemnitz <sup>2</sup> GKSS-Forschungszentrum, Geesthacht	
<b>Date(s) of Experiment:</b>	December 2003	

### Scientific Objective

Owing to their optical and electrical properties including large secondary electron emission, magnesium-oxide (MgO) films are used as insulating layers in plasma display panels (PDP) [1]. The fabrication of MgO layers is possible with the use of reactive pulsed magnetron sputtering. The layer structure of MgO films is intrinsic to the properties of the MgO film. This structure is related to the deposition parameters used for film fabrication. Reflectometry gives information on layer density, surface and interfacial roughness and layer thickness. Here, reflectometry experiments have been carried out to determine whether the film properties are independent of layer thickness. The results of the measurements will be compared to values carried out by other methods including Rutherford backscattering (RBS), atomic force microscopy (AFM) and the spectral reflectometer FTP500 (Sentech Instruments GmbH).

### Experimental Technique

MgO films were deposited by a reactive pulsed magnetron sputtering technique onto polished Si-single crystal wafers (20 mm × 20 mm) with native oxide intact. The process gas was a composite of argon and oxygen with a process gas pressure of 1.2 Pa. Argon was released into the chamber at a rate of 120 sccm whilst oxygen was introduced at 18 sccm. The film deposition rate was 90 Å.s<sup>-1</sup>. The layer thickness was time controlled.

The films were characterised using both x-ray (XRR) and neutron (NR) reflection. In this way a layer model with greater reliability is obtained from the final analysis as the model is less prone to seed values and user manipulation of the model.

RÖDI, a  $\theta$ -2 $\theta$  diffractometer, was employed to make the x-ray reflectivity measurements. It was configured with a multilayer mirror for a parallel beam set-up giving a resolution better than 0.025° and a CuK $\alpha$  source ( $\lambda = 1.5406$  Å). PNR, used for the neutron reflectivity measurements, was operated with an angular divergence of 0.02° and wavelength resolution of  $\Delta\lambda/\lambda = 5$  % for a selected wavelength of 6.37 Å.

Both data sets were modelled using the program Parratt3.2, v.1.5, which is available through the Berlin Neutron Scattering Centre.

### Results

The normalized NR curves are shown in figure 1. The model parameters and preliminary results are listed in table 1.

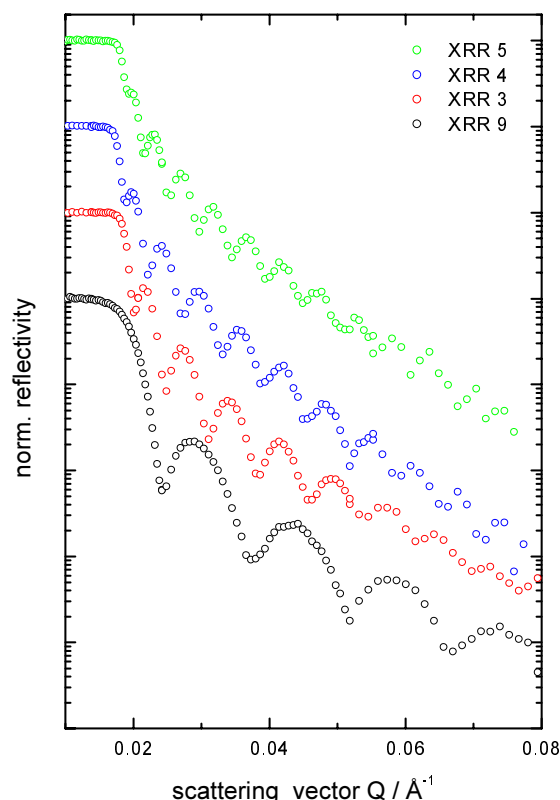


Figure 1: Normalized NR curves.

The modeled native silicon oxide layer is within known limits [2]. The MgO thickness determined from modelled NR data is smaller with respect to values obtained with FTP500.

The mass density of MgO layers is found to be  $3.62 \text{ g.cm}^{-3}$  for three of the films measured and independent of layer thickness. This value is comparable to the density of bulk MgO which is  $3.58 \text{ g.cm}^{-3}$  [3]. Sample XRR 4 was modeled with a lower density. This may be a result of an alignment error whereby the 'measured' position of the critical angle (related to the material density [4]) is shifted.

No trend is apparent for the surface roughness. The values are larger than those obtained by AFM i.e.  $20 \pm 5 \text{ Å}$ . This could be a result of a too large tip-size which may result in roughness values lower than actual [5].

Table 1: Sample comparison; <sup>1</sup>Thickness from FTP500, <sup>2</sup>Thickness from simulated NR curve.

	Thickness <sup>1</sup> (MgO) Å	Thickness <sup>2</sup> (MgO) Å	Mass density (MgO) $\text{g.cm}^{-3}$	Roughness (MgO) Å	Thickness <sup>2</sup> (SiO <sub>2</sub> ) Å	Roughness (SiO <sub>2</sub> ) Å
XRR 9	440	383	3.62	29.7	13	3.9
XRR 3	830	739	3.63	39.1	18	5.5
XRR 4	970	895	3.40	39.4	15	5.5
XRR 5	1170	1060	3.61	34.2	23	6.7

## Concluding Remarks

XRR and NR have shown to be strong tools for the study of these films. In the near future work will continue in order to optimize film properties with respect to the deposition parameters with particular emphasis on deposition rate.

## References

- [1] J. Deschamps, Plasma Display Panels, Euro Display '96 (1996), 31
- [2] Ghez, R. (1988), 'A Primer of Diffusion Problems', John Wiley & Sons.
- [3] <http://www.crystran.co.uk/mgodata.htm>, 18th Dec. 2003
- [4] Knoll, A. and Bruggemann, L., Journal de Physique IV – Colloque C4 supplement au Journal de Physique III, 6, C4 (1996), 385
- [5] Westra, K. L., Thomson, D. J., J. Vac. Sci. Technol. B 13 (1995), 344

**Diffractometer for the analysis of residual stresses ARES**

**Short Instrument Description:**

The diffractometer ARES is designed for the analysis of residual stresses ('strain scanner') in specimens with technical sizes (up to approx. 100 kg) using thermal neutrons.

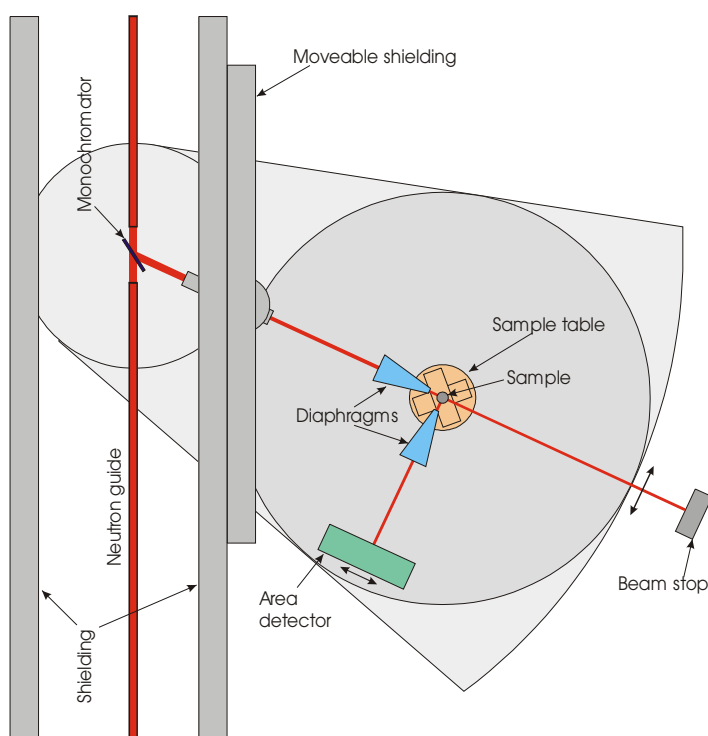
**Local Contact:**

Dr. Peter Staron

Phone/Fax : +49 (0)4152 87-1208 / +49 (0)4152 87-1356

e-mail: [peter.staron@gkss.de](mailto:peter.staron@gkss.de)

**Schematic View of ARES:**




**Instrument Details:**

Location at FRG-1:	beamline 7; thermal neutron guide, cross section 42 × 90 mm <sup>2</sup> , (supermirrors on top and bottom wall)
Monochromator:	elastically bent perfect Si monochromator, Si (311), Si (220), double focussing
Take-off angle:	57° to 120°, continuously selectable
Wavelength:	$\lambda = 0.16\text{--}0.23$ nm (with Si 311)
Flux at sample position:	$\Phi \approx 5 \cdot 10^5 \text{ cm}^{-2} \text{ s}^{-1}$
Sample displacements:	x, y (range 200 mm), z (range 150 mm), $\Omega$
Detector:	2-dim. position-sensitive <sup>3</sup> He-counter
Distance sample-detector:	100–150 cm
Sample environment:	load frame for in-situ tests planned





	<b>EXPERIMENTAL REPORT</b>	<b>GeNF ARES</b>
<b>Residual stress analysis of an LBW joint of 6013 Al alloy</b>		
<b>Principal Proposer:</b>	<b>W. Vaidya<sup>1</sup> and M. Koçak<sup>1</sup></b> <sup>1</sup> GKSS Research Centre	
<b>Experimental Team:</b>	<b>P. Staron<sup>1</sup></b>	
<b>Date(s) of Experiment:</b>	04.03.–06.03.2003	

Laser beam welding (LBW) is a powerful technique for joining Al alloys that is currently under investigation for the use in aerospace applications. Details of the process parameters have to be optimized for different alloys and different sheet thicknesses.

The specimen investigated was a 6 mm thick laser beam welded butt joint of the alloy 6013-T6. The size of the sheet and the position of the scan line is given in Figure 1.

A matchstick-like gauge volume of approximate size  $3 \times 3 \times 30 \text{ mm}^3$  was used for scanning the transverse ( $y$ ) and normal ( $z$ ) strains for improving the intensity. This choice of the gauge volume implies that the stresses are constant along  $x$  over the length of the volume element, which should be approximately true. A cubic gauge volume of approximate size  $3 \times 3 \times 3 \text{ mm}^3$  had to be used for longitudinal ( $x$ ) strain scanning since larger stress gradients are present along the transverse ( $y$ ) direction. The Al (311) diffraction peak was recorded with an area detector at an angle of about  $84^\circ$ . The position of the scan line was across the weld at mid thickness of the sheet, 150 mm away from the edge near the weld finishing point.

In general, diffractometric elastic constants have to be used for  $E$  and  $\nu$  that depend on the  $hkl$  of the reflection that is used for the strain measurement. However, the crystallographic anisotropy of the elastic constant is small for Al and, therefore, the macroscopic values were used ( $E = 70 \text{ GPa}$  and  $\nu = 0.33$  for AA6013). For the determination of a triaxial stress state, the knowledge of the unstrained lattice parameter  $d_0$  (or the peak position  $\theta_0$ ) at each measured point inside the sheet is required. As the lattice parameter can change with the solute content, the  $d_0$  value also depends on the heat input the material has experienced during welding. This problem was overcome by assuming a plane stress state in the relatively thin sheet. From the condition  $\sigma_z = 0$ ,  $d_0$  (or  $\theta_0$ ) can be calculated for each point.

Figure 2 shows the residual stresses in longitudinal and transverse direction as obtained through the plane stress hypothesis. Tensile longitudinal peak stresses of about 200 MPa are observed on both sides of the weld. In the weld center there is a stress minimum of 70 MPa. Compressive longitudinal stresses of about  $-30 \text{ MPa}$  are observed from 10 mm to 50 mm away from the weld center. There are small tensile transverse stresses between 10 and 20 MPa across the weld.

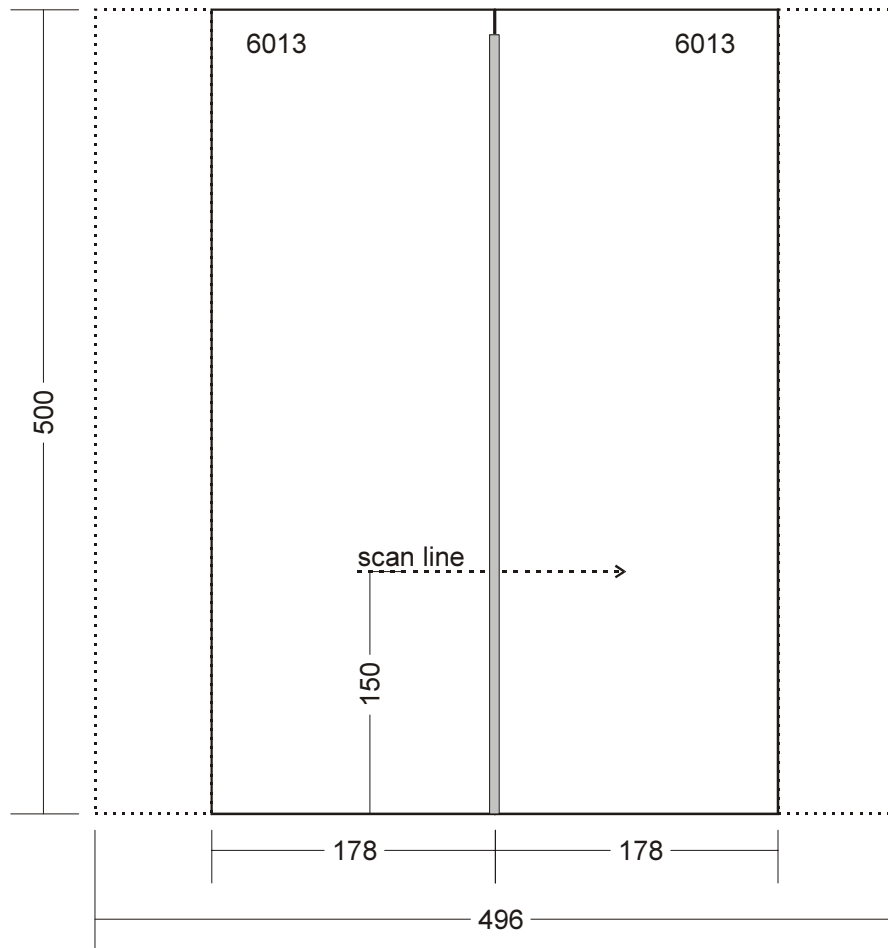


Figure 1: Dimensions of the sheet and position of the scan line.

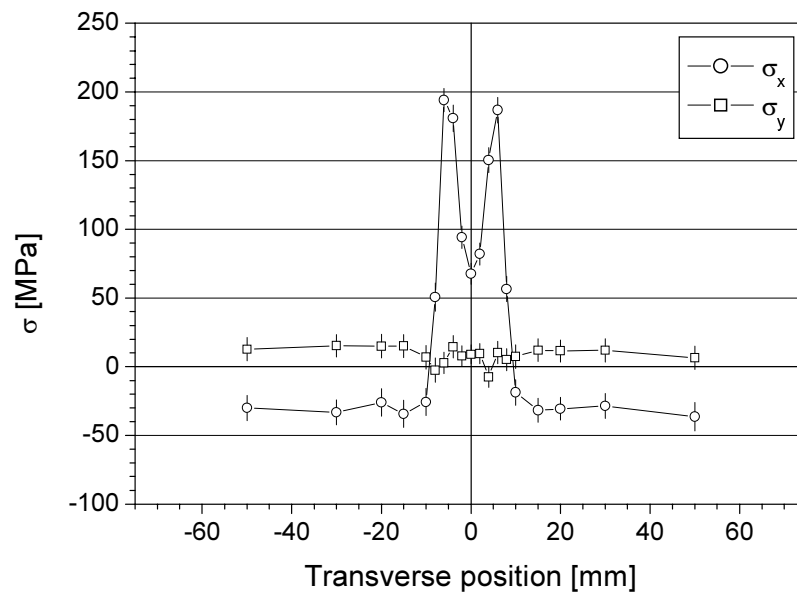



Figure 2: Residual stress results in the similar 6013/6013 LBW joint as obtained from the plane stress hypothesis.

	<b>EXPERIMENTAL REPORT</b>	<b>GeNF ARES</b>
<b>Residual stress in ferritic steel welds</b>		
<b>Principal Proposer:</b>	<b>O. Doerk</b> Technical University of Hamburg-Harburg	
<b>Experimental Team:</b>	<b>P. Staron</b> GKSS Research Centre	
<b>Date(s) of Experiment:</b>	13.03.–24.03.2003	

The fatigue behaviour of welded ferritic steel structures is crucial for ship-building applications. At fillet welded joints, which are favoured by the practice because they show much lower fabrication costs compared to full penetration joints, fatigue cracks can start at weld toes (toe cracks) as well as at unwelded root gaps (root cracks). Up to now there exists no satisfying procedure for the assessment of root cracks at attachment ends. Therefore this problem has been investigated within an international industrial R & D project. The coordinator of the project which was mainly financed by oil companies was DNV from Norway. Several fatigue tests with small scale specimens has been carried out which partly showed unexpected fatigue behaviour. It had been assumed that residual stresses are responsible for this. In order to varify this assumption and to obtain reliable residual stress data, two welded specimens were investgated using neutron diffraction strain measurements. The neutron diffraction method is the most suitable method for the residual stress determination for the actual case because stresses in front of the root gap are most interesting with respect to root cracks.

The investigated specimens were two ferritic steel (RSt37-2) joints made of 12 mm thick plates as shown in Figure 1. Sample A was welded in 3 passes with a weld size  $a = 6$  mm, sample B was welded in a single pass with a weld size  $a = 4$  mm. Internal strains were measured at three different locations: location 1 was 60 mm away from the lower edge of the arc-shaped part of the specimen (i.e. in the middle of the plate), location 2 was 5 mm away from it, location 3 was in the middle of the front side. At each location, four points were measured; an additional point was measured only at location 1 (Figure 2). Reference to the positions is made in the form 'Xmn', where X means the sample (A, B),  $m$  means the location (1...3), and  $n$  means the point (1...5). Stress-free references were gained by cutting small pieces out of the base material, heat affected zone, and weld by spark erosion, in which macro-stresses are expected to relax largely.

Initiation of fatigue cracks had originally been expected at both ends of the welds around the attachment ends (location 3), where a large curvature of the weld is present and large stress concentrations were expected due to the cut outs above. However, within the fatigue tests it has often been observed that cracks were initiated in the middle of the plate (location 1). The explanation was given by the measurements: The largest tensile stresses were found in y-direction at location 1: 290 MPa in sample A (Fig. 2), and 420 MPa in sample B. In contrast, at location 3, the largest compressive stresses were found in x-direction: –310 MPa in sample A (Fig. 2), and –250 MPa in sample B. The stresses at location 2 are in between the two extremes. In general, the stresses in sample B, which was welded in one single pass, are more tensile than in sample A. The conclusion is that the large tensile stresses in the middle of the plate are the reason for crack initiation in this region.

With the help of the results of the residual stress measurements (compressive stresses at the attachment ends and tensile stresses in the middle part) it is possible to explain the results of the fatigue test.

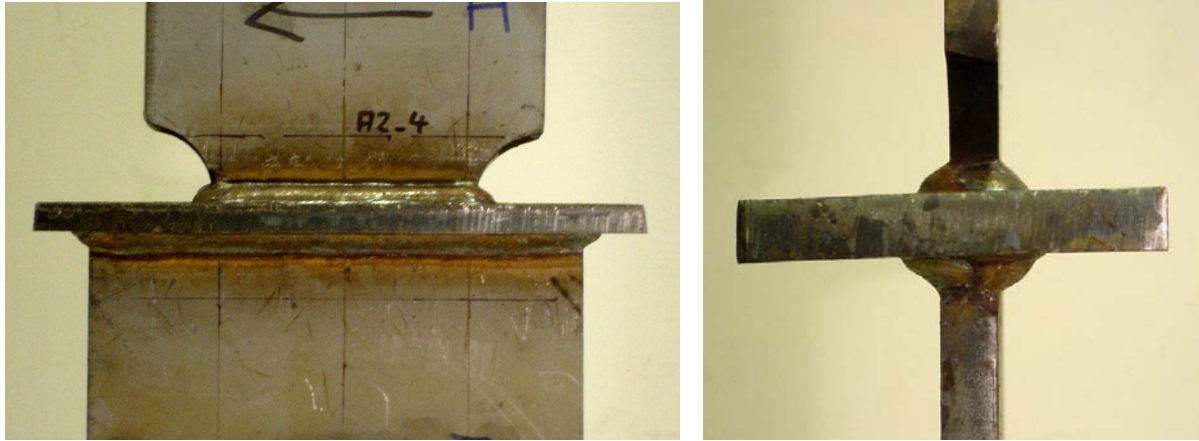


Figure 1: Photographs of the specimen A. The width of the lower plate is 220 mm, the thickness of the plates is 12 mm.

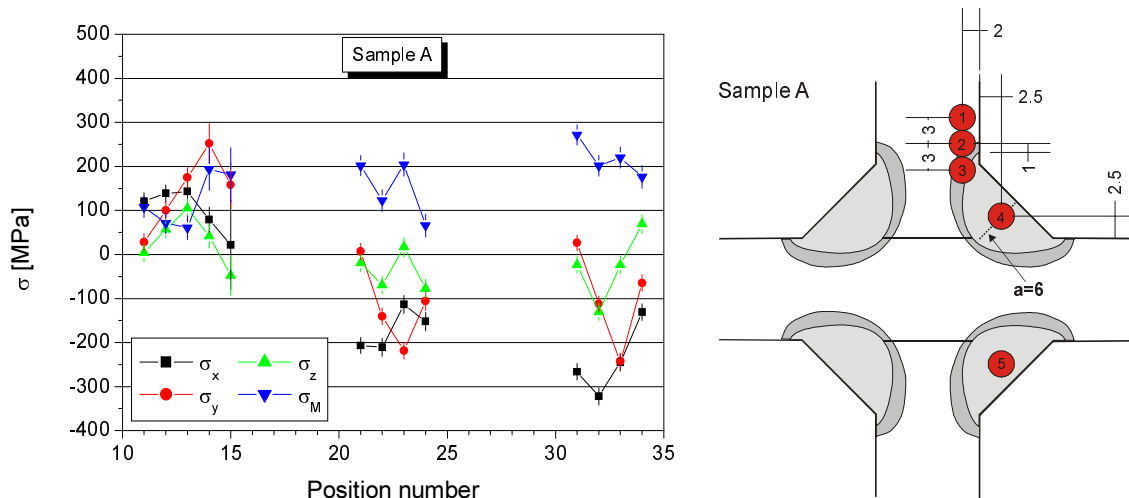



Figure 2: Residual stress results for the 13 points in sample A (see text for the nomenclature of the position numbers). The positions of the measured points 1–5 are shown on the right.  $\sigma_M$  is the effective stress after Von Mises.

	<b>EXPERIMENTAL REPORT</b>	<b>GeNF ARES</b>
<b>Residual Stress in IN718 Turbine Discs</b>		
<b>Principal Proposer:</b>	<b>W. Marketz<sup>1</sup></b> <sup>1</sup> Böhler Schmiedetechnik, Kapfenberg, Austria	
<b>Experimental Team:</b>	<b>U. Cihak<sup>2</sup>, P. Staron<sup>3</sup></b> <sup>2</sup> Mining University Leoben, Leoben, Austria <sup>3</sup> GKSS Research Centre	
<b>Date(s) of Experiment:</b>	1. 24.03.2003 – 13.04.2003 2. 22.06.2003 – 18.07.2003 3. 23.08.2003 – 19.09.2003 4. 08.11.2003 – 08.12.2003	

## Aim

Residual stresses play an important role in the production of forged components like turbine discs. Variations in the processing parameters can lead to different residual stress states, which complicate subsequent processing steps, e.g. turning to the final shape. Therefore, a deeper understanding of the residual stress evolution during thermo-mechanical processing and the resulting distortions during machining is essential in order to optimize the manufacturing process with respect to cost efficiency and quality of the product. Consequently, the development of residual stresses in a forged turbine disc made of nickel-based superalloy IN718 was simulated using a finite element model. Obviously, the experimental verification of the model predictions is necessary to adjust the simulation parameters. To this end, non-destructive analyses of residual stresses were performed using neutron strain scanning. For a disc quenched in water after forging (so-called direct ageing processing route) the results show that the residual stresses predicted by the used FE model agree well with the stresses obtained from strain measurements.

## Experimental

In the as-forged and water-quenched (WQ) condition three different discs have been measured along the radius of the disc and through the thickness of the disc, one of the discs has been examined along three radii having an offset of 120° to each other to check the rotational symmetry of the internal stress state. The discs had a diameter of 320 mm and a thickness of up to 25 mm. The measurement positions are indicated by the symbols in Figure 1. Following the standard processing route, one of the discs has subsequently been solution annealed and measured again. Additionally, more detailed information about the through-thickness variation of the stress gradient proved to be necessary. Therefore, measurements with a higher spatial resolution have been performed along three radial positions indicated by dashed lines in Figure 1. For all measurements the (311) reflection of the  $\gamma$ -phase with a diffracting angle  $2\theta$  of approximately 100° was used. Radial and axial strains were determined using a gauge volume of 3x3x30 mm<sup>3</sup>, for tangential strains a gauge volume of 3x3x14 mm<sup>3</sup> was used. For the detailed through-thickness scans the gauge volume was reduced to 2x2x30 mm<sup>3</sup> and 2x2x14 mm<sup>3</sup> respectively. Reference samples for the unstrained lattice parameter  $d_0$  had a size of 4x5x6 mm<sup>3</sup> and were cut out by spark erosion.

## Main Results

At first, cutting out reference samples was avoided in order to preserve the internal stress state and enable further examination of the same disc after the heat treatment step. The evaluation was then based on the simulation results, which predict no axial stresses except for the edge region of the part. Instead of calculating absolute stress values, the differences between the radial respectively tangential stresses and the axial stresses have been determined, because then the reference value  $d_0$  for the unstrained lattice parameter cancels out. According to continuum mechanics, which is the basis for the FE simulation, these differences should approximately be equal to the actual radial and tangential stresses due to the absence of any axial stresses.

The results have shown that all three as-forged and water quenched discs had approximately the same residual stress levels. Each scan along the radii shows a stress maximum near the outer edge of the disc. The discs also seem to be fairly homogeneous concerning their rotational symmetry (Figures 2a/b). Through the thickness of the disc the measured stresses suggest a parabolic trend with a maximum in the central region, but the stress distribution is slightly asymmetric (Figures 3a/b). A comparison with results of the finite element simulation using the package DEFORM shows that the basic tendencies of the stress gradients found in the measurements agree well with the simulation results for the radial stresses, but there is an offset for the tangential values.

In order to verify these results a reference sample for the unstrained lattice parameter  $d_0$  has been cut out at the edge of the disc intending to preserve most of the initial stress condition of the disc and still be able to obtain absolute stress values. Applying this  $d_0$  value, the stress values and the simulated results diverge in the thinner region of the part. Although this can partly be attributed to geometric effects of the cooling process, a detailed study of the unstrained lattice parameters at different positions of the cross section has been started. Small cubes have been cut out at all measurement positions to examine if the lattice parameter of the unstrained lattice is varying over the cross section. However, until now no conclusions can be drawn as the data is not completely analysed yet.

The solution annealed condition displays very low stresses, which was expected as the solution annealing is followed by an air cooling step. Comparisons with simulated results cannot be given, because metallurgical effects like recrystallisation occurring during annealing are not implemented in the model so far.

The obtained results proved that the production process leads to fairly homogeneous residual stress states in the turbine discs. This applies for different discs with the same geometry as well as for their rotational symmetry. Based on the large and detailed amount of data obtained from discs in the as-forged, water quenched condition, the simulation model can now be improved.

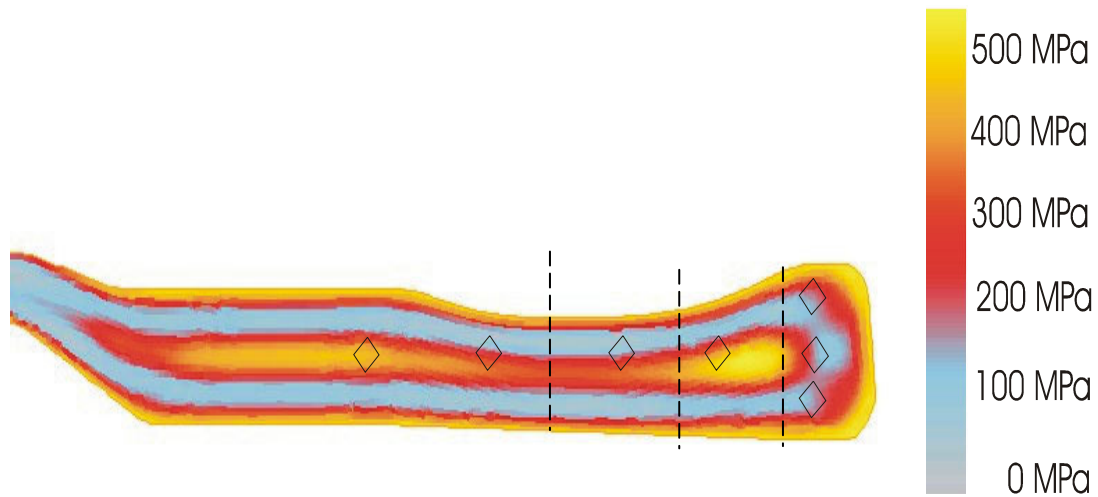


Figure 1: Simulated effective residual stress in the as-forged condition and cubes indicating the measurement positions.

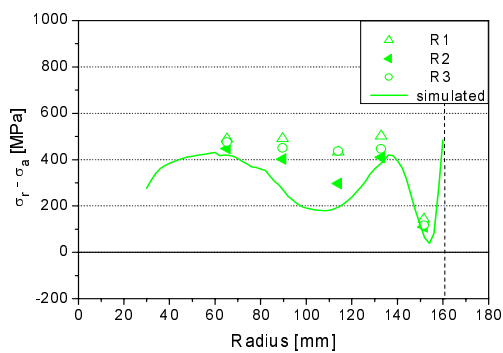


Figure 2a: Radial stresses in a WQ disc determined by strain measurements along three radii (R1 - R3) and FE-simulation.

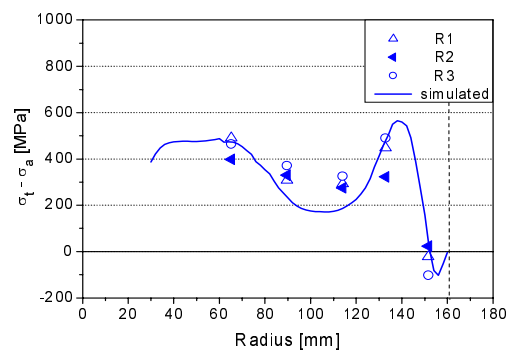


Figure 2b: Tangential stresses in a WQ disc determined by strain measurements along three radii (R1 - R3) and FE-simulation.

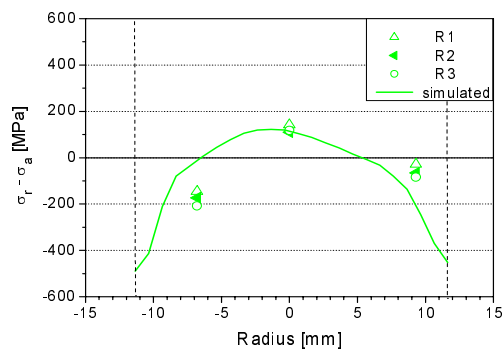


Figure 3a: Radial stress variations through the thickness of the disc determined at three radii (R1 - R3) and by FE simulation.

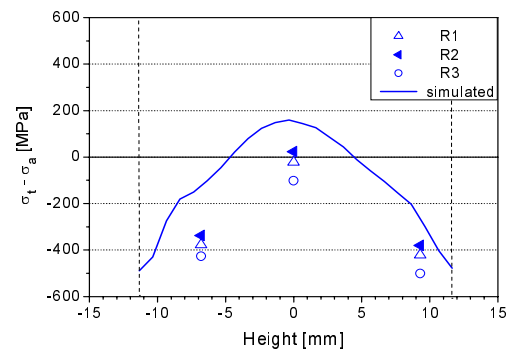



Figure 3b: Tangential stress variations through the thickness of the disc determined at three radii (R1 - R3) and by FE simulation.





	<b>EXPERIMENTAL REPORT</b>	<b>GeNF ARES</b>
<b>Residual Stress in a Ti 6Al 4V fan-shaft</b>		
<b>Principal Proposer:</b>	<b>W. Marketz<sup>1</sup></b> <sup>1</sup> Böhler Schmiedetechnik, Kapfenberg, Austria	
<b>Experimental Team:</b>	<b>U.Cihak<sup>2</sup>, P. Staron<sup>3</sup></b> <sup>2</sup> Mining University Leoben, Leoben, Austria <sup>3</sup> GKSS Research Centre	
<b>Date(s) of Experiment:</b>	14.04.2003 – 01.05.2003	

## Aim

Residual stresses resulting from different hot-forming operations and intermediate heat treatment steps play an important role during the production process of complex structures as well as during their operation. An understanding of the residual stress evolution during the manufacturing process, from the starting ingot material to the final part, allows prediction of possible machining problems and distortion that can occur. This study is devoted to residual stress analysis of a forged shaft made of Ti-6Al-4V after heat treatment and machining. The production of this high performance turbine engine part has been simulated based on an extensive material database. This numerical simulation is accompanied by stress measurements using neutron diffraction. Once the results of the simulation are verified, it can be used to optimize the forging process and the pre-form geometry. The current results show that the used heat treatment steps lead to an almost stress-free final part. According to the experimental results, the employed simulation gives a good description of the physical processes occurring during manufacture.

## Experimental

The as-forged geometry of the commercial fan-shaft had been turned to a near-final shape geometry. The modified part with the fictitious model geometry has then been measured in the as-forged, machined condition.

The axi-symmetric shaft has been examined along two radii having an offset of 120°. Radial and axial strains were determined using a gauge volume of 3x3x30 mm<sup>3</sup>, for tangential strains a gauge volume of 3x3x14 mm<sup>3</sup> was used. The measurement positions along a radius are indicated in Figure 1. As mechanical as well as metallurgical examinations have indicated that the whole part is homogeneous, one reference sample has been cut out from the top region of the central, cylinder-shaped part of the fan-shaft. All strains have been determined using the (103) reflection at 76° of the hexagonal  $\alpha$  phase. As this phase has a volume percentage of over 80 %, the strains in this phase have been considered representative for the whole part.

## Main Results

The measurements have shown that the remaining stresses in the fan-shaft along both radii are compressive and very low. In Figure 2, which shows the stress distribution along radius 1, it can be seen that the stress maximum only reaches -85 MPa. Near the outer region of the part the stresses actually are zero. As the part has been air cooled the stresses were supposed to be rather low. However, further work is planned for 2004 including measurements on the same part after solution annealing and subsequent water quenching. The aim of additional investigations is the study of higher residual stress levels. Together with the present examination the FE model can be verified for all relevant quenching cycles occurring during production of forged structural parts.

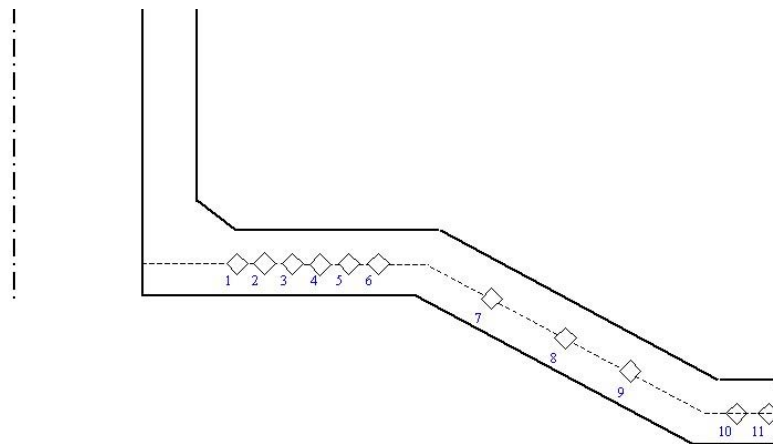


Figure 1: Measurement positions along the cross section of the model fan-shaft. The cubes indicate the size of the gauge volume.

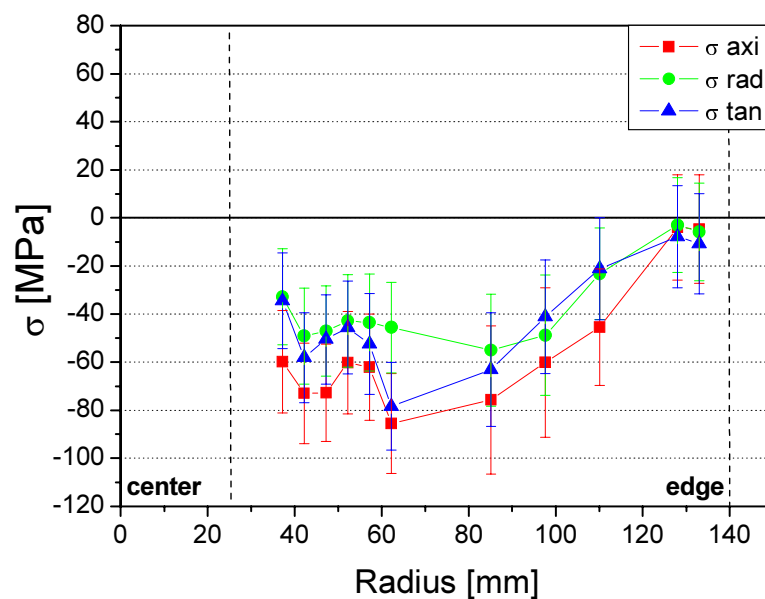



Figure 2: Residual stresses along on radius of the fan-shaft, measured in the forged and heat treated condition followed by cooling on air, which is in accordance with GE's "class I" specifications.

	<b>EXPERIMENTAL REPORT</b>	<b>GeNF ARES</b>
<b>Residual stress analysis in FSW steel plates using neutron diffraction</b>		
<b>Principal Proposer:</b>	<b>J. F. dos Santos</b> GKSS Research Centre	
<b>Experimental Team:</b>	<b>P. Staron</b> GKSS-Research Centre	
<b>Date(s) of Experiment:</b>	19.05.–05.06.2003	

Friction stir welding (FSW) is a promising joining technique that was patented in 1991 and has been extensively studied for joining Al alloys. It can produce high quality welds with good mechanical properties. More recently, this technique has also been applied to steels, which is far more challenging due to the greater hardness and strength at temperature of these materials. The overall objective of this work is the optimization of processing conditions and tool geometries for FSW of steels. The welds were produced at TWI in Cambridge, U.K.. Table 1 presents a summary of the dimensions of the welded plates, including the identification codes, the welding length, material and eventual comments. All the welds are butt joints. The specimens subjected to residual stress measurements were three ferritic steel (St355) friction stir welded (FSW) joints made of 13 mm thick plates (specimens 3AB, 7AB and 10). Specimens 3AB and 7AB were double sided butt joints whereas specimen 10 is a single sided butt joint. The size of the specimens was approx. 250 mm × 300 mm. The directions x, y, z of the sample coordinate system are as indicated in Figure 1. Internal strains were measured along a scan line that was 145 mm away from one edge of the sample, i.e. approximately in the middle of the plate (Fig. 1).

*Table 1:* eneral information on all welded plates received from TWI for testing purposes.

Identification code	Material	Dimensions (mm)		Weld lenght (mm)	Comments		
ST_EB_10	C-Mn steel S355J2G3	Lenght	342	332	Single- Pass	-	Residual stress analysis
		Width	390				
		Thikness	12				
ST_EB_12	C-Mn steel S355J2G3	Lenght	349	343	Single- Pass	-	Cut for testing
		Width	390				
		Thikness	12				
ST_EB_3AB	C-Mn steel S355J2G3	Lenght	320	310	Double- Pass	Same direction of travel speed	Residual stress analysis
		Width	390				
		Thikness	12				
ST_EB_6AB	C-Mn steel S355J2G3	Lenght	331	321	Double- Pass	Same direction of travel speed	Cut for testing
		Width	390				
		Thikness	12				
ST_EB_7AB	C-Mn steel S355J2G3	Lenght	338	300	Double- Pass	Opposite direction of travel speed	Residual stress analysis
		Width	390				
		Thikness	12				
ST_EB_18AB	C-Mn steel S355J2G3	Lenght	325	317	Double- Pass	Same direction of travel speed	Cut for testing
		Width	390				
		Thikness	12				

Figure 1 presents a macrograph of the specimen “10” as an example of a single sided butt joint. Figure 2 presents a double sided butt joint (specimen 3AB).

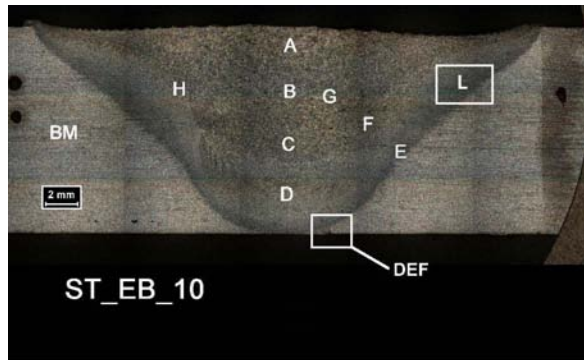


*Fig. 1: Macrograph of the specimens “10”.*  
The area indicated by the letters DEF indicate a minor root flaw caused by a incorrect dimensioning of the tool pin.

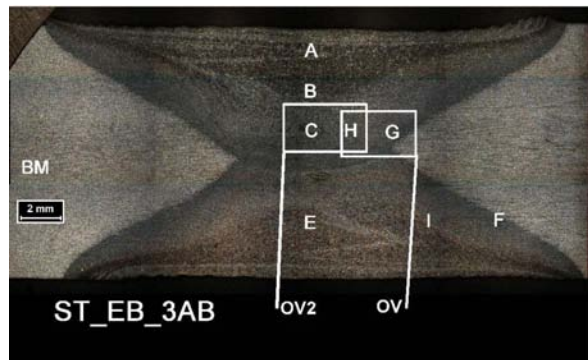


*Fig. 2: Macrograph of the specimens “3AB”.*

One small sample of size  $5 \times 13 \times 105 \text{ mm}^3$  was cut out of plate 3AB at the location indicated in Figure 3. Cuts were made each 5 mm to allow additional stress relaxation in the small bar. All cutting was done by spark erosion to minimize mechanical work on the reference sample. This reference sample is assumed to be free of macro stresses and was thus used to determine the stress free lattice parameter  $d_0$ .

A matchstick-like gauge volume of nominal size  $2 \times 2 \times 30 \text{ mm}^3$  was used for measurements of transverse ( $y$ ) and normal ( $z$ ) strains for improving the intensity. A cubic gauge volume of approximate size  $2 \times 2 \times 2 \text{ mm}^3$  was used for measurements of longitudinal strains, because large stress gradients are expected in the transverse direction. The grain size of the material proved to be small enough to ensure a good grain statistics even in the small gauge volume of approx.  $8 \text{ mm}^3$ . The Fe (211) diffraction peak was recorded with an area detector at an angle of about  $89^\circ$ . Elastic constants  $E = 222 \text{ GPa}$  and  $\nu = 0.28$  were used for the Fe(211) reflection for the calculation of stresses. The stress free lattice parameter  $d_{0, \text{plane stress}}$  determined under the plane stress assumption ( $\sigma_z = 0$ ) is very similar to  $d_0$  obtained from the reference sample, indicating that the plane stress assumption is a good approximation even for the 13 mm thick plates. A reference sample was only cut out of one sample (3AB), which might not be exactly representative for the other two samples. Therefore, the stresses in all three samples were finally calculated under the plane stress assumption.

The stress results show that all three samples exhibit significant tensile longitudinal stresses ( $\sigma_x$ ) with peak values between +280 and +300 MPa in the weld region, and smaller compressive stresses far away from the weld (Figures 4–6). Transverse stresses ( $\sigma_y$ ) are below +100 MPa in the weld region and slightly compressive (sample 3AB) or close to zero (samples 7AB, 10) far away from the weld. There seems to be a slight asymmetry in the longitudinal stress above 20 mm from the weld line in sample 7AB and sample 10, which is not observed in sample 3AB. Sample 10 deviates significantly from the other two samples, showing a much broader longitudinal stress field (60 mm) than samples 3AB and 7AB (40 mm).

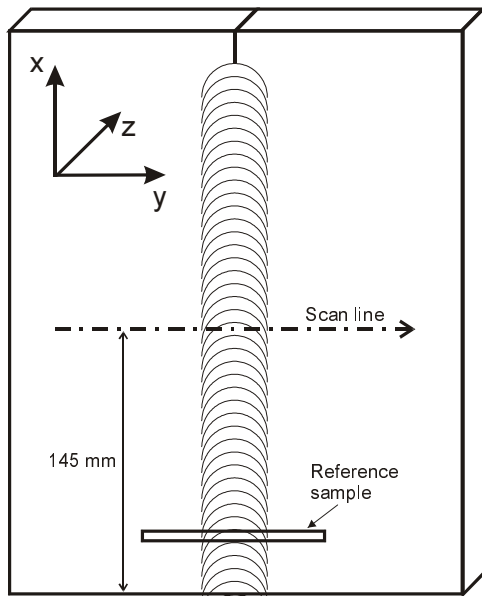


Figure 3: Position of the scan line in the approximately 250 mm × 300 mm large plates. The directions x, y, z are indicated. The location of the reference sample, cut out of sample 3AB, is indicated.

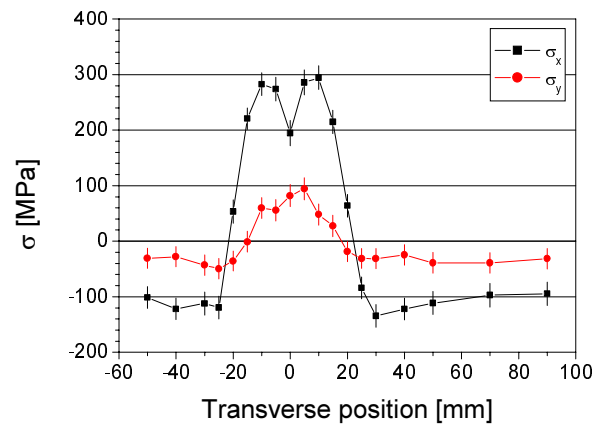


Figure 4: Residual stress results for sample 3AB.

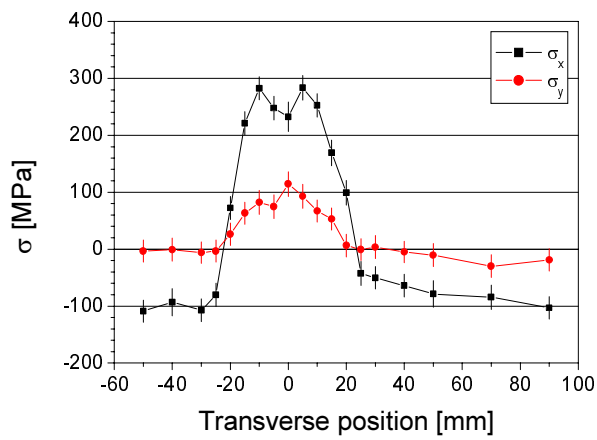


Fig. 5: Residual stress results for sample 7AB.

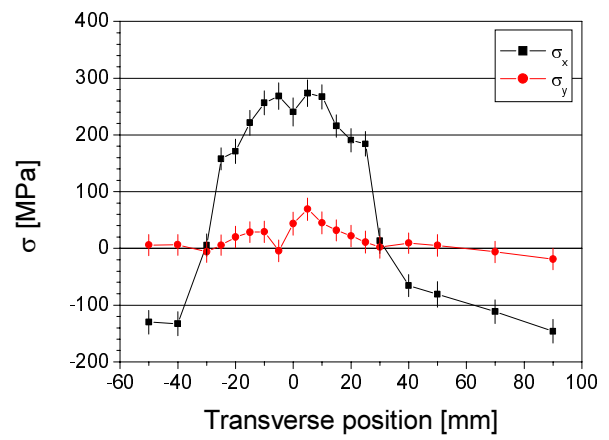



Fig. 6: Residual stress results for sample 10.



	<b>EXPERIMENTAL REPORT</b>	<b>GeNF FSS</b>
<b>Neutron time-of-flight spectrometer FSS</b>		

### Short Instrument Description:

The spectrometer FSS is a Fourier reverse time-of-flight spectrometer (system Hiismäki) to investigate residual stresses in polycrystalline material specimens with technical sizes using thermal neutrons. Details can be found in P. Hiismäki, Modulation Spectrometry of Neutrons with Diffraction Applications, World Scientific, 1997.

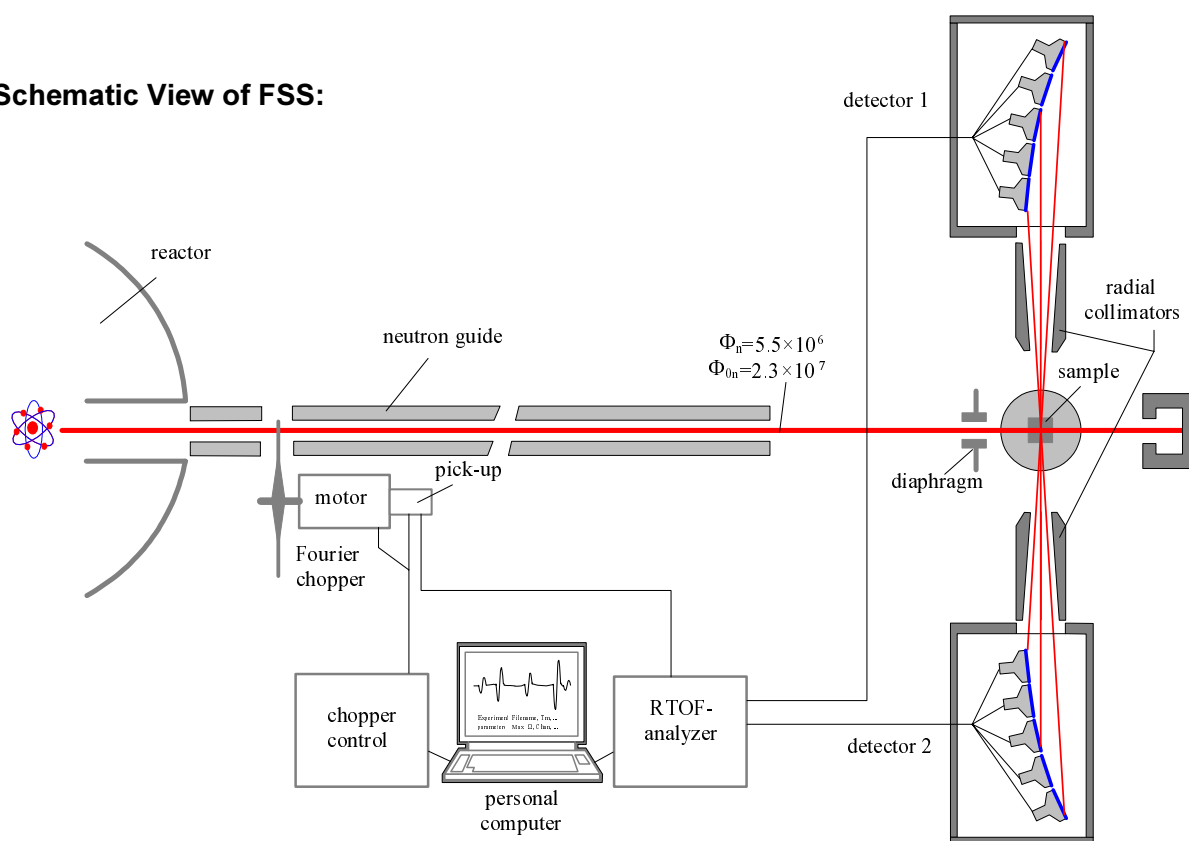
### Local Contact:

Prof. Dr. Hans Georg Priesmeyer

Phone/Fax : +49 (0)4152 87–1315 / +49 (0)4152 87–1338

e-mail: [priesmeyer@gkss.de](mailto:priesmeyer@gkss.de)

### Schematic View of FSS:




### Instrument Details:

Location at FRG-1:	beam line 9, thermal neutrons
Flight path:	21.15 m Ni-coated curved neutron guide, radius of curvature: 3000 m characteristic wavelength: $\lambda_{\text{char}} = 0.183 \text{ nm}$ beam size: $2 \times 20 \text{ mm}^{-2}$ to $15 \times 108 \text{ mm}^{-2}$
Fourier chopper:	1024 slits, 1760 rpm max. operating speed
Flux at sample position:	$\Phi = 5.5 \cdot 10^6 \text{ cm}^{-2} \text{ s}^{-1}$
Wavelength range:	$\lambda = 0.1 \text{ nm}$ to $0.4 \text{ nm}$

**Instrument Details** (continued):

Timing resolution:	ca. $4 \cdot 10^{-3}$ ( $\lambda = 0.1\text{--}0.4$ nm)
TOF analyser:	reverse time of flight correlator 2 x 3072 channels, 1 $\mu$ s minimum channel width
Detector:	2 Li-6 glass scintillation detector banks (90° & 270°) in time-focussing geometry
Ancillary equipment:	sample positioner for strain tensor determination – heater (up to 1000 °C) – stress rig: max. force: 30 t



	<b>EXPERIMENTAL REPORT</b>	<b>GeNF FSS</b>
<b>Characterisation of stress relief in a cast break disk</b>		
<b>Principal Proposer:</b>	<b>W. Stets<sup>1</sup></b> <sup>1</sup> Institut für Giessereiforschung (IfG), Düsseldorf	
<b>Experimental Team:</b>	<b>Hans G. Priesmeyer<sup>2</sup>, Gizo Bokuchava<sup>3</sup></b> <sup>2</sup> Institut für Experimentelle und Angewandte Physik, Universität Kiel <sup>3</sup> Institut für Werkstoffforschung, GKSS-Forschungszentrum	
<b>Date(s) of Experiment:</b>	February/March 2003	

### Neutron diffraction reveals stress relief in cast break disks

As part of Project E 289 (Cooperation GKSS/IfG) through-wall scans have been made near the edge of cast break disks, in order to determine residual stresses in axial, radial and tangential directions. The material is 100 % perlite with lamellar graphite (GJL). The disks were cast in October 2002 and first measured immediately after receipt. The first disk was measured again after a month, while the second disk was measured four and a half months later.



*Figure 1:* Break disk in measuring position at FSS (arrow showing scan position).

One of the aims of the project was the verification of Finite Element (FE) calculations of the residual stresses, as shown for the axial direction in figure 2.

While calculated stresses vary between  $-45$  MPa and  $+30$  MPa, measurements made immediately after the casting show compressive stresses as low as  $-100$  MPa. It has to be emphasized that the latter are phase stresses of  $\alpha$ -iron. The measurements repeated after a time interval, during which the material was allowed to relax, have shown that the compressive stresses had undergone stress relief, despite the fact that their values are far from the yield point. These findings confirm the experience of the casting engineers.

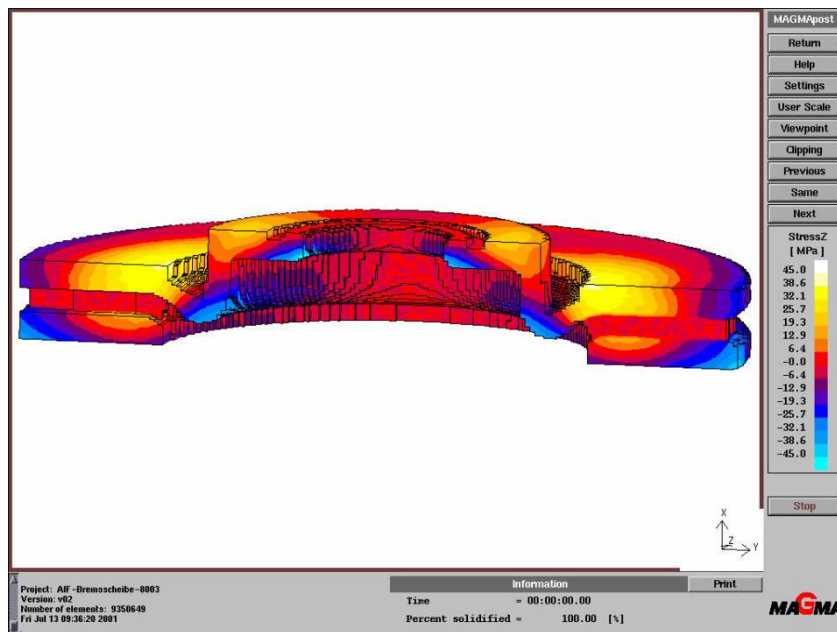


Figure 2:  
Residual stresses in  
break disk, calculated  
by FE methods.

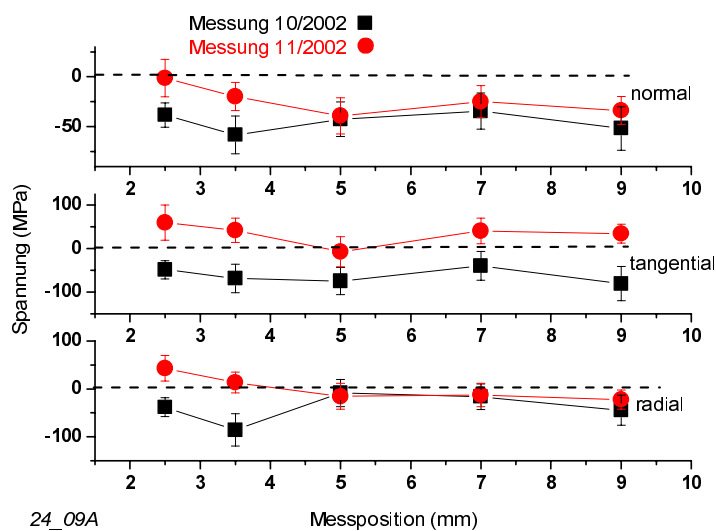


Figure 3:  
Stress comparison disk 1  
(1 month between first and  
second measurement).

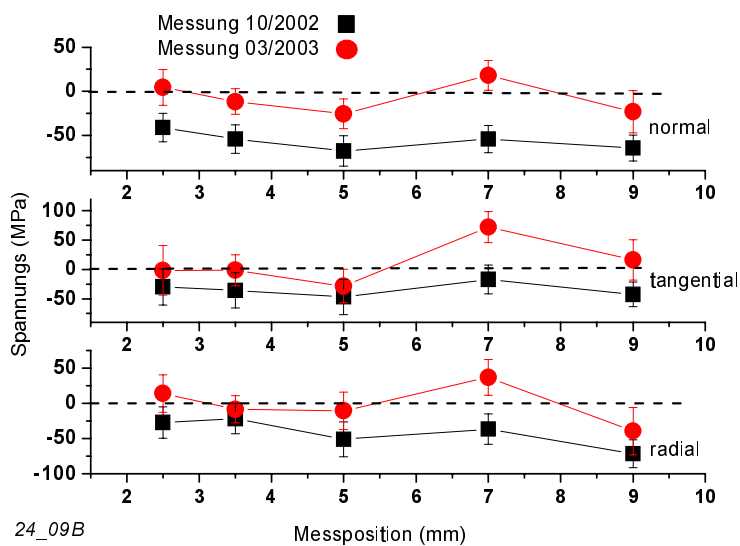



Figure 4:  
Stress comparison disk 2  
(4.5 months between first and  
second measurement).

	<b>EXPERIMENTAL REPORT</b>	<b>GeNF FSS</b>
<b>Residual stress characterization in rolled AZ 31 Mg-alloy sheets</b>		
<b>Principal Proposer:</b>	<b>Dietmar Letzig<sup>1</sup></b> <sup>1</sup> Institut für Werkstofforschung, GKSS	
<b>Experimental Team:</b>	<b>Hans G. Priesmeyer<sup>2</sup>, Gizo Bokuchava<sup>2</sup>, Jürgen Göken<sup>1</sup>, Dietmar Letzig<sup>1</sup></b> <sup>1</sup> Institut für Werkstofforschung, GKSS <sup>2</sup> Institut für Experimentelle und Angewandte Physik, Universität Kiel	
<b>Date(s) of Experiment:</b>	May 2003	

### Neutron diffraction characterization of residual stresses in rolled AZ 31 sheets

Strains in rolled AZ 31 magnesium alloy sheets (appr. 150 x 150 x 1.5 mm) have been investigated in three orthogonal directions, in order to determine the residual stresses introduced by the rolling process.

The following figure shows the experimental setup.



*Figure 1: AZ 31 material in measuring position at FSS.*

The two opposite detector banks (east and west detector) at FSS reveal the strong texture within the material, as can be seen from figure 2.

Three samples have been measured ("as delivered" and after two different heat treatments).

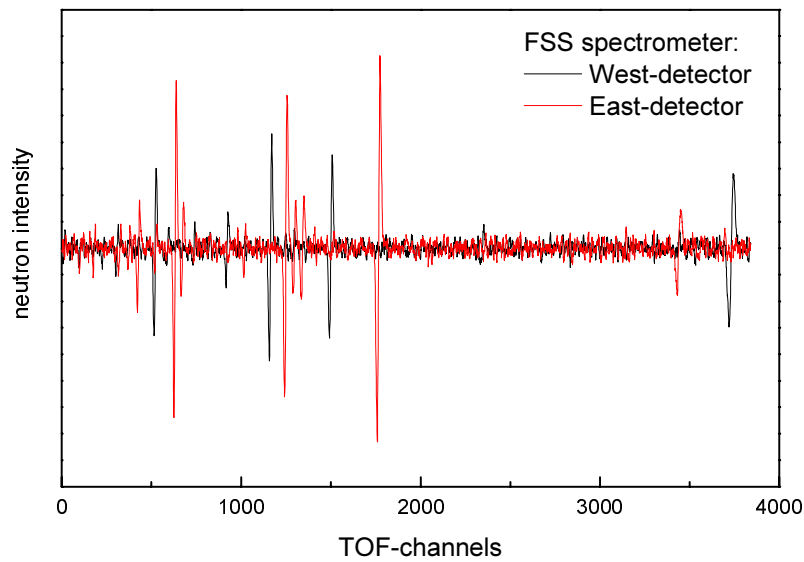


Figure 2:  
Fourier neutron time-of-flight  
spectrum of rolled AZ 31  
sheet material.

Results are shown in the next two figures, where the stress values must be revised after improved diffraction – elastic constants have been determined from another experiment on AZ 31.

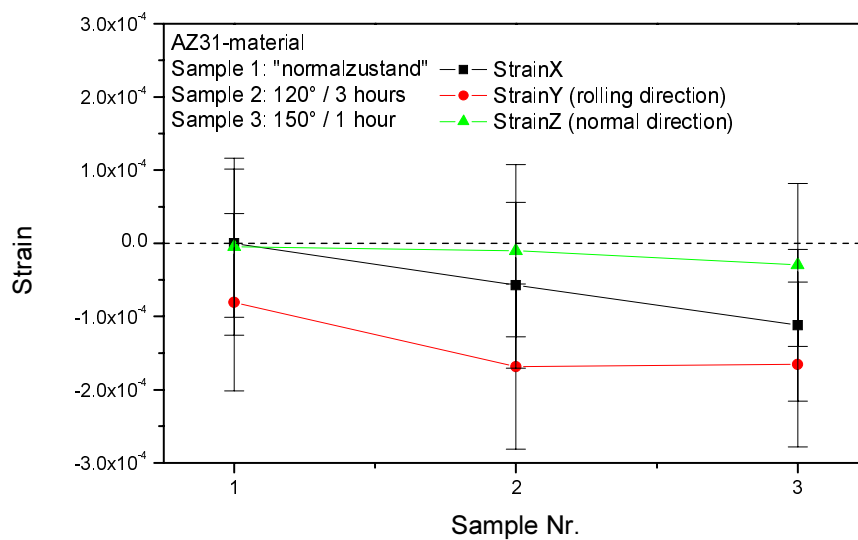


Figure 3: x-y-z strain  
components in the rolled  
sheet material.

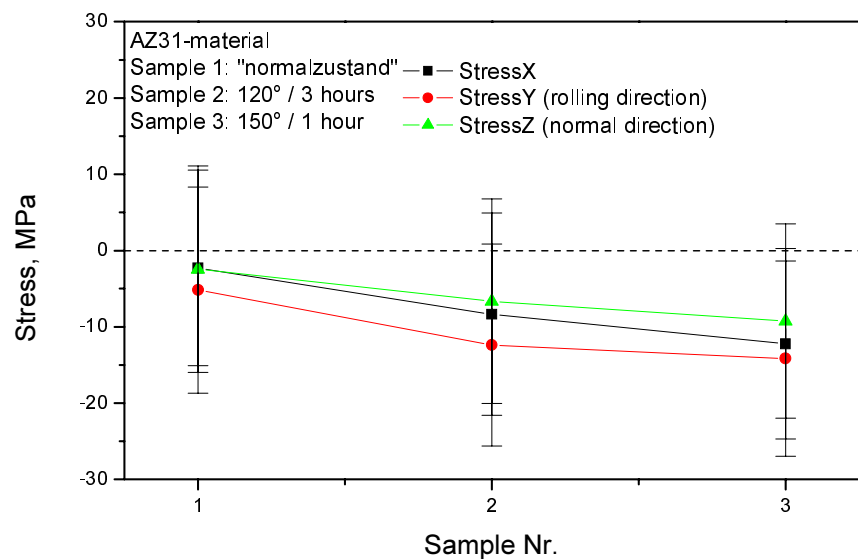


Figure 4: x-y-z stress  
components in the rolled  
sheet material

	<b>EXPERIMENTAL REPORT</b>	<b>GeNF FSS</b>
<b>Diffraction-elastic properties of AZ 31 Mg-alloy at RT and elevated temperatures</b>		
<b>Principal Proposer:</b>	<b>Dietmar Letzig<sup>1</sup></b> <sup>1</sup> Institut für Werkstoffforschung, GKSS	
<b>Experimental Team:</b>	<b>Dietmar Letzig<sup>1</sup>, Jürgen Göken<sup>1</sup>, Hans G. Priesmeyer, Gizo Bocuchava<sup>2</sup></b> <sup>1</sup> Institut für Werkstoffforschung, GKSS <sup>2</sup> Institut für Experimentelle und Angewandte Physik, Universität Kiel	
<b>Date(s) of Experiment:</b>	May/July/October/November 2003	

### Determination of the diffraction – elastic constants of magnesium alloy AZ31

To be able to calculate stresses from strains measured by diffraction methods it is vital that the  $hkl$  – dependent, so – called diffraction – elastic properties of the material are known. Since these properties depend also on the temperature of the material, several experiments have been performed during 2003, in order to determine  $E_{hkl}$  and  $\nu_{hkl}$ .

The proposers had asked for a series of measurements up to 450 °C, with special emphasis to the range near 250 °C, where a so far unexplained change of the internal friction of the material was found.

Uniaxial compressive stress experiments were made at room temperature (RT) and at elevated temperatures using the 30 - ton stress rig at FSS shown in figure 1:

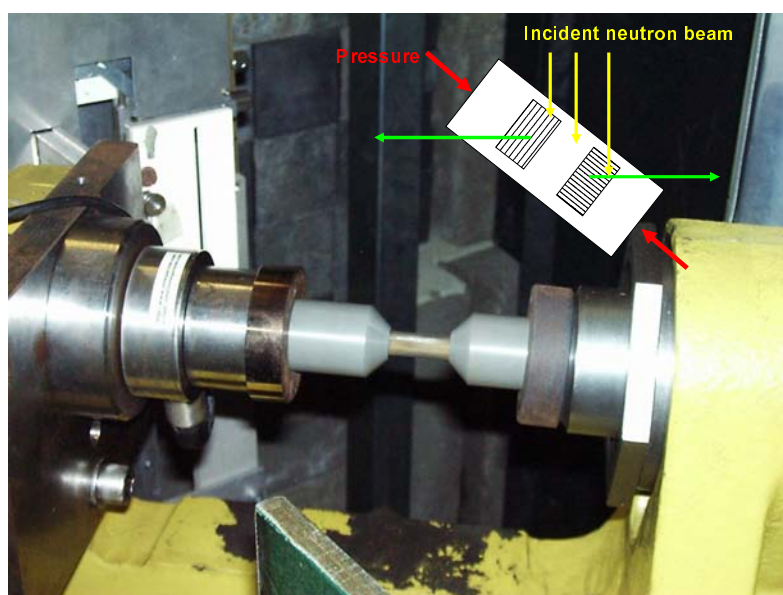


Figure 1: AZ 31 cylinder (30 mm x 10 mm Ø) mounted to the FSS stress rig (RT experiment).

As can be seen from the insert, both Young's modulus and Poisson's ratio may be determined simultaneously for each individual reflection, due to the two opposite detectors at  $+90^\circ$  and  $-90^\circ$  at FSS.

The results for RT and 60 °C are shown in the following figure:

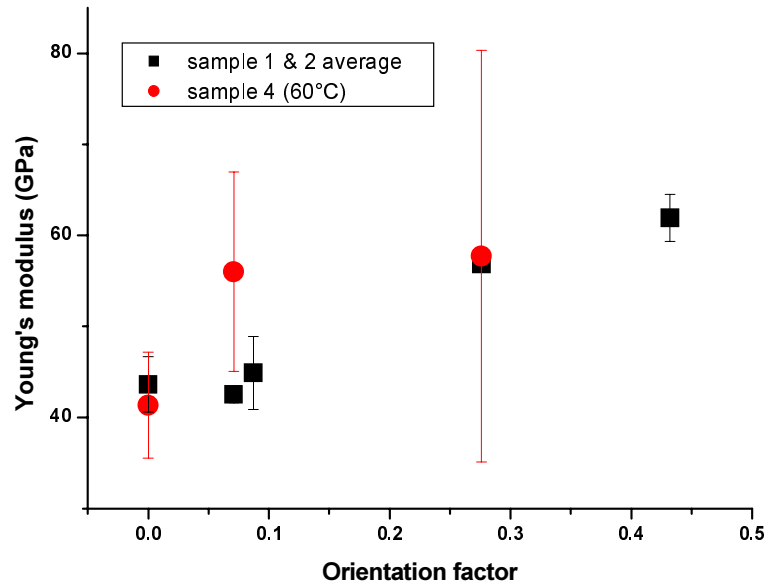


Figure 2: Young's moduli as a function of the orientation factor  $H^2$ .

The following table shows the averages of the measured elastic constants, which may be compared to the bulk value  $E = 42.1 \pm 0.5$  GPa. It is still an open question, why the measurements show differing results for the two load conditions. A change of the material texture has been observed during loading. This results needs further interest.

Table 1: Orientation - averaged elastic constants.

Sample	Temp.	Load conditions	E, GPa	$\nu$
Sample #1	RT	load	55.1	0.45
Sample #1	RT	unload	42.5	0.34
Sample #2	RT	load	53.0	0.37
Sample #2	RT	unload	44.0	0.28
Sample #4	T=60 °C	load	61.6	0.44
Sample #4	T=60 °C	unload	51.	0.34

The experimental setup used to perform the measurements at higher temperatures can be seen in the next figure. Heat is applied by a stabilised hot – air fan and the temperature measured and recorded by a thermocouple in a drilled hole within the specimen.



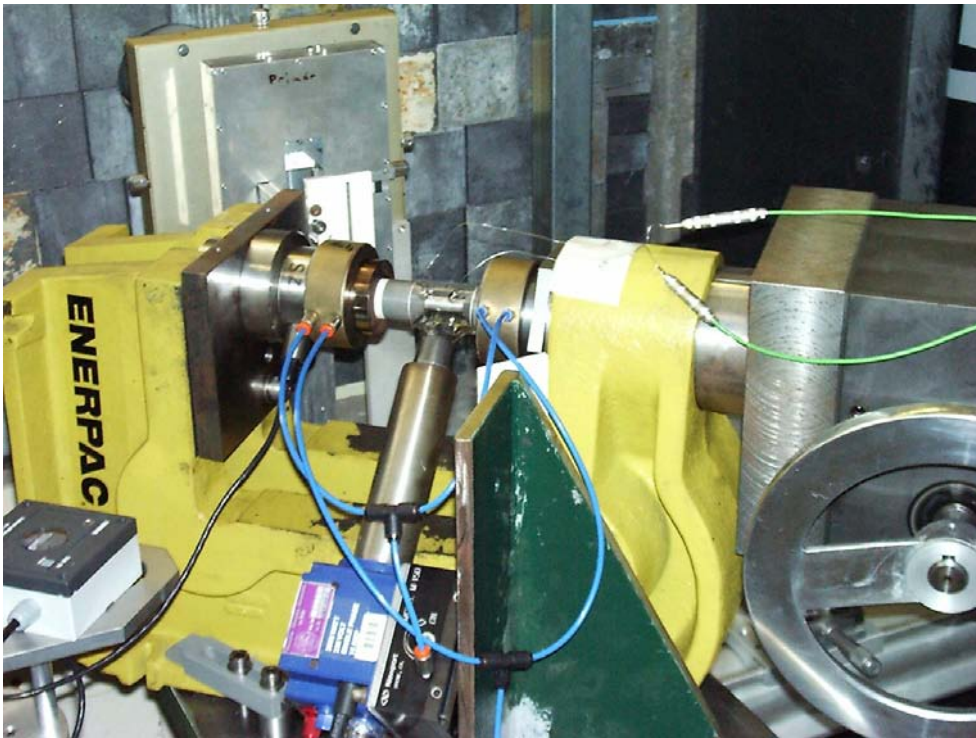


Figure 3: Stress rig with sample in heating mode.


Measurements at 150 °C ended with no useful results, since material creep was so high, that strains and stresses could not be built up within the specimen, which became plastically deformed.



Figure 4: Outlines of two AZ31 specimens after the compressive tests. (Sample #2 was measured at 150 °C).





	<b>EXPERIMENTAL REPORT</b>	<b>GeNF FSS</b>
<b>Feasibility study on DSPS specimens</b>		
<b>Principal Proposer:</b>	<b>Werner Skrotzki<sup>1</sup></b> <sup>1</sup> Institut für Kristallographie und Festkörperphysik, TU Dresden	
<b>Experimental Team:</b>	<b>Werner Skrotzki<sup>1</sup>, Hans G. Priesmeyer<sup>2</sup>, Gizo Bokuchava<sup>2</sup></b> <sup>1</sup> Institut für Kristallographie und Festkörperphysik, TU Dresden <sup>2</sup> Institut für Experimentelle und Angewandte Physik, Universität Kiel	
<b>Date(s) of Experiment:</b>	June 2003	

### **Neutron diffraction feasibility to characterize residual stresses in double-scale particle strengthened materials (DSPS)**

The residual stresses in both the matrix material and the reinforcing fibers are responsible for long-life material quality. Such investigations require information about all contributing phases in that material. Therefore this is a task for energy-dispersive diffraction experiments, like neutron time-of-flight at the FSS diffractometer.

Several specimens were supplied by TU Dresden. The matrix consisted of mechanically alloyed Cu-Al<sub>2</sub>O<sub>3</sub> powder, while the reinforcements were tungsten fibers (3 mm x 0.3 mm Ø), coated with a Cu-Ni layer. The fiber volume fraction was 4 %, 7.5 % and 15 %. The processing procedure consists of cold compression, followed a 1h, 700 °C heat treatment under Argon atmosphere. Subsequently two hot extrusion steps follow, the final extrusion ratio reaching 16:1.

In the following figure a typical specimen is shown in measuring position.

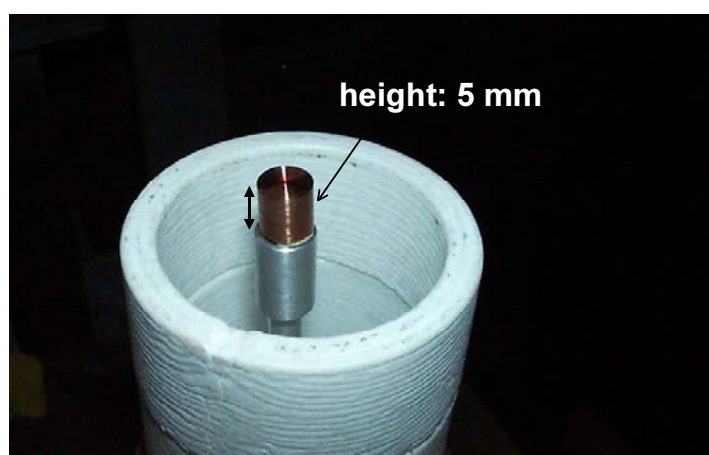



*Figure1:* Test specimen in measuring position at FSS the holder is shielded by Li-6 – loaded lithiumcarbonate.

The measured diffraction spectra looked like the one shown in figure 2.

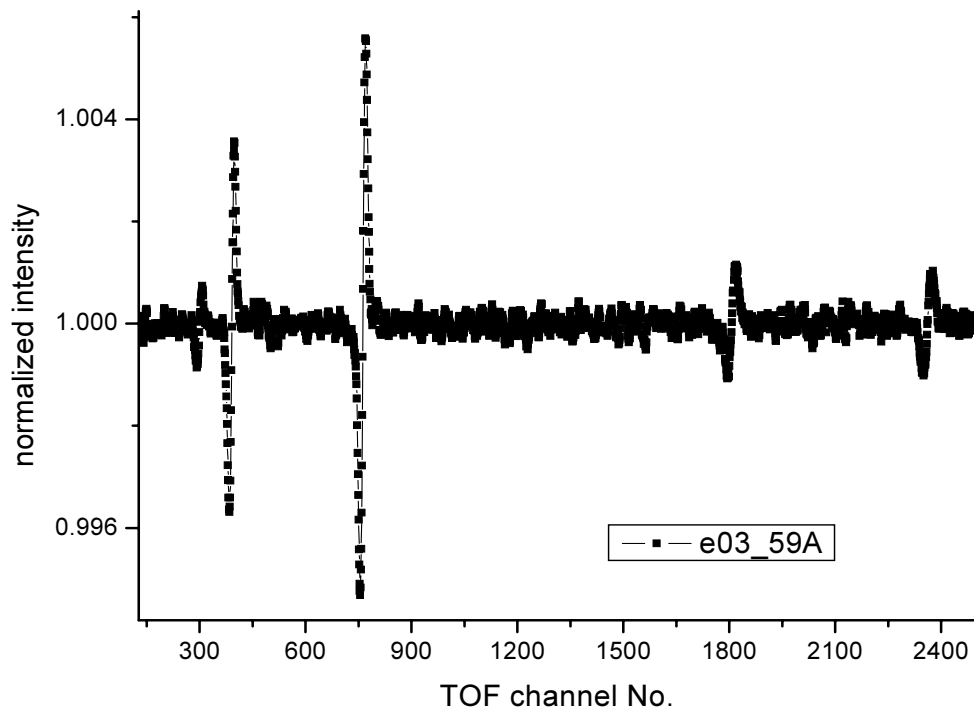


*Figure 2: Typical Fourier neutron time-of-flight spectrum of DSPS material.*

All reflections identified could only be attributed to copper, while any reflexions from the tungsten fiber material were too weak to be seen. It was therefore proposed that the experiments should be transferred to a synchrotron source and be measured in energy – dispersive mode. Nevertheless it is possible to determine the residual stresses in the copper phase from the performed measurements.

	<b>EXPERIMENTAL REPORT</b>	<b>GeNF FSS</b>
<b>Elastic constants of cast iron with differing carbon content and morphology</b>		
<b>Principal Proposer:</b>	<b>Hans G. Priesmeyer<sup>1</sup></b> <sup>1</sup> Institut für Experimentelle und Angewandte Physik, Universität Kiel	
<b>Experimental Team:</b>	<b>Hans G. Priesmeyer<sup>1</sup>, Gizo Bokuchava<sup>2</sup>, Wolfram Stets<sup>3</sup></b> <sup>1</sup> Institut für Experimentelle und Angewandte Physik, Universität Kiel <sup>2</sup> Institut für Werkstoffforschung, GKSS <sup>3</sup> Institut für Giessereiforschung, Düsseldorf	
<b>Date(s) of Experiment:</b>	July 2003	

### Elastic constants of cast iron materials (IfG Project E-289)

Diffraction methods determine elastic strains, from which stresses can be calculated if the appropriate elastic constants are known. It was noticed in the discussion of the results of Project E-289 (GKSS 7.T.100.F.07), that stresses characterised by neutron diffraction differed considerably from stresses calculated by Finite Element methods. One of the reasons identified to contribute to this difference was the choice of the elastic constants of the materials. While FE calculations are based on bulk moduli, diffraction needs orientation dependent, reflection specific Young's moduli and Poisson's ratios. It was qualitatively known, that carbon content and carbon morphology have a great influence on the bulk elastic properties. Specimens suitable for uniaxial compressive load tests have been cut from the motor block (GJV; vermicular graphite), break disk (GJL; lamellar graphite) and suspension (GJS; globular graphite) and have been measured using the 30 to stress rig at FSS. In the following, the results for cast iron with lamellar graphite (GJL) are shown as a representative example:

**Microstructure GJL, 100% Perlite, 500 x**



*Figure 1: Micrograph of cast iron with lamellar graphite.*

The following figure shows the measured stress strain curves for three different reflections of the  $\alpha$  – iron component in comparison to the macroscopic relation (cf. also Table 1):

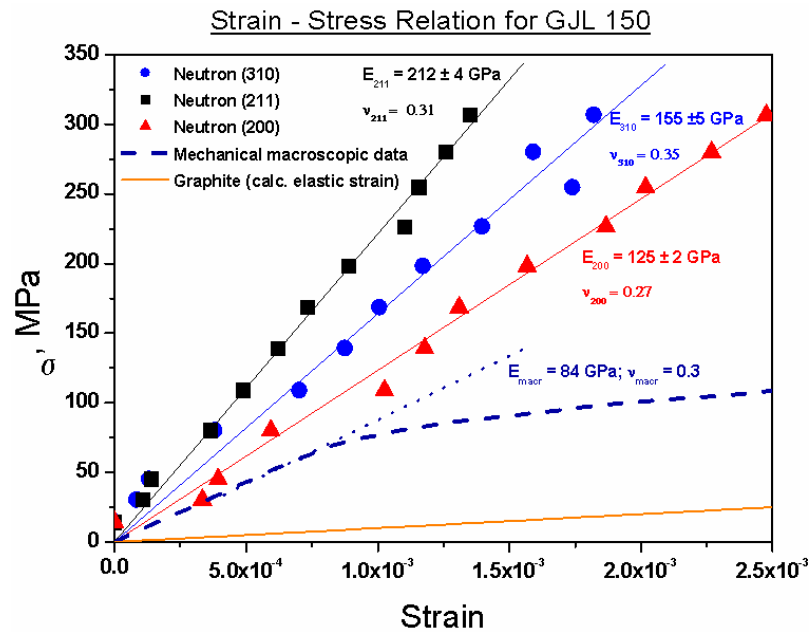


Figure 2: Elastic behaviour of GJL cast iron.

Table 1: Numerical values of the relevant elastic constants.

Reflection	E [GPa]	$\nu$
200	$126 \pm 2$	0.27
211	$155 \pm 5$	0.35
310	$212 \pm 4$	0.31
Macrosc.	84	0.3

The low value of the macroscopic modulus can be understood using appropriate theoretical models, as seen in Figure 3:

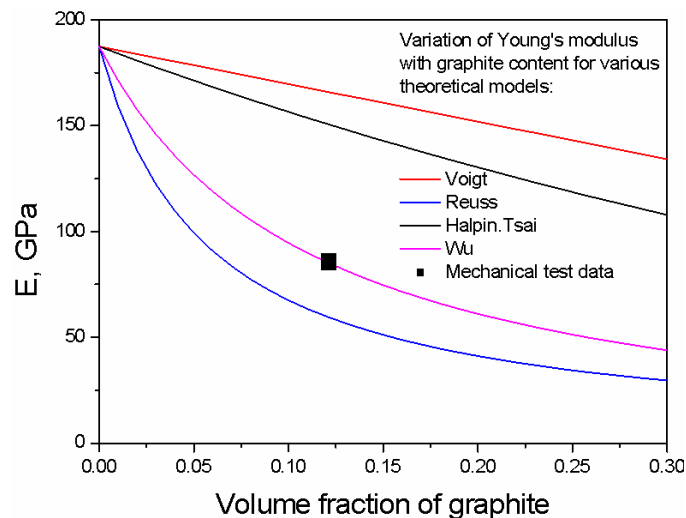



Figure 3: Best agreement for the macroscopic Young's modulus for GJL material is achieved by the theoretical approach of Wu et al..

 <b>GKSS</b> <small>FORSCHUNGSZENTRUM in der HELMHOLTZ GEMEINSCHAFT</small>	<b>EXPERIMENTAL REPORT</b>	<b>GeNF FSS</b>
<b>Orientation-dependent thermal expansion of anisotropic materials</b>		
<b>Principal Proposer:</b>	<b>Hans G. Priesmeyer</b> Institut für Experimentelle und Angewandte Physik, Universität Kiel	
<b>Experimental Team:</b>	<b>Hans G. Priesmeyer, Gizo Bokuchava</b> <sup>1</sup> Institut für Experimentelle und Angewandte Physik, Universität Kiel	
<b>Date(s) of Experiment:</b>	August 2003	

### The orientation-dependent thermal expansion of copper

The six independent components of the stress tensor  $X_i$  in Voigt notation are related to the six independent components  $x_i$  of the strain tensor by

$$X_i = \sum_j c_{ij} \cdot x_j$$

(i,j = 1, ..., 6)

The elastic constants  $c_{ij}$ , which enter this relation may be calculated as

$$c_{ij} = \frac{\partial^2 E(x_1, \dots, x_6)}{\partial x_i \cdot \partial x_j}$$

where  $E$  is the energy per unit volume of the crystals a function of the strains. The general behaviour of this energy as a function of separation of the atoms is determined by a strong repulsive force component close to an atom, followed by an attractive minimum, which then slowly levels off towards zero. The asymmetrical well in this simple model of the potential energy can explain thermal expansion: the mid-point locus of the oscillating atoms is shifted towards greater separation with increasing temperature. It is generally assumed, that thermal expansion for cubic crystals is isotropic. But some cubic systems are elastically anisotropic, which means different shapes of the potential in different directions. So the question must be raised, whether in a polycrystalline elastically anisotropic aggregate the individual thermal expansion coefficients for different lattice planes  $hkl$  will also be influenced and to what extent. Copper has been used as a model substance, since its elastic anisotropy is rather significant:

$$E_{111} = 2.87 \cdot E_{200}$$

It could therefore be expected, that the “softer” (200) lattice planes are hindered by harder planes to thermally expand in the same manner. This would result in a lower thermal expansion coefficient for elastically softer planes. A cylindrical copper specimen has been heated up to 700 °C and the shift of the diffraction peak positions has been determined. The following figures show second order polynomial fits to the (200) and (111) reflection data.

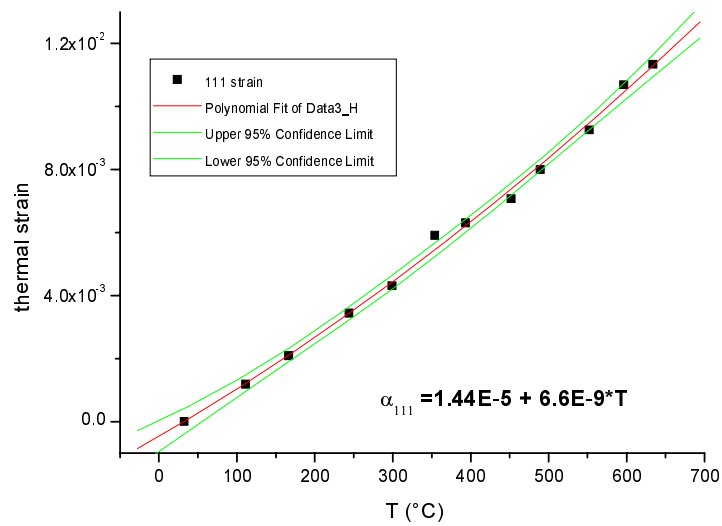


Figure 1:  
Measured thermal strain  
for the (111)-reflection.

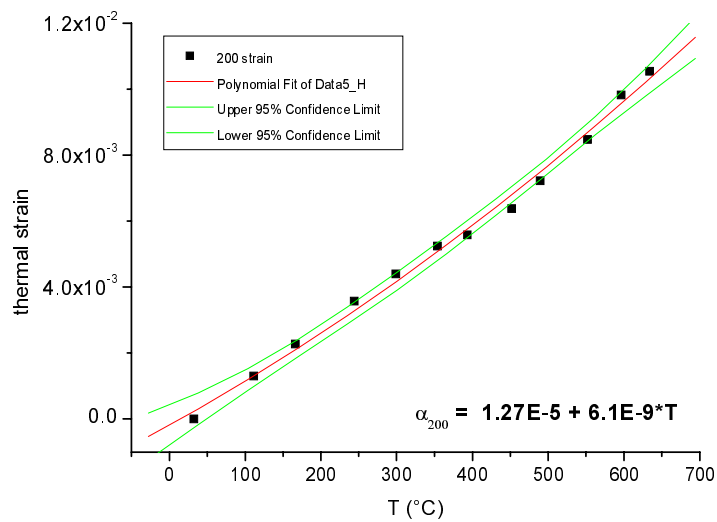


Figure 2:  
Measured thermal strain  
for the (200)-reflection.

An as yet unexplained change in lattice strains between the (200) and the (111) reflection was observed starting at about 300  $^{\circ}\text{C}$ , as can be seen in the following figure:

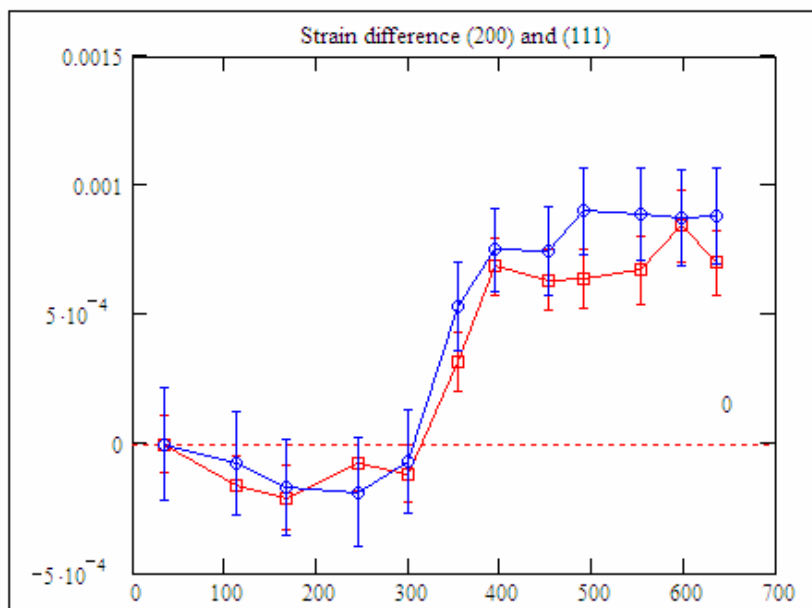
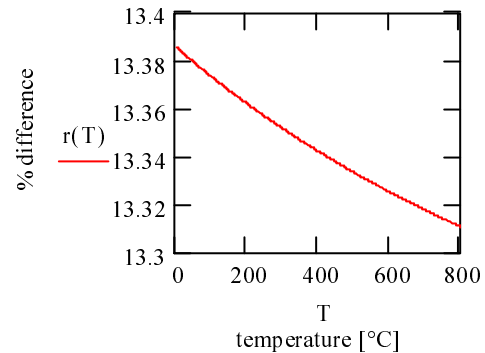


Figure 3: Strain difference  
 $\epsilon_{200} - \epsilon_{111}$ , as observed with  
the east (red) and the west  
(blue) detector.

As possible explanation of this behaviour could be, that an annealing process has been observed, since a decrease of the peak widths can also be seen. It seems to be necessary to repeat the experiment.

We find that the expansion coefficient  $\alpha_{111}$  exceeds the coefficient  $\alpha_{200}$  by approx. 13 % in the temperature range investigated.

$$r(T) := \left( \frac{1.44 \cdot 10^{-5} + 6.9 \cdot 10^{-9} \cdot T}{1.27 \cdot 10^{-5} + 6.1 \cdot 10^{-9} \cdot T} - 1 \right) \cdot 100$$




*Figure 4:*  
Relative difference  $r(T)$  in %  
between Cu (111) and (200)  
expansion coefficients.

Tabulated recommended macroscopic values for the linear thermal expansion coefficient of copper vary from  $1.65 \times 10^{-5} \text{ K}^{-1}$  at RT to  $2.03 \times 10^{-5} \text{ K}^{-1}$ .





 <b>GKSS</b> FORSCHUNGSZENTRUM in der HELMHOLTZ GEMEINSCHAFT	<b>EXPERIMENTAL REPORT</b>	<b>GeNF FSS</b>
<b>Orientation-dependent thermal expansion of AZ 31</b>		
<b>Principal Proposer:</b>	<b>Hans G. Priesmeyer<sup>1</sup></b> <sup>1</sup> Institut für Experimentelle und Angewandte Physik, Universität Kiel	
<b>Experimental Team:</b>	<b>Hans G. Priesmeyer<sup>1</sup>, Gizo Bokuchava<sup>2</sup>, Jürgen Göken<sup>2</sup>, Dietmar Letzig<sup>2</sup></b> <sup>1</sup> Institut für Experimentelle und Angewandte Physik, Universität Kiel <sup>2</sup> Institut für Werkstofforschung, GKSS	
<b>Date(s) of Experiment:</b>	September 2003	

In preparation of measurements of the elastic properties of Mg alloys (cf. contract GKSS – CAU Kiel 7.T1.00.G.01-HS1 ) at elevated temperatures, the orientation – dependent thermal expansion of AZ31 has been investigated in the temperature range from RT to 440 °C. Both thermal expansion and stresses caused by external load will cause shifts of the diffraction peaks and it may be necessary to correct for variations in temperature during the longer lasting uniaxial compression experiments to be made to determine diffraction elastic constants resp. Poisson’s ratios.

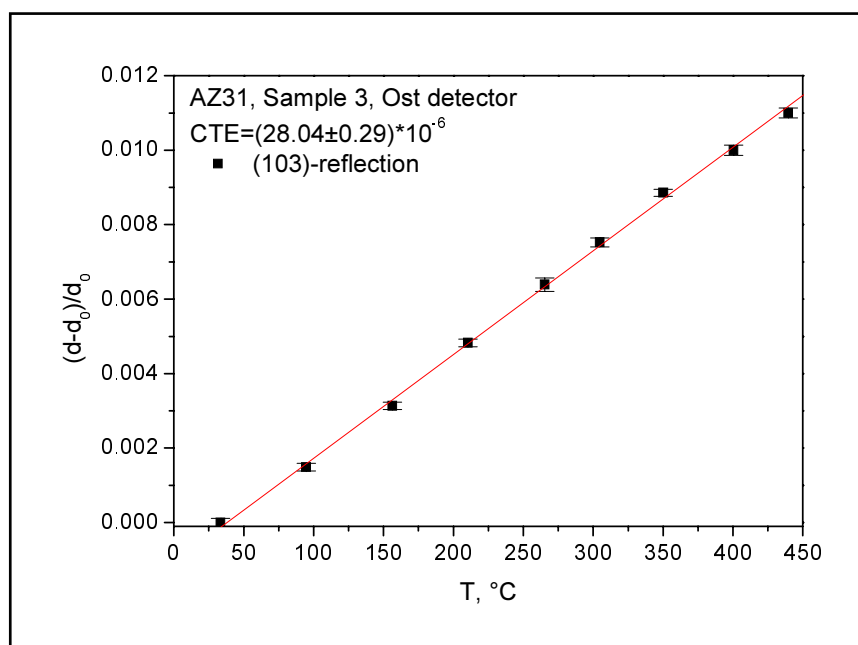


Figure 1: Thermal strain for the (103)-reflection in AZ31 Mg alloy as a typical example.

From the slope of curves like the one shown in figure 1, thermal expansion coefficients can be calculated. Error bars reflect the statistical accuracies of the diffraction peaks (weak or strong).

Results are shown in the following figure.

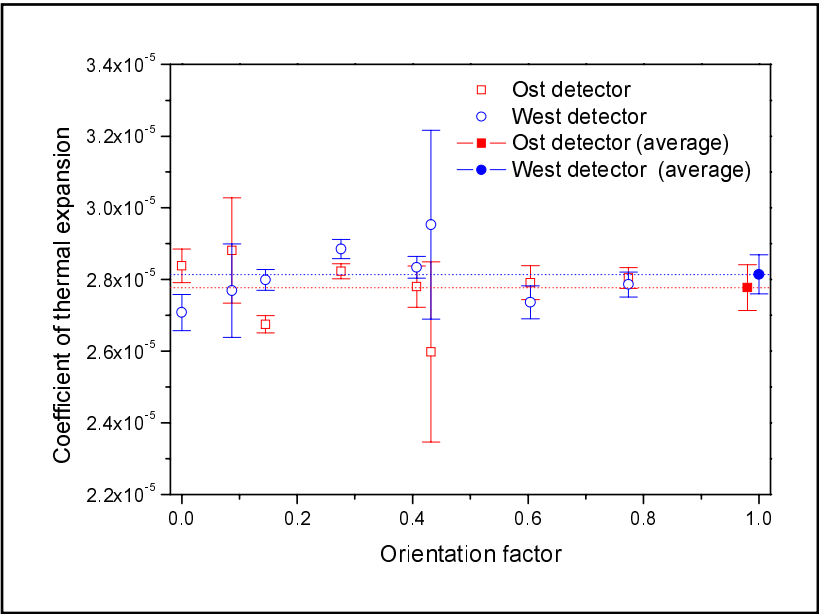



Figure 2: Orientation dependent linear thermal expansion coefficients for AZ 31.

	<b>EXPERIMENTAL REPORT</b>	<b>GeNF FSS</b>
<b>In-situ Investigation of Plastic Deformation by Neutrons and Positrons – a novel approach</b>		
<b>Principal Proposer:</b>	<b>Hans G. Priesmeyer<sup>1</sup></b> <sup>1</sup> Institut für Experimentelle und Angewandte Physik, Universität Kiel	
<b>Experimental Team:</b>	<b>Hans G. Priesmeyer<sup>1</sup>, Gizo Bokuchava<sup>1</sup> Bernd Witassek<sup>2</sup></b> <sup>1</sup> Institut für Experimentelle und Angewandte Physik, Universität Kiel <sup>2</sup> GKSS Research Centre, Geesthacht, - Health Physics Group	
<b>Date(s) of Experiment:</b>	November /December 2003	

### **In-situ Investigation of Plastic Deformation by Neutrons and Positrons**

When characterizing residual stresses by neutron diffraction, neutron absorption is always a competing process. It leads to the emission of high-energy, so-called prompt gamma radiation, which in turn produces positrons within the bulk of the specimen. The decay of these antiparticles and the resulting annihilation radiation are influenced by material properties like defects. Plastic deformation and the resulting increase of the dislocation density leads in the neutron scattering case to an increase in the mosaic width of the BRAGG reflections, while on the other hand the shape of the 511 keV annihilation radiation line has also changed measurably. Suitable collimation can assure that the information gathered by neutron diffraction comes from the same gauge volume as the information from positron annihilation. It is the aim of this project to investigate the correlation between the width of the BRAGG reflections and the S-parameter, by which the width of the annihilation line is described, as a function of the degree of plastic deformation. So more can be learned about a material, since during strain measurements by diffraction additional information is available through simultaneous gamma-ray spectroscopy.

The project has been started with investigations considering the stability of the data acquisition electronics and background reduction. As test positron emitter neutron-activated copper has proven to be successful. Figure 1 shows the experimental setup to detect the annihilation radiation, using an NaJ(Tl) integral line scintillation detector, which will be replaced by a HPGe detector in the actual measurements.

Test experiments (cf. Figure 2) have also been performed with a high-resolution HPGe detector. As positron emitters, pure annealed copper and GLIDCOP<sup>®</sup> (a copper MMC with Al<sub>2</sub>O<sub>3</sub> particle reinforcement) have been used after being activated by short term neutron irradiation.

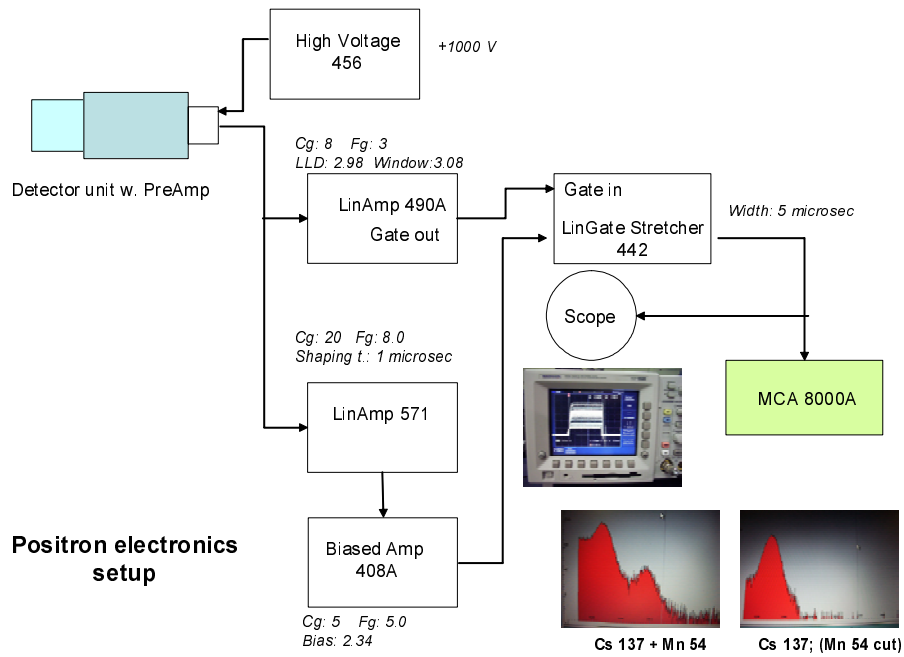


Figure 1: Electronic setup to cut off the contributions of gamma radiation with energies outside a defined range (511 keV). Further background reduction will be achieved by gamma-gamma coincidence.

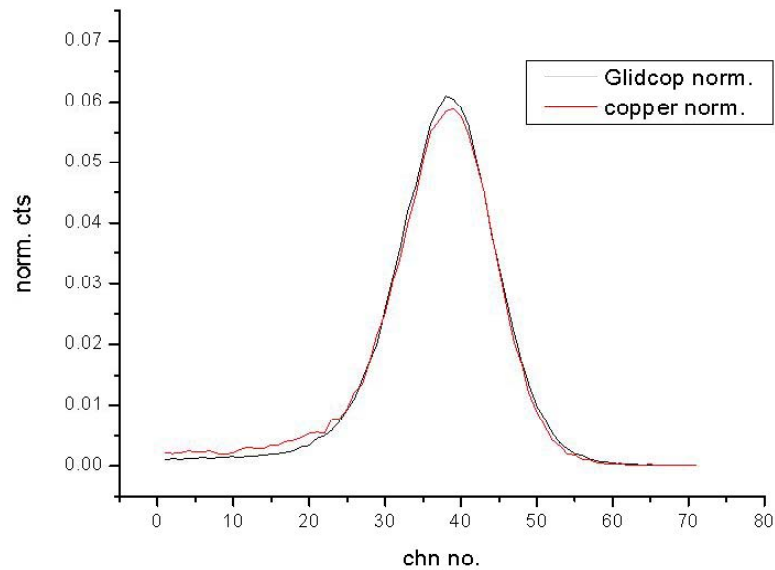



Figure 2: Difference in the shape parameter of the 511 keV annihilation spectra for Cu and GLIDCOP, measured with a HPGe detector.

This work is financed by GKSS and DFG project Pr267/13-1.

	<b>EXPERIMENTAL REPORT</b>	<b>GeNF FSS</b>
<b>Neutron TOF diffraction test experiments on reinforced materials</b>		
<b>Principal Proposer:</b>	<b>Anke Pyzalla<sup>1</sup></b> <sup>1</sup> Institut für Werkstoffkunde und Materialprüfung, TU Wien	
<b>Experimental Team:</b>	<b>Anke Pyzalla<sup>1</sup>, Hans G. Priesmeyer<sup>2</sup>, Gizo Bokuchava<sup>2</sup></b> <sup>1</sup> Institut für Werkstoffkunde und Materialprüfung, TU Wien <sup>2</sup> Institut für Experimentelle und Angewandte Physik, Universität Kiel	
<b>Date(s) of Experiment:</b>	December 2003	

### Neutron time-of-flight diffraction tests on carbon-fiber resp. $\text{Al}_2\text{O}_3$ loaded Mg and Al

Experiments aimed at strain measurements in multiphase materials are preferentially performed using high-resolution neutron time-of-flight spectroscopy. In order to prove the feasibility and to estimate measuring times, test experiments have been made at the FSS diffractometer on carbon – fiber resp.  $\text{Al}_2\text{O}_3$  loaded aluminium and magnesium alloys. The final goal of such investigations is to follow the degree of thermal stress relief in these metal matrix composites at temperatures up to 200 °C and to get information about the load transfer between matrix and fibers at room temperature by uniaxial compressive load experiments.

The following figures show a typical specimen in measuring position and first results, which still have to be analysed.

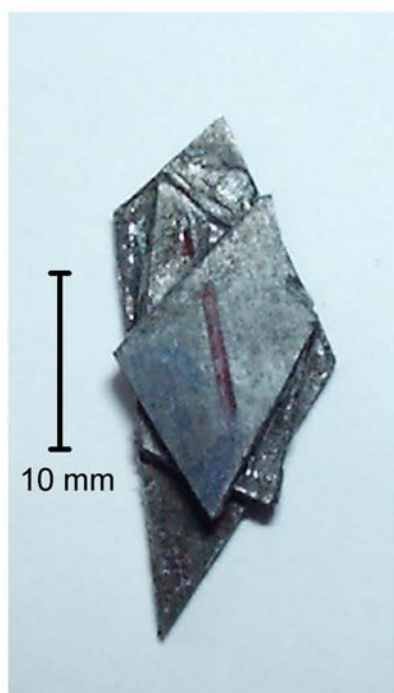


*Figure 1: Shape of a sample, composed of different cuttings, glued together.*

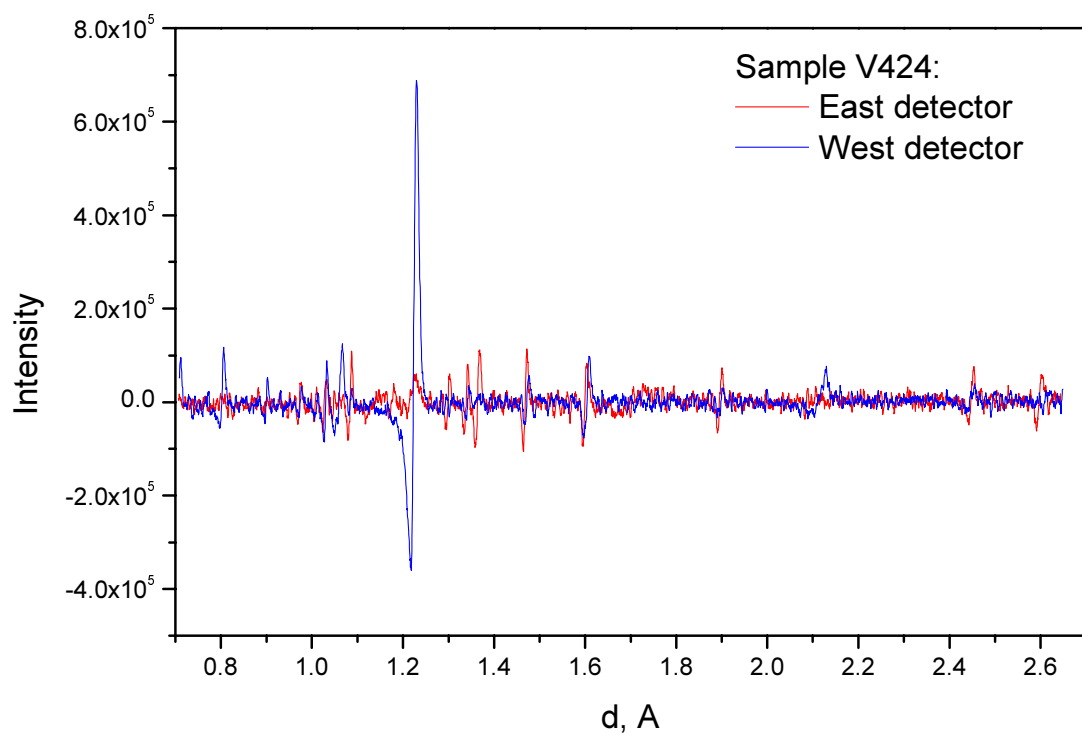


Figure 2: Neutron time-of-flight spectrum of V424 material (Mg + 0.6% Al + 70 Vol.% carbon fibers).

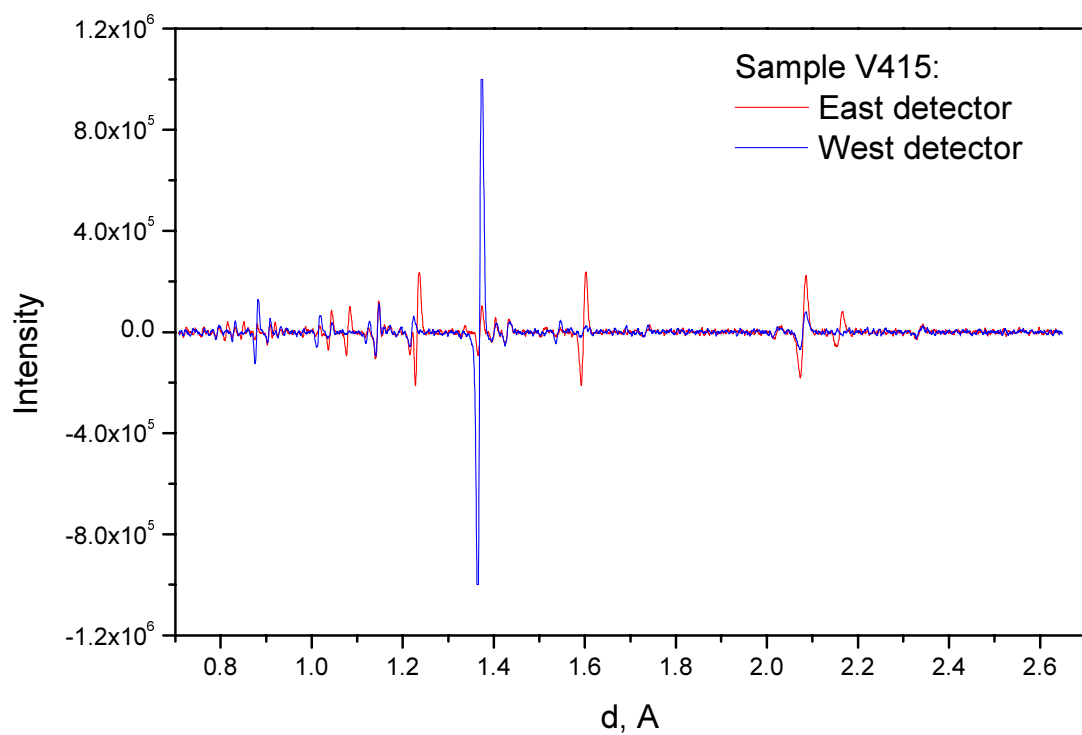


Figure 3: Neutron time-of-flight spectrum of V415 material (Al + 1 % Mg + 70 Vol.%  $\text{Al}_2\text{O}_3$ ).

	<b>EXPERIMENTAL REPORT</b>	<b>GeNF TEX-2</b>
<b>Neutron texture diffractometer TEX-2</b>		

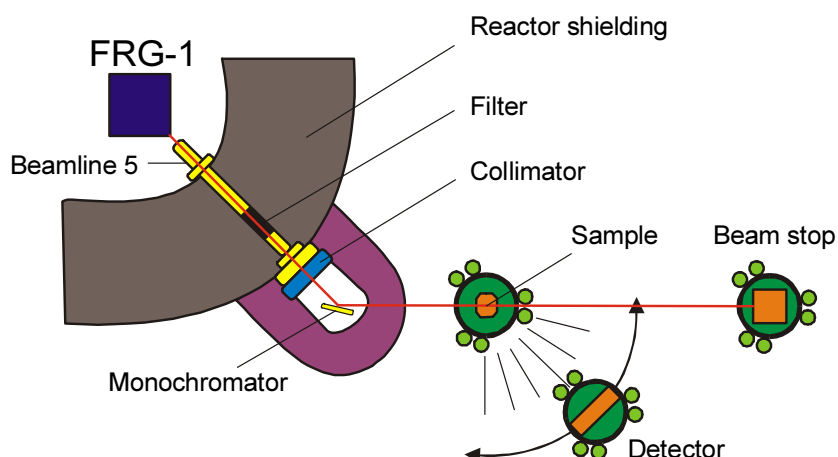
### Short Instrument Description:

The four circle neutron texture diffractometer is used to characterise textures in metallic, ceramic and geologic materials applying thermal, non-polarised neutrons.

### Local Contact:

Prof. Dr. Heinz-Günter Brokmeier  
Phone/Fax: +49 (0)4152 87–1207 / +49 (0)4152 87–1338  
e-mail: [brokmeier@gkss.de](mailto:brokmeier@gkss.de)

### Schematic View of TEX-2:




### Instrument Details:

Location at FRG-1:	beamline 5, thermal neutrons maximum beam cross section: 45 x 45 mm <sup>2</sup>
Primary collimation:	30', 42', 51'
Monochromator:	Cu (111), Cu (200), PG (002), Ge (311)
Take-off angle:	17.2°, 27.2°, 37.2°, 47.2°, 57.2°
Wavelength range:	$\lambda = 0.0\text{--}0.27$ nm (in steps)
Flux at sample position:	$\Phi = 0.3\text{--}2 \cdot 10^6$ cm <sup>-2</sup> s <sup>-1</sup>
Angular range	$\Phi$ : -360° to +360° X: -360° to +360° $\Omega$ : -46° to + 46° 2 $\Phi$ : -75° to +120°
Detector:	<sup>3</sup> He- single detector 38° JULIOS-PSD 2-D-pos. sensitive detector (active area 30 x 30 cm <sup>2</sup> )

**Instrument Details** (continued):

Sample geometries (standard):  (various):	cube 10 mm edge, sphere 15–20 mm Ø cylinder 10–15 mm Ø, 10–15 mm high e.g. wires, tubes, tensile samples
Distances: sample– <sup>3</sup> He detector sample–JULIOS	40–200 cm 70–100 cm
Sample environment:	mirror furnace up to 2000 K loading device: tension up to 15 kN, compression up to 20 kN sophisticated set of sample holders



	<b>EXPERIMENTAL REPORT</b>	<b>GeNF TEX-2</b>
<b>Global textures of thermomechanically processed TiAl</b>		
<b>Principal Proposer:</b>	<b>Werner Skrotzki, Guang-Hui Cao</b> Dresden University of Technology, Institute of Structural Physics, Division of Mtal Physics, D-01062 Dresden	
<b>Experimental Team:</b>	<b>Anke Günther, Heinz-Günter Brokmeier</b> Institut für Werkstoffkunde und Werkstofftechnik, TU Clausthal	
<b>Date(s) of Experiment:</b>	December 2002	

During hot-working of titanium aluminides dynamic recrystallization leads to a fine-grained microstructure. However, the mechanism of dynamic recrystallization, which is important for the workability of these advanced materials, is still not understood. In the research done the deformation of two-phase titanium aluminides ( $\text{TiAl} + \text{Ti}_3\text{Al}$ ) is carried out by high strain torsion under confining pressure at different temperatures, yielding a well-defined strain gradient from the center to the rim of the cylindrical samples. The evolution of the microstructure and texture with strain is studied by scanning and transmission electron microscopy (SEM, TEM) and local texture measurements by synchrotron radiation, respectively. Emphasis is put on the break-down of the lamellar structure leading to a globular ultrafine-grained microstructure, and on the crystallographic relationships between the TiAl and  $\text{Ti}_3\text{Al}$  phase. Moreover, mechanical twinning and dislocation slip is studied as a function of strain and temperature. These investigations yield detailed informations about the mechanism of dynamic recrystallization of titanium aluminides allowing a better understanding of their thermomechanical processing.

To get the starting texture of the four samples used for torsion tests neutron texture measurements have been done. The samples were of different origin (Plansee:  $\gamma$ -MET (A), GKSS:  $\gamma$ -TAB (B)) and had been processed differently. Therefore, they had different starting grain structures: coarse-grained lamellar type (A1 and B1) and fine-grained globular type (A2 and B2). Because of the different processing conditions during extrusion and annealing, the textures of the samples (Fig. 1) are different, too, and therefore represent a good selection of starting textures for the torsion tests. However, the textures are quite weak, except for A2.

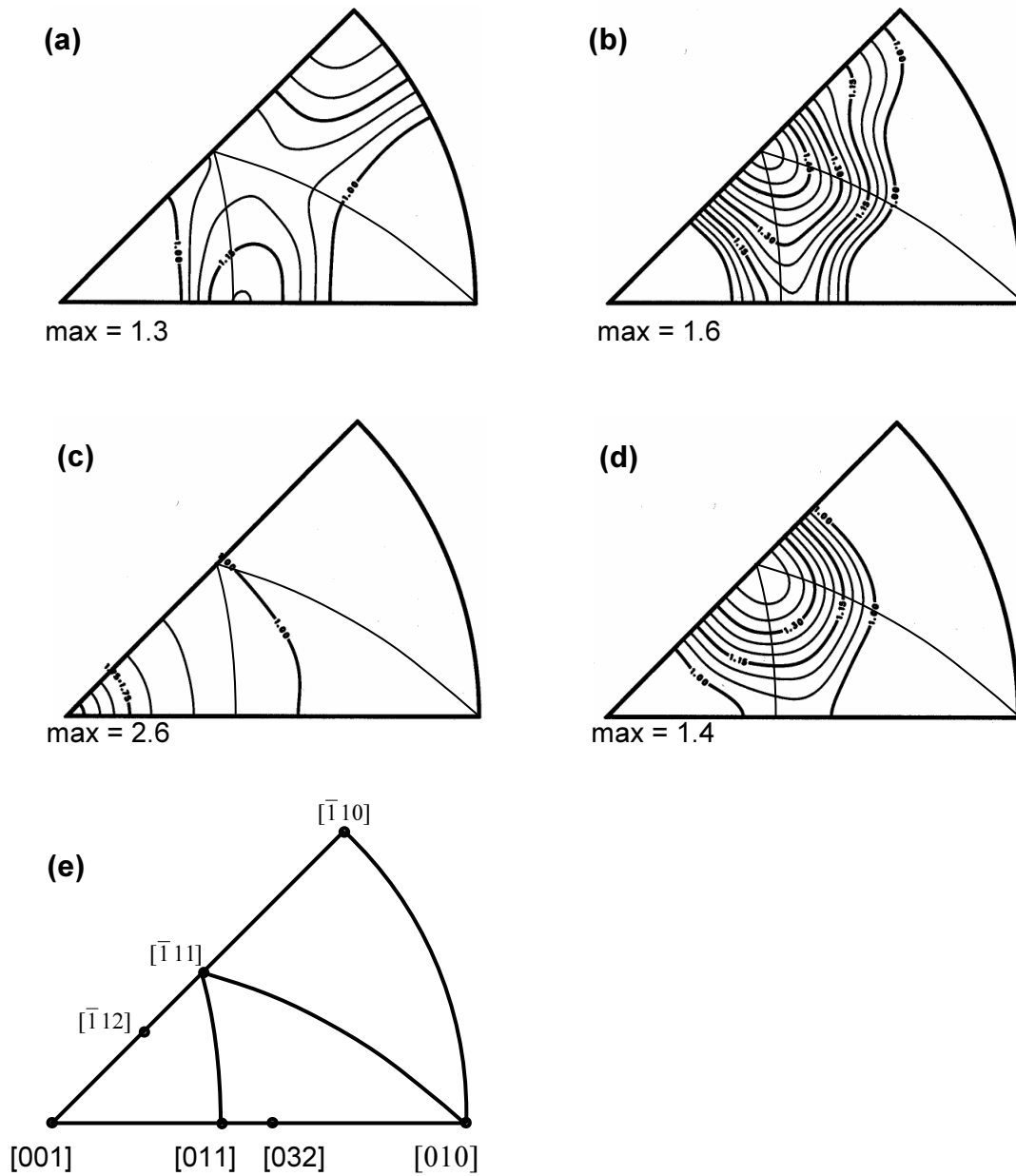



Figure 1: Inverse pole figures of the extrusion direction of TiAl of different two-phase titanium aluminides. Intensities are given in multiples of a random distribution, m.r.d.:

- (a) A1: Extrusion (71/1) at 1000 °C and annealing at 1340 °C for 2 h
- (b) B1: Extrusion (7/1) at 1380 °C
- (c) A2: Extrusion (71/1) at 1000 °C
- (d) B2: Extrusion (7/1) at 1250 °C and annealing at 1030 °C for 2 h
- (e) Orientation triangle showing the relevant crystal directions.

	<b>EXPERIMENTAL REPORT</b>	<b>GeNF TEX-2</b>
<b>Correlation between the phyllosilicate preferred orientation, low and high-field magnetic anisotropy</b>		
<b>Principal Proposer:</b>	<b>Martin Chadima</b> Masaryk University, Brno, Czech Republic	
<b>Experimental Team:</b>	<b>Martin Chadima, Anke Günther<sup>1</sup></b> <sup>1</sup> Institut für Werkstoffkunde und Werkstofftechnik, TU Clausthal	
<b>Date(s) of Experiment:</b>	February, April 2003	

### Experimental objectives

The neutron texture goniometry was used to analyse the phyllosilicate preferred orientation of the selected mudstone and greywacke samples from the easternmost Rhenohercynian Zone of the Bohemian Massif. The method was combined with anisotropy of magnetic susceptibility (AMS) and high-field anisotropy (HFA) measured at Agico, Inc., Brno, Czech Republic, and the Palaeomagnetic laboratory, Institute of Geophysics, ETH, Zürich, Switzerland, respectively. The combination of these techniques provides a better insight into the control of the magnetic fabric and enables us to establish a quantitative correlation between magnetic anisotropy and phyllosilicate preferred orientation.

### Calculation of theoretical anisotropy

In order to compare the preferred orientation of phyllosilicates to the measured AMS and HFA, the orientation tensor of phyllosilicate (001) planes was calculated. The principal values of the theoretical AMS were calculated from the principal values of the orientation tensor [1].

### Qualitative correlation

The neutron diffraction shows that chlorite and biotite are dominant phyllosilicate minerals in the rock composition. In most cases, the principal directions of the AMS, high-field paramagnetic component (HFP), and the orientation tensor derived from chlorite *c*-axes are subparallel (Figure 1). No systematic deviation of paramagnetic fabric from whole-rock magnetic fabric can be observed.

### Quantitative correlation

Results are presented in terms of the standard deviatoric susceptibility  $k'$  [2] and the difference shape factor  $U$  [3] (Figure 2).

The standard deviatoric susceptibility enables comparisons of the degrees of chlorite anisotropy, paramagnetic and whole-rock anisotropy. Each of the three possible correlations has very high correlation coefficient,  $R > 0.95$ , implying nearly the same degree of anisotropy for all the employed methods. It is evident that the chlorite anisotropy reasonably represents the whole-rock anisotropy. This fact further supports the assumption that chlorite is the dominant control of magnetic fabric.

The correlations of the shapes of all investigated anisotropies show more significant scatters compared to the degree of anisotropy. Despite this dispersion, the prolate and oblate shapes still remain to be well defined. It seems that the most noticeable differences from one-to-one relationship can be observed for the samples with the lowest anisotropy where the shape is poorly defined. As the range of chlorite anisotropy shapes is similarly wide as that of AMS it seems that the HFP is less sensitive to the shape variability than AMS.

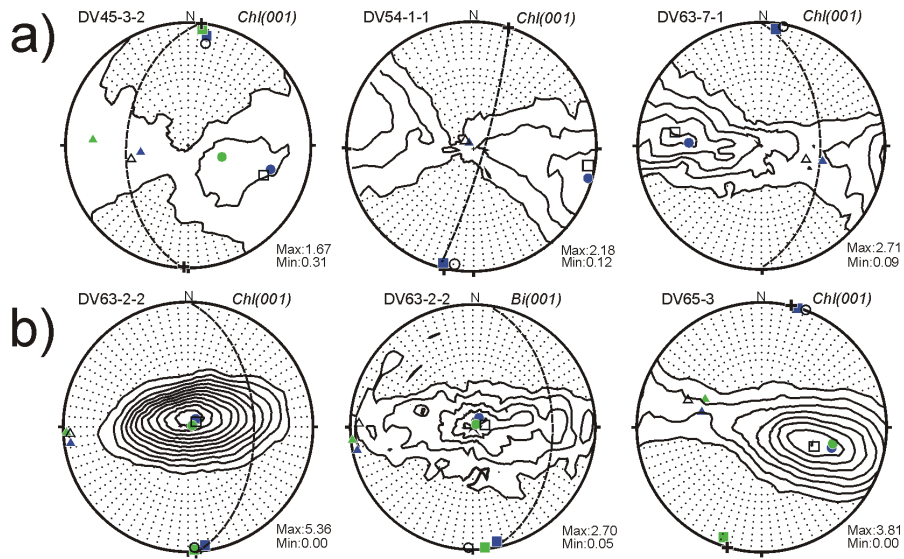


Figure 1:

Examples of pole figures of the chlorite (001) or biotite (001), denoted as *Chl(001)* or *Bi(001)*, respectively. Plots are contoured in multiples of random distribution (m.r.d.), contour interval is 0.4 m.r.d. Maximum and minimum intensity values are in the lower right of each plot. The principal directions of the orientation tensor, HFP tensor and AMS tensor are represented with open, grey, and black symbols, respectively. Squares, triangles, and circles represent the maximum, intermediate and minimum directions, respectively. The great circle represents the cleavage plane, crosses represent either strike of bedding, bedding-cleavage intersection or fold axis.

a) greywacke samples, b) mudstone samples.

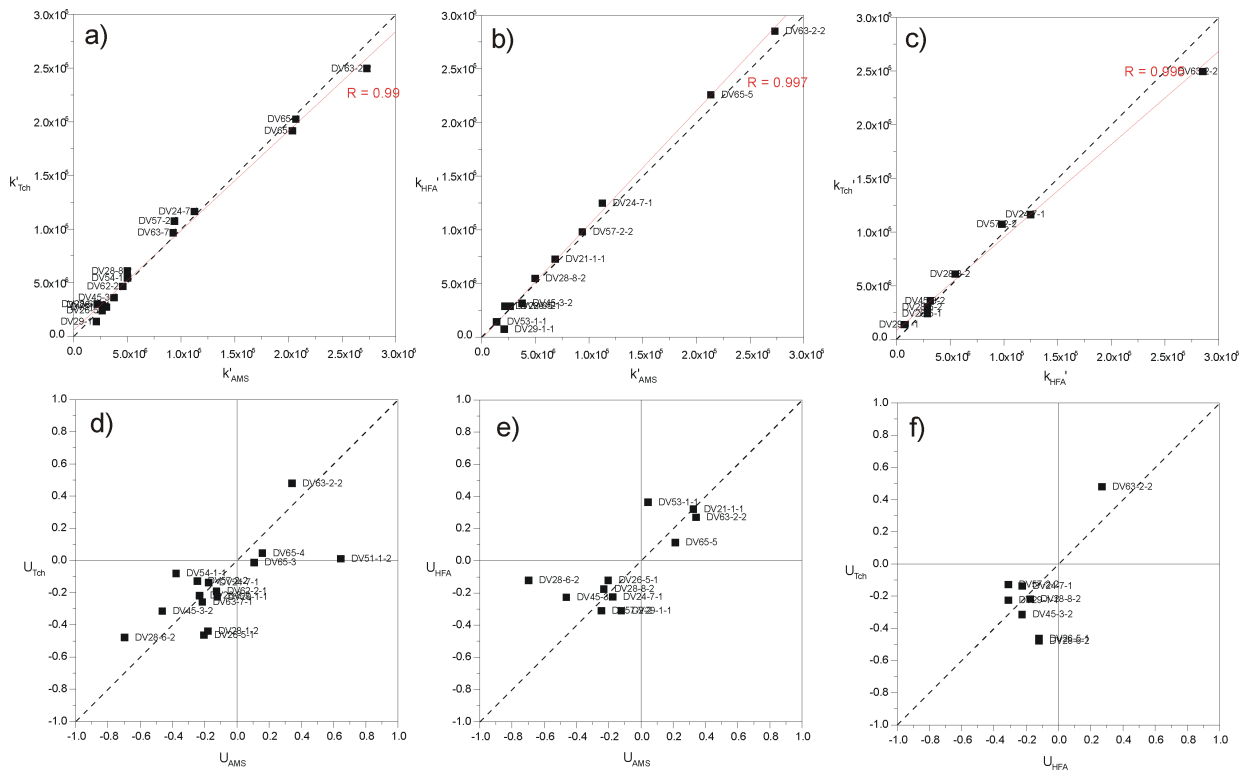



Figure 2:

- Correlation between the theoretical standard deviatoric susceptibility calculated from chlorite *c*-axis distribution ( $k'_{Tch}$ ) and the standard deviatoric susceptibility of AMS ( $k'_{AMS}$ )
  - Correlation between the standard deviatoric susceptibility of HFP ( $k'_{HFP}$ ) and the standard deviatoric susceptibility of the AMS ( $k'_{AMS}$ )
  - Correlation between the theoretical standard deviatoric susceptibility ( $k'_{Tch}$ ) and the standard deviatoric susceptibility of HFP ( $k'_{HFP}$ )
- Linear regression line and correlation coefficient is added.
- Correlation between the theoretical shape parameter ( $U_{Tch}$ ) calculated from chlorite *c*-axis distribution and the shape parameter of AMS ( $U_{AMS}$ )
  - Correlation between the shape of HFP ( $U_{HFP}$ ) and the shape parameter of the AMS ( $U_{AMS}$ )
  - Correlation between the theoretical shape parameter ( $U_{Tch}$ ) and the shape of HFP ( $U_{HFP}$ ).

## References

- [1] Hrouda, F., Schulmann, K. 1990. Conversion of magnetic susceptibility tensor into orientation tensor in some rocks. *Phys. Earth Planet. Inter.*, 63, 71–77.
- [2] Jelínek, V. 1984. On a mixed quadratic invariant of the magnetic susceptibility tensor. *J. Geophys.*, 56, 58–60
- [3] Jelínek, V. 1981. Characterization of the magnetic fabric of rocks. *Tectonophysics*, 79, T63–T67



	<b>EXPERIMENTAL REPORT</b>	<b>GeNF TEX-2</b>
<b>Microstructure Characterization of extruded magnesium profiles</b>		
<b>Principal Proposer:</b>	<b>Sören Müller<sup>1</sup></b> <sup>1</sup> Institut für Werkstoffwissenschaften und -technologien, TU Berlin	
<b>Experimental Team:</b>	<b>Sören Müller<sup>1</sup>, Sangbong Yi<sup>2</sup>, Bernd Schwebke<sup>2</sup>, Heinz-Günter Brokmeier<sup>2</sup></b> <sup>2</sup> Institut für Werkstoffkunde und Werkstofftechnik, TU Clausthal	
<b>Date(s) of Experiment:</b>	March, May, June 2003	

## Introduction



Extruded magnesium profiles have an enormous potential for the lightweight construction in the automobile- and airline industry. With its density of  $\rho_{\text{Mg}} \sim 1.8 \text{ g/cm}^3$  magnesium is the lightest metall that can be used as a construction material ( $\rho_{\text{St}} \sim 7.8 \text{ g/cm}^3$ ;  $\rho_{\text{Al}} \sim 2.7 \text{ g/cm}^3$ ). But despite that fact the usage of extruded magesium products is very rare compared to cast magnesium alloys.

Magnesium wrought-alloys are principally extrudable. In contrast to the cubic face centered (fcc) crystal lattice of aluminium is the crystal lattice of magnesium hexagonal closed packed (hcp). That implies considerable differences in the deformation behavior of aluminium and magnesium. During the extrusion process of magnesium textures and deformation twins are occuring which are influencing the process itself (high peak force) as well as the mechanical properties of the product (assymetry under tensile and compressive load). The intensified usage of extruded magnesium products will depend on the possibiltiy to lower the peak force and increase the yield point under compression as well as the realization of product rates that can be compared to those of Al-alloys.

## Extrusion trials

Continuous casted billets of the magnesium alloys AZ31 and AZ61 with a diameter of 107 mm were used. For the extrusion the billets were heated up to 300 °C in an induction furnace. The container and die temperature were 300 °C also. As shown in following table the process parameters product rate, product shape and the cooling of the product were varied.

Table 1: Extrusion conditions.

Product Shape				
Die	Ø 20 mm			
Container	110 mm	110 mm	110 mm	110 mm
Extrusion Ratio	30:1	29:1	16:1	33:1
Alloy	AZ31, AZ61	AZ31	AZ31	AZ31
Product Rate	0,9 m/min, 27 m/min, 63 m/min	0,9 m/min, 27 m/min	28 m/min	1,4 m/min
Cooling	Air, Water	Air	Air	Air
Other		Moving Mandrel	Moving Mandrel	

## Texture analysis

The texture analyses of the different profiles and the casted billets were performed at the Beamline TEX-2 at the research reactor of the GKSS. Figure 1 shows that the casted billets do not exhibit any texture in the 0002-direction. As a result of the extrusion process the materials shows a strong fibre texture afterwards (Figure 2).

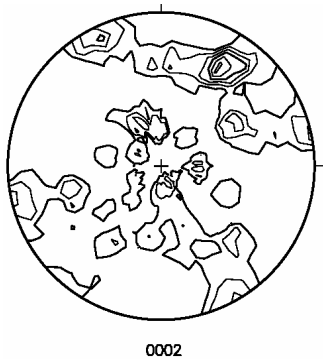


Figure 1: Pole figure of the casted billet.

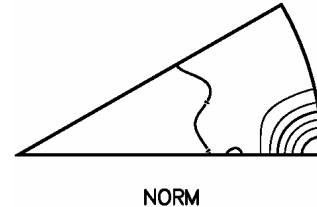


Figure 2: Inverse Pole figure of the rod.

The texture analysis of the U-shaped profile shows a dependence of the texture on the position in the profile. Thereby the basal planes in the side walls with a thickness of 4 mm are oriented perpendicularly to the extrusion- and transverse-direction (Figure 3). On the other hand the basal planes in the basis with a thickness of 2 mm are centered to the extrusion direction (Figure 4).

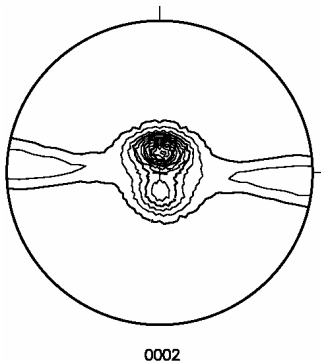


Figure 3: Pole figure of the side wall (4 mm).

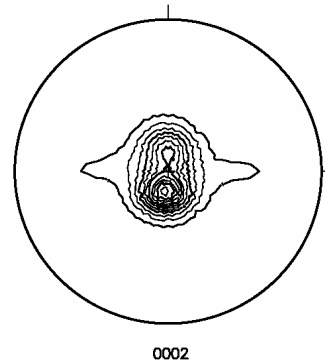


Figure 4: Pole figure of the basis (2 mm).

As observable of Table 1 the extruded tubes differ in their wall thickness. These are 2 and 4 mm. These dimensions were chosen to ensure the comparability of the tubes with the U-shaped profile. The pole figures of the texture analysis of the basal plane show a shearing fraction which is due to the production process (extrusion with a moving mandrel). This shearing fraction decreases with an increasing all thickness. This can be observed in Figure 5 (tube with 2 mm wall thickness) and Figure 6 (tube with 4 mm wall thickness).

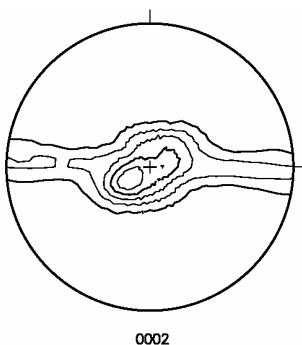


Figure 5: Pole figure, tube 2 mm thickness.

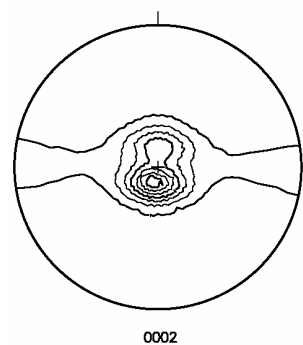



Figure 6: Pole figure, tube 4 mm thickness.



	<b>EXPERIMENTAL REPORT</b>	<b>GeNF TEX-2</b>
<b>Global textures of ECAP deformed fcc metals</b>		
<b>Principal Proposer:</b>	<b>Werner Skrotzki, Nils Scheerbaum</b> Dresden University of Technology, Institute of Structural Physics, Division of Metal Physics, D-01062 Dresden	
<b>Experimental Team:</b>	<b>Anke Günther, Heinz-Günter Brokmeier</b> Institut für Werkstoffkunde und Werkstofftechnik, TU Clausthal	
<b>Date(s) of Experiment:</b>	March – May 2003	

ECAP is one of the promising techniques for grain refinement to micron, submicron or in some cases up to nanometer size. In this process, a billet is deformed in a narrow deformation zone at the plane of intersection of two die channels of equal area cross-section and the strain mode approximates closely to simple shear (Figure 1). As the overall billet geometry remains nearly constant during ECAP, multiple passes through the die are possible without any reduction in cross-sectional area. This allows materials to be deformed to very high plastic strains that cannot be readily obtained in more conventional processes, such as rolling. Large plastic deformation results in the development of texture, which will be demonstrated here for different face-centred cubic (fcc) metals: Al, Cu, Ag.

The materials used were received in the form of extruded bars. The purity of the metals was: Al 5N, Cu 4N and Ag 3N. Prior to ECAP, the as-received material was annealed for 1h at 200 °C and 300 °C in the case of Al and Cu, Ag, respectively, in order to obtain a strain-free microstructure with equiaxed grains of the order of 100 µm grain size. The specimens with 10 mm x 10 mm square cross section and 100 mm length were machined from these annealed bars. ECAP was carried out at a crosshead speed of 1 mms<sup>-1</sup> at room temperature using a Zwick 200 kN screw driven machine and a die set with rectangular intersection of the extrusion channels without any rounding of the corner region. The specimens were extruded in series. Exiting the die they showed more and more sheared shape, as if they were sheared on the ND plane in the direction of ED. The number of ECAP passes was limited to 3. Between individual passes the specimen was introduced in the same sense (route A, that is no rotation around the specimen longitudinal axis between intermediate passes).

Neutron texture measurements were done on a cube of 10 mm x 10 mm x 10mm taken from the middle part of the extruded bar. The results are presented in Figure 2 in the form of (111) pole figures. While Al already recrystallized during ECAP the textures of Cu and Ag represent deformation textures. It is obvious that the shear process during ECAP produces a characteristic type of texture, which not only depends on recrystallization but also on the stacking fault energy, as is seen by comparison of Cu and Ag. A detailed analysis of the texture components is in process.

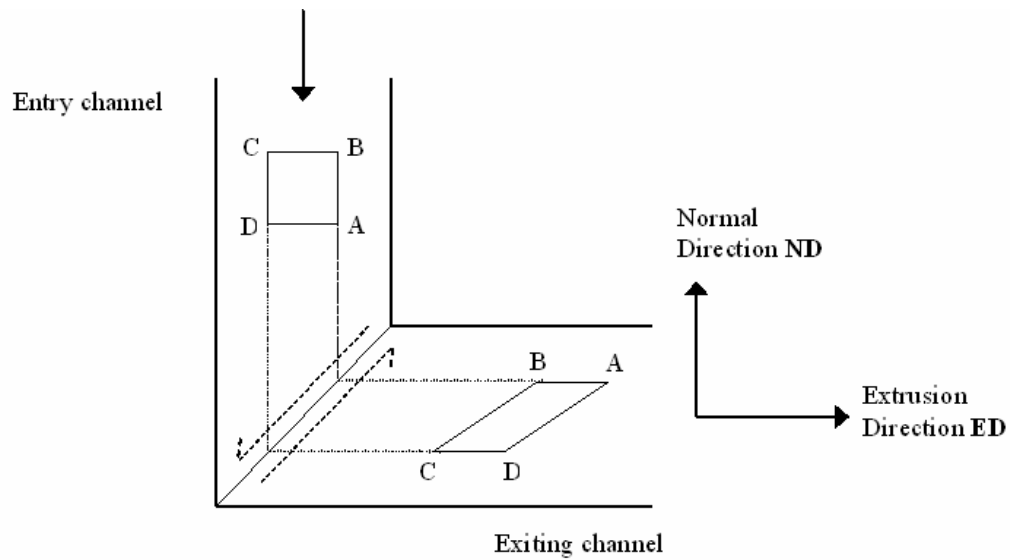


Figure 1: Simple shear model of ECAP testing.

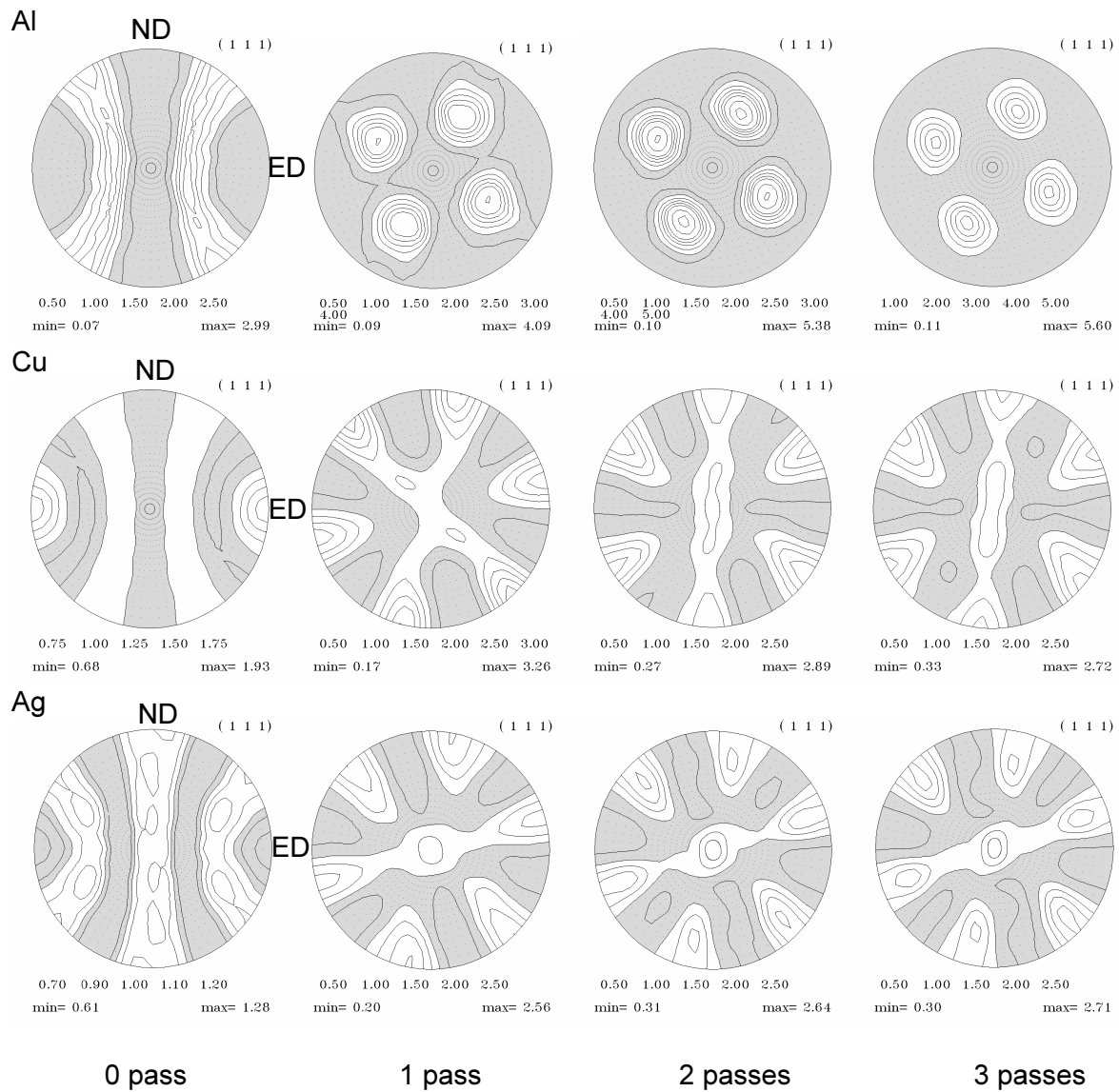



Figure 2: (111) pole figures of fcc metals deformed by ECAP.

	<b>EXPERIMENTAL REPORT</b>	<b>GeNF TEX-2</b>
<b>Texture Investigation and the Physical Modelling of the Graphite Texture Forming. Part 1</b>		
<b>Principal Proposer:</b>	<b>Tatiana Lychagina<sup>1</sup>, Dmitry Nikolayev<sup>1</sup></b> <sup>1</sup> Frank Laboratory of Neutron Physics, JINR, Dubna, Russia	
<b>Experimental Team:</b>	<b>Tatiana Lychagina<sup>1</sup>, Dmitry Nikolayev<sup>1</sup>, Sangbong Yi<sup>2</sup>, Heinz-Günter Brokmeier<sup>2</sup></b> <sup>2</sup> Institut für Werkstoffkunde und Werkstofftechnik, TU Clausthal	
<b>Date(s) of Experiment:</b>	April 2003	

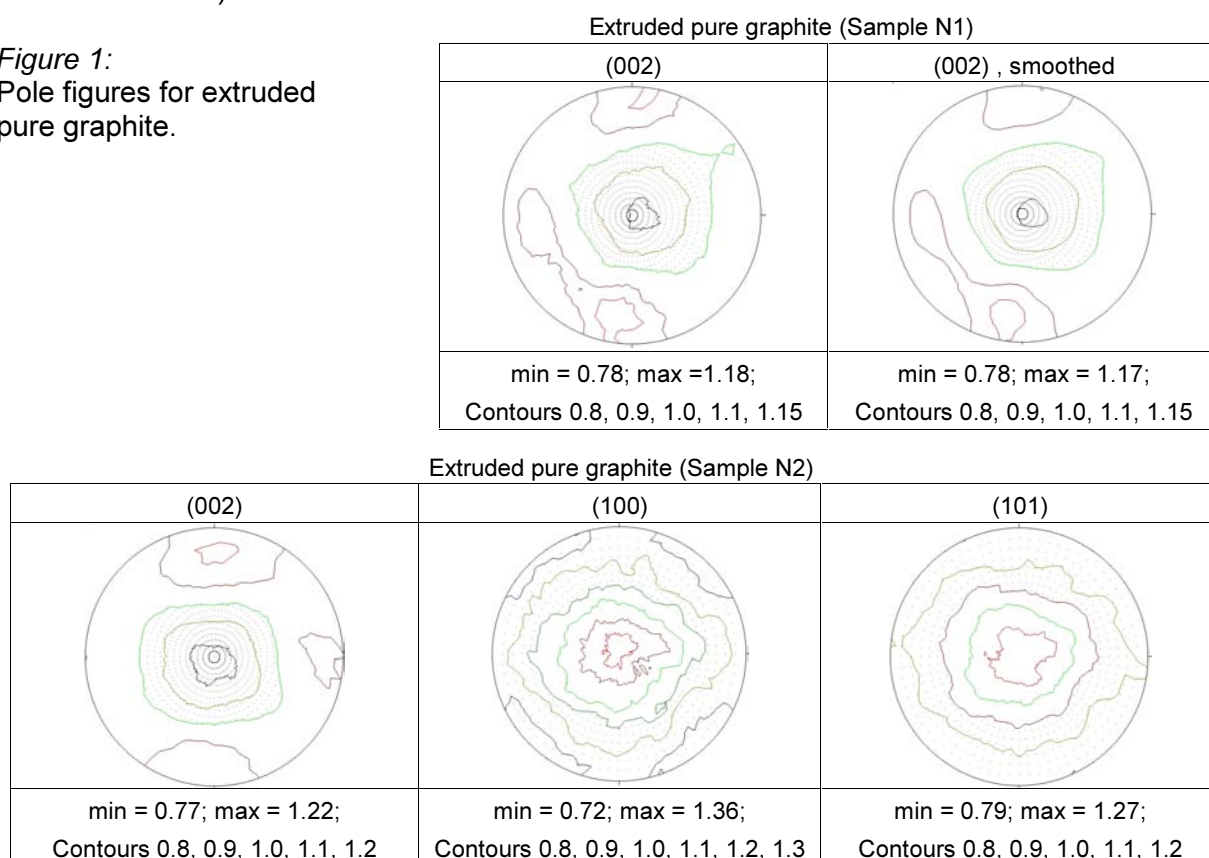
## Motivation

Graphite is one of the widespread and applicable materials. The main application of graphite is for reactor's moderators. It was established that reactor graphite has high anisotropic mechanical properties and it was implied that it was caused by texture formed during extrusion. However, the measurements of several graphite samples made at SKAT spectrometer (JINR, Dubna) discovered the unusual behavior of these samples. Actually, samples cut from a block obtained by 30 % extrusion have almost no texture. These examples hint that texture forming in graphite may be different from the other hexagonal materials. The main goal of the project is to study of graphite texture forming by physical modeling using neutron facility at GKSS (Dubna's reactor is shut down now for about one year).

## Experimental

First, the texture measurements for two graphite samples were carried out at TEX-2 (GKSS Research Centre).

*Figure 1:*  
Pole figures for extruded pure graphite.



As can be seen from the Figure 1 the 30 % extruded pure graphite is texture free. Then it was measured the texture of SiC sample to observe the texture sharpness, that is possible for graphite. As can be seen from the Figure 2, this sample has rather strong texture (about 7 mrd in maximum of PF (002)).

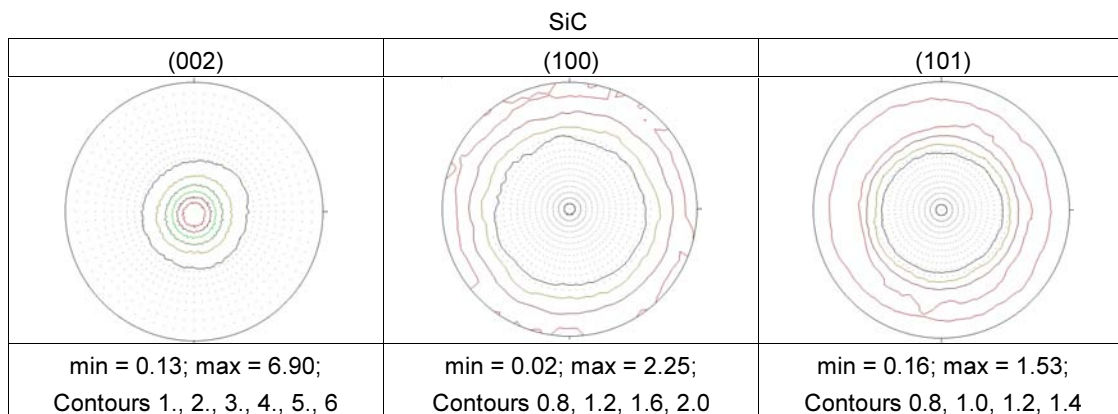


Figure 2: Pole figures of sample SiC (Si ? %, C ? %).

Then texture of graphite powder with grain size 50  $\mu\text{m}$  was measured. As can be seen from the Figure 3, the graphite powder has “texture” of the approximately same sharpness as has extruded reactor graphite (see Fig. 1).

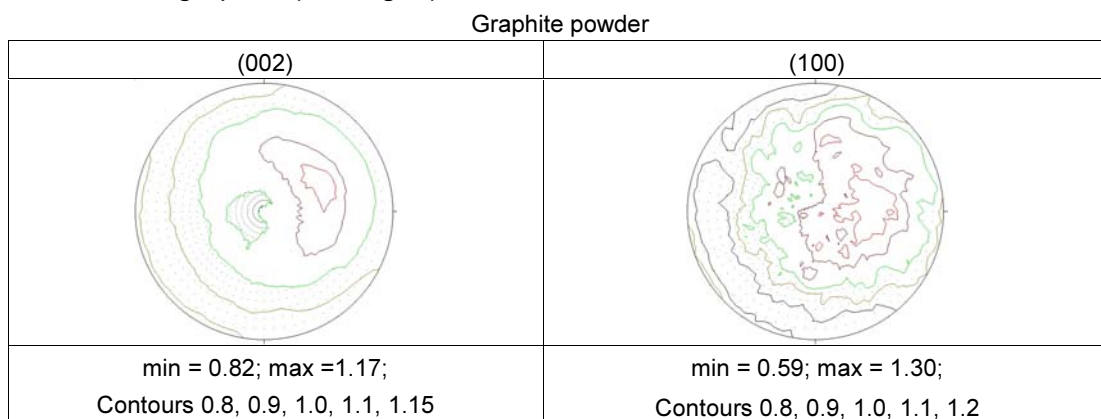


Figure 3: Pole figures of graphite powder (50  $\mu\text{m}$ ).

Then texture measurements were carried out after 50 % compaction of same graphite powder (see Figure 4). As can be seen from the Fig. 4, the graphite powder has texture with maximum about 2.2 mrd at PF(002). In future, it seems very interesting to investigate grain size influence on graphite texture forming.

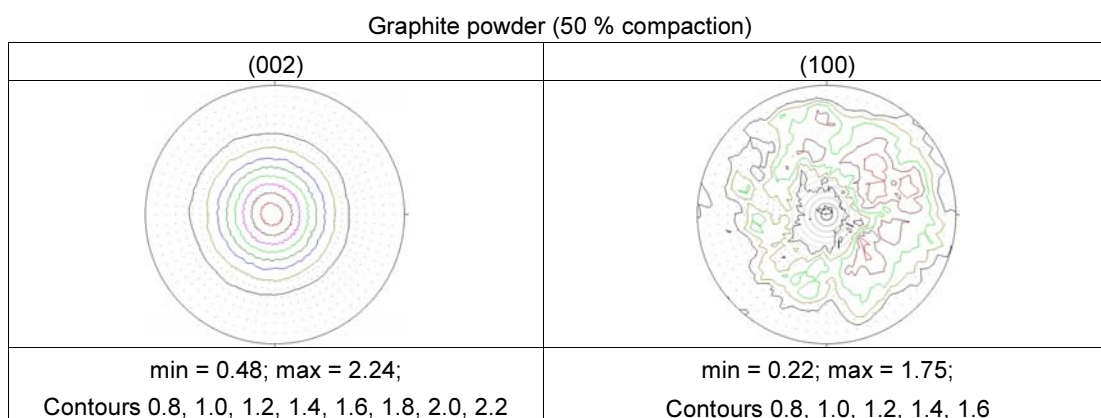



Figure 4: Pole figures of graphite powder (50  $\mu\text{m}$ ) after 50 % compaction.

	<b>EXPERIMENTAL REPORT</b>	<b>GeNF TEX-2</b>
<b>Microstructure Characterization of extruded magnesium profiles</b>		
<b>Principal Proposer:</b>	<b>Joachim Konrad, Stefan Zaefferer, Dierk Raabe</b> Max-Planck-Institut für Eisenforschung, Düsseldorf	
<b>Experimental Team:</b>	<b>Anke Günther, Heinz-Günter Brokmeier</b> Institut für Werkstoffkunde und Werkstofftechnik, TU Clausthal	
<b>Date(s) of Experiment:</b>	April – June 2003	

## Introduction

Sheet material of alloys based on the intermetallic  $\text{Fe}_3\text{Al}$  phase is promising material for high temperature application. They are produced from a cast ingot by thermomechanical processing. During the whole process the material exhibits a rather inhomogeneous microstructure and texture. The recrystallized material shows large elongated grains of rotated cube  $\{001\}<110>$  texture component which are surrounded by small equiaxed grains of typical recrystallized rolling texture (Kobayashi et al. Proc. ICSMA13, 2003).

The rotated cube component is inherited from the cast material because it is stable during rolling as well as during recrystallization. Controlling the crystallographic texture of the as cast  $\text{Fe}_3\text{Al}$  alloy may thus be an adequate method to optimize the microstructure and texture of the final sheet material. Due to the large grain size of  $\text{Fe}_3\text{Al}$  cast alloys conventional techniques of crystallographic texture analysis by x-ray or electron diffraction techniques show a lack of statistical confidence because of limited sample areas and small number of grains analyzed. Texture analysis by neutron scattering provides a better statistical confidence because of the high penetration power of neutrons which allows to investigate the texture of large bulk samples providing an order of magnitude higher number of analyzed grains. The texture measurements were accomplished in a cooperative work with the neutron texture diffractometer TEX-2 team at the FRG-1 neutron source of GKSS.

## Experimental

The binary  $\text{Fe}_3\text{Al}$  alloy (26 at.% Al) was produced in a vacuum induction furnace and cast under vacuum into a cold copper mould that was placed on a massive copper base. The ingot had the dimension of  $87 \times 30 \times 205 \text{ mm}^3$ .

Micrographs of the sampling sites were prepared by grinding, polishing and etching to give an overview of the grain structure. Sample cubes of the dimension  $10 \text{ mm}^3$  were cut from sites representing typical areas of the cast microstructure. The positions are indicated in Figures 1 and 2.

The texture of the samples was investigated by measuring the (111), (200) and (220) pole figures using the TEX-2 neutron diffractometer at the FRG-1 neutron source.

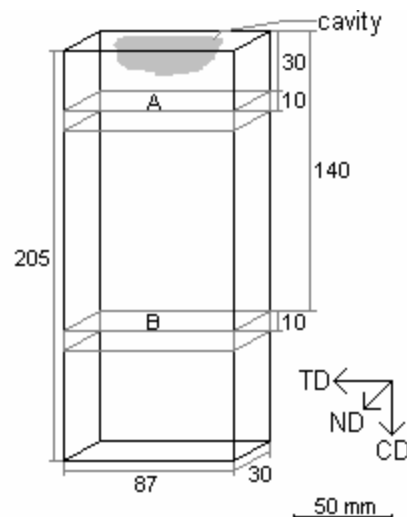


Figure 1: Sampling sites A and B.

## Results

The micrographs in Figure 2 show the two sections of the ingot. The grain structure in the upper part of the ingot reveals mainly two zones with different grain morphologies: A zone of 5 to 10 mm thickness built up by columnar crystallites that grew radially from the walls towards the center (a) and a large area of medium sized globular crystallites in the center (b). In the lower part this large central area does not appear. Besides small deranged areas (b) the columnar area occupies almost the whole visible sample plane.

The results of the texture analysis are also shown in Fig. 2 in form of (111) and (200) pole figures. In cut A the areas 2 and 4 show clear  $\langle 100 \rangle$  fiber textures with the fiber axes lying parallel to the long axis of the crystals in these areas. Sample A3 consisting of grains with circular intersections shows an almost random texture. However, also here a slight  $\langle 100 \rangle$  fiber texture with the fiber axis parallel to the cast direction is visible. In the lower part of the cast block, cut B, the samples 2 and 3 show a  $\langle 100 \rangle$  fiber textures with the fiber axis parallel to the growth direction. In contrast, sample B4 reveals a strong cube texture  $\{001\}\langle 100 \rangle$ .

## Discussion

The observed textures can be assigned to the respective grain morphologies. The longitudinal axis of the columnar grains correspond in all cases to the  $\langle 100 \rangle$  fiber axis of the texture. Columnar grains emerge from the sites of preferred nucleation at the cold mould walls and grow into the direction of the highest temperature gradient. The fact that this preferred growth direction coincides with the  $\langle 100 \rangle$  direction of the crystals shows that  $\langle 100 \rangle$  is the direction of highest growth rate in this material. The texture can thus be interpreted in terms of a growth selection process: Random nucleation takes place at the mould walls. This is visible from the high number of smaller grains immediately at the walls. During the subsequent solidification a selective growth of grains having their  $\langle 100 \rangle$  crystal direction parallel to the highest temperature gradient occurs. In the lower part of the cast block the heat flux is sufficient for an almost complete directional solidification. In the case of sample B4 the heat flux from both sides superimposes thus creating two preferred growth directions resulting in the cube texture of this sample. For the upper part the resulting cooling rate is lower and parts of the melt in the centre of the mould crystallize by nucleation in the melt and grow almost undirected. However, the slight  $\langle 100 \rangle$  fiber texture indicates that also here a preferred temperature gradient exists in casting direction.

The cooling conditions generated by casting into a cold copper mould lead to an inhomogeneous grain structure and a pronounced crystallographic texture. The microstructure and texture is governed by preferred  $\langle 100 \rangle$  crystal growth into the directions of highest heat flux at different positions in the mould. If the cast material is subsequently rolled in casting direction the solidification texture provides a strong rotated cube component for the start material which is inherited through the different process steps all the way into the final material.



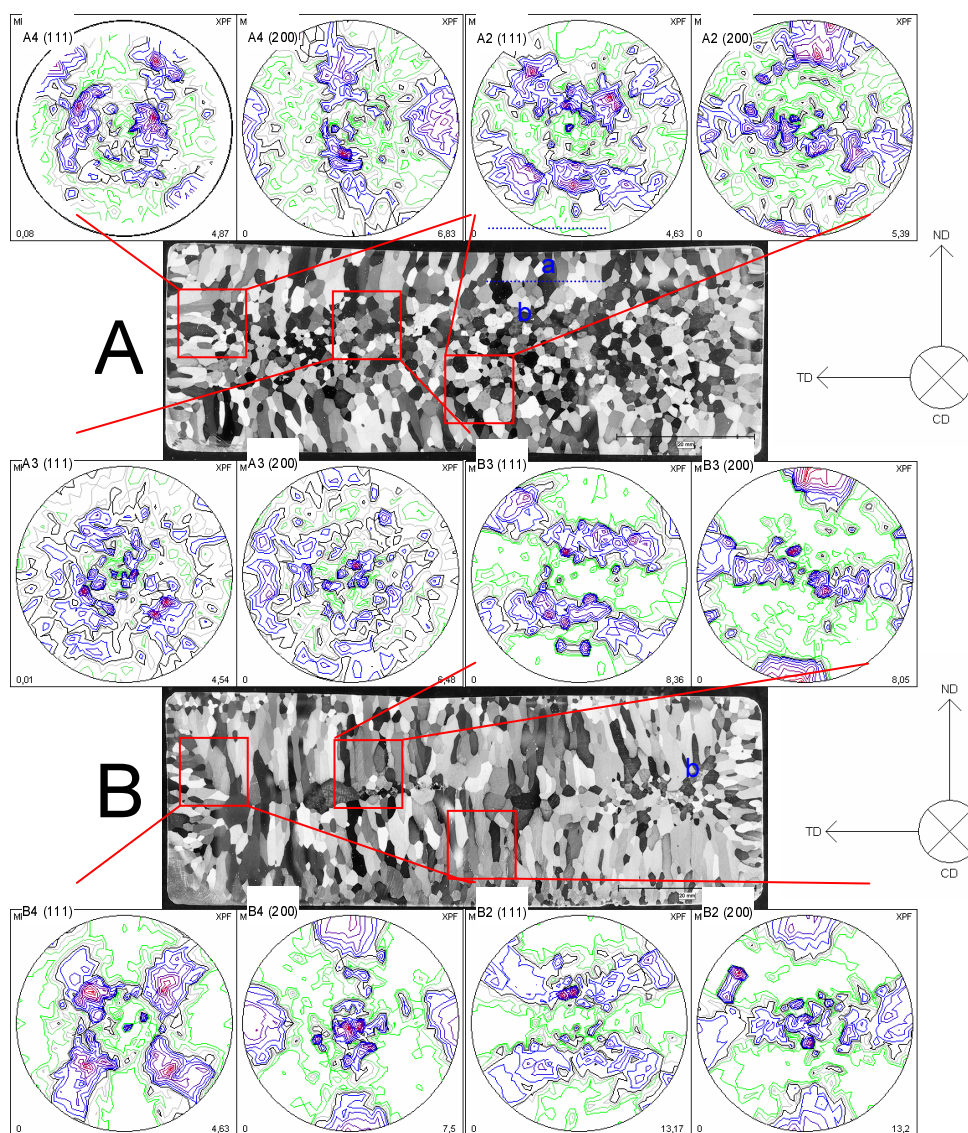



Figure 2: Pole figures and corresponding micrographs of the sample sites (samples are 1 cm<sup>3</sup> cubes).





	<b>EXPERIMENTAL REPORT</b>	<b>GeNF TEX-2</b>
<b>The texture variations of AZ31 magnesium alloy during tensile tests at different temperatures</b>		
<b>Principal Proposer:</b>	<b>Sangbong Yi<sup>1</sup>, H.-G. Brokmeier<sup>1</sup>, K. U. Kainer<sup>2</sup></b> <sup>1</sup> Institut für Werkstoffkunde und Werkstofftechnik, TU Clausthal <sup>2</sup> GKSS-Forschungszentrum Geesthacht GmbH	
<b>Experimental Team:</b>	<b>Sangbong Yi, Bernd Schwebke, Heinz-Günter Brokmeier</b> Institut für Werkstoffkunde und Werkstofftechnik, TU Clausthal	
<b>Date(s) of Experiment:</b>	March – July, September 2003	

For manufacturing the lighter transporting vehicles there have been in past decades the increasing attempts for the practical applications of magnesium alloys. However, as known in the most of metals with hexagonal crystal structure, magnesium alloys show the low formability at the relatively low temperature. This behavior is related with the limited amount of the activities of deformation systems. Nevertheless these alloys show the surprisingly high deformation degree at higher temperature and behave similarly as the super-plastic materials. This phenomenon is originated from the fact that the new slip systems besides of the grain boundary sliding, which are not the case for the deformation at room temperature, are activated at higher temperature. The aim of this study is to understand the influence of newly activated deformation systems at higher temperature on the texture developments, and vice versa. In this report we describe shortly about the mechanical responses and texture developments during the tensile tests of AZ31 (3 Al – under 1 Zn – balanced Mg, in wt.%) from room temperature to 250 °C.

The starting material is the rectangular extruded AZ31 with the section of 10 × 40 mm<sup>2</sup>. The round tensile samples with  $\phi$  4 mm and 24 mm of gauge length were cut from perpendicular to extrusion direction after the DIN-50125. The initial loading rate for tensile tests was fixed to  $5 \times 10^{-4} \text{ s}^{-1}$  for each temperature condition. Texture measurements were carried out using neutron diffractometer TEX-2. Due to its high penetration depth the neutron diffraction method make possible to measure directly the broken tensile samples without any sample preparation.

The flow curves during tensile tests at different temperatures are shown in Figure 1. With increasing temperature the sample has the lower tensile strength and the higher fracture strain, 70 MPa and 94 % at 250 °C. The tensile strength of 307 MPa at room temperature decreases dramatically to 155 MPa at 150 °C, and the fracture strain increases from 18 % to 49 %. These intense variations verify that there is already a transition point under 150 °C, from hard to soft manner of mechanical behavior. Fig. 2 shows the (0002) pole figures of the tensile samples fractured at different temperatures, recalculated using series expansion method. It should be noted that the pole figure of the initial tensile sample is different from the extrudate due to the change of sample coordinate system, i.e. the center of pole figure corresponds to the tensile axis, not to the normal direction of extrudate. In all temperature-conditions the basal pole laid initially at the center of pole figure disappears during deformation. The basal planes parallel to tensile axis appears newly as a result of the tensile twinning, Fig. 2(b). However, the new component becomes rapidly weaker with increase of the temperature, and this disappears completely at 250 °C. This texture change can be caused by the high activity of pyramidal dislocations at high temperature,  $\langle a \rangle$  and  $\langle c+a \rangle$  slips. The mutual relation between the dynamic recrystallization and the high activity of non-basal slips at high temperature induces the soft manner of mechanical behavior and the texture changes.

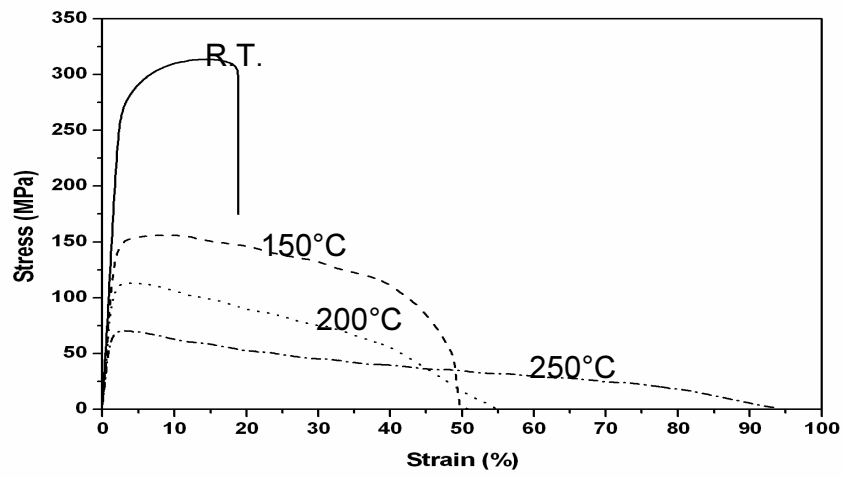


Figure 1: Stress-strain curves during tensile tests at different temperatures.

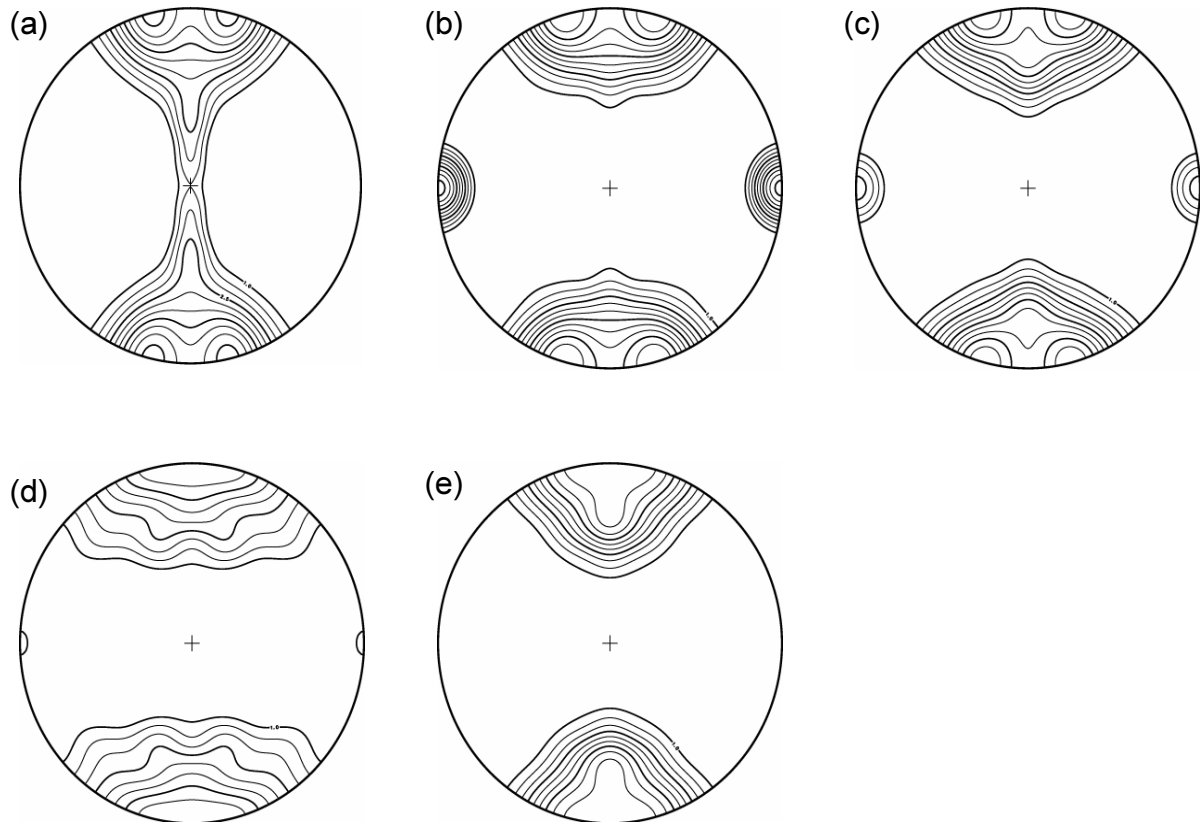


Figure 2: (0002) pole figures of tensile samples fractured at different temperatures. (a) initial ( $P_{\max} = 5.74$ ), (b) room temperature ( $= 6.49$ ), (c) 150 °C ( $= 6.41$ ), (d) 200 °C ( $= 4.95$ ), (e) 250 °C ( $= 5.39$ ), Contour levels = 1.0, 1.5, 2.0 ... 5.0, 5.5, 6.0.

	<b>EXPERIMENTAL REPORT</b>	<b>GeNF TEX-2</b>
<b>Growth strategy of sauropod dinosaurs studied by pole figure analysis</b>		
<b>Principal Proposer:</b>	<b>Magdalena Stempniewicz, Anke Pyzalla</b> Institut für Werkstoffkunde und Materialprüfung, TU Wien	
<b>Experimental Team:</b>	<b>Anke Günther</b> Institut für Werkstoffkunde und Werkstofftechnik, TU Clausthal	
<b>Date(s) of Experiment:</b>	March – May, August, September 2003	

## Scientific Background

This work extends the study of sauropod dinosaurs bone mineral orientation distribution reported in previous GeNF Experimental Report [3]. There we showed that in the middle shaft of long bones of sauropod dinosaurs, *Barosaurus africanus* and *Brachiosaurus brancai*, bone mineral orientation follows the bone axis direction. This fact was interpreted as adaptability of the apatite distribution to the mechanical load (long bones of large animals carry mostly axial loads). Additionally, differences between individuals that died in adolescence and adulthood were presented. Since the applicability of pole figure analysis for the study of life history was shown, in this work we aimed to explore the growth strategy of *Barosaurus africanus*. The long bones of *Barosaurus africanus* individuals from Tendaguru Beds (Tanzania, East Africa) [2] record two different types of growth [4]. A very rapid and continuous growth with very limited remodelling produced type A histology (mostly primary fibrolamellar bone with irregularly oriented lumina and sparse secondary osteons in the inner cortex, Figure 2). The growth that was slower and interrupted, at least partially cyclical, and accompanied by much remodelling produced type B histology (isolated secondary osteons in outer cortex and dense Haversian bone in inner cortex, Figure 3). Since these two types of histology exist in individuals of the same species dimorphism is of the question. Pole figure analysis of bone mineral helps to understand the reasons and consequences of the growth strategies.

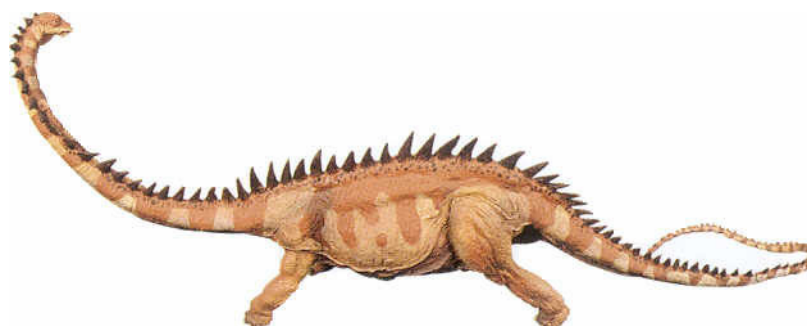


Figure 1:  
An artistic reconstruction of a diplodocid [1].

## Experimental Techniques

Neutrons were chosen for the collection of pole figures for two reasons: (i) they enable measurement on bulk of a sample, thus the delivered result is a spatial average, (ii) artefacts from large grains of digenetic minerals, e.g. calcite, are minimized. Experiments were carried at the TEX-2 instrument by Dr. A. Günther. The (0002) reflex of bone apatite was chosen for pole figure analysis because it is well resolved and relatively easy to interpret. The 00/ crystallographic direction is known to be the main direction probe to show preferred orientation in modern bone.

The pole figures presented in Figure 2. were measured for a sample collected from middle shaft of *Barosaurus africanus* right humerus (sample BaA1). The original length of the bone is 99 cm and it is the largest known humerus of *Barosaurus*. It shows type A histology indicating fast, continuous growth. As an example of the contrary growth strategy sample Ki4 (left femur, original length 120 cm) was used. Pole figures are collected in Figure 3.

## Main Results

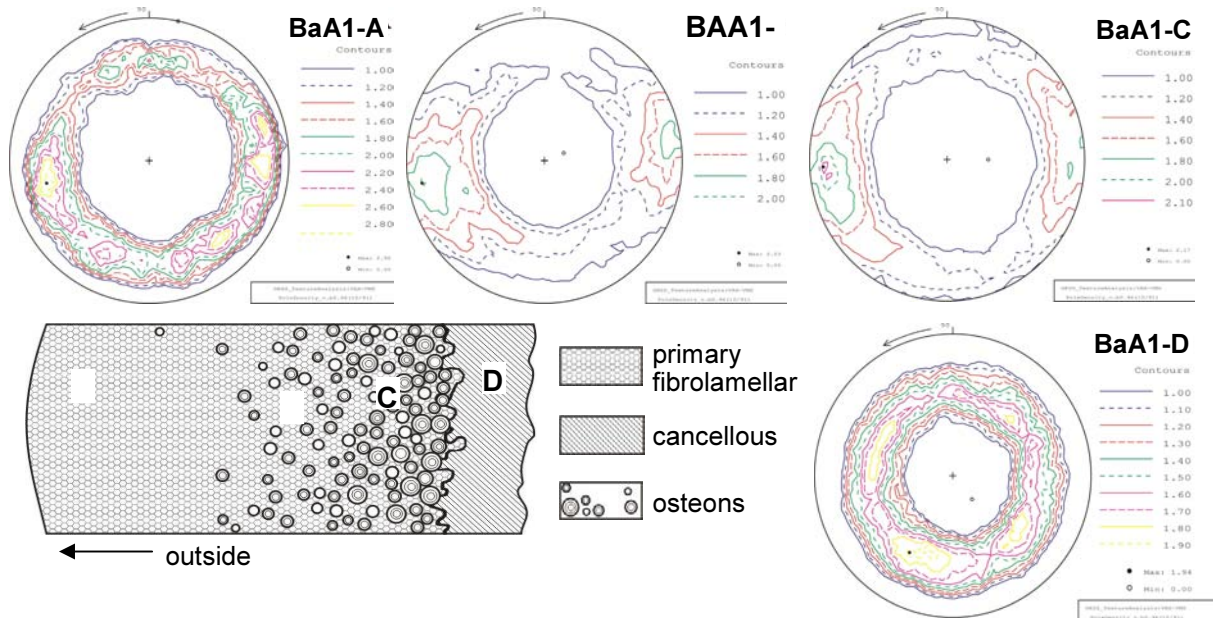


Figure 2: [002] pole figures of apatite for bone growing rapidly and continuous (type A histology).

The two growth strategies observed in *Barosaurus africanus* affect not only bone histology but also the orientation distribution of the associated bone mineral. The most obvious to notice is the change of the orientation distribution across the cortex. For the slow growing bone apatite crystallites are preferentially oriented along the bone axis and this orientation is nearly constant going from outside to inside of the bone (Figure 3). Meanwhile, fast growing bone shows this kind of orientation distribution only in the remodelled part (Figure 2, BaA1-B and -C). Further, we note that the texture index is clearly higher for the sample Ki4 than BaA1. This effect can be accounted for the ontogenetic differences in the bone age. The sample of type A histology is mostly primary bone, while the sample of type B histology is heavily remodelled.

This can be enhanced by the body plan. The body mass is unevenly distributed so that the hind-legs are loaded to higher degree than the forelegs.

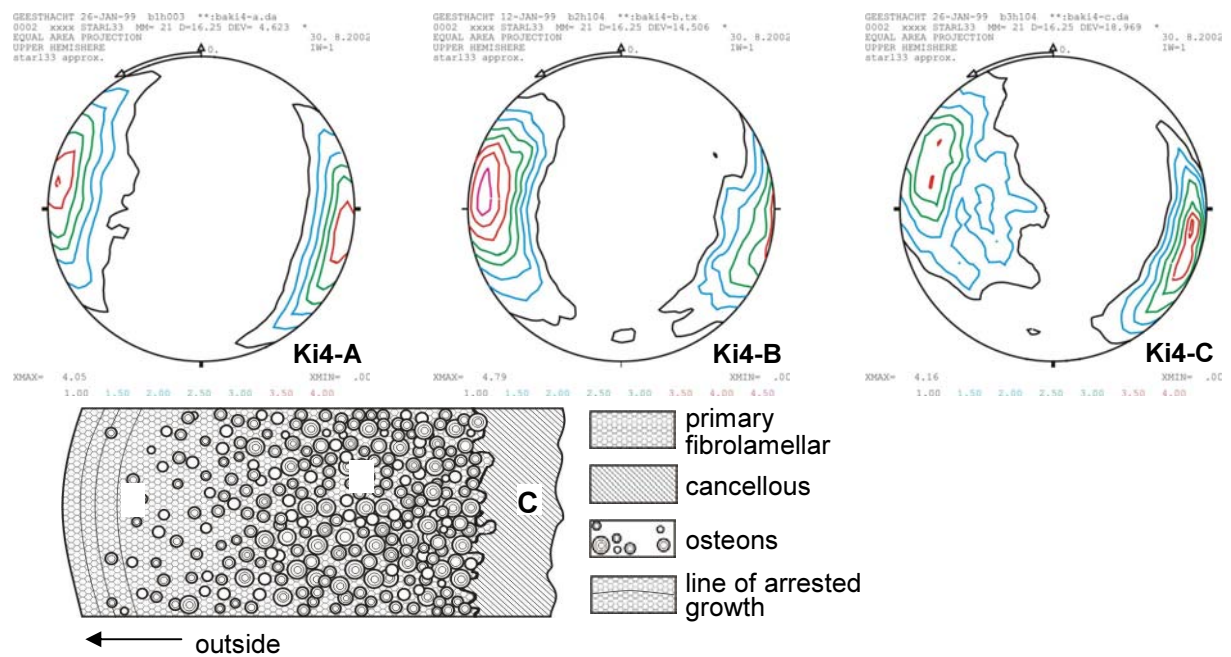



Figure 3: [002] pole figures of apatite for bone that grew slower and partially cyclical (type B histology).

## References

- [1] Ayer, J. "The Howe Ranch Dinosaurs" Sauriermuseum Aathal, 2000
- [2] Heinrich, W-D. *Mitt. Mus. Nat. kd. Berl. Geowiss.* 2: 25-61, 1999
- [3] Pyzalla, A., Stempniewicz, M. *GeNF Experimental Report* 2002, 151–152
- [4] Sander, M. *Paleobiology* 2000, 26, 466–488





	<b>EXPERIMENTAL REPORT</b>	<b>GeNF TEX-2</b>
<b>Texture in weakly deformed mudstones: a correlation between magnetic and mineral fabrics and tectonic implications</b>		
<b>Principal Proposer:</b>	<b>Francesca Cifelli<sup>1</sup>, Massimo Mattei<sup>1</sup></b> <sup>1</sup> Dipartimento di Scienze Geologiche Università ROMA TRE, Rom	
<b>Experimental Team:</b>	<b>Francesca Cifelli<sup>1</sup>, Anke Günther<sup>2</sup>, Sangbong Yi<sup>2</sup>, Bernd Schwebke<sup>2</sup></b> <sup>2</sup> Institut für Werkstoffkunde und Werkstofftechnik, TU Clausthal	
<b>Date(s) of Experiment:</b>	March, August – October 2003	

In some geological areas, the difficulty to reconstruct the deformation history of a sedimentary basin arises from the scarcity or absence of strain markers available at the outcrop scale. Some sediments, such as clays, can appear not to be affected by tectonic processes that drive the geological evolution of an area. For these sediments typical strain markers, as faults and fractures, are not available and therefore the structural analysis cannot be used. In order to define the deformation pattern of these weakly deformed sediments alternative methods must be used.

The aim of the measurements carried out at TEX-2 was to compare AMS analyses with measurements of neutron pole figures as an alternative approach to studying the deformation mechanisms that act in sedimentary basins in the incipient phases of extensional processes. Weakly deformed clays from the southern margin of the Tyrrhenian extensional Basin were sampled and investigated.

In the past few years several magnetic studies have shown that the anisotropy of magnetic susceptibility (AMS) analysis represent a sensitive tool for the investigation of rock strain even in weakly deformed sediments that appear nearly undeformed at the outcrop, because of the correspondence between the orientation of its tensor and that of the regional strain. In particular, in extensional regimes the magnetic lineation (represented by the maximum value of the AMS tensor  $K_{\max}$ ), is parallel to the stretching direction at regional scale.

For the investigated samples, magnetic analysis detected paramagnetic minerals to be the main carrier of the magnetic fabric. A phase analysis of the clay sediments was carried out at TEX-2 so that chlorite was identified to be the paramagnetic mineral responsible for the magnetic fabric.

Texture analyses were carried out by neutron pole figure measurements in order to define the preferred orientations of chlorite and to verify if the AMS signal reflects their spatial distribution. There are several reasons why TEX-2 was chosen to investigate this kind of sediments. Due to the high beam cross section of a neutron beam this method allows to measure complete pole figures. Compared to other texture analysis techniques, such as X-ray goniometry and optical analysis, the penetration depth of a neutron beam is  $10^2$  to  $10^4$  times higher for most materials and therefore allows a 3D analysis of a significant rock volume ( $11 \text{ cm}^3$ ) in a non-destructive way. This volume is equivalent to the volume of the sample used for AMS measurements. It also avoids possible artefacts due to mineral texture arising from sample cutting and polishing, especially for clays that are very delicate samples.

The orientation distributions of the poles to the basal planes (002) of chlorite in selected samples are shown in Figure 1, together with the minimum and maximum principal axes of the orientation tensor and AMS tensor. In all the exposed cases, the maximum of the poles corresponds to the direction of the minimum magnetic susceptibility and the maximum of the orientation tensor, whereas the direction of maximum magnetic susceptibility is arranged in the basal planes of chlorite crystals, is perpendicular to the elongated distribution of the poles to the basal plane, and corresponds to the orientation of the minimum value of the orientation tensor.


Neutron pole figure measurements demonstrate that the orientation of the magnetic lineation is connected with the spatial distribution of chlorite. During deformation, the basal planes of chlorite rotate around an axis sub-parallel to the stretching direction (defined by  $K_{\max}$ ). The magnetic lineation lies at the common directions between the differently oriented basal planes and, therefore, is an intersection lineation generated at the common axis of rotated surfaces. These results show that homogeneous, “undeformed” clay sediments are truly deformed by grain-scale extensional-parallel folds and crenulations.

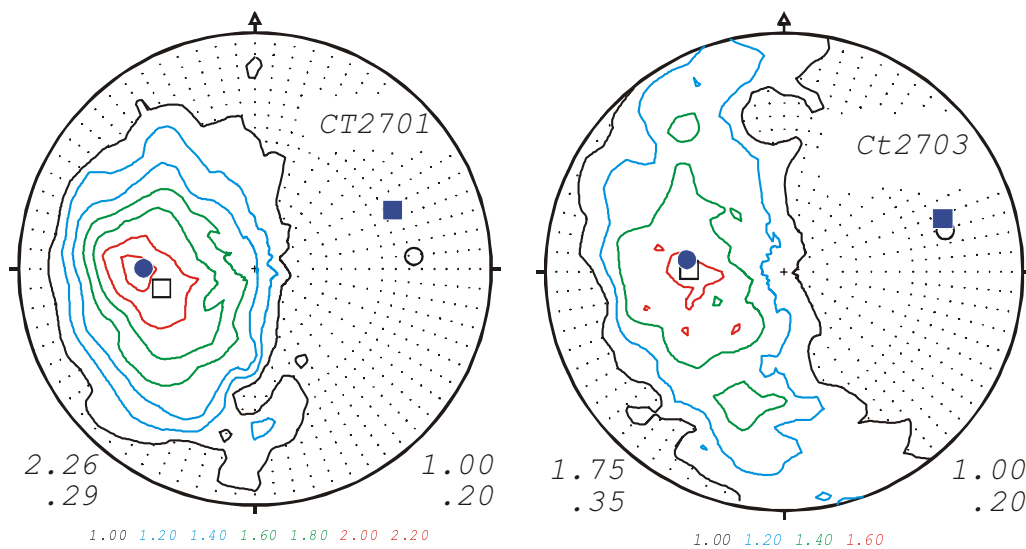


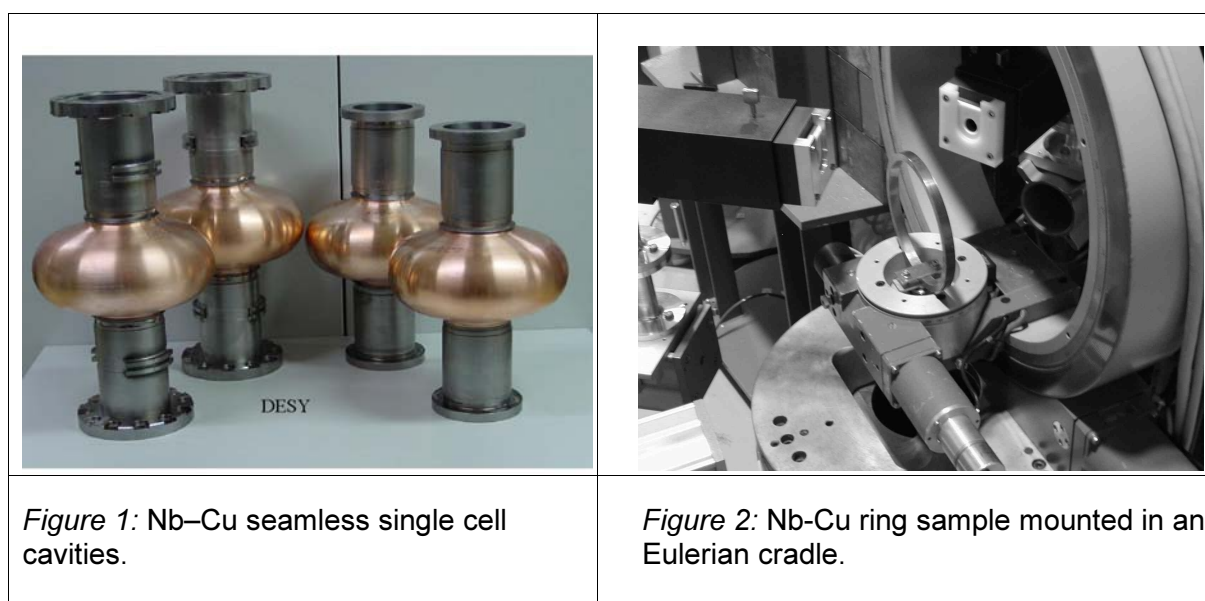
*Figure 1:* Representative pole figures of chlorite measured by means of TEX-2. The coloured numbers represent the mrd (multiply of random distribution) contours. The blue squares and circles are the maximum and minimum AMS susceptibilities, respectively. The white squares and circles are, respectively, the maximum and the minimum values of the orientation tensor.

In conclusion, neutron texture analysis confirms that the AMS ellipsoid reflects the spatial distribution of the basal planes of phyllosilicates (chlorite) and demonstrates the great potential of the AMS to determine the mineral orientation fabric. The integration of these techniques can represent a valid alternative for the investigation of regional deformation patterns in “undeformed” extensional basins.



	<b>EXPERIMENTAL REPORT</b>	<b>GeNF TEX-2</b>
<b>Texture development of Nb-Cu tubes</b>		
<b>Principal Proposer:</b>	<b>W. Singer<sup>1</sup>, Wen-Hai Ye<sup>2</sup>, H.-G. Brokmeier<sup>2</sup>, X. Singer<sup>1</sup></b> <sup>1</sup> DESY – Hamburg, <sup>2</sup> Institut für Werkstoffkunde und Werkstofftechnik, TU Clausthal	
<b>Experimental Team:</b>	<b>Wen-Hai Ye<sup>2</sup>, Bernd Schwebke<sup>2</sup>, Heinz-Günter Brokmeier<sup>2</sup></b> <sup>2</sup> Institut für Werkstoffkunde und Werkstofftechnik, TU Clausthal	
<b>Date(s) of Experiment:</b>	May – August 2003	

As one of the candidates for producing accelerator units for a linear collider Cu-Nb seamless cavities are developed. Independent of the material of the accelerator unit an excellent homogeneity of the cavities itself and of the tubes to hydro-form the cavities is required. Texture analysis provides a good tool to control the homogeneity of the tube material. The present investigation mainly focuses on the texture variation with the heat treatments of Cu-Nb tubes by different temperatures. Therefore ring samples were cut from different tubes manufactured by co-extrusion or explosive bonding. Figure 1 shows Cu-Nb cavities. Figure 2 indicates one Cu-Nb ring mounted in the centre of the Eulerian cradle.



In order to get the quantitative texture for Cu as well as for Nb three pole figures for each phase were measured. Due to the geometrical limitations of the current equipment, a ring diameter of 130 mm was at the upper limit.

The samples we present here are explosive bonding by the treatments with different temperatures. The pole figure measurements of the crystallographic planes (111), (200) and (220) of Cu-rings were shown in Figures 3a and 3b. The texture type with the dominant complicated component was found for all investigated positions of the two rings, but the intensity of the component varies. Consequently the tube will behave anisotropically forced by the copper.

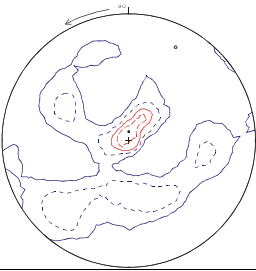
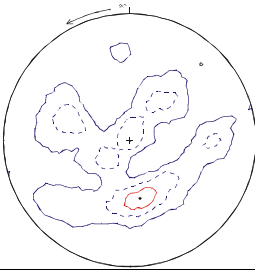
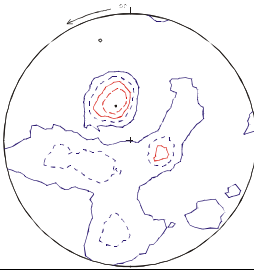
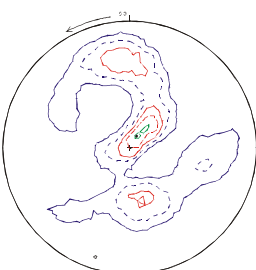
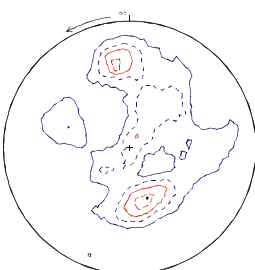
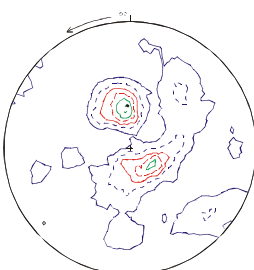
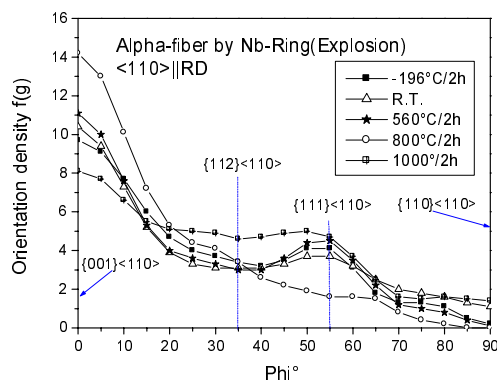
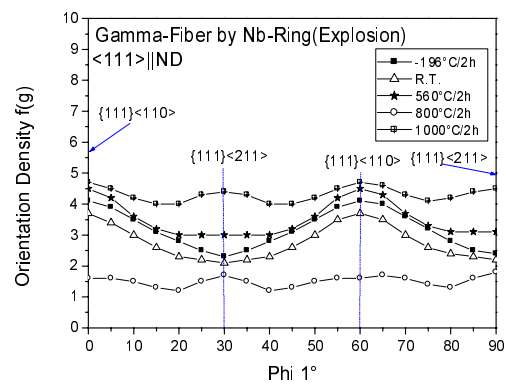
Cu111 max: 2.97m.r.d.	Cu200 max: 2.47m.r.d.	Cu220 max: 2.94m.r.d.
		
R.T. 3a)	R.T.	R.T.
Cu111 max: 3.17m.r.d.	Cu200 max: 2.77m.r.d.	Cu220 max: 3.59m.r.d.
		
560°C/2h 3b)	560°C/2h	560°C/2h

Figure 3: Cu-Pole figures of the Cu-Nb rings by explosive bonding under the treatments with room temperature and 560 °C/h.

Figures 4a–4b illustrate the distribution of the textures about Nb-rings. The comparison of the  $\alpha$ - and the  $\gamma$ -fibre shows a typical result of the deformation texture. The orientation density varies under the treatments with different temperatures.



4a)  $\alpha$ -fibre



4b)  $\gamma$ -fibre

Figure 4: Nb-ring-orientation densities along the  $\alpha$ -fibre (4a) and  $\gamma$ -fibre (4b) of the Cu-Nb rings by explosive bonding under the treatments with different temperatures.

	<b>EXPERIMENTAL REPORT</b>	<b>GeNF TEX-2</b>
<b>Texture Evolution During Severe Plastic Deformation</b>		
<b>Principal Proposer:</b>	<b>H.-J. Rack<sup>1</sup>, Heinz-Günter Brokmeier<sup>2</sup></b> <sup>1</sup> School of Materials Engineering, Clemson University, USA <sup>2</sup> Institut für Werkstoffkunde und Werkstofftechnik, TU Clausthal	
<b>Experimental Team:</b>	<b>Anke Günther</b> Institut für Werkstoffkunde und Werkstofftechnik, TU Clausthal	
<b>Date of Experiment:</b>	July 2003	

This study is examining the texture evolution during severe plastic deformation of Ti-6Al-4V. The experimental portion, initiated during this reporting period, will examine Ti-6Al-4V deformed by equal channel angular extrusion to true strains of 6.5 utilizing neutron texture measurements of bulk samples. These studies are being complimented by concurrent x-ray and transmission electron microscopy of deformation substructure evolution at Clemson and plasticity modeling of the texture evolution at GKSS.

During this reporting period, texture measurements of samples from the as-received condition and others that had been deformed to true strains of 0.5, 2 and 4 have been completed. These showed that the original material had a texture characteristic of hot-rolled plate, this texture slowly evolving towards an axisymmetric rod texture with increasing strain. Stress-strain data for equi-axed alpha+ beta Ti-6Al-4V have also been transmitted to GKSS. These will allow modeling efforts to be initiated.

Future efforts will focus on extending these measurements of Ti-6Al-4V to higher strains, extending the measurements to material initially possessing a rod texture and modeling the observed texture evolution.

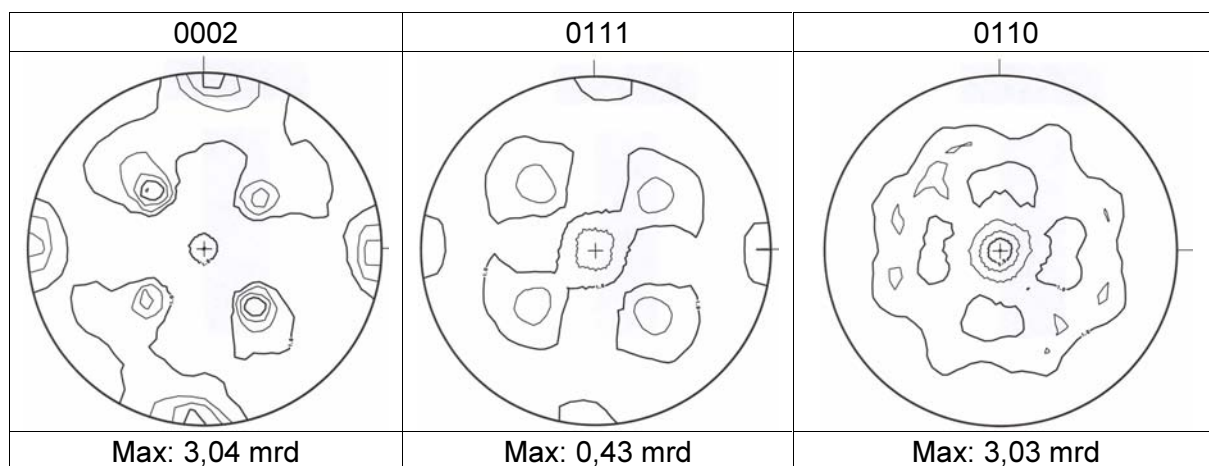



Figure 1: First pole figures of Ti-6Al-4V.

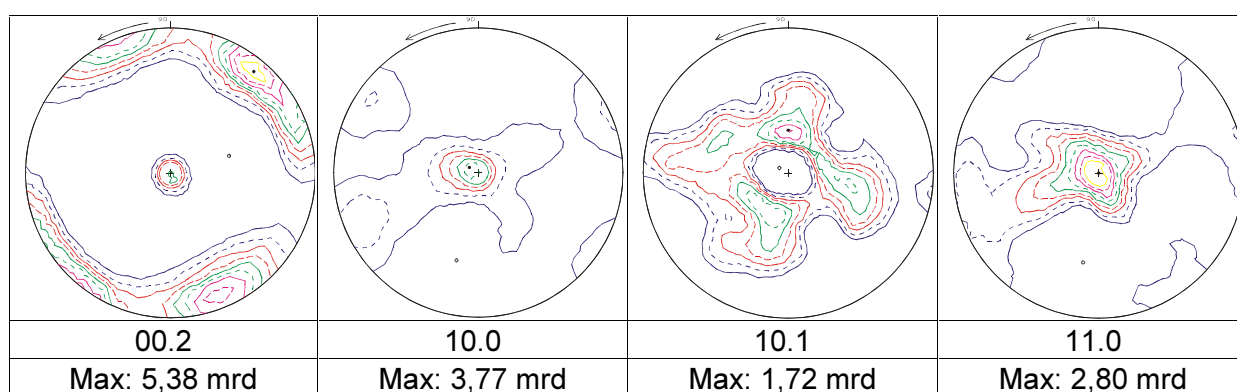


	<b>EXPERIMENTAL REPORT</b>	<b>GeNF TEX-2</b>
<b>Directional Properties in the Wrought Magnesium Alloy AZ80</b>		
<b>Principal Proposer:</b>	<b>M. Kocan, L. Wagner</b> Institut für Werkstoffkunde und Werkstofftechnik, TU Clausthal	
<b>Experimental Team:</b>	<b>Anke Günther, Heinz-Günter Brokmeier</b> Institut für Werkstoffkunde und Werkstofftechnik, TU Clausthal	
<b>Date(s) of Experiment:</b>	August 2003	

Single crystals of HCP metals such as titanium and magnesium exhibit a pronounced directionality in mechanical properties, e.g., regarding Young's modulus, yield stress and fatigue strength [1]. This directionality is also present in polycrystals of these metals and alloys if the grains are not randomly oriented, i.e., if the materials exhibit crystallographic textures. Wrought magnesium alloys tend to exhibit pronounced deformation-induced crystallographic textures due to typical thermomechanical processing routes such as rolling, extruding or forging at elevated temperatures [2, 3]. The type and sharpness of the resulting textures mainly depend on the slip systems activated during processing and thus, on deformation mode, deformation temperature and deformation degree.

Earlier work on an extruded high-strength AZ80 alloy had shown that the as-fabricated texture can be markedly changed by subsequent thermomechanical treatments such as 1-dimensional and 3-dimensional pressing, unidirectional rolling and swaging [4]. These treatments not only resulted in characteristic changes of the crystallographic texture but also led to significant variations in the resulting mechanical properties, particularly regarding fatigue performance.

The pole figures show the first results of this ongoing study.



## References

- [1] A. D. Rollett and S. I. Wright, *Texture and Anisotropy* (U. F. Kocks, C. N. Tome and H.-R. Wenk, eds.), Cambridge University Press (1998)
- [2] S. R. Agnew and O. Duygulu, *Magnesium Alloys 2003, Materials Science Forum Vols.*, 419-422 (2003), 177.
- [3] F. Kaiser, D. Letzig, J. Bohlen, A. Styczynski, C. Hartig and K. U. Kainer, *Magnesium Alloys 2003, Materials Science Forum Vols.*, 419-422 (2003), 315
- [4] M. Hilpert, A. Styczynski, J. Kiese and L. Wagner, *Magnesium Alloys and their Applications* (B. L. Mordike and K. U. Kainer, eds.), *MATINFO* (1998), 319



	<b>EXPERIMENTAL REPORT</b>	<b>GeNF TEX-2</b>
<b>Texture measurement on as-cast form of AZ31 alloy</b>		
<b>Principal Proposer:</b>	<b>Joanna Dzwonczyk, K. U. Kainer</b> GKSS-Forschungszentrum	
<b>Experimental Team:</b>	<b>Sangbong Yi, Heinz-Günter Brokmeier, Anke Günther, Bernd Schwebke</b> Institut für Werkstoffkunde und Werkstofftechnik, TU Clausthal	
<b>Date(s) of Experiment:</b>	August, September 2003	

## Introduction

The automotive industry within the last decay strongly accomplished the use of Mg-based materials due to their lightweight and reasonable mechanical properties, which can compete with other construction materials like aluminium. However Mg due to its hcp structure possess poor formability at ambient temperature. This is a reason to employ a hot deformation processes like rolling or extrusion with the aim to develop a high quality material with sufficient properties and homogeneous microstructure. To achieve this goal it is important to control these properties right in the beginning of the process. Within this study the as-cast AZ31 alloy was subjected to texture measurement, before its application to deformation process. The aim of the study was to check out the correlation between the microstructure and texture of the material in as-cast state of the material.

## Experimental part

The microstructural observations on the investigated material have been done using light microscopy and then applied to texture analysis. The texture measurement has been performed at GKSS-Forschungszentrum Geesthacht GmbH using neutron diffractometer – TEX-2 (Figure 1).

Specimens subjected to the analysis were selected from three parts of the billet (the diameter 76mm): from the center outer part and the midlayer. The size of specimens was 1 cm<sup>3</sup> (cubic shape). Each of the samples was first subjected to microstructural observation and then – to texture analysis.

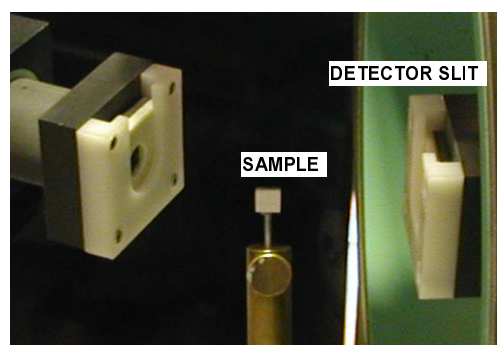


Figure 1: Texture measurement on neutron diffractometer TEX-2.

## Results and discussion

The micrographs recorded on AZ31 alloy, taken in different positions on the billet are presented in Figure 2. It should be considered that the structure has a dendritic character. After casting procedure the recrystallization effects like the grains nucleation were not observed. The whole structure contains the irregular dendrites developed in random



directions, typical for as-cast material. The dendrites indicate the further grain boundaries. However in this state was impossible to measure their size, since the shape of the dendrites was changed on the irregular way and refined progressively from outer part to the center of the billet, what is also clearly shown in the Figure 2.

Moreover, the dark contaminations observed within the dendritic forms were recognized as intermetallic  $\beta$ -phase ( $\text{Mg}_{17}\text{Al}_{12}$ ).

Figure 3 presents the texture pole figures for as-cast material in crystallographic plane  $\{0002\}$ . The iso-intensity contours are labelled as multiples of random units.

The texture measurement revealed random orientation distribution. It is clearly indicated that as-cast condition has no preferred orientations. The similar results were obtained for  $\{10\cdot10\}$  and  $\{11\cdot20\}$  planes, for which the pole figures were also developed. The random plane distribution was affected by casting method itself (DC method).

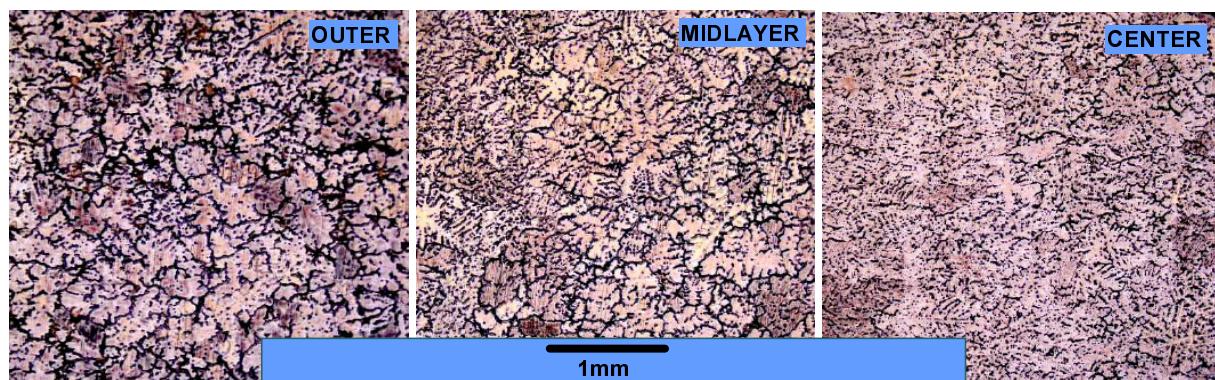


Figure 2: AZ31 as-cast micrographs recorded (a) close to the edge of billet, (b) in midlaer and (c) in the center of the billet.

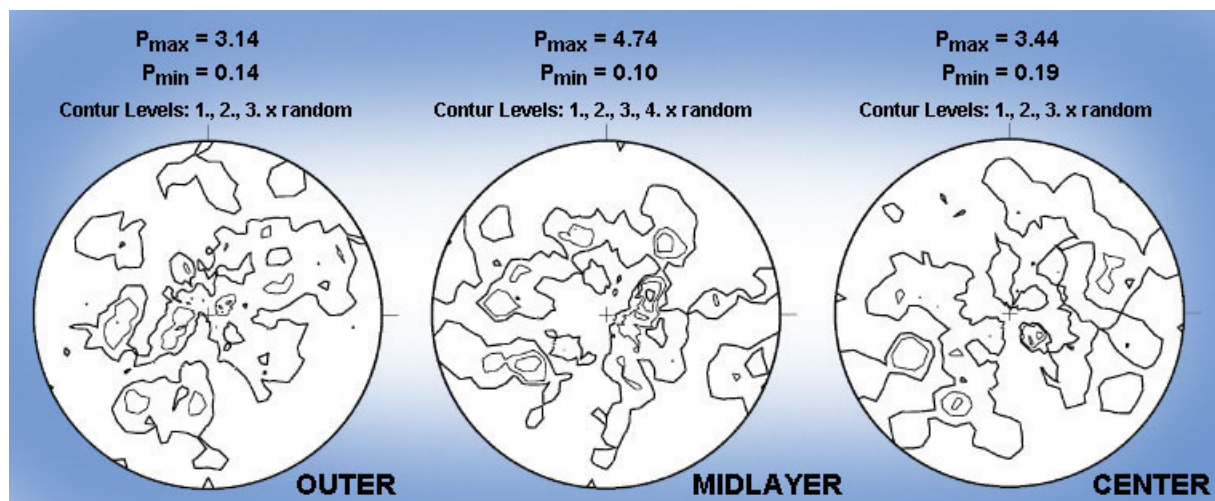



Figure 3: AZ31 as-cast condition: random texture distribution. 0002 pole figures.

The segregation within the dendrites, revealed during microstructural observations was not the case of the texture and no correlation can be assumed since the material shows very weak and random texture intensity distribution.



	<b>EXPERIMENTAL REPORT</b>	<b>GeNF TEX-2</b>
<b>Texture measurement on AZ31 alloy extruded via different extrusion methods</b>		
<b>Principal Proposer:</b>	<b>Joanna Dzwonczyk, K. U. Kainer</b> GKSS-Forschungszentrum	
<b>Experimental Team:</b>	<b>Sangbong Yi, Heinz-Günter Brokmeier, Bernd Schwebke</b> Institut für Werkstoffkunde und Werkstofftechnik, TU Clausthal	
<b>Date(s) of Experiment:</b>	August, September 2003	

## Introduction

Magnesium based alloys within the last years have accomplished a large interest from industry side, especially in automotive applications. Due to the lightweight and higher specific strength the wrought form of Mg-alloys started to play significant role apart from the cast forms. Since Mg-based material exhibits hcp crystallographic structure, the processing of the material at ambient temperatures is limited to restricted slip system and deformation twinning occurring simultaneously. These two major mechanisms and their interrelations strongly affect then the mechanical properties of the material. Moreover the hcp materials exhibit a strong anisotropy within the mechanical properties, what has a particularly important bearing on the mechanical response of the initially textured polycrystalline Mg and other hcp materials. Within this study the AZ31 alloy, extruded to a rod shape via different extrusion methods: direct, indirect and hydrostatic was subjected to texture measurement. The aim was to find out the influence of applied extrusion methods on texture and microstructure of investigated material.

## Experimental part

The microstructural observations on the investigated material have been done using light microscopy and then applied to texture analysis. The texture measurement has been performed at GKSS-Forschungszentrum Geesthacht GmbH using neutron diffractometer – TEX-2.

Specimens subjected to the analysis were selected from the central part of the extruded AZ31 rods for each extrusion condition – direct, indirect and hydrostatic. The extrusion parameters were as follow: for direct and indirect methods the extrusion ratio 1:23, for hydrostatic 1:26. All extrusion trials were done at constant temperature – 300 °C. The size of the samples was approximately 40 mm in height and in the original extrudate diameter – 20 mm for direct/indirect and 15 mm for hydrostatically extruded.

Using recommendation from the literature source [1] it was decided to evaluate the inverse pole figures, since their form is especially useful for such deformation process like extrusion, where only a single axis specification is required (the texture possess in this case an axial symmetry). For the texture analysis of the round extruded material the three inverse pole figures were developed for each principle strain axes: in ND (normal), RD (rolling) and TD (transverse) direction of the samples. However, in case of hcp-structured Mg alloy extrude to a round-shaped form should be expected that rolling and transverse directions would have mirror intensity on the pole figures.

## Results and Discussion

The micrographs recorded on AZ31 alloy in different extrusion conditions are presented in Figure 1. It is clearly indicated that the microstructures of AZ31 extruded via direct and indirect methods at 300 °C exhibit large similarity. It is obvious that the DRX (dynamic recrystallization) took place during hot deformation process, since the micro-photos revealed well visible grains. However the inhomogeneous distribution of recrystallization nuclei, which lead to the variation in stored energy, which are responsible for inhomogeneous growth rates of the grains was also observed. This resulted in fibered character of the structure and is also typical for extruded material [2, 3]. The calculated average grain size for all materials is shown also in Figure 2. Here no significant differences between direct and indirect extrusion methods were revealed as well, since the average diameter of direct extruded material was approximately 12  $\mu\text{m}$  and for indirectly extruded one – 13  $\mu\text{m}$ . The micrograph recorded on AZ31 extruded via hydrostatic method indicates very fine grain structure (approximately 2  $\mu\text{m}$ ) in comparison to other materials. This is a direct result of applying this extrusion method, where no friction between the container and the material like also between ram and the billet exist. However it must be emphasis that the elongated grain forms were found in a higher amount than that in direct and indirect method.

The texture results are presented in Figure 2. The iso-intensity contours are labelled as multiples of random units. The general indication of this measurement is that the basal plane  $\{0002\}$  has the strongest intensity in the direction parallel to the extrusion axis and at the same time to the material flow.

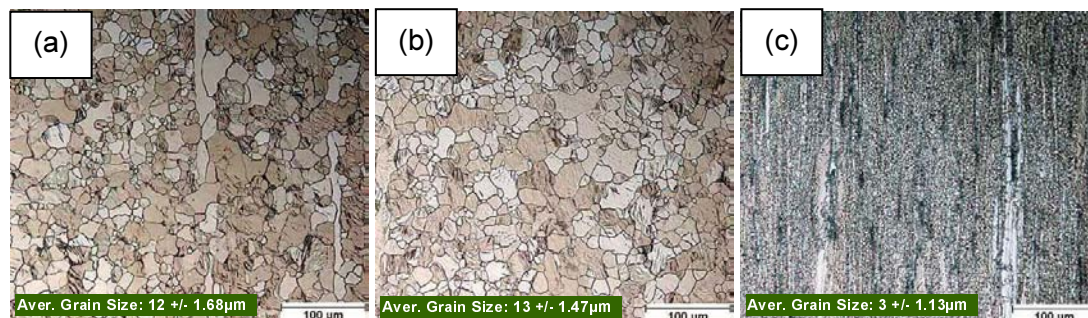


Figure 1: AZ31 extruded via (a) direct, (b) indirect and (c) hydrostatic extrusion methods at 300 °C.

In the rolling and transverse directions of the specimens (in this case they are the same), which are perpendicular to extrusion axis, pyramidal planes  $\{10\bar{1}0\}$  and  $\{11\bar{2}0\}$ , on which the slip systems are activated during hot deformation process, turn out to be more significant in their concentration.

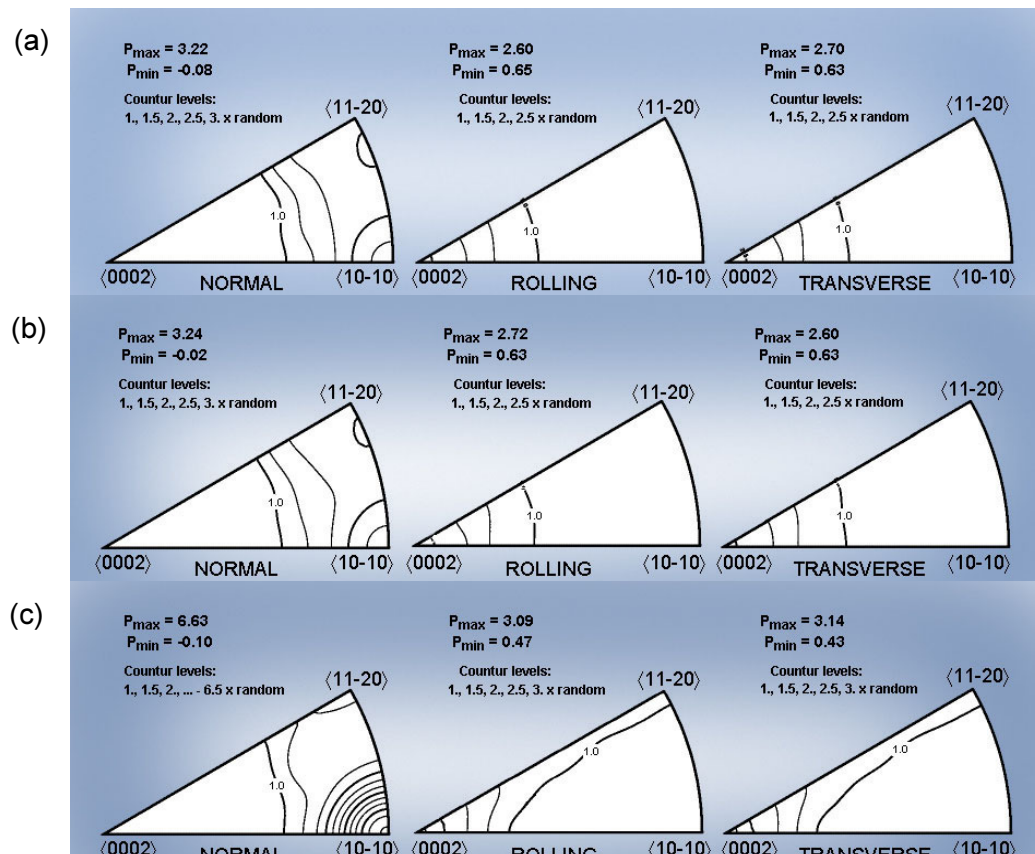



Figure2: AZ31 texture measurement for (a) direct, (b) indirect and (c) hydrostatic extruded material.

In the same time concerning the influence of the extrusion method on the material texture it is clearly indicated that hydrostatically extruded AZ31 exhibited higher intensity of preferable directions then other extrusion methods.

## References

- [1] F. J. Humphreys: Recrystallization and related annealing phenomena; Prergamon (1996), pp. 435–436
- [2] S. Müller et al: Magnesium DGM 6<sup>th</sup> conference; Wiley-VCH (2003), pp. 254–259
- [3] B. Closset; Mechanical properties of extruded magnesium alloys (-)



	<b>EXPERIMENTAL REPORT</b>	<b>GeNF TEX-2</b>
<b>Textures of Al-Nb Composite Sheet</b>		
<b>Principal Proposer:</b>	<b>L. Q. Chen<sup>1,2</sup>, N. Kanetake<sup>2</sup>, Wenhai Ye<sup>3</sup>, H.-G. Brokmeier<sup>3</sup></b> <sup>1</sup> IMR, CAS, Shenyang 110016, P.R. China; <sup>2</sup> Dept. Mater. Processing Eng., Nagoya University, Japan	
<b>Experimental Team:</b>	<b>Wenhai Ye</b> <sup>3</sup> Institut für Werkstoffkunde und Werkstofftechnik, TU Clausthal	
<b>Date(s) of Experiment:</b>	September 2003	

Deformation processed powder metallurgy (PM) Al-Nb composite sheets are one of the typical metal-metal composites (fcc/bcc-type) due to their anomalous high strength and electrical and thermal conductivities, etc. The high strength of fcc/bcc type composites is usually believed to be associated with the certain textures existing within both matrix and reinforcement metals and they can restrict the plastic deformation to plane strain. Owing to the lower volume percentage of Nb and low resolution at Al-{111} and Nb-{110} planes, it is generally very difficult to measure the textures of the reinforcement phase Nb in usual XRD. The present investigation deals with the texture variation of Al-Nb composite sheets at extruded and rather severe cold rolling reductions by neutron diffraction. Two kinds of composite (20 vol.% and 40 vol.% Nb/Al) and pure Al sheet were used as experimental materials after hot co-extrusion and co-deformation up to 90 % cold rolling reduction. Figure 1 shows one Al-Nb sheet mounted in the center of the Eulerian cradle. In the usual way the average textures of the specimens throughout the thickness were independently obtained and expressed by pole figures, and they can easily be converted to inverse pole figures and ODFs.

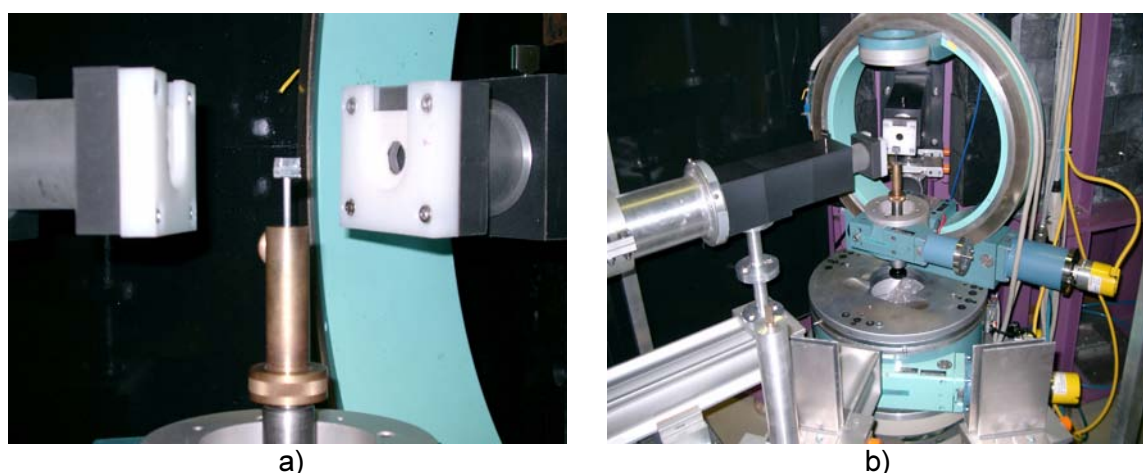


*Figure 1: Al-Nb sample mounted in an Eulerian cradle from a near (a) and a far (b) views.*

In order to get the quantitative texture for Al as well as for Nb, two complete pole figures for each phase in composite sheets were measured and three were done for hot extruded pure Al sheet. The results we will present here contain the measured pole figures of: 1) hot-extruded (extrusion ratio: 31) Al-{111},-{200} and -{220} planes of pure Al sheet; 2) Al-{200}

and  $\{220\}$ , and Nb- $\{200\}$  and  $\{211\}$  planes of hot extruded 20 vol.%Nb/Al composites (extrusion ratio:31.4); and 3) Al- $\{200\}$  and  $\{220\}$ , and Nb- $\{200\}$  and  $\{211\}$  planes of 40 vol.%Nb/Al composite sheet after hot extruded (extrusion ratio:15.7) and cold rolled deformation up to 90 %.

As illustrated in Figure 2–4, the textures of Al and Nb at different stages of deformation process varied and we can trace the links of the texture related plastic deformation.

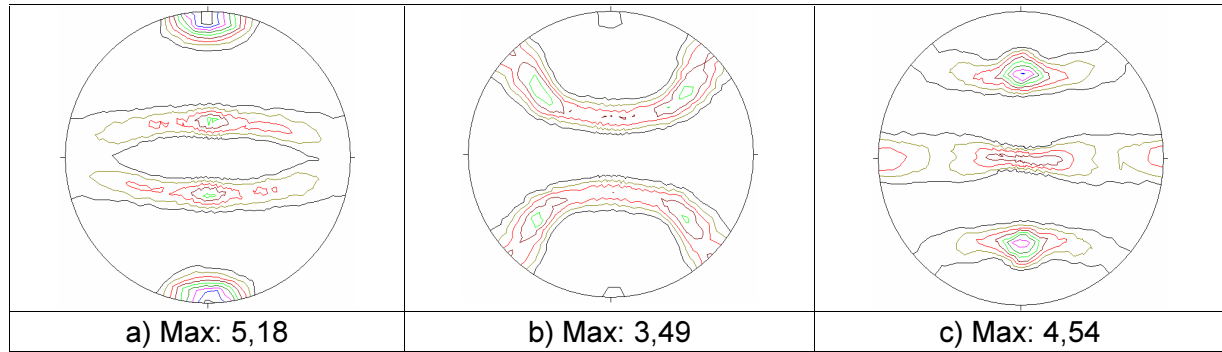


Figure 2:  $\{111\}$ (a),  $\{200\}$ (b) and  $\{220\}$ (c) pole figures for hot- extruded pure Al sheet.

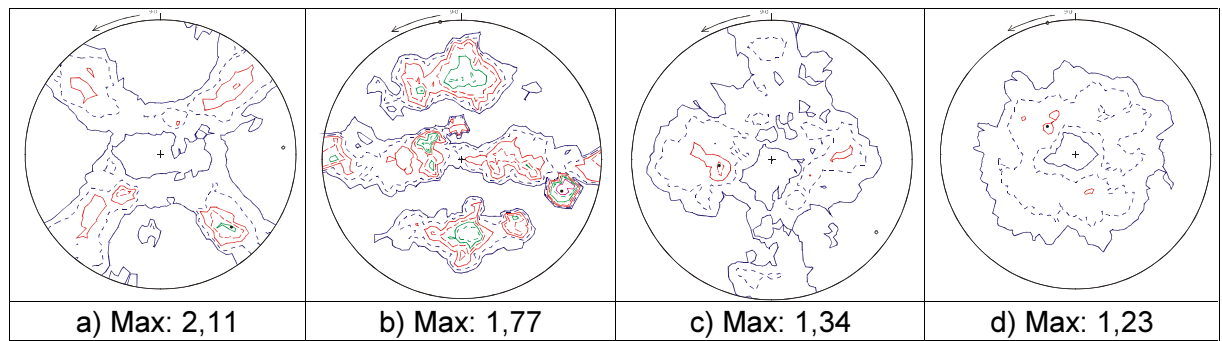


Figure 3:  $\{200\}$ (a),  $\{220\}$ (b) pole figures for matrix Al and  $\{200\}$ (c),  $\{211\}$ (d) pole figures for reinforcement Nb of 20 vol.Nb/Al composites after hot extrusion.

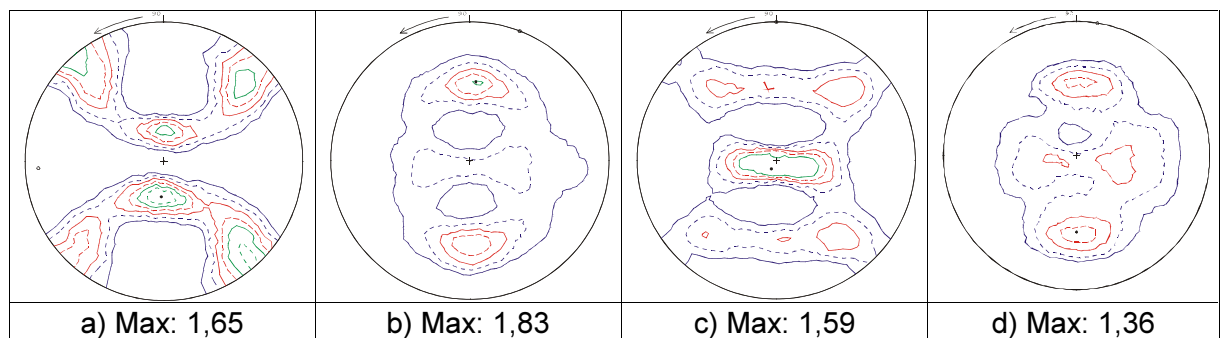



Figure 4:  $\{200\}$ (a),  $\{220\}$ (b) pole figures for matrix Al and  $\{200\}$ (c),  $\{211\}$ (d) pole figures for reinforcement Nb of 40 vol.Nb/Al composites after hot extrusion and cold rolling deformation up to 90 %.



	<b>EXPERIMENTAL REPORT</b>	<b>GeNF POLDI</b>
<b>Polarised diffractometer POLDI</b>		

### Short Instrument Description:

With the polarised diffractometer 3-D depolarisation analysis is used to investigate magnetic properties and correlations in magnetic materials. With minor modifications a time of flight option in non-polarised mode is additionally available for the purpose of dosemeter calibration.

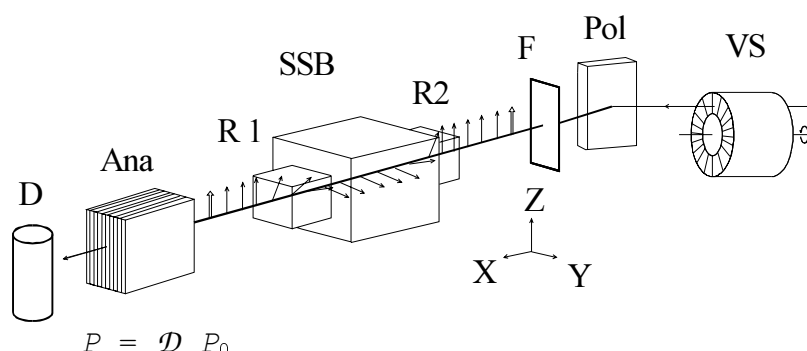
### Local Contact:

Dr. Volker Wagner, PTB – Physikalisch Technische Bundesanstalt, Braunschweig

Phone/Fax : +49 (0)531 592–6550 / +49 (0) 531 592–7505

e-mail: [volker.wagner@ptb.de](mailto:volker.wagner@ptb.de)

### Schematic View of POLDI:




*Set-up for full 3-dimensional neutron depolarisation analysis in the transmitted beam.*

### Instrument Details:

Location at FRG-1:	beamline 7, thermal neutrons cross section 10 x 4 cm <sup>2</sup> ,
Polariser / monochromator (Pol)	Cu <sub>2</sub> MnA (111), PG(002), Si (311) doubly focussing; helical slot selector (VS)
Take-off-angle:	10° < 2 Θ <sub>M</sub> < 65°
Wavelength:	λ = 0.1 to 0.36 nm, 2 <sup>nd</sup> order suppression by velocity selector (VS)
Flux at sample position:	Φ <sub>max</sub> = 0.8 · 10 <sup>5</sup> cm <sup>-2</sup> s <sup>-1</sup> (polarised)
Analyser (Ana):	Co/Ti-supermirror
Overall polarisation:	0.94
3D depolarisation analysis in transmitted beam:	accuracy < 1 % for any component of <b>D</b>
Sample environment fitting in the magnetically shielded sample box (SSB) for 3D depolarisation analysis:	– refrigerator T > 12 K, Orange cryostat T > 1.5 K – DC magnetic field < 160 A/cm – pulsed field < 8.0 kA/cm
Detector (D):	<sup>3</sup> He-counter
Instrument control / data acquisition:	remote internet PC control IEEE bus, serial bus and special interfaces





	<b>EXPERIMENTAL REPORT</b>	<b>GeNF POLDI</b>
<b>The PTB thermal neutron reference field at GeNF</b>		
<b>Principal Proposer:</b>	<b>R. Böttger</b> Physikalisch-Technische Bundesanstalt (PTB) 38116 Braunschweig, Germany	
<b>Experimental Team:</b>	<b>R. Böttger, H. Friedrich, S. Löb</b> Physikalisch-Technische Bundesanstalt 38116 Braunschweig, Germany	
<b>Date(s) of Experiment:</b>	August 2002, March 2003	

### Progress in the characterization of the thermal reference field

The reduction of the beam intensity by the second diaphragm outside the casematte was abandoned, as extensive time-of-flight measurements had shown dependence of the spectral distribution of the thermal neutrons on the beam divergence defined by this diaphragm.

Instead, a remote-controlled first diaphragm was constructed inside the casematte allowing the approved maximum size of 3 mm x 3 mm to be reduced to nearly zero cross section, while the cross section of the second diaphragm was kept constant at 25 mm x 25 mm.

Further time-of-flight experiments showed that this concept allowed the beam intensity to be varied down to 5% of the full intensity without the spectral distribution being changed. This is of particular importance, as the  $^3\text{He}$  transmission monitor, calibrated by a black-detector, is sensitive to changes of the spectral distribution of the thermal neutrons as well as radiation detection instruments to be calibrated in this reference field.

The reproducibility of the field parameters is good, as for both measuring campaigns the mean energy of the spectral distribution was determined as 45(1) meV. Due to intensity problems at the black-detector, the calibration of the transmission monitor can only be performed at a strongly reduced beam current. With the spectral distribution now being independent of the beam intensity, the monitor calibration factor can also be applied to the full beam intensity, which is used for most applications.

In these measuring campaigns Au activation measurements were performed for this reference field for the first time in order to determine the absolute neutron beam current and to compare with the described method for monitor calibration by the black-detector system.

The activity of the  $^{198}\text{Au}$  was analysed by the  $4\pi\beta\text{-}\gamma$  coincidence method at the PTB reference laboratory allowing the average neutron current during irradiation of 2 to 3 days to be determined with a high accuracy of about 2 % (1  $\sigma$ ). Due to the analysis procedure, the size of the disc-shaped Au foils (thickness 18/23  $\mu\text{m}$ ) was limited to a diameter of 22 mm. Thus the beam cross section had to be reduced with a circular diaphragm. For this low divergence field (pencil beam), time-of-flight experiments were performed. Higher mean energies (up to 50 meV in August 2002) were determined for these spectral energy distributions and, consequently, larger calibration factors for the transmission monitor were analysed for this configuration. The average activation cross section was determined by folding the spectral distribution of the pencil beam with the well-known standard activation cross section. Figure 1 shows the neutron energy distribution for the Au activation measurement in August 2002, together with a Maxwellian distribution with  $kT = 25.3$  meV, which is a suitable representation of the spectrum.

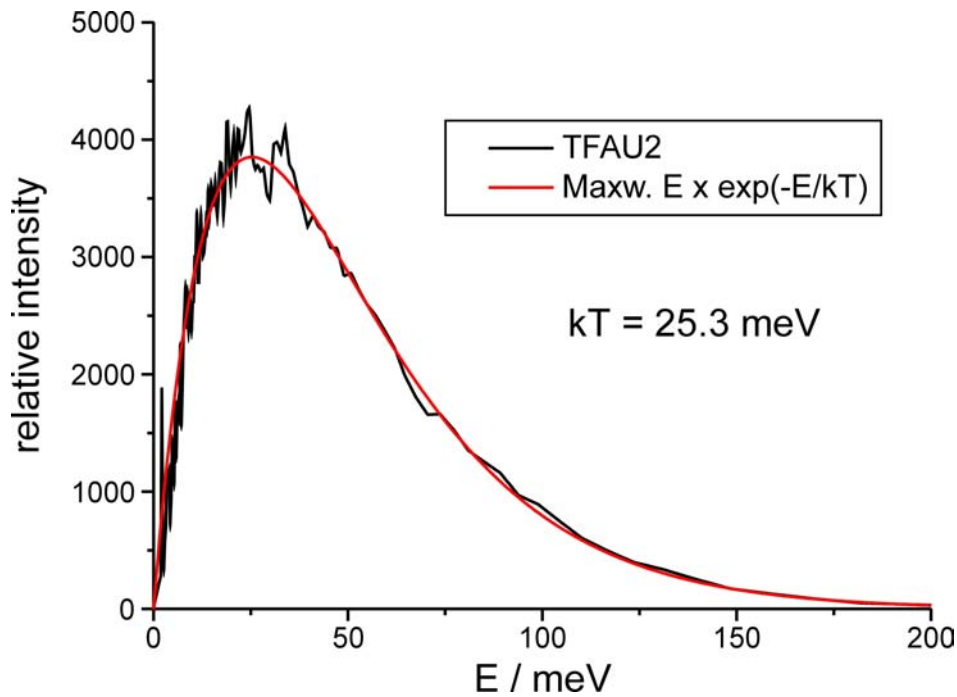



Figure 1: Spectral neutron fluence for the Au activation measurement in August 2002, compared with a Maxwellian distribution with an energy parameter  $kT = 25.3$  meV.

As the transmission monitor is simultaneously applied during the activation measurement, the two different methods can be directly compared. Excellent agreement within 2 % between the results of the two different approaches to determining the thermal beam intensity is found. Although the full beam cross section used for the practical radiation instrument calibration could not be the subject of this comparison, there is evidence that with this configuration of adjustable beam intensity with nearly constant beam divergence, the calibration of the transmission monitor is also valid for the full beam current.

As in previous measuring campaigns, the thermal neutron reference field was used routinely in combination with the scanner system for the calibration of radiation detection devices, with special emphasis on the development of electronic personal dosimeters.

	<b>EXPERIMENTAL REPORT</b>	<b>GeNF POLDI</b>
<b>Magnetic inter-particle correlations in a system of single-domain particles</b>		
<b>Principal Proposer:</b>	<b>V. Wagner<sup>1</sup>, J. Hesse<sup>2</sup></b> <sup>1</sup> Physik. Tech. Bundesanstalt, 38116 Braunschweig <sup>2</sup> Inst. f. Metallphysik der TU, 38106 Braunschweig	
<b>Experimental Team:</b>	<b>V. Wagner, S. Braun</b> Physik. Tech. Bundesanstalt, 38116 Braunschweig	
<b>Date(s) of Experiment:</b>	<b>May, October 2003</b>	

Single-domain particles constitute the magnetic pigment for the production of recording materials like video tapes etc. In the ideal case the magnetic particles would behave as Stoner-Wohlfarth particles with no interaction between the individual particles. However, in closely packed pigments inter-particle correlations may arise due to dipolar interaction and preferred orientation of the nano-particles.

Samples of nano-sized Fe-particles were investigated by magnetic methods on a *macroscopic* length scale and by Moessbauer spectrometry on a *microscopic* length scale at the research group of Hesse at TU Braunschweig. These investigations showed increasing deviations from Stoner-Wohlfarth behaviour the closer the packing of the particles in the sample [1, 2]. The temperature dependence of the magnetic properties was attributed to the blocking of the magnetization of  $\gamma$ -FeO<sub>3</sub> shell around the Fe-particles at 60 K.

We aimed to study these systems by neutron depolarization on a *mesoscopic* scale at different temperatures. In detail we studied the correlation  $\langle \Delta \mathbf{B}(\mathbf{x}) \Delta \mathbf{B}(\mathbf{x}') \rangle$  of the fluctuations of the magnetic induction  $\mathbf{B}$  by spherical neutron depolarization analysis (NDA) of the beam transmitted through the sample:  $\mathbf{P} = D \mathbf{P}_0$ , where  $\mathbf{P}$ ,  $\mathbf{P}_0$  were the final and initial beam polarization, the macroscopic magnetization  $M$  and the correlation length  $\zeta$  being related to the rotation  $\Phi$  and the depolarization respectively.

So far a powder sample of 5 vol.% magnetic material was studied in its remanent state for  $20 \text{ K} < T < 290$ . The sample was mounted in a solenoid closed by a soft magnetic yoke and was magnetized by a series of magnetic field pulses of increasing strength ( $0 < H_{\text{app}} < 800$  kA/m). After each pulse both the depolarization of a beam of thermal neutrons transmitted through the sample and the rotation of the beam polarization were observed. The domain structure was deduced from the depolarization and the remanent magnetization from the rotation of the polarization of the transmitted beam [3].

The measurements were taken along the initial branch of remanent magnetization  $M_{\text{rem}}$  and after reversal of the magnetic field pulses, along the demagnetized branch  $M_{\text{dem}}^{(1,2)}$  until the complete magnetization reversal (see Figure 1). Typically the mean domain size (as measured by the correlation length  $\zeta$  of the magnetic fluctuations) was about 60 nm – comparable to the particle size – in the virgin state. The anisotropy of the depolarization indicated some magnetic texture in the virgin sample. The mean domain size in the remanent state increased up to 200 nm at saturation remanence. At same time texture continually developed with preferred orientation of the domain magnetization along the magnetizing field. Upon magnetization reversal the mean domain size passed through a minimum at magnetization reversal ( $\zeta \cong 100$  nm) (cf. Figure 2).

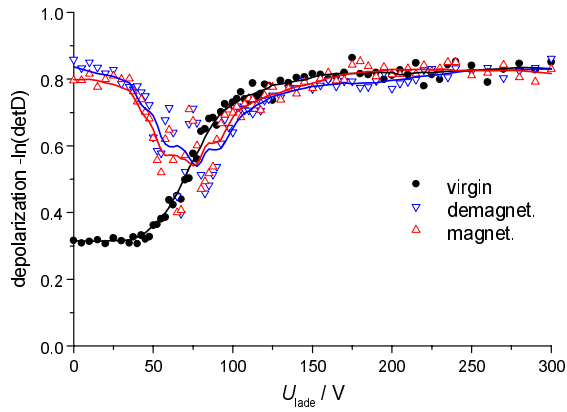


Figure 1: Remanent magnetization  $M_{\text{rem}}$  and  $M_{\text{dem}}^{(2)}$  as observed by the rotation  $\Phi$  vs. applied field  $H_{\text{app}} = 0.451 \cdot T \ U_{\text{lade}}/V$  for magnetization starting from the virgin state and after magnetization reversal.

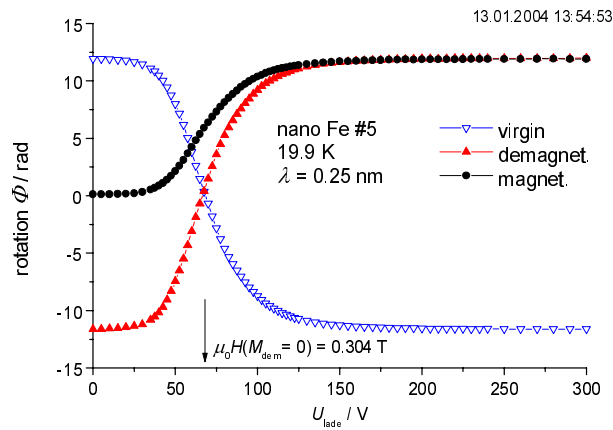



Figure 2: Magnetic correlation length  $\zeta$  as observed by the depolarization  $-\ln(\det D)$  vs.  $H_{\text{app}} = 0.451 \cdot T \ U_{\text{lade}}/V$  for the initial branch starting from the virgin state (full circles) and during magnetization reversal (triangles).

Although a Henkel plot did not indicate an interaction between the particles in this sample ( $\varepsilon = 0.05$ ), the correlation length of  $\langle \Delta \mathbf{B}(\mathbf{x}) \Delta \mathbf{B}(\mathbf{x}') \rangle$  introduced by the magnetization was partially maintained during magnetization reversal.

Investigation of more compact samples, where a Henkel plot indicates deviations from Stoner-Wohlfarth behaviour, are planned.

## References

- [1] S. Thamm, Untersuchung an Pigmenten magnetischer Datenträger und Vergleich mit den Eigenschaften idealer Stone-Wohlfarth-Teilchen, Dissertation TU Braunschweig, 1997, Cuvillier Verlag, Göttingen 1997, ISBN 3-89588-984-0
- [2] S. Thamm, J. Hesse, JMMM 154 (1996), pp. 254–262
- [3] R. Rosman and M. Th. Rekveldt, Phys. Rev. B:Condens. Matter 43 (1991) 8437

	<b>EXPERIMENTAL REPORT</b>	<b>GeNF POLDI</b>
<b>Search of chiral spin glass transition in alloy (Pd<sub>0.984</sub> Fe<sub>0.0016</sub>)<sub>0.95</sub>Mn<sub>0.05</sub></b>		
<b>Principal Proposer:</b>	<b>L. A. Axelrod<sup>1</sup>, G. P. Gordeev<sup>1</sup>, V. N. Zabenkin<sup>1</sup>, I. M. Lazebnik<sup>1</sup>, V. Wagner<sup>2</sup></b> <sup>1</sup> Petersburg Nuclear Physics Institute (PNPI), Russia <sup>2</sup> Physik.Tech.Bundesanstalt (PTB), Braunschweig, Germany	
<b>Experimental Team:</b>	<b>L. A. Axelrod<sup>1</sup>, G. P. Gordeev<sup>1</sup>, L. A. Axelrod<sup>1</sup>, V. Wagner<sup>2</sup>, S. Braun<sup>2</sup></b>	
<b>Date(s) of Experiment:</b>	Oktober 2003	

### Scientific Objective

The experiment was aimed to continue a study of the static spin correlations in alloy (Pd<sub>0.984</sub>Fe<sub>0.0016</sub>)<sub>0.95</sub>Mn<sub>0.05</sub> with competition interactions between spins. This alloy has a ferromagnetic state transition at T = 41 K and a spin glass like state transition at more lower temperature. But according to neutron depolarization measurements the temperature of the latter is hardly determined. Nevertheless a magnetic viscosity, prehistory influence and irreversibility inherent for spin glass systems are observed by depolarization measurements. However the specific behavior of the spin system observed in this alloy is not seen in conventional magnetics. For example there is nonmonotonic temperature dependence of neutron depolarization in FC regime [1]. Probably it is caused by particular type of spin ordering at the temperature below a spin glass transition. Kawamura [2] predicts a new type of transition in Heisenberg magnetics, named chiral spin glass transition. In the light of these ideas, we are trying to understand specific behavior of the spin system using neutron polarimetry.

### Experimental Techniques

The measurements with 3 dimensional neutron depolarisation analysis were carried out by Poldi set-up of FRG-1 reactor of GKSS Research Centre. A monochromatic neutron beam with neutron wave length  $\lambda = 0.25$  nm and polarization  $\mathbf{P}_0$  impinges on the sample and the polarization of the transmitted beam  $\mathbf{P} = D \mathbf{P}_0$ . The depolarization matrix D carries the information both on the spatial fluctuations of the magnetization and on the mean magnetization. The sample was a plate of 25×11×1.2 mm<sup>3</sup>. It was magnetized along each of tree its dimensions. The studied temperature range was 5<T[K]< 60 and applied magnetic fields 5<H[Oe]<100 were used. The depolarisation  $\Delta P = -\ln(|D|)$  and the mean magnetization were determined from the received data. The macroscopic magnetization is  $\mu_0 M = \Phi_1 / c \lambda d$  where  $\Phi_1$  is angle of polarization rotation around *i*-axes

$$\tan \Phi_i = (D_{jk} - D_{kj}) / (D_{jj} + D_{kk}) \quad (i, j, k) = (x, y, z),$$

*d* is the size of the sample along neutron trajectory,  $c = 4.63 \cdot 10^{14} \text{ T}^{-1} \text{ m}^{-2}$ .

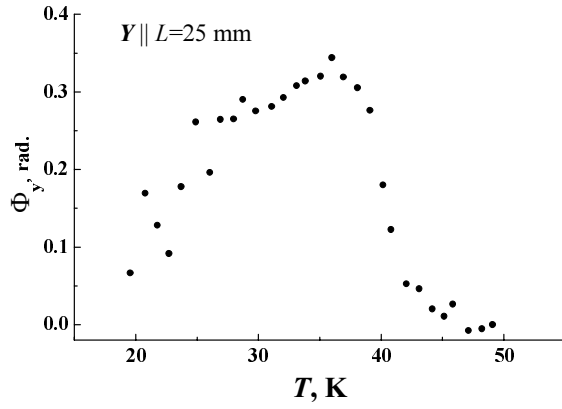


Figure 1.

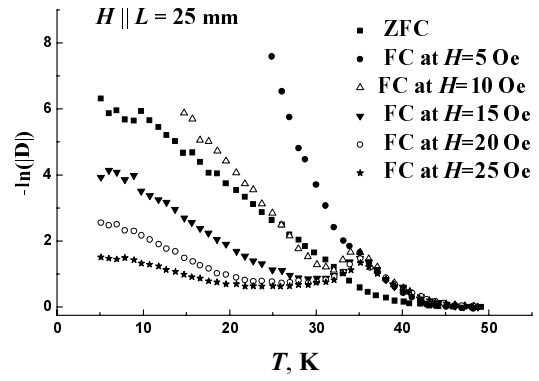


Figure 2.

## Results

It is surprising the mean macroscopic magnetization ( $\Phi \neq 0$ ) was observed at  $H=0$ . The temperature dependence of both  $\Phi \sim M$  and depolarization in FC regime for  $H = 0, 5, 10, 15, 20$  and  $25$  Oe applied along the largest dimension of the sample are shown in Figure 1 and Figure 2 respectively. Angle  $\Phi \neq 0$  in ZFC is obviously caused by influence of shape anisotropy and the yoke used to prevent stray field. The depolarization anisotropy was taken into account to determinate angle  $\Phi$  more correctly. From comparing one can see that the depolarization in small magnetic fields (less than 5 Oe) is larger than in ZFC regime for whole temperature region.

The field increasing leads firstly to the depolarization decreasing and then to its slow growth. Thus the peak at  $T = 35$  K is drawn in detail. The position of the following minima depends on magnetic field. Any saturation of depolarization does not observe at low temperature even at high values of applied field. Magnetization has the tendency to fall down to  $T = 35$  K. The similar behavior of depolarization is observed in the case when the field is applied along shorter dimension (11 mm) (Figure 3). The maximum at  $T = 35$  K outlines also. The possible reasons of its small clearness are short neutron wave length ( $\lambda = 0.15$  nm) and considerable influence of demagnetization factor. Even greater demagnetization influence is demonstrated under magnetizing the sample along the smallest dimension (1.2 mm). In the given case (Figures 4 and 5) the applied field of 100 Oe corresponds to the inner field  $H_{in} \sim H \cdot N \sim 4.5$  Oe. But there is no pick in Fig. 2 for the same field value. Thus the pick is a demonstration of physical processes, reflected an appearance of the pseudovector (field  $\mathbf{H}$ ) in the system. It verified the symmetry changes of the system and took place below  $T = 35$  K.

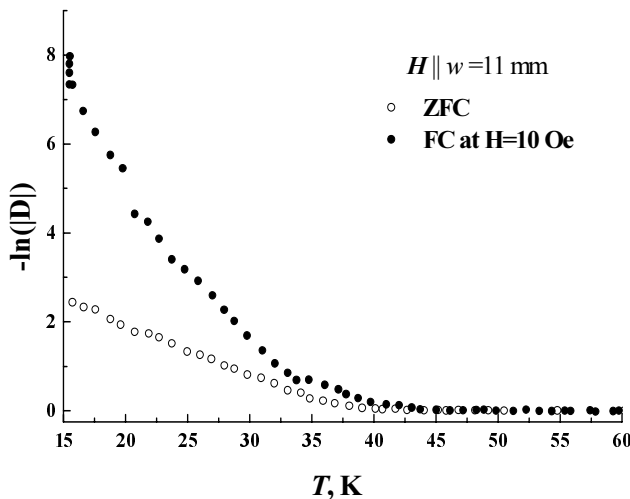


Figure 3.

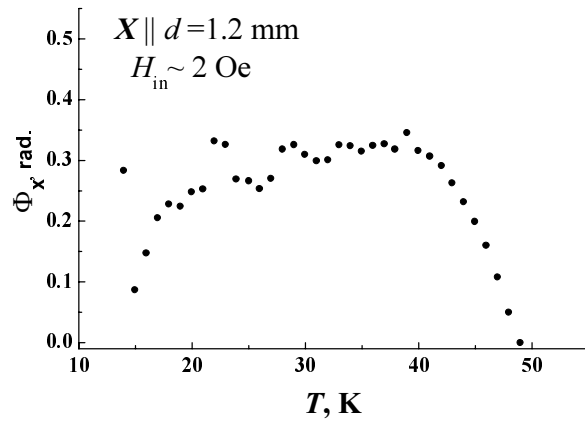


Figure 4.

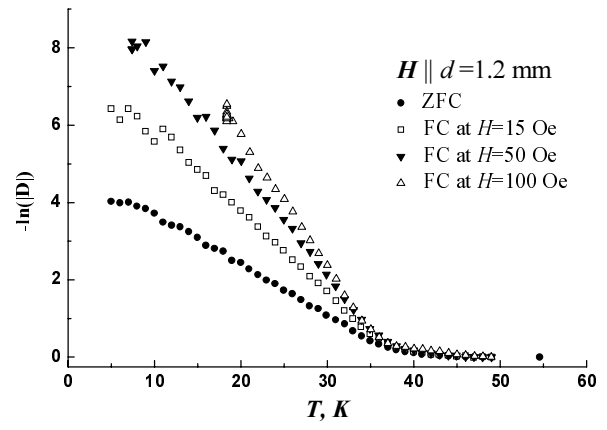


Figure 5.

## Conclusion


The SANS measurements show that the strong dependence of asymmetrical part of cross section, i.e. static chirality [3], on polarization takes place at  $T = 28$  K. May be here does the chiral spin ordering originate?

## References

- [1] G. P. Gordeev, L. A. Axelrod, V. N. Zabenkin, I. M. Lazebnik, V. Wagner, H. Eckerlebe, Physica B 335 (2003), pp. 127–129.
- [2] H. Kawamura, M. Suan Li, Phys. Rev. Lett. 87 (2001) 187204 (1–4).
- [3] G. P. Gordeev, L. A. Axelrod, S. V. Grigoriev, V. N. Zabenkin, I. M. Lazebnik, V. Wagner, H. Eckerlebe, GeNF Experimental report, 2003.





	<b>EXPERIMENTAL REPORT</b>	<b>GeNF POLDI</b>
<b>Neutron diffraction study on EuSe</b>		
<b>Principal Proposer:</b>	<b>D. Lott<sup>1</sup>, A. Schreyer<sup>1</sup>, R. Lechner<sup>2</sup></b> <sup>1</sup> GKSS Forschungszentrum GmbH, Institut for Material Science, Max-Planck Str. 1, D-21502 Geesthacht, GERMANY <sup>2</sup> Institut für Halbleiterphysik, Johannes Kepler Universitaet, A-4040 Linz, Austria	
<b>Experimental Team:</b>	<b>D. Lott<sup>1</sup>, V. Wagner<sup>3</sup>, S. Braun<sup>3</sup></b> <sup>3</sup> PTB, Braunschweig, Germany	
<b>Date(s) of Experiment:</b>	November 2003	

## Introduction

Magnetic multilayers have recently attracted substantial interest due to the modifications of the magnetic interactions by strain, finite thickness, as well as interlayer couplings across magnetic or non-magnetic spacer layers. A possible realization of such multilayers is based on heteroepitaxial growth of wide band gap Eu chalcogenide semiconductors EuX (X = O, S, Se, Te) on the lead salt layers (PbSe) by molecular beam epitaxy because both groups of materials crystallize in the rock salt structure. The EuX compounds are classical Heisenberg magnets due to the exchange interactions between the localized magnetic moments of the half-filled 4f levels of Eu<sup>2+</sup> ions (spin 7/2) in the crystals. As shown recently for EuTe [1] and EuS [2] multilayers, the pronounced dependence of the exchange interactions on interatomic distances in EuX [3] strongly affects the magnetic properties of the samples.

## Experiment

In a previous ADAM beamtime at the ILL reactor in Grenoble, EuSe bulk samples grown by molecular beam epitaxy on BaF<sub>2</sub> (111) substrates were examined by neutron diffraction [4]. The method allows easily to distinguish between ferro-, antiferro- and ferrimagnetic contributions which appear at the first, 1/2 and 1/3 order Bragg peak position of the diffraction scans, respectively. Here, the experiment was repeated at the POLDI diffractometer at the GKSS Research Centre. Goal was to test the feasibility of such an experiment at the GKSS Research Centre considering the low magnetic signal expected from the relatively small amount of magnetic material of 0.3 mm<sup>3</sup> EuSe. Figure 1 shows temperature dependent q-scans from q = 0.2 to q = 0.8 along the Eu(111) Bragg reflection. The two observed peaks indicate the existence of two antiferromagnetic (AFM) configurations with an oscillatory repetition of NS (AFM II at q = 0.5) and NNSS (AFM I at q = 0.25 and q = 0.75). At low temperature both AFM phases coexist. Between T = 2.5 and T = 3 K the AFM II state vanishes rapidly while the AFM I state remains still present until about T = 5 K. It should be noted that both AFM phases were predicted by theory (see figure 2), but the transition temperature from AFM II to AFM I is shifted to higher values. The theoretically predicted ferrimagnetic component could not be observed at all. The result differs from the measurement at the EuSe bulk sample at ILL, at which the ferrimagnetic contribution and the AFM I could be observed, but not the AFM II phase. A possible reason could be the different azimuthal orientations of the samples during the measurements.

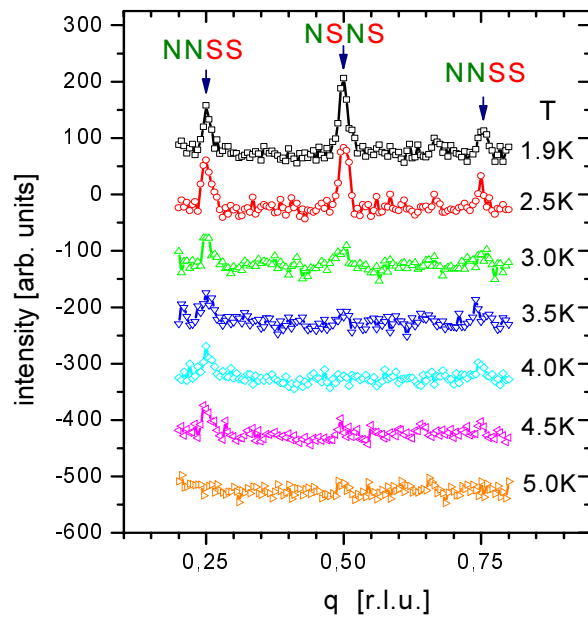


Figure 1: q-scans along (111) Bragg reflection of EuSe. AFM I and AFM II states are indicated with NS and NNSS, respectively.

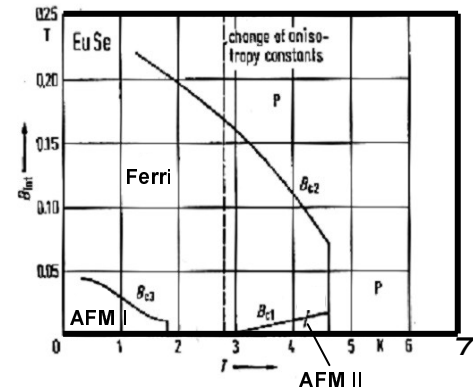



Figure 2: Magnetic Phase Diagram of EuSe. AFM I and AFM II states are indicated with NS and NNSS, respectively [5].

## Conclusion

The results clearly demonstrate the feasibility for magnetic diffraction experiments on the POLDI diffractometer at the GKSS neutron research facility even for very small signals in thin film samples. The low background of the GKSS neutron source compensates well for the approximately one order magnitude of reduced flux compared to the ILL reactor. Measurement times only triples to obtain comparable statistics. It must be noted that the POLDI diffractometer is particular designed for these kinds of experiment, while the ADAM instrument at ILL is a high resolution reflectometer which also permits diffraction measurements at higher angles. Encouraged by the result, even challenging diffraction experiments with low signals will be carried out at the GKSS neutron facility in the future.

## References

- [1] H. Kepa et al., Physica E 2, 399 (1998).
- [2] A. Stachow-Wojcik, Phys. Rev. B 60, 1522 (1999).
- [3] I. N. Goranchenko and I. Mirebeau, Phys. Rev. Lett. 80, 1982 (1998).
- [4] Experimental report of ILL (2002)
- [5] Griessen et al., Solid State Comm. 9, pp. 2219–2223 (1971).

	<b>EXPERIMENTAL REPORT</b>	<b>GeNF POLDI</b>
<b>Multiple reflection <i>Umweganregung</i> monochromator</b>		
<b>Principal Proposer:</b>	<b>P. Mikula</b> Nuclear Physics Institute, 250 68 Řež, Czech Republic	
<b>Experimental Team:</b>	<b>M. Vrána<sup>1</sup>, V. Wagner<sup>2</sup></b>	
	<sup>1</sup> Nuclear Physics Institute 250 68 Řež, Czech Republic	
	<sup>2</sup> Physikalisch-Technische Bundesanstalt, Braunschweig	
<b>Date(s) of Experiment:</b>	November 24–30, 2003	

Excitation of multiple reflection effects in cylindrically bent perfect Si single-crystals which result in *Umweganregung* were experimentally studied in 2002 and many strong umweg effects were determined [1] (see Figure 1). For the present experimental studies we chose the effect observed at  $\theta = 29.956^\circ$  which is related to the simulation of the forbidden 222 reflection through a co-operative action of two pairs 153/1-3-1 and -31-1/513 (secondary/tertiary) reflections at  $\lambda = 0.156$  nm. In order to estimate the instrumental resolution the monochromatic beam obtained in this way was then used for powder diffraction test carried out with a solid  $\alpha$ -Fe polycrystalline standard sample ( $\Phi = 8$  mm and 2 mm input and output slits were used).

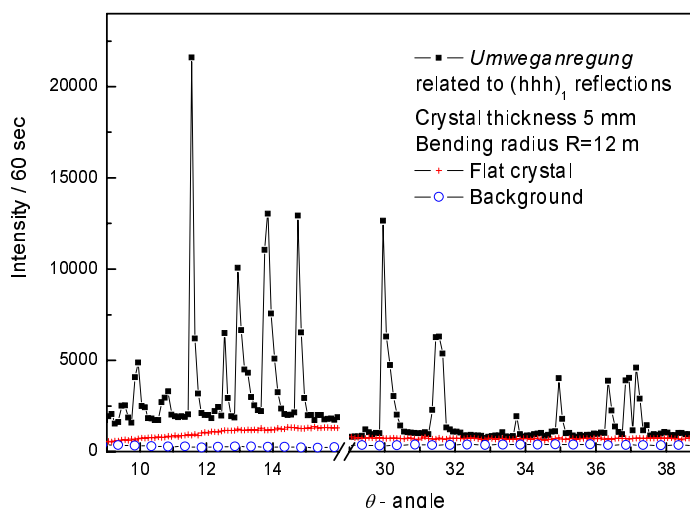


Figure 1: Part of  $\theta$ - $2\theta_b$  scan for the crystal slab having the largest face parallel to the planes (110) and set for  $(hhh)_1$  reflections in the symmetric transmission geometry.

Figure 2 displays several diffraction profiles that clearly prove the applicability of the umweg-monochromator for high-resolution diffraction studies. FWHM of the diffraction profiles are however, determined by the spatial resolution of the used PSD and the width of the slits [2].

Then, such a high-resolution diffraction performance we used for investigation of Fe-reflections in an induction hardened S45C rod ( $\Phi = 20$  mm) having different phase composition at different distances from the axis. Fig. 3 and 4 display the diffraction profiles obtained at

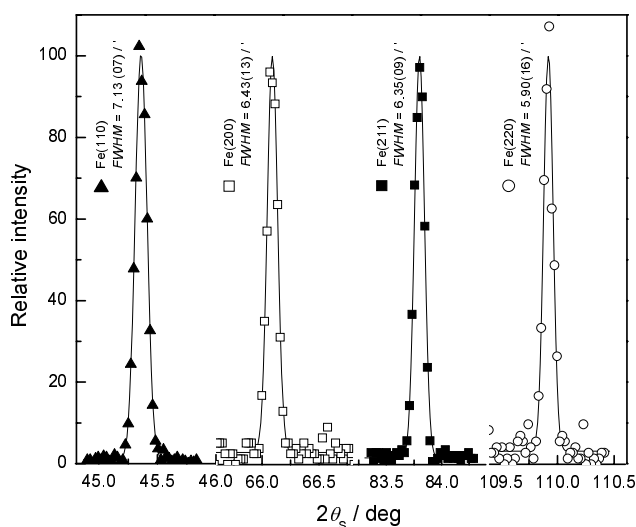
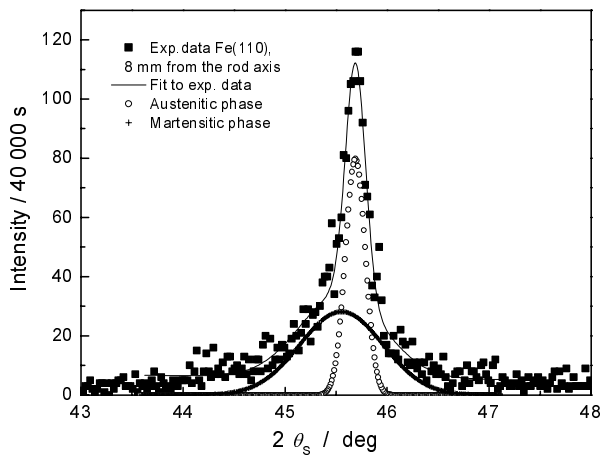
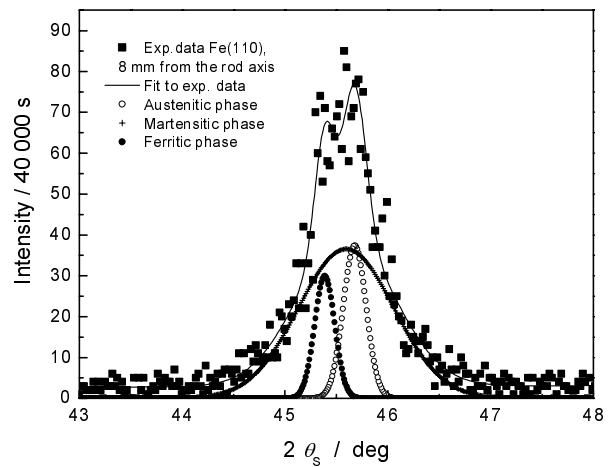


Figure 2: Examples of the  $\alpha$ -Fe diffraction profiles taken with the umweg-monochromator.

the distance 6 and 8 mm from the axis, respectively. Thanks to the used high-resolution monochromatic beam, after a fitting procedure we could reliably determined contributions of the individual phases.



*Figure 3:* Induction-hardened S45C steel diffraction profile taken at the distance of 6 mm from the rod axis with the fitted profiles corresponding to the martensitic and austenitic phases.

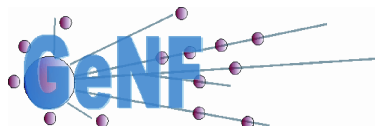


*Figure 4:* Induction-hardened S45C steel diffraction profile taken at the distance of 8 mm from the rod axis with the fitted profiles corresponding to the ferritic, martensitic and austenitic phases.

Diffraction meters employing umweg-monochromator can provide ultra-high resolution with a rather low take-off angles. The resolution is comparable to that of back-scattering instruments. Of course, they can be efficiently used namely at high-flux neutron sources.

## References

- [1] P. Mikula, M. Vrána and V. Wagner, *On a possible use of multiple Bragg reflections for high resolution monochromatization of neutrons*, In Proc. of the ECNS 2003 Conference, September 3–6, 2003, Montpellier, France, Physica B, accepted.
- [2] P. Mikula, M. Vrána, M. Furusaka, V. Wagner, Y. N. Choi, K. Moon, V. T. Em and C. H. Lee, *Bragg Diffraction Optics Based on Cylindrically Bent Crystals in Neutron Scattering Instrumentation*, In Proc. of the Int. Conf. NOP 2004, January 13–16, 2004, Tokyo, Japan, Nucl. Instrum. Methods, submitted.



## Geesthacht Neutron Facility (GeNF)

Max-Planck-Strasse,  
D-21502 Geesthacht

Telephone +49 4152 87-1205  
Telefax +49 4152 87-1338

### ***Application for the use of Neutron Scattering Facilities at FRG-1***

Electronic file download at: <http://genf.gkss.de>

**Experiment title:**

**Organisation:** ☐ University ☐ Research Institute ☐ Industry ☐ internal

This is

- ☐ a new proposal;  
☐ a continuation proposal; then please attach a report on previous results  
☐ Tick box if support by EU programme "Access to Research Infrastructure" is requested

**Category** ☐ Material Science ☐ Chemistry ☐ Biology ☐ Physics  
☐ Engineering ☐ Geoscience ☐ Medicine ☐ Other

<b>Proposer:</b> (title, surname, initials)	Address:	Phone: Fax: E-Mail:
<b>Co-Proposer 1:</b>	Address:	Phone: Fax: E-Mail:
<b>Co-Proposer 2:</b>	Address:	Phone: Fax: E-Mail:
<b>Other Proposers:</b>	Address:	Phone: E-Mail:
Instrument required:	Days required:	Requested starting date:

**Experimental details:**

- ☐ Polarized neutrons      Wavelength [nm]:  
☐ Non- polarized neutrons      Approx. range of momentum transfer:

### Sample environment

To be provided by GKSS:

- ☐ Magnet, horizontal      ☐ Cryostat, horizontal      ☐ Closed cycle refrigerator  
☐ Magnet, vertical      ☐ Cryomagnet, vertical

Temperature range:

Magnetic field strength:

Others:

If sample environment equipment will be provided by user, please give details:

### Experimental details:

- ☐ Polarized neutrons      Wavelength [nm]:  
☐ Non- polarized neutrons      Approx. range of momentum transfer:

### Description of sample

Substance formula:

- ☐ solid      ☐ liquid      ☐ powder  
☐ single crystal      ☐ polycrystal      ☐ gas  
☐ other

Size:

Weight:

Container required:

### Safety aspects

Is the sample

yes

no

toxic?

☐☐

explosive?

☐☐

flammable?

☐☐

radioactive?

☐☐

contaminant?

☐☐

corrosive?

☐☐

Is there any other danger associated with  
the proposed sample or sample environment?

☐☐

If yes, what are the risks?:

Estimated sample activation during experiment (Bq):

After the experiment the sample will be

- ☐ removed by user      ☐ stored at GKSS      ☐ given to GKSS-disposal

Are the experimentalists licensed to handle radioactive materials?

(§ 3 Strahlenschutzverordnung)

☐ yes

☐ no

Are the experimentalists security screened?

(§ 12b Atomgesetz)

☐ yes

☐ no

– Access is limited to persons whose trustworthiness is predetermined –

***The proposer is obliged to send a report on the experimental results to GKSS not later than 3 months after finishing the experiment.***

***The proposer certifies that the above details are complete and correct.***

Date:

Signature of proposer:

**Description of the proposed experiment:**

*(Outline of the scientific background and relevant features of the envisaged experiment; aims of the experiment and results to be achieved; preliminary work carried out – about 1 to 2 pages.)*





## **Appendix I**

### **Progress Report 2003 of the REFSANS Project**



## Introduction

REFSANS is a time-of-flight (TOF) instrument with three double disc choppers which allow setting the wavelength resolution in the broad range of  $0.25 \% < \Delta\lambda/\lambda < 15 \%$  to meet the different experimental demands comprising high and low resolution reflectometry and small-angle scattering at grazing incidence (GI-SANS) [1, 2 ,3]. The instrument is being built at the end of the cold neutron guide NG-2b with 12mm high and 170mm wide beam cross-section. This unusually broad beam is used to install radially collimating neutron optics to substantially improve the GI-SANS capability of REFSANS.

## Neutron optical design

REFSANS is equipped with novel Neutron guide elements (NGE) which allow continuing the beam of NG-2b through REFSANS (upper channels in Figures 1a and 1b), collimating the beam vertically while maintaining the horizontal divergence (lower channel in Fig. 1b).

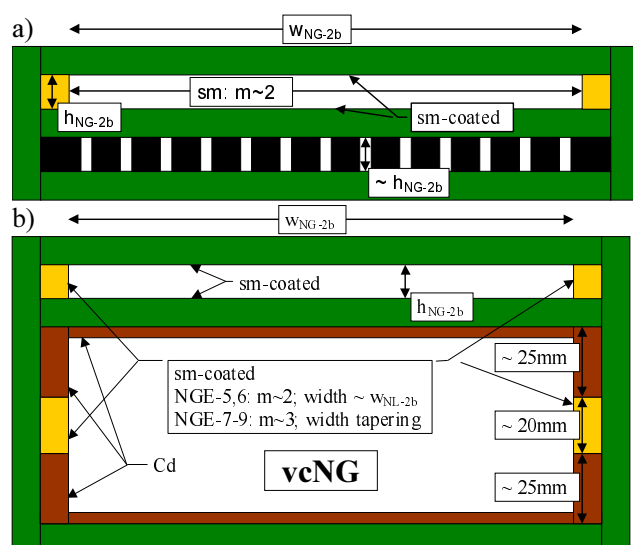


**Figure 1:** Cross-sections of neutron guide elements (NGE) of REFSANS, perpendicular to the beam direction (a: NGE-3 and -4; b: NGE-7 and -8).

reflecting the beam from top to bottom (or vice versa) onto the sample surface by means of the upper channels of NGE's-3, -4, -7, and -8 (Figure 1 and upper chart in Figure 2). A further possibility for declining the beam at an angle of  $\approx 180$  mrad is provided by a special bender (see beam B4 in upper chart of Figure 2). Finally, the lower channels of NGE-3 and -4 (Fig. 1a) may be moved into the beam to separate and pre-collimate 13 partial beams which are focused in the detector plane at a distance of  $\approx 9$  m from the sample. The separation of the latter is maintained in the beam guide chamber over  $\approx 8$  m by ancillary diaphragms with comb-like apertures (Figure 2, central chart and Figure 3).

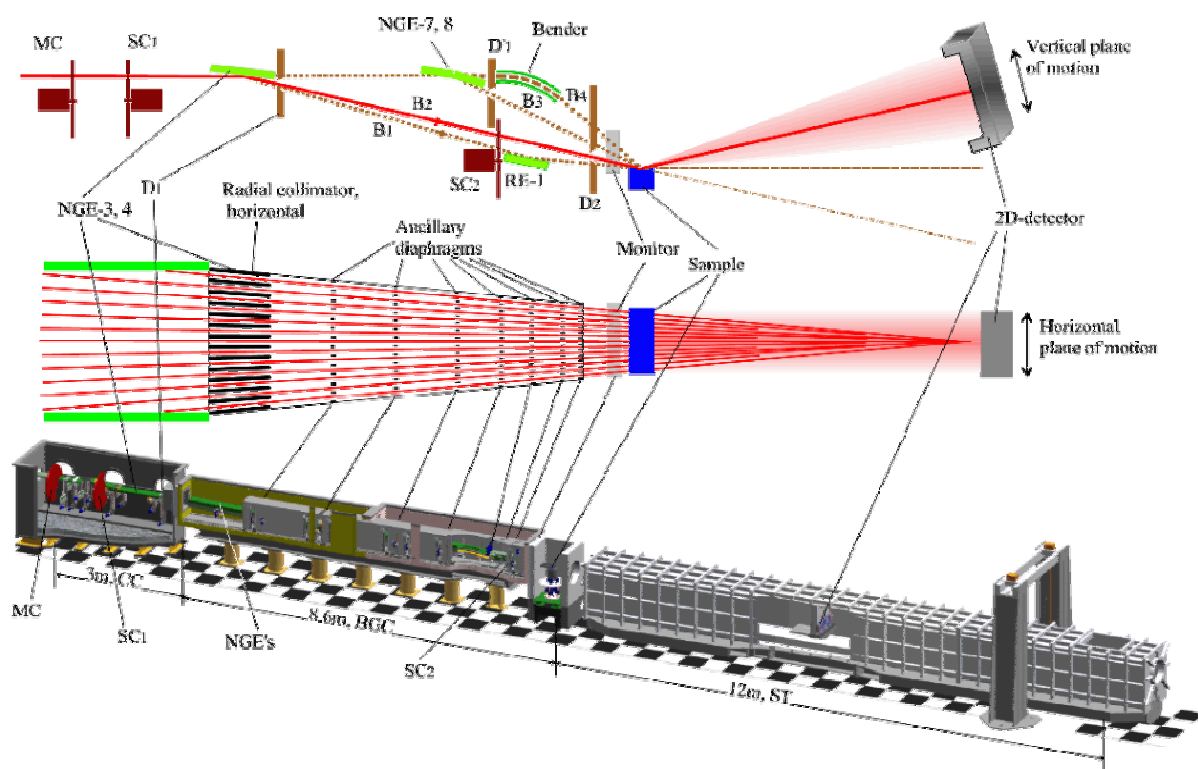


Figure 2: Schematic view of REFSANS and its neutron optics, details are mentioned in the text.

The intensity of such radially focused beams hitting a sample with a size of  $\approx 60 \text{ mm} \times 60 \text{ mm}$  has been calculated on the basis of the brilliance of the cold source of FRM-II and accounting for the expected transmission of the chopper, the neutron optics and the radially

collimating system [3]. An excellent peak intensity is calculated for the case of a resolution in momentum transfer of  $\Delta q/q \approx 14\%$  (Figure 4). It is pointed out that this results on the one hand from the excellent transmission of the 3-double-disc chopper which is close to that of a 10 % selector and on the other hand from focussing of 13 beams in the detector plane. This altogether results in an intensity which would be expected if 13 modern SANS facilities at a high flux reactor would be arranged in focussing and grazing incidence geometry.

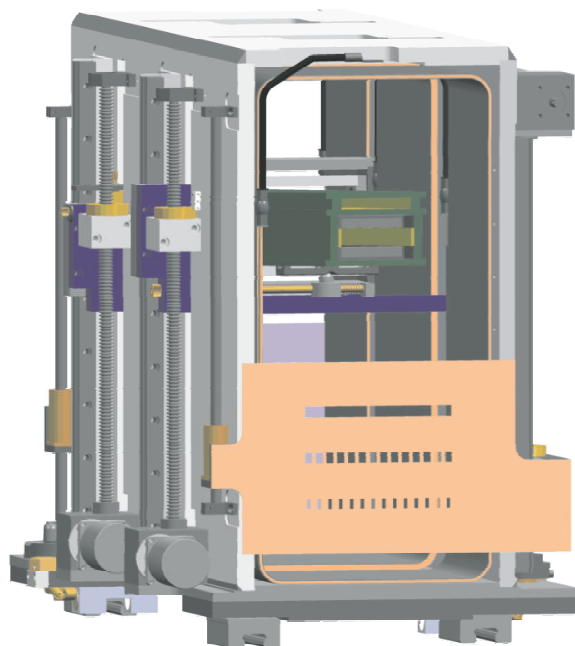


Figure 3: Neutron optical body in the beam guide chamber with the mechanics for vertically aligning a NGE and an ancillary diaphragm.

Due to this very high beam intensity at grazing incidence REFSANS is expected to offer new GI-SANS perspectives. Today's measuring times could be decreased by an order of magnitude and time dependent GI-SANS studies will become feasible. All investigations may be performed at the air-water interface with

horizontally aligned samples and may be combined with further measurements of the specular reflectivity to characterise comprehensively vertical and horizontal surface structures.

The intensity may be further increased by almost one order of magnitude by increasing the vertical beam divergence (Fig. 4). This can easily be achieved by guiding the 13 partial beams in the upper channels of the neutron guide elements in the beam guide chamber (Figs. 1 and 2). This geometry will especially allow of measuring extremely weak diffuse surface scattering from very small lateral structures and of following the tails of diffuse surface scattering patterns.

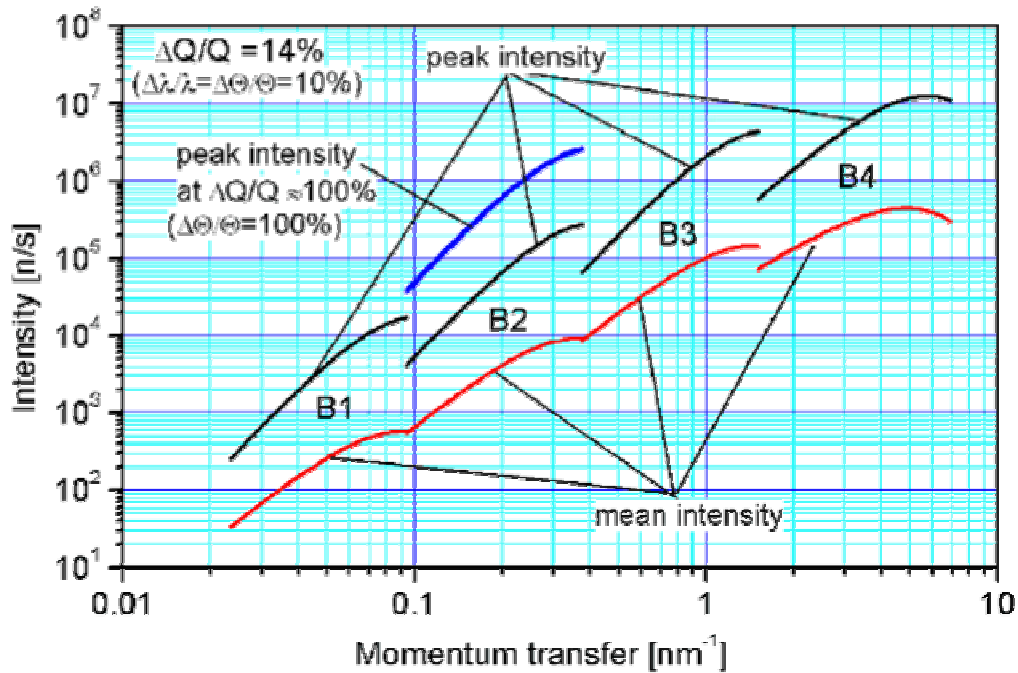


Figure 4: Calculated peak and time averaged beam intensities  $I_{\text{peak}}$  and  $I_{\text{mean}}$  of 13 beams horizontally focused in the detector plane (details in the text).

## Acknowledgements

The great contribution of the technical department of GKSS to constructing and manufacturing of REFSANS components is gratefully acknowledged. The development of REFSANS has been supported by the German Federal Ministry of Education, Research, and Technology (BMBF) under Contracts Nos. 03-KA5FRM-1 and 03-KAE8X-3.

## References

- [1] Kampmann, R., Haese-Seiller, M., Marmotti, M., Burmester, J., Deriglazov, V., Syromiatnikov, V., Okorokov, A., Frisius, F., Tristl, M., Sackmann, E. *Applied Physics A*, 74, (2002), 249–251.
- [2] Kampmann, R., Haese-Seiller, M., Kudryashov, V., Deriglazov, V., Tristl, M., Daniel, C., Toperverg, B., Schreyer, A., Sackmann, E. *Applied Physics A*. In press.
- [3] Kampmann, R., Haese-Seiller, M., Kudryashov, V., Deriglazov, V., Tristl, M., Schreyer, A., Sackmann, E. *Nuclear Instruments and Methods A*. Submitted.



## **Appendix II**

**Reports of experiments carried out  
at HASYLAB / DESY by GKSS personel  
– GKSS outstation HARWI-II at DESY –  
as responsible experimenters in support of external users.**

**These reports have been taken from  
HASYLAB Annual Report 2003.**

(reprints by courtesy of DESY, Hamburg)





# HARWI-II Materials Science Beamline

The GKSS-Forschungszentrum Geesthacht, Germany, is building a new high-energy beamline at DORIS storage ring. The outstanding characteristic of this beamline will be the use of Xrays in the energy range from 20 - 250 keV. The project is a collaboration of the HGF centres DESY Hamburg, GFZ Potsdam and GKSS Geesthacht. While DESY provides the source, the two other HGF labs in the collaboration focus on reserach on engineering (GKSS) and on geological (GFZ) materials, respectively.

## A: High-energy beamline HARWI-II

*F. Beckmann, T. Lippmann, J. Metge, R.V. Martins, T. Dose, and A. Schreyer*

GKSS-Forschungszentrum Geesthacht, Max-Planck-Str. 1, 21502 Geesthacht, Germany

The GKSS-Forschungszentrum Geesthacht, Germany, will setup the new high-energy beamline HARWI-II specialized for texture, strain and imaging measurements for materials science. Four different experiments will be installed at the new wiggler HARWI-II. A high pressure cell will be run by the GFZ Potsdam, Germany, a high-energy diffractometer together with a microtomography camera will be run by the GKSS. A further station will allow space for the diffraction enhanced imaging setup. The optics will provide for a small white beam ( $0.5 \text{ mm} \times 0.5 \text{ mm}$ ) and a large monochromatic X-ray beam ( $50 \text{ mm} \times 10 \text{ mm}$ ) with an energy range of 20 to 250 keV.

The beamline consists of three hutches: a 8 m long optics hutch, a 12 m long first experimental hutch, and a 5 m long second experimental hutch (fig. 1). The optics hutch mainly contains the vacuum tank for the different monochromators. In the first experimental hutch a big diffractometer, a tomography camera, a diffraction enhanced imaging (DEI) station, and various detector systems up to 9 m away from the diffractometer are foreseen. The second experimental hutch houses the GFZ high pressure (HP) device MAX200x for geophysical studies. Fig. 2 gives a 3-dimensional impression of the future beamline.

## New wiggler HARWI-II

The design goal for the new HARWI wiggler was a maximized flux at 100 keV at an aperture of about  $10 \times 10 \text{ mm}^2$ . The insertion device has a period length of 110 mm and total length of 4 m giving a flux of about  $5 \times 10^{13} \text{ ph/s/0.1\% BW}$  at 100 keV and at an aperture of  $30 \times 5 \text{ mm}^2$ . Fig. 3a shows that at this energy the new device delivers a factor of 20 more than the existing wiggler at the HARWI beamline and still a factor of 2 compared to the BW5 beamline. The figure shows the curves calculated for  $1 \times 1 \text{ mm}^2$ . In a wide range the flux scales linearly with the area of aperture. The minimal gap will be 14 mm, the peak field 1.96 T and the wiggler will have a K-value of 21 all together giving a critical energy of 26 keV. The total power is 28 kW and the on-axis power density reaches  $41 \text{ kW/mrad}^2$ . The horizontal/vertical divergence at 30 keV will be 4 mrad/0.15 mrad and at 100 keV 2.2 mrad/0.05 mrad. For other energies (10, 20, and 100 keV) fig. 3b shows the flux density distribution in horizontal and vertical direction and indicates the beam divergence near the entrance of the optics hutch.

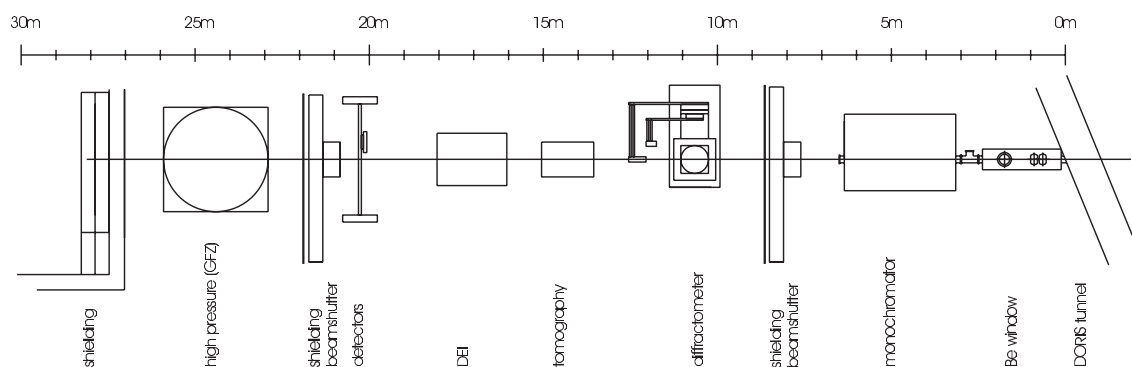


Figure 1: Scheme of the new high-energy beamline HARWI-II at HASYLAB.

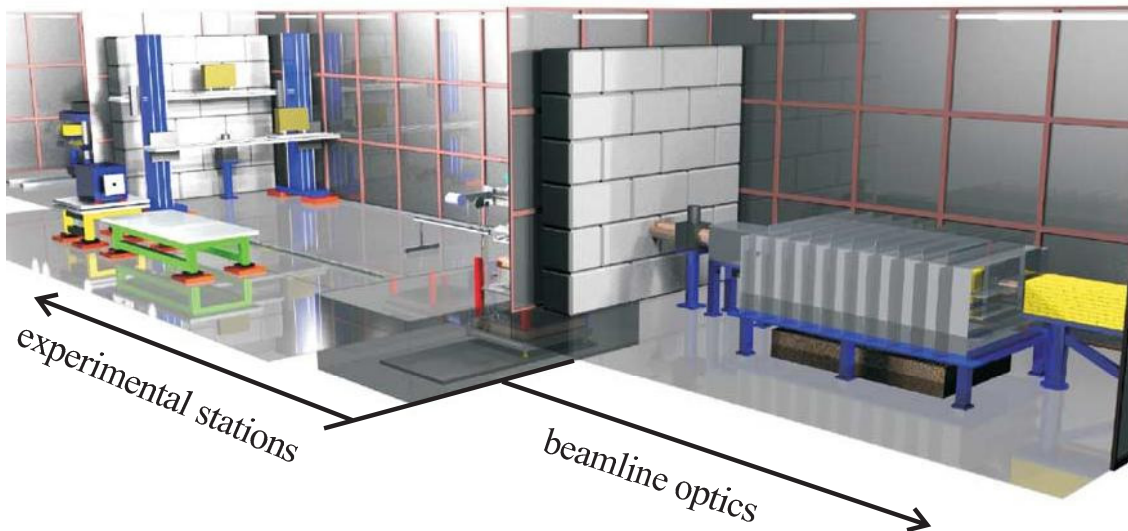


Figure 2: 3-dimensional view of the beamline. Three hutches: a 8 m long optics hutch (right), a 12 m long first experimental hutch (middle), and a 5 m long second experimental hutch (left).

## Beamline optics

The entrance of the monochromator tank is about 39 m downstream of the new HARWI wiggler. An 1.5 mm Al filter will be permanently installed as a high pass filter. For the use of high photon energies (above 60 keV) a 1 mm Cu filter can be placed into the beam. For the GFZ high pressure experiment at the end of the beamline a white beam with a size of  $0.5 \times 0.5 \text{ mm}^2$  is foreseen. Two different types of monochromators which both will be operated in vacuum will be set up.

### Horizontal monochromator

The first type of monochromator will be a double Laue monochromator in horizontal geometry which will deliver beams of  $10 \times 10 \text{ mm}^2$  in size. The energy range will be 50 to 250 keV and an offset of 3 cm of the diffracted beam. These parameters determine the length of the monochromator tank which will be about 3 m long, 2 m broad and 1 m high s. fig. 2.

### Vertical monochromator

The second monochromator will produce a beam size of 50 mm in width and 10 mm in height in a vertical diffraction geometry optimized for imaging techniques like tomography and diffraction enhanced imaging (DEI). The energy ranges from about 20 keV up to 200 keV. In order to accept the relatively divergent wiggler beam the first crystal will be a bent Laue Si single crystal. As the 2nd crystal either another bent Laue crystal of the same type or a Bragg crystal can be used. The beam offset will be about 4 cm.

## Experimental stations

### Diffractionmeter

One of the instruments at the new material science beamline at HARWI will be a diffractometer specialized for high photon energies. In order to allow many different experiments we defined the following boundary conditions: The instrument will have a standard, permanently installed, tower setup with an interface on top of it. Users can attach further optional goniometers and their own sample environment and equipment. The standard setup will be flexible enough to allow many different experimental setups and will therefore be equipped with various translation, rotation and tilt stages in order to have many degrees of freedom. The tower will be large enough to carry heavy samples and heavy environments as tanks, cryostats, stress rigs or superconducting magnets. And finally, a high resolution and a good reproducibility of the movements is intended in order to

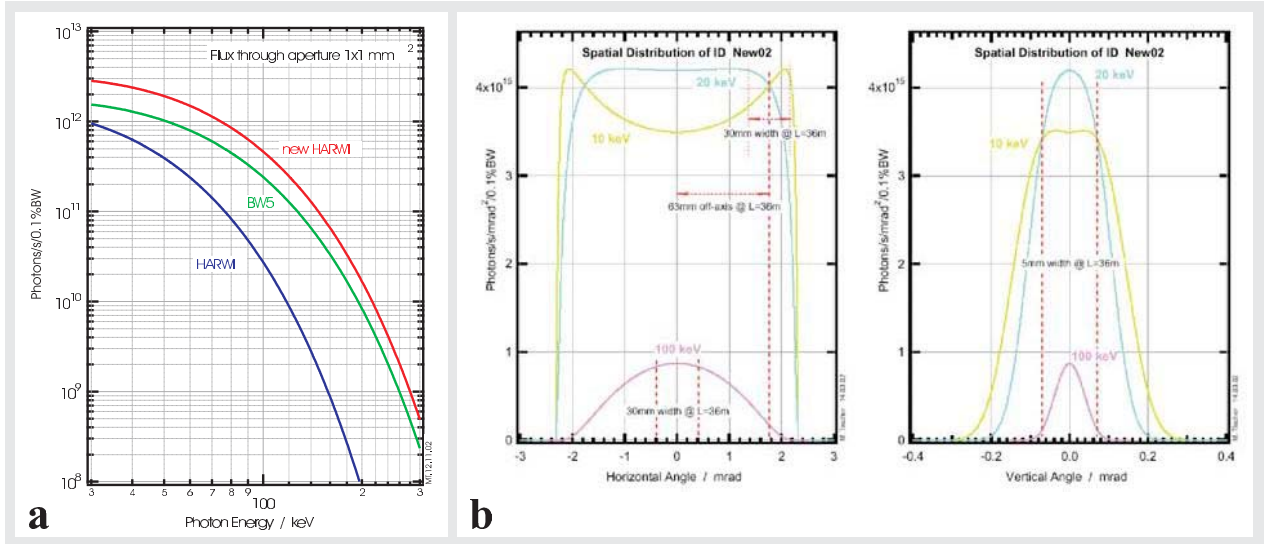


Figure 3: a: Comparison of wiggler spectra for the new HARWI-II, the old HARWI and the BW5 beamline. BW5 is the only other high-energy beamline at HASYLAB. b: Flux density at different energies in the horizontal (left) and vertical (right) direction.

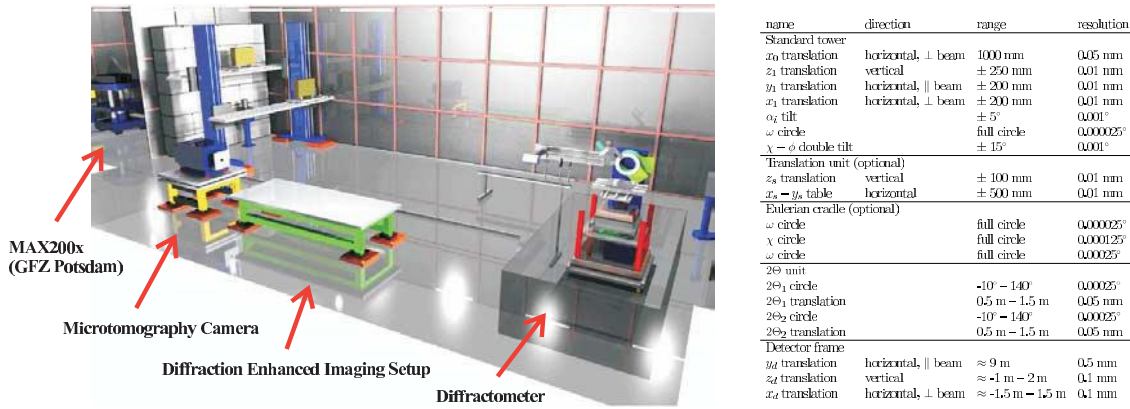


Figure 4: Left: 3-dimensional view of the experimental stations. Right: Components for the sample tower of the diffractometer (from bottom to top).

investigate small volumes (even single grains) inside large samples. The table shown on the right side in fig. 4 lists all components of the sample tower.

As shown on the right side in the 3-dim. view (fig. 4 left), detectors can be mounted on two 2 $\Theta$ -arms for scattering in the vertical plane. The sample-detector distance will be adjustable via additional translation stages mounted on the arms. It is planned to offer different kinds of 2-dimensional detectors: a CCD, an image plate scanner and Gas-Wire detectors as well as new detector developments. Moreover, an energy-dispersive Ge detector and a scintillation counter will be available. In addition, detectors can be mounted on a large movable frame in order to position them at any desired location behind the sample. The maximum sample-detector distance will be  $\approx 9$  m.

## Microtomography setup

The tomography camera mainly consists of an efficient X-ray detector and a high-precision sample-manipulator stage. The 2-dim. X-ray detector is specially equipped to detect the high-energy X-ray beam. Using an optics with variable focus the field of view can be adapted to the diameter of the investigated sample in the range of 3 to 50 mm. Spatial resolution up to 3  $\mu$ m can be achieved in the tomogram. The sample manipulator provides a high precision rotation, translation and repositioning of the sample. This is the prerequisite for scanning micro-tomography allowing the investigation of samples larger than the field of view of the detector. The system will be designed to operate

with photon energies from 20 to 200 keV.

### Diffraction enhanced imaging (DEI) setup

DEI is a relatively new imaging method for biological and other light materials. Boundary layers inside the sample produce small angle scattering which can be analyzed with single crystal reflections. At the slope of a rocking curve a high contrast enhancement can be achieved even for boundaries where the refraction index varies only little.

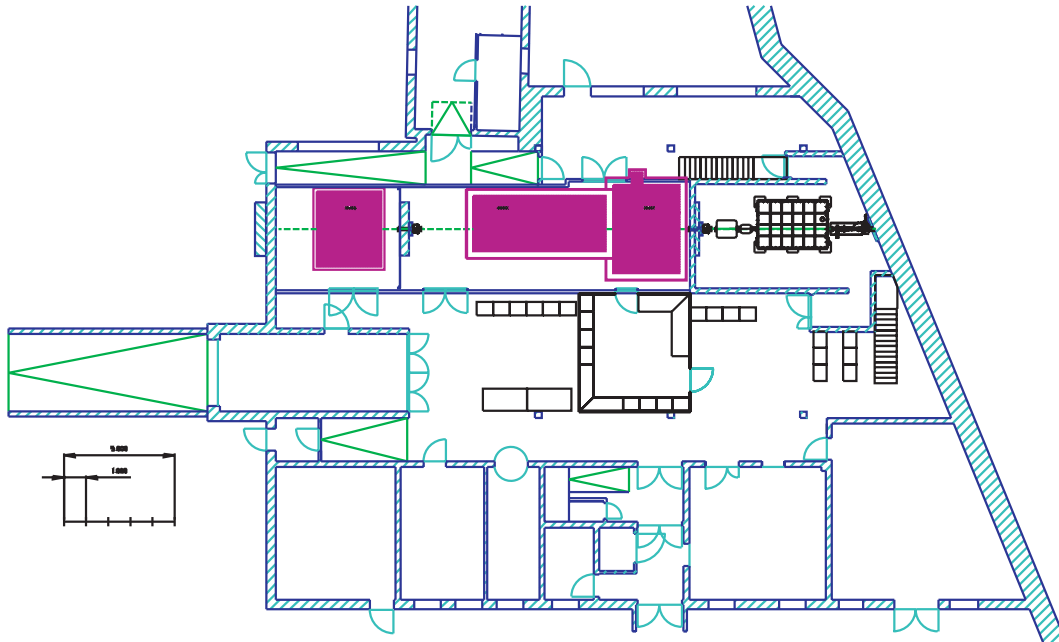


Figure 5: Scheme of the current layout of the HARWI-II beamline. The monochromator hutche will be built out of concrete. In the experimental hutches three pits will house the different experiments.

### Status and Time Table

In September 2003 the last experiments at the old HARWI wiggler were performed. From September to November 2003 the old experimental environment and beamline hutches were removed. The reinstallation of the beamline will start January 2004. In figure 5 the current beamline layout is presented. During the summer shutdown in August 2004 the new wiggler will be installed. First operation of the new beamline HARWI II is supposed to be in September 2004.

# Analysis of Bony Tissue around Titanium Implants with Synchrotron Radiation Microtomography and Histology

*R. Bernhardt, E. Pilling<sup>1</sup>, R. Mai<sup>1</sup>, D. Schamweber, F. Beckmann<sup>2</sup>, H. Worch*

*Max Bergmann Center for Biomaterials, Dresden University of Technology, Dresden, Germany*

*<sup>1</sup> Department of Maxillo-Facial Surgery, Faculty of Medicine, University of Technology, Dresden, Germany*

*<sup>2</sup> GKSS-Research Center, Geesthacht, Germany*

## Introduction

A main field in biomaterials research is the surface modification of titanium implants to improve the implant healing behaviour. There are various methods to confirm the success of such bio-functionalizations.

Beside histological investigations, in this work we have used x-ray microtomography with synchrotron radiation (SR  $\mu$ CT) as a non-destructive method to detect and analyse the osteointegration of titanium implants in all three dimensions. The aim of this work was the comparison of bone detection in the SR  $\mu$ CT-volume to filtered images from histological slices with similar analysis procedures.

## Materials and Methods

From a mini-pig experiment samples containing bio-functionalised Ti-implants with surrounding tissue after a healing time of 6 months in the jaw were selected for a comparative investigation.

The SR  $\mu$ CT experiments were performed at HASYLAB BW5 (DESY, Hamburg, Germany). Formalin fixed cylindrical samples were prepared with a diameter of about 8 mm, containing the implant nearly centred within the bony tissue. With a photon energy of 70 keV and an image size of 1536 x 1536 pixels from each sample 720 projections were recorded. A filtered back projection algorithm was used to obtain the three-dimensional data of x-ray absorption for the samples. The visualization of the reconstructed data was done with a volume rendering software (VGStudio, Volume Graphics, Germany). After SR  $\mu$ CT measurements the samples were histologically prepared (embedding: Technovit 9100 neu, slice spacing: 500  $\mu$ m, staining: Masson-Goldner). Automatic and semi-automatic analysis procedures were created to record the amount of mineralized bone around titanium in the SR  $\mu$ CT volume and the histological images.

## Results

The rendering procedure of the x-ray absorption values for bony tissue from SR  $\mu$ CT resulted in a detailed visualization of bone morphology with a spatial resolution of about 9  $\mu$ m (Fig. 2). Also a sharp implant/bone interface is visible. To find bone thresholds in microscopical images from histological slices (Fig.1, bottom), we had to use colour splitting and histogram arrangements. The cavity analysis for an exemplary sample shows no significant difference in the mean bone value between microtomography and histology (Fig. 3). Slicing the whole CT volume (281 slices) with the same orientation used for histology we detected bone amounts in the cavity of 17 % - 54 % compared to 23 % - 38 % from 6 histological slices. The standard error of the mean bone value (SE) was 0.4 % using the  $\mu$ CT volume and 2.7 % with the histological images.

# Discussion

Related to the detailed three-dimensional visualization of bony tissue around titanium implants, the SR  $\mu$ CT measurements have proven their reliability in the field of osteointegration analysis. Taking the wide range of detected bone amounts with SR  $\mu$ CT into account, the results in histology depend on a much too limited number of randomly positioned slices with a large slice distance. A further problem for an automated histological image analysis is the non-uniform staining of the bony tissue, which makes distinction between tissues sometimes difficult. This also concerns the geometrical setting of reference areas in the images. The advantage of histological imaging is still the superb lateral resolution and the visualization of biochemical tissue properties. But with a view to a statistical relevant analysis of a large tissue volume and high samples number, visualization and quantification is more practicable with SR  $\mu$ CT. Considering all these aspects, a combination of classical histology with SR  $\mu$ CT will be a powerful instrument for an improved understanding of biological reactions around bio-functionalized implants.

This study will be continued with different bio-functionalized implants using strategies of contrast enhancement in SR  $\mu$ CT in conjunction with bone mineralization.

# Acknowledgments

The authors kindly acknowledge the DFG (DFG-FG 308/3) and the HASYLAB (II 00-41) for the support.

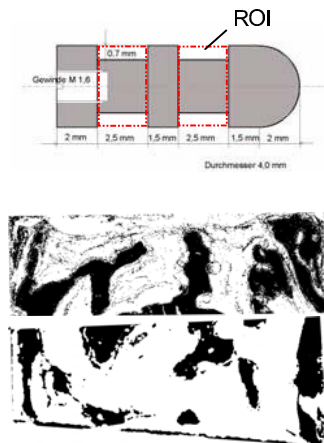


Figure 1: top: implant design; bottom: images from histological slices inside the marked region of interest (ROI)

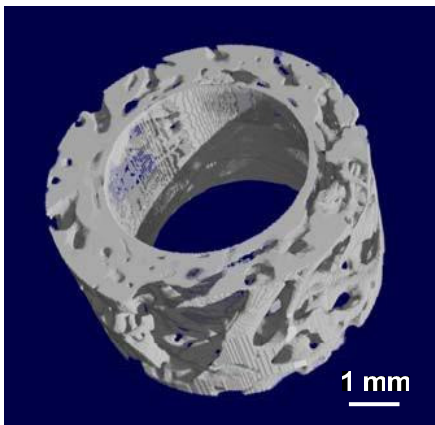


Figure 2: 3D view of bony tissue inside the ROI from SR $\mu$ CT at HASYLAB BW5 (implant transparent)

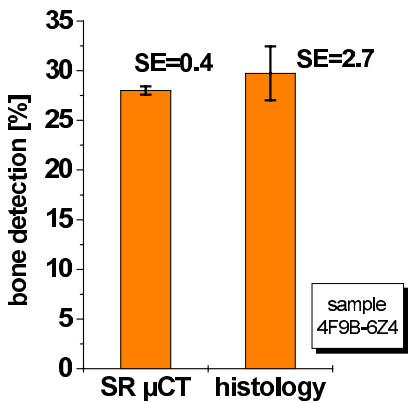


Figure 3: Analysis of bone values inside the ROI from SR  $\mu$ CT and histological data

# Investigation of Material Flow in Friction Stir Welds of Aluminium Alloys using Micro CT

R. Zettler<sup>1</sup>, T. Donath<sup>1</sup>, F. Beckmann<sup>1</sup>, J. dos Santos<sup>1</sup>, D. Lohwasser<sup>2</sup>, T. Lippmann<sup>1</sup>,  
and A. Schreyer<sup>1</sup>

<sup>1</sup>GKSS-Forschungszentrum Geesthacht, Max-Planck-Straße 1, 21502 Geesthacht, Germany

<sup>2</sup>Airbus Deutschland GmbH

Friction Stir Welding (FSW) is a solid state welding process i.e. no bulk melting of the base material occurs. The process was invented and patented by The Welding Institute (TWI) of Cambridge, 1991 [1]. Further development of the process through research centres such as the GKSS-Forschungszentrum has meant that FSW has become one of the most rapidly expanding technologies for the welding and joining of aluminium alloys within the Northern Hemisphere. The process essentially relies on frictional heating and plastic deformation via the use of a rotating and profiled tool consisting of a shoulder and pin, Figure 1.



Figure 1. FSW tool pin and shoulder.

The tool is plunged into and then traversed along the join line between typically two abutting workpieces. Intimate contact between the tool and workpiece surfaces causes the interfacing material to soften, flow and mix. A schematic of the process can be found in Figure 2.

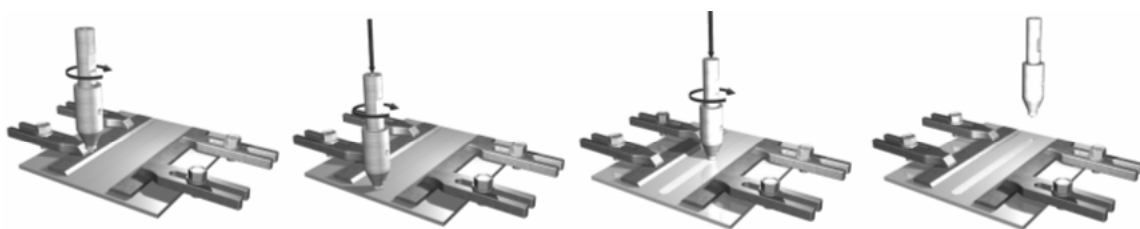


Figure 2. Schematic of FSW process. Left to right: tool plunge, traverse, retraction.

High hydrostatic compressive stresses and recrystallisation of workpiece material i.e. grains, in the vicinity of the so called weld nugget, as a result of specific tool geometry and processing parameters, helps to enhance material workability and mixing at the join line. The ability to mix and join abutting aluminium alloys at temperatures well below that of the melting point of the base material i.e. for cold welding conditions has shown for some heat treatable alloys that their ultimate strength is able to be increased to values approaching that of the base material [2].

Although many aluminium alloys can be joined by conventional fusion welding techniques, the difficulty of making high strength, fatigue and fracture resistant welds in aluminium alloys such as the highly alloyed 2xxx and 7xxx series have long inhibited the use of fusion welding processes for their joining.

Material flow studies of the FSW process have demonstrated that material is forced to flow in the direction of tool rotation [2]. Because the deformation process is generally not symmetric about the weld join line geometric and microstructural differences within the weld nugget zone and for both sides of a friction stir welded joint can arise. These can inhibit the potential of the material achieving optimum outcomes for the welded structure in terms of static and cyclic loading. The use of minute embedded marker materials within the friction stir weld has allowed for a much clearer visualisation of material flow resulting from the FSW process. In most cases the evaluation has occurred using metallographic examination. Metallographic examination, has proven to be extremely labour intensive and allows only for a 2D portrayal of the weld zone. A method to help facilitate a 3D perspective and much more rapid mapping of the deformation flow resulting from FSW is through the tracking of the embedded markers using Computer Tomography (CT). Work has been conducted by the GKSS Forschungszentrum GmbH, in Geesthacht Germany at the HASYLAB beamline W2 using micro-tomographic techniques to investigate material flow in friction stir welds produced for a number of aluminium alloys. The work forms part of a wider study titled “Effect of Material Flow Patterns on the Properties of Friction Stir Welds in Aluminium Alloys for Aircraft Structures” [EMFASIS]. The results to date for a friction stir welded 2024-T351 aluminium alloy embedded with marker material in the form of a Ti powder have demonstrated that marker flow, homogeneity of the weld zone structure and welding temperatures are very much influenced by tool geometry. Figure 3 (a and b) are representative renderings for marker material flow where the powder marker material has been embedded on the left and then right hand side of the weld join line respectively while being friction stir welded using identical welding pins and welding parameters.

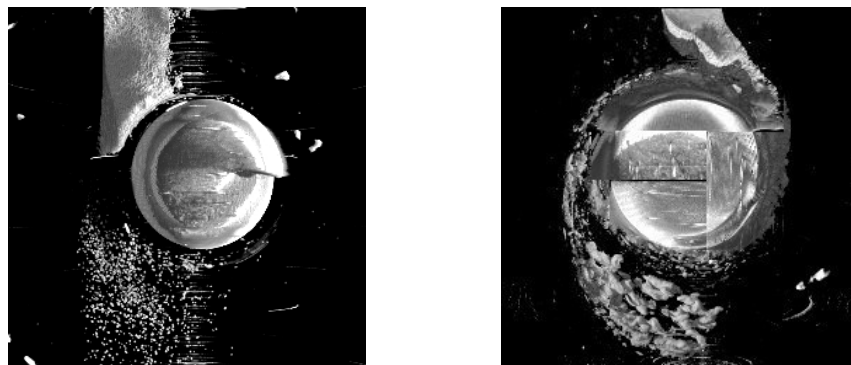


Figure 3(a),(b). Rendering of marker distribution around a welding pin of 5 mm diameter as seen from the top. Left hand caption reveals marker flow where marker embedded on left hand side of join line. Right caption revealing marker flow where marker embedded on right hand side of join line. Tool rotation clockwise travel direction up the page.

## References

- [1] Thomas WM, Nicholas ED, Needham JC, Church MG, Templesmith P, Dawes CJ: International Patent Application No. PCT/GB92/02203 and GB Patent Application No. 9125978.9, 1991.
- [2] London B, Mahoney M, Bingel W, Calabrese M, Waldron D; Experimental Methods For Determining Material Flow In Friction Stir Welds. The 3rd International Symposium on Friction Stir Welding, Kobe, Japan 27-28 September 2001.



# Measurement of metallic foam structure parameters by means of synchrotron $\mu$ CT

O.Brunke, S. Odenbach and F. Beckmann

<sup>1</sup>ZARM Universität Bremen, Am Fallturm, 28359 Bremen, Germany

<sup>2</sup>GKSS, Max-Planck-Str. 1, 21502 Geesthacht

Porous structures made from various metals like Al, Zn, Ti, Ni or Pb are referred to as metallic foams. Their unique combination of properties like high stiffness to weight ratio and a good resistivity against heat and aggressive media opens a wide field of possible applications in the construction of vehicles or aircrafts. Up to now several routes for the production of these foams have been developed. The method (FOMINAL) used for the samples examined during this study was developed by IFAM in Bremen. Following this method, a metal powder, in this case Al, is mixed with a so-called blowing agent, in this case  $\text{TiH}_2$  [1]. After that, the mixed powders are compacted at high pressure and temperature. This precursor material can now almost be machined like aluminium. The final step to produce the foam is the melting of the precursor in a furnace.  $\text{TiH}_2$  releases hydrogen and generates a foam-like melt. In order to conserve this porous structure the samples are cooled down below their melting point.

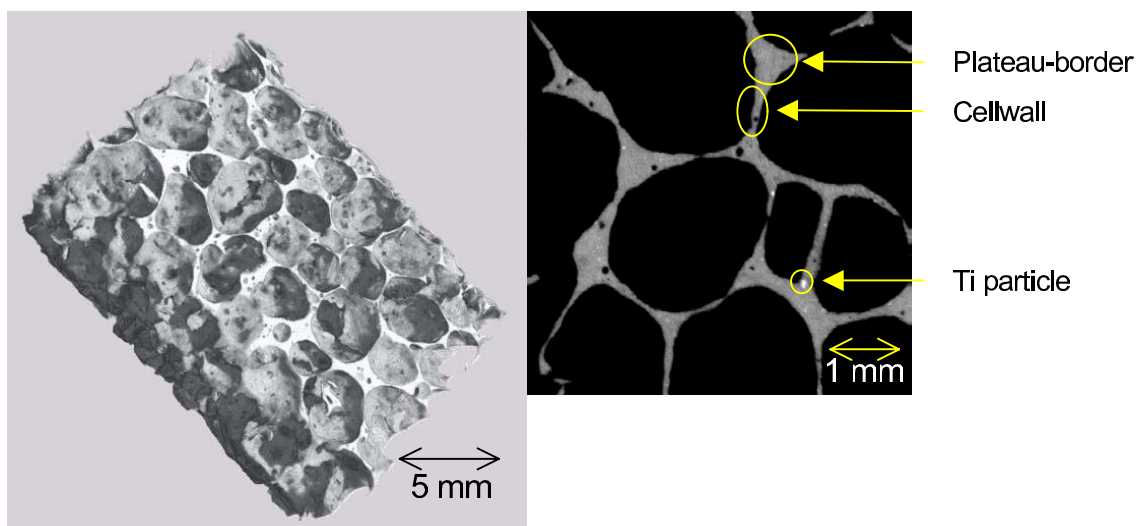


Figure 1: 3D representation of an Al-foam samples and a slice of the same dataset showing Ti particles with marked cell wall and Plateau borders

The most versatile tool for the non-destructive characterisation of the foam structure is the use of x-ray absorption tomography. Especially the properties of monochromatic synchrotron radiation offer the opportunity to get tomography datasets with a very high resolution combined with absorption contrast sensitivity. Though some studies using  $\mu$ CT for examining metallic foams have been studied, just a very few deal with quantitative analysis of the 3D datasets [2]. The goal of the present study is to determine a set of characteristic foam parameters, like density, pore size, cell wall size, plateau border size, etc. and their spatial distribution from these datasets. Accordingly, using these parameters the variation of external variables like temperature, time, blowing agent content, etc., which influence the foam structure, can be quantified and analysed. Figure 1 shows a typical rendered presentation of a Al-foam dataset and at the inset one can easily determine small bright spots which are the residuals of the Ti of the blowing agent.

The methods which have been developed and used for the quantitative analysis of the 3D-datasets are based on algorithms of the freeware image processing library DIPlib [3]. A detailed description will be presented elsewhere [4]. Figure 2 shows results for the pore (a) and cell wall (b) size distribution of an Al-foam which has been in the liquid state for  $t_f = 40$  s at a furnace temperature of  $T_f = 750^\circ\text{C}$ . The characteristic parameters which can be determined from the pore size diagram are the mean pore size and its standard deviation. Diagram (b) shows the size distribution of the solid

(Al) phase of the foam for the sample shown in Figure 1, derived by means of a granulometry algorithm. The two peaks correspond to the mean cell wall thickness and the mean plateau border diameter, as indicated in Figure 1, respectively. For the granulometry analysis, the position, width and integral of these two peaks are the corresponding characteristic parameters which can be used to describe the foam structure.

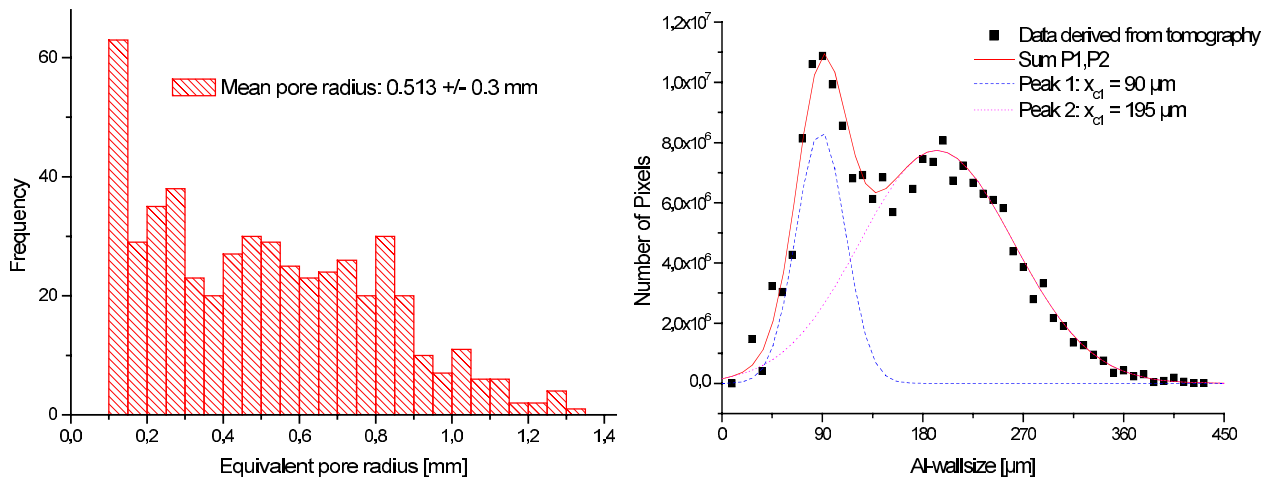


Figure 2 Pore size (a) and solid phase size distribution (b) of the sample shown in Figure 1

During the measurement campaigns at HASYLAB-beamline W2, Al-foam samples using different processing parameters like foaming time and temperature and being exposed to additional influence like e.g. Lorentz forces have been examined by means of  $\mu\text{CT}$ . Currently, the evaluation of these datasets with respect to the characteristic structure parameters is in progress and will be published soon [5].

## References

- [1] F. Baumgärtner, I. Duarte, J. Banhart, *Adv. Eng. Mat.* 2 (4), 2000
- [2] E. Maire, A. Fazekas, et al., *Comp. Sci. Tec.*, in Press (2003)
- [3] [www.ph.tn.tudelft.nl/DIPLib](http://www.ph.tn.tudelft.nl/DIPLib)
- [4] O. Brunke, S. Odenbach, F. Beckmann, Quantitative methods for the analysis of  $\mu\text{CT}$  datasets of metallic foams, to be published
- [5] O. Brunke, S. Odenbach, F. Beckmann, Determination of characteristic structure parameters of differently grown metallic foams by means of  $\mu\text{CT}$ , to be published

# Measurements of plastic displacement gradient components in 3D

S.F. Nielsen<sup>(1)</sup>, F. Beckmann<sup>(2)</sup>, H.F. Poulsen<sup>(1)</sup> and J.A. Wert<sup>(1)</sup>

<sup>(1)</sup> Materials Research Department, Risø National Laboratory, Denmark

<sup>(2)</sup> Hamburger Synchrotronstrahlungslabor HASYLAB at Deutsches Elektronen – Synchrotron DESY, Notkestrasse 85, 22607 Hamburg, Germany

A project was initiated in 2001 with the goal of using X-ray absorption microtomography to detect marker particle displacements inside a metallic material undergoing plastic deformation. The displacements of marker particles as a function of externally imposed strain are then used to deduce the internal strain in local regions, which is expected to differ from the externally imposed strain as a consequence of material inhomogeneity.

Data were acquired at the dedicated microtomography instruments at beamline BW2 and W2 at HASYLAB, for a cylindrical aluminium sample containing W particles with an average particle diameter of 7  $\mu\text{m}$ .

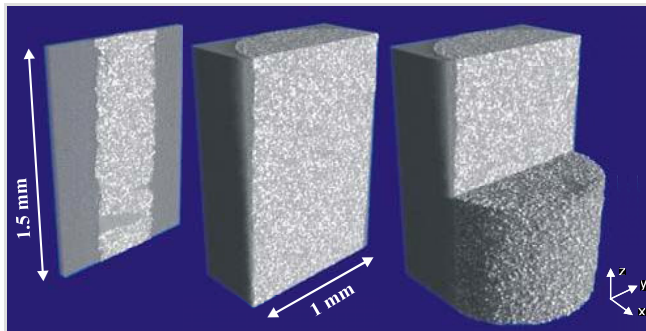
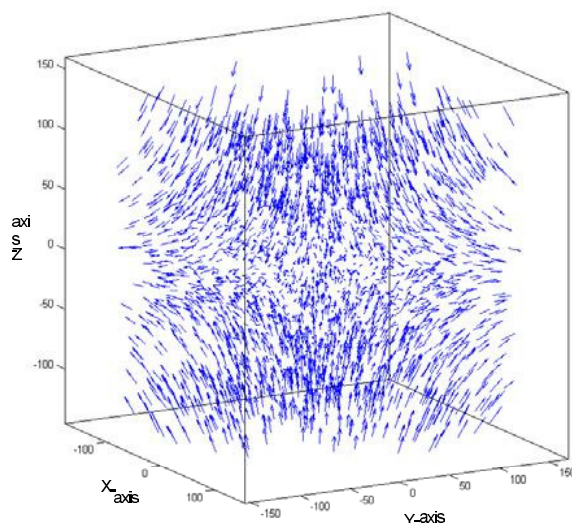


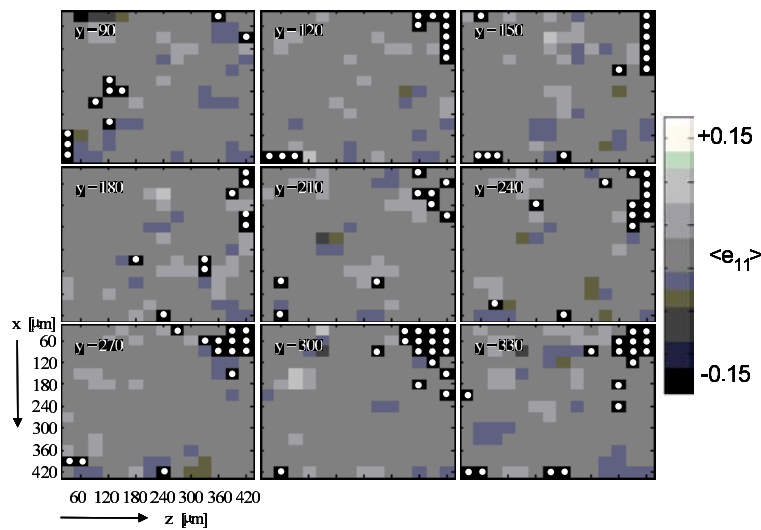
Illustration of the reconstruction of the Al-W sample after about 10% deformation: the W particles are shown as white within the cylindrical aluminium sample (grey).

The sample was compressed incrementally along the axis of the cylinder, with data for a tomographic reconstruction being acquired after each deformation step. By applying image analysis steps to identify the centre of mass of individual particles and align the successive tomographic reconstructions, the displacements of individual particles could be tracked as a function of external strain.



The vector displacement tracks of 2544 particles within a 0.4 mm cube inside the sample. The numbers on the axes are in units of pixels of 1.5  $\mu\text{m}$ .

The particle displacements are then used to identify local displacement gradient components in 3D. This allows us, for the first time, to map the strain tensor as a function of location inside a deforming metallic solid.



The figure shows a series of maps representing the strain component parallel to x direction indicated in the previous figure.

The strain is expected to be fairly uniform in this fine-grained sample, but regions of modestly greater and lesser values of this normal strain component can be identified in the maps.

The project until now has been in a technique evaluation phase. We have demonstrated a universal method for bulk materials that contain particles or voids observable by X-ray microtomography. The method has been demonstrated using an Al alloy containing W particles. The strain resolution is  $10^{-2}$  on the measurements of displacement gradient components while the spatial resolution depends on particle spacing, in the present case 30  $\mu\text{m}$ .

In upcoming stages of the project, we will use this technique to evaluate the effect of local grain orientation on local plastic strain in coarse grain materials, allowing us to test 6 decade-old theories of metal deformation that remain incompletely tested. We also envision that this technique can be used to study deformation of foams, strain fields around cracks, deformation of biological materials, etc. Since the technique does not depend on diffraction, the evaluation can be applied to any material, crystalline or amorphous, to which marker particles providing sufficient X-ray absorption contrast have been introduced. We believe that the technique we have demonstrated provides an avenue for quantitative analysis of microtomography images with a great number of possible applications.

## References

S.F. Nielsen, H.F. Poulsen, F. Beckmann, C. Thorning, J.A. Wert. Measurements of plastic displacement gradient components in three dimensions using marker particles and synchrotron X-ray absorption microtomography. *Acta. Mater.* **51** (2003) 2407-2415.

# Micro-CT Investigations of Bone Absorption caused by Rheumatoid Arthritis in an Animal Model

R. Bernhardt, K.-P. Hummel<sup>1</sup>, D. Schamweber, F. Beckmann<sup>2</sup>, H. Worch

*Max Bergmann Center for Biomaterials, Dresden University of Technology, Dresden, Germany*

*<sup>1</sup>Faculty of Medicine, University of Technology, Dresden, Germany*

*<sup>2</sup>GKSS-Research Center, Geesthacht, Germany*

## Introduction

The rheumatoid arthritis (RA) is a chronic-inflammatory system illness of unclear cause, which leads in the process to an increasing destruction of joint cartilage and bone. In addition to the bone absorption within the joint area, it comes to a generalized bone absorption and/or osteoporosis. According to the current level of knowledge osteoclasts particularly apply as the cells, which absorb the bone substance by an increased production of matrix degrading proteases.

Beside collagenases, mainly the cysteineprotease cathepsin K is of importance. At present, the specific neutralization of cathepsin K is considered as a promising therapeutic approach. The transgene mouse Tg197 expresses the human TNF protein and develops spontaneously a strong destructive arthritis, which shows histologically many characteristics of the rheumatoid arthritis. Therefore, this model is particularly suitable for the investigation of the rheumatoid joint destruction mechanisms.

## Materials and Methods

The meaning of the protease cathepsin K is examined with the rheumatoid arthritis in an animal model. Therefore cathepsin K knockout mice (cathepsin K  $-/-$ ) are crossed with Tg197 transgene mice. In the F2 generation Tg197 mice, which are cathepsin K homozygote negative (cathepsin K  $-/-$ ), will be compared with Tg197 mice, which are cathepsin K heterozygote positive (cathepsin K  $+/-$ ). The further genetic background is identical. The bony destruction near the joint (near joint osteoporosis) and the systematically joint destruction (generalized osteoporosis) has been examined. In a preliminary test with micro-CT cathepsin K  $-/-$  mice, Tg197-mice  $-/+$  and C57/Bl6 wild-type mice were prepared. Thus knee joints were fixed for about 24h in paraformaldehyd and embedded without previous decalcification in paraffin. For the SR  $\mu$ CT investigations at the beamline HARWI II (W2) the samples were prepared to cylinders with a diameter of about 7 mm and examined with a photon energy of 22 keV using 720 projections angles and an image size of 1536 x 1536 pixels.

## Results

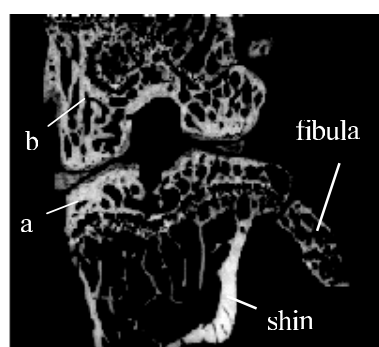
For the breeding the Tg197-mice had to be treated with neutralizing anti- TNF anti-bodies (weekly intraperitoneal injections). So far 30 mice of the F2 generation could be bred. These will afterwards be genetically typed and assigned to the appropriate experimental groups. The preparations were measured in paraffin, the x-ray absorption data were digitalized and the appropriate joint regions were reconstructed (see figures 1-3). The joint of the C57/Bl6 type mouse serves as control. In the reconstruction (Fig. 2) the two joint bones and the intermediate joint gap are represented. In low density portions of the cartilaginous menisci and the joint cartilage are recognizable. Under the gel cartilage the joint bone coat (compacta) of higher density as well as the following spongy network are visible. The cathepsin K  $-/-$  mouse points, as known, a quantitative bone development disturbance with a thickened bone coat (compacta) and a thickened spongia. This characteristic

could be remarkably recognized in the comparison to the C57/Bl6 mouse in the micro-CT measurements (Fig. 1). In Figure 3 the reconstruction of the knee joint of a Tg197-mouse with a advanced joint destruction is represented. The morphologic details from the preceding illustration are only hard to identify (Fig. 3). Compared with the other illustrations, the bony joint outlines are destroyed by the inflammation process. Also the amount of trabecular bone is clearly reduced.

These preliminary SR  $\mu$ CT measurements of the joint structure have proven their suitability in the field of rheumatoid arthritis investigations. The micro-CT measurement could properly represent the joint details. Apart from bony tissue also cartilage tissue was visible. In order to have morphologic details still recognizably for the Tg197-mice, an earlier preparation time must be intended, which have to serve as reference points for a quantitative comparison.

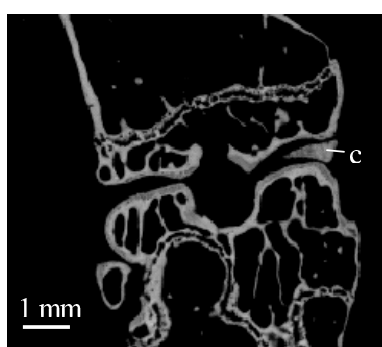
## Acknowledgments

Professor G. Kollias (National Institutes of Immunology, Athens) is kindly acknowledged for Tg197 mice, and Professor P. Saftig, (Department of Biochemistry, University of Kiel) for the cathepsin K  $-/-$  mice. The mouse breeding and the molecular-biological genetic classification was accomplished by Prof. R. Bräuer and Mrs. Dr. J. Schurigt (Group for Experimental Rheumatology, University of Jena).



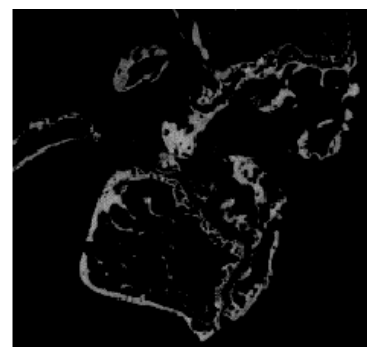
Cath. K

Figure 1: SR  $\mu$ CT-slice of the knee joint of a cathepsin K  $-/-$  mouse. Due to disturbances during bone decomposition with this mouse, it comes to a well-known development of a thickened compacta and spongiosa. Compared with Figure 2 both, the bone coat (a) and the trabecular bone (b) are clearly thickened.



C57/Bl6

Figure 2: SR  $\mu$ CT-slice of the knee joint of a C57/Bl6 mouse as control for a normal joint. The communicating joint surfaces with joint cartilage and underlying joint bone coat (compacta) and a cartilaginous meniscus (c) are to be recognized. In the inner bone the trabecular bone of the spongiosa and the growth-joint is represented.



Tg197

Figure 3: SR  $\mu$ CT-slice of the knee joint of a Tg197 transgene mouse. This mouse develops spontaneously a joint inflammation (arthritis) and in the following heaviest destruction of the joint cartilage and bone. Compared with Figure 2, despite same cutting plane, the joint outlines can be only suspected. The amount of trabecular bone is clearly reduced.

# Microtomography and FE-simulation of tensile specimens of the metal-matrix-composite Al/TiN

H.-A. Crostack, H. Blum<sup>1</sup>, J. Nellesen, F. Beckmann<sup>2</sup>, T. Rauscher<sup>1</sup>, G. Fischer

*Lehrstuhl für Qualitätswesen, Fakultät Maschinenbau, Universität Dortmund, D-44221 Dortmund, Germany*

<sup>1</sup> *Chair X of Scientific Computing, Institute of Applied Mathematics, University of Dortmund, D-44221 Dortmund*

<sup>2</sup> *GKSS, Max-Planck-Str. 1, D-21502 Geesthacht, Germany*

## 1 Introduction

The macroscopically observable behaviour of a material under load is composed of micro-deformation and -damaging processes. Such processes in metal matrix composites (MMCs) during tensile test can be uncovered with high resolution microtomography utilizing synchrotron radiation. From the comparison of the material behaviour in three-dimensional microstructural areas studied in tensile experiments with the one obtained by computer simulations based on the method of finite elements (FEM) understanding of these processes can be deduced.

## 2 Experimental procedure

From a sub-volume in the gauge length of a tensile test specimen of the Al/10%TiN composite, manufactured on a powder metallurgic route, high resolution microtomograms at different load, respectively deformation, stages were created. The energy of the photons generated at beamline BW2 amounted to 24 keV. For each 3D-tomogram consisting of 1536x1536x1024 voxels 720 projections were acquired using a CCD camera with a  $(9\text{ }\mu\text{m})^2$  pitch. A magnification of 5.5 was set with the optical lens between the fluorescent screen and the detector resulting in an effective voxel size of  $(2.5\text{ }\mu\text{m})^3$ .

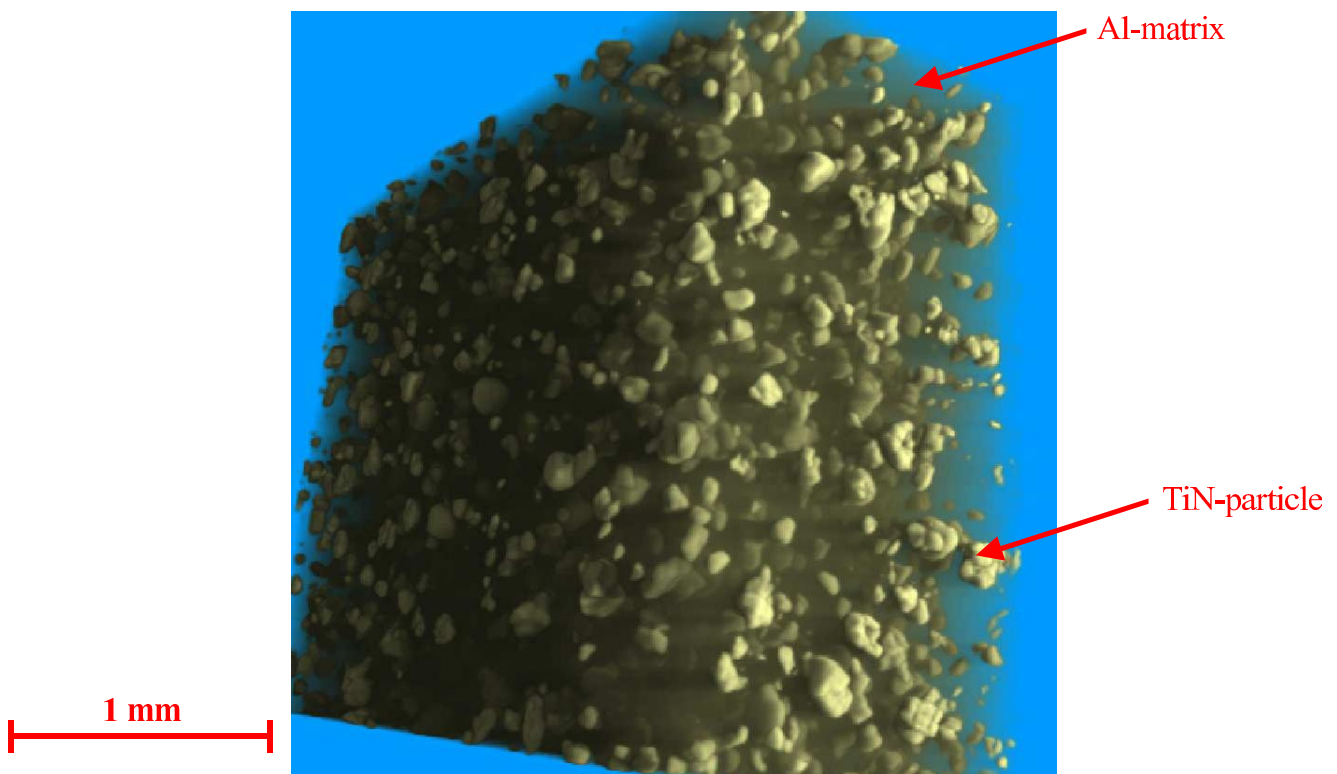


**fig. 1:** 3D-tomogram of a microstructural region in a Al/TiN specimen

## 3 Analysis procedure, results and discussion



A 3D-representation of the tomogram with a semi-transparent Al-matrix and opaque TiN-particles is shown in fig. 1. On the basis of an extracted 2D-CT-slice (fig. 2a) in the unloaded state the microstructural region was characterized which means that the different phases in the system were identified and the voxels in the tomogram were attributed with phase properties like e.g. surrounding air, particle and matrix (fig. 2b, c). The FE-model of the area of interest was set up by this means (fig. 2d). For the simulation the displacement field at a rectangular border was calculated from the tomogram data with a mapping algorithm [1]. The normalized results of the simulation of stress for the matrix and the particle are visualized in fig. 2e, f) and coded in false colours. The simulation reveals that at those loci where cracks were detected experimentally high values of stress emerged in the FE-calculation.

In future work criteria for particle cracking or other damaging mechanisms will be derived from the comparison of experimental with the simulated results. Based on these criteria the FE-calculations can be steered and adapted to the experimental results iteratively. Moreover the simulations which are currently carried out in 2D will be extended to the 3D case. In this manner knowledge about the behaviour of a composite on the micrometer scale can be gained which will help to manufacture tailored composites and to optimize the manufacturing process.

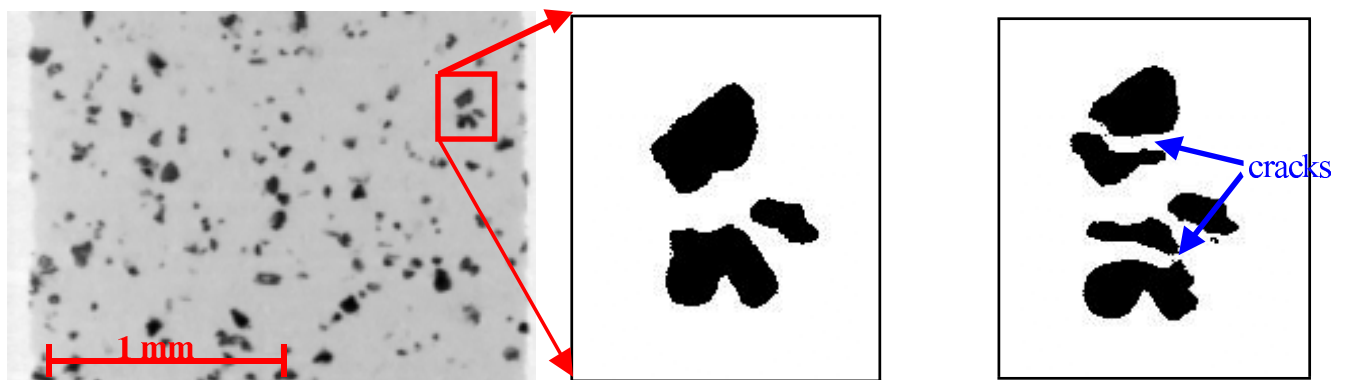
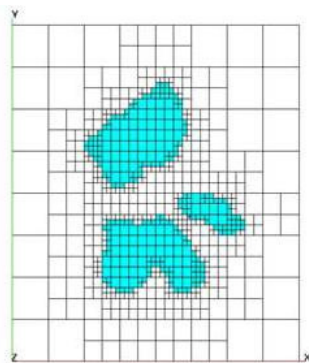
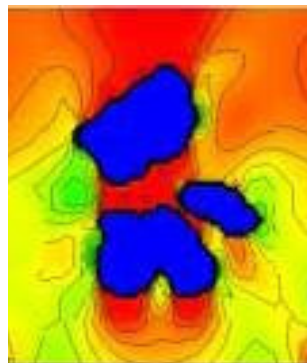


fig. 2: a) CT-slice

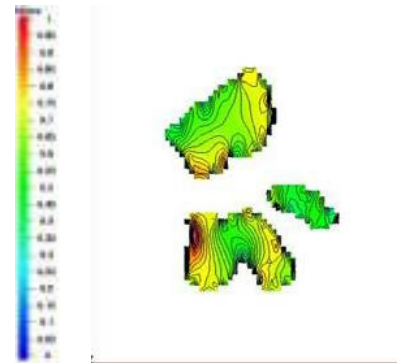
b, c) binarised images (different deformation steps)



d) FE-mesh



e) matrix stress map



f) particle stress map

#### 4 Acknowledgement

The financial support of this work in the scope of the research projects Cr4/100-3,-4 is gratefully acknowledged.

#### 5 Reference

- [1] H.-A. Crostack, G. Fischer, H.-D. Steffens, J. Wilden, F. Riazzi, "Dehnungsfeldmessung im Rasterelektronenmikroskop mittels Objektgitterverfahren", Beitr. Elektronenmikroskop. Direktabb. u. Analyse v. Oberfl. **27** (1994), S. 89-98



# Porosity analysis of thermally sprayed mullite utilizing synchrotron radiation based microtomography

H.-A. Crostack, J. Nellesen, F. Beckmann<sup>1</sup>, G. Fischer

*Lehrstuhl für Qualitätswesen, Fakultät Maschinenbau, Universität Dortmund, D-44221 Dortmund, Germany*

*<sup>1</sup> GKSS, Max-Planck-Str. 1, D-21502 Geesthacht, Germany*

## 1 Introduction

Mullite is a refractory material with the nominal composition  $\text{Al}_6\text{Si}_2\text{O}_{13}$  ( $3\text{Al}_2\text{O}_3 \cdot 2\text{SiO}_2$ ). Due to its excellent high temperature properties like low thermal conductivity, good thermal shock and thermal stress resistance owing to low thermal expansion it is very interesting for the application in thermal barrier coatings. The thermal conductivity depends not only on the material itself but also on the porosity which is strongly affected by the manufacturing process like e.g. thermal spraying. An increase in porosity leads to a reduced thermal conductivity and, in consequence, to a better thermal protection but to a higher proneness to failure. For the simulation of heat transfer knowledge of the porosity is essential. In order to visualize and quantify the porosity value in a Mullite coating high resolution microtomographs generated with the help of monochromatic synchrotron radiation were analyzed by image processing.

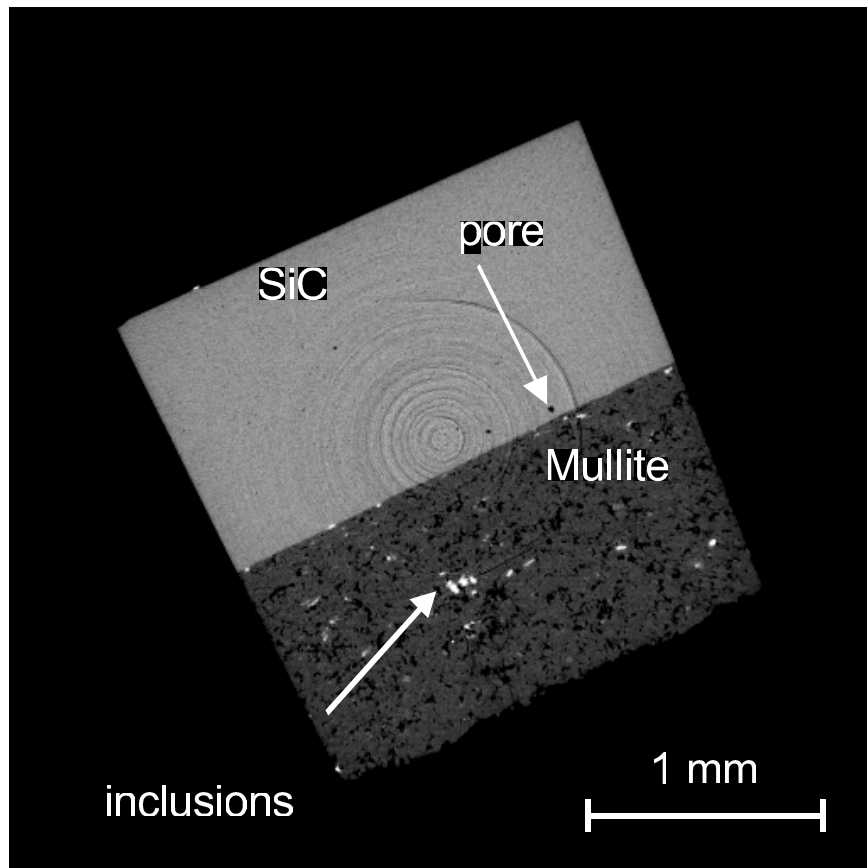


**fig. 1:** 2D-CT-slice of the SiC coated with Mullite

## 2 Experimental and analysis procedure

With a diamond wheel saw a specimen was cut from a plate consisting of a SiC substrate coated with thermally sprayed Mullite. Its cross-sectional areas to  $1.5 \times 1.5 \text{ mm}^2$ , which is an appropriate size for microstructural analysis. The  $\mu\text{CT}$ -measurements were carried out at beamline BW2 at a photon energy  $E = 22 \text{ keV}$ . Projection images were recorded at 720 positions, equally spaced in the angle interval  $[0, \pi[$ . An optical magnification  $m = 5.5$  was set with the optical lens system between

the fluorescence screen and the CCD camera which results in an effective voxel size of about  $2.5^3 \mu\text{m}^3$ . Because of the well-suited approximation of parallel beam geometry, the reconstruction process was performed slice by slice. A stack of 1024 slices was afterwards tied up to get a 3D tomogram. From the histogram of the 3D tomogram the voxels representing the SiC substrate and Mullite coating were attributed. With the *a priori* information about the envelope of the entire specimen the pores in the Mullite coating could be collated.

### 3 Results and discussion

The images in fig. 1 and 2 reveal the results of tomography. In the 2D-CT-slice (fig. 1) the large value of porosity can easily be deduced. Pores in the SiC substrate are also visible. Highly absorbing particles or inclusions in the coating can be seen, which are coded with a high grey value. These inclusions are supposed to be impurities introduced by the milling of Mullite taking place in the powder processing route before the thermal spraying. In figure 2 a 3D representation of stacked 2D-slices is visualized. The stack was cut at an arbitrary plane and the scene was illuminated with two light sources in virtual reality to give an insight into the specimen. With the help of image processing the porosity level in the Mullite coating could be determined to  $9 \pm 1 \%$  which proves the metallographic result (6-8 %). Further investigations will be carried out to discover the origin and nature of the inclusions in the near future.

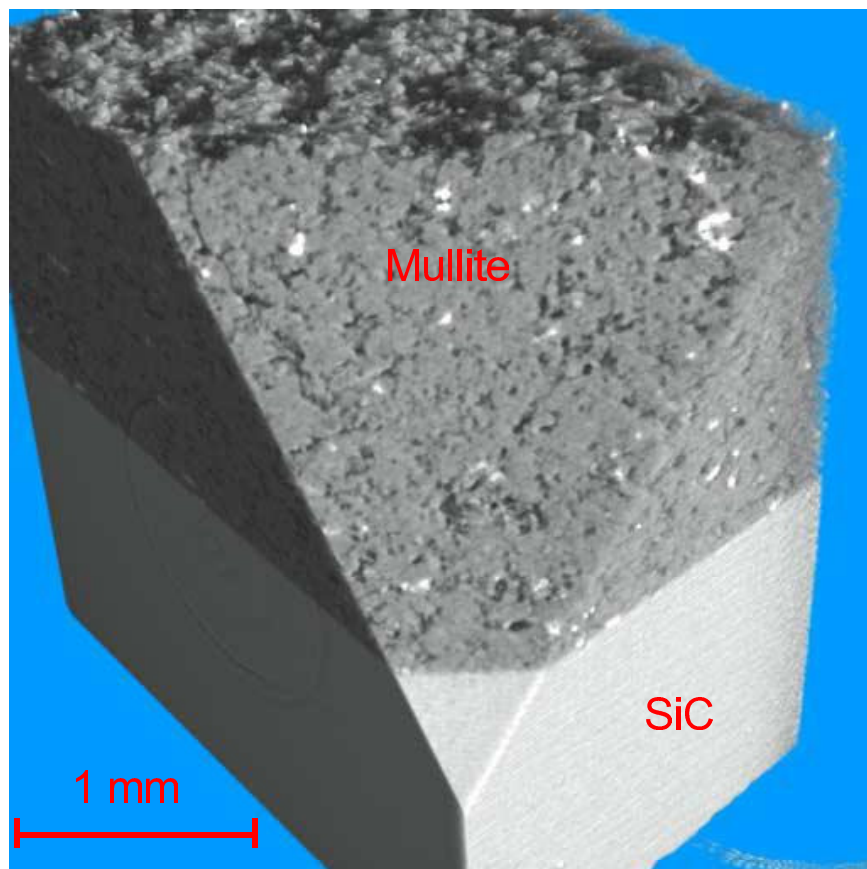


**fig. 2:** Cut 3D-tomogram of the SiC specimen coated with mullite

### 4 Acknowledgement

The financial support of this work in the scope of the research project ENK5-CT 2000-00068 CINDERS is gratefully acknowledged.

# Texture developments of extruded Mg-alloy during tensile loading

S.-B. Yi<sup>1,2</sup>, H.-G. Brokmeier<sup>1,2</sup>, B. Schwebke<sup>1,2</sup>, T. Lippmann<sup>2</sup>, W.H. Ye<sup>1,2</sup> and J. Homeyer<sup>3</sup>

<sup>1</sup>Institut für Werkstoffkunde und Werkstofftechnik, TU-Clausthal, Agricolarstr. 6, D-38678 Clausthal-Zellerfeld, Germany

<sup>2</sup>GKSS-Forschungszentrum, Max-Planck-Str., D-21502 Geesthacht, Germany

<sup>3</sup>HASYLAB at DESY, Notkestr. 85, D-22603 Hamburg, Germany

With increasing demands on magnesium and its alloys for industrial applications, especially for automobile industries, there are many efforts on the improvements of mechanical properties of these alloys. For improving the mechanical properties of these alloys the profound understanding on the crystallographic texture is necessary because most magnesium alloys show high directional anisotropy originated from its hexagonal crystal structure.

The effect of a pre-formed texture in an AZ31 (Mg – 3 Al – 1.0 Zn – 0.1 Mn in wt.%) extruded bar on the mechanical anisotropy and on further developments of the texture during tension is shown in this report. For investigating the texture changes during tensile tests, our group has constructed a tensile- compression-test machine at beam line HARWI II for in-situ texture measurements. The transmission method using synchrotron X-rays is ideal for in-situ texture measurements because several complete pole figures can be obtained in a relatively short time and the diameter of the diffraction cone is very small. Three tensile samples were cut in different directions from the extruded bar, parallel, 45 ° inclined and perpendicular to the extrusion direction. The tensile tests and in-situ texture measurements were performed at room temperature with the initial strain rate of  $5 \times 10^{-4} \text{ sec}^{-1}$ .

Fig. 1 shows the (00.2) pole figure of the extruded bar and the flow curves of three tensile samples. The stress fall-off on the curves indicate the texture measuring points, which might be caused by room temperature creep. The sample cut parallel to extrusion direction (0°) shows the highest yield strength of 260 MPa, which is higher about 45 MPa than other samples. On the other hand, the sample cut perpendicular to extrusion direction (90°) shows fast strain hardening which is not the case in the 0° and 45° samples.

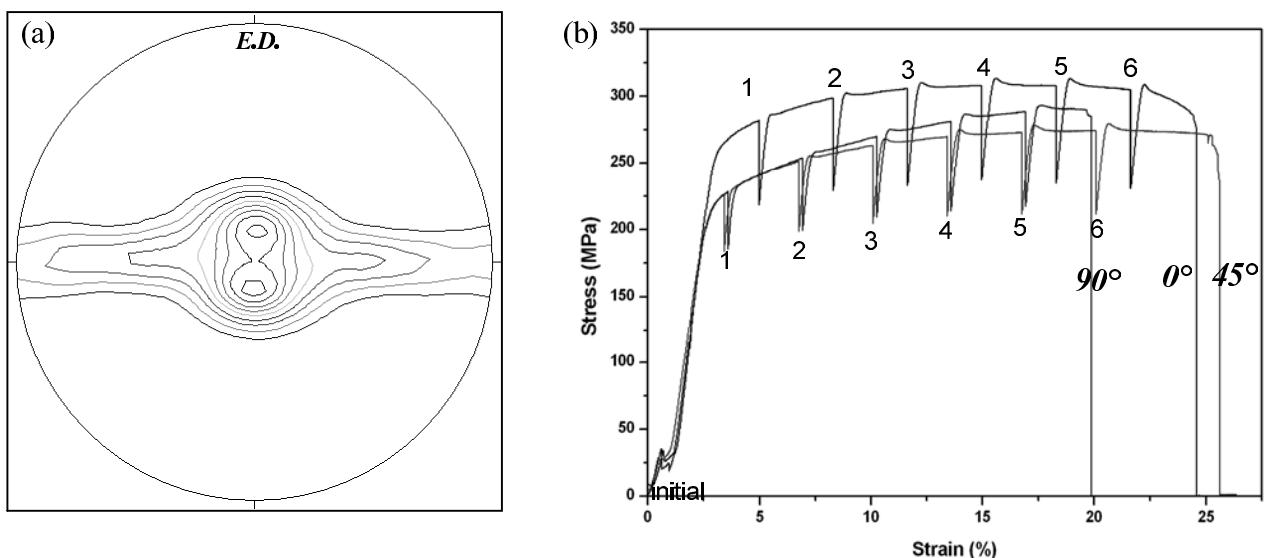


Figure 1: (a) (00.2) pole figure of the extruded bar.

E.D. indicates the extrusion direction. ( $P_{\max} = 5.5 \text{ mrd}$ , Level = 1, 1.5 ... 5.0)

(b) The flow curves of tensile samples, parallel (0°), 45° and perpendicular (90°) to the extrusion direction. Stress fall-off positions on curves coincide with the in-situ texture measuring points.

The 45° sample shows the lower value for tensile strength and for yield strength as well as for the high failure strain of 26 % including the strains during reloading after texture measurements. This different tensile behaviour can be explained by the initial texture of the samples and different activities of deformation modes that are possible in Mg-alloys. Fig. 2 shows the changes of (00.2) pole figures of three tensile samples during tensile tests. The loading axis lies always on the centre of the pole figures, and the pole density of the initial samples is same with that of extruded bar in Fig. 1. The initial texture of 0° sample can be represented by the alignments of c-axis perpendicular to loading axis, which is unfavourable for the activation of basal <a>-slips. This type of initial texture caused the highest yield strength of this sample, and no significant change of texture is shown, since this type of texture is already stable under uniaxial loading condition. On the other hand the 90° sample shows the intense changes of texture after reaching the yield point, which can be explained by the activation of tensile twinning. Because the twin boundaries act as a barrier against further slip, moreover, the rotated grains by twinning have lower Schmid's factor for <a>-slip this sample shows the highest value of strain hardening. As a result of favourable orientations of crystallites for the activation of <a>-slip modes in the 45° sample, this sample shows the lowest yield strength. Though the basal planes laid initially 45° relative to the loading axis disappeared during the tension, the alignments of crystallite are enough for the high value for Schmid's factor for further activation of <a>-slip. Therefore the 45° sample has the lowest tensile strength.

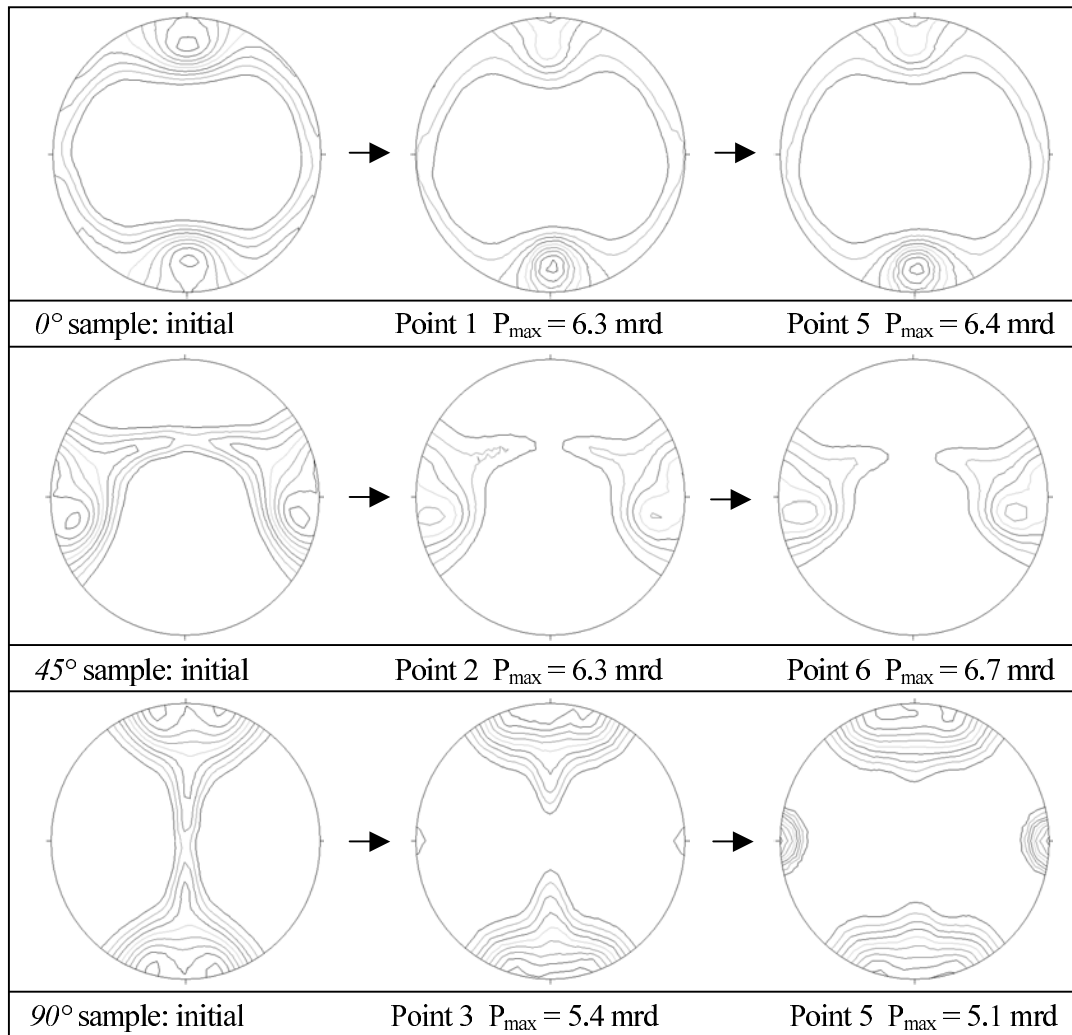


Figure 2 : The variation of (00.2) pole figures during tensile test of each sample. The measuring points are indicated in Fig. 1. (mrd: multiple random distribution)

# The evolution of internal strain during uniaxial tension of Mg-alloy, AZ31

S.-B. Yi<sup>1,2</sup>, H.-G. Brokmeier<sup>1,2</sup>, B. Schwebke<sup>1,2</sup>, T. Dose<sup>2</sup> and J. Homeyer<sup>3</sup>

<sup>1</sup>Institut für Werkstoffkunde und -technik, TU-Clausthal, Agricolarstr. 6, D-38678 Clausthal-Zellerfeld, Germany

<sup>2</sup>GKSS-Forschungszentrum, Max-Planck-Str., D-21502 Geesthacht, Germany

<sup>3</sup>HASYLAB at DESY, Notkestr. 85, D-22603 Hamburg, Germany

Despite of the advantages of magnesium alloys such as a high specific strength, the poor cold formability is a facing problem for industrial applications of these alloys. The problem is linked with an inadequate number of independent deformation systems. Furthermore the initial texture and the loading (straining) direction play critical roles in determining the possible deformation systems. During deformation of polycrystalline materials develop the internal stains. In the current study we are focusing on peak shift, which is caused by Type I and II stresses. The image-plate technique, which is offering a set of reflections, allows the investigation of type II internal strain, the so called intergranular strain, which is associated with elastic and plastic anisotropy at the grain level. Since their evolution is controlled by the active slip systems and their interaction, the investigation on intergranular strain give some meaningful information on the anisotropic response of different lattice planes during deformation. It should be noticed that internal strains can originated from plastic anisotropy, thermal expansion or elastic anisotropy [1]. The dominant mechanism in magnesium is the plastic anisotropy of individual grains during loading and there orientation to the loading direction [1], because of nearly isotropic elastic coefficients and thermal expansion of magnesium single crystals.

In this report we will shortly describe a new in-situ measuring method for internal strain determination using hard X-rays and preliminary results of this study. From the diffraction profile of annealed pure magnesium powder the X-ray wavelength was determined as 0.1366Å. The loading device [2] was installed at beam line BW5 for performing the in-situ measurement. A tensile sample cut from the extruded bar of AZ31 magnesium alloy (Mg-3Al-1Zn-0.1Mn in wt. %) was tensioned at room temperature with 0.0018 mm/sec. of loading ram speed. Under loading condition some sets of Debye-Scherrer cones were continually registered with a MAR345 area detector at different macro strain levels. The sample strain and the load were taken by using an extensometer, HBM - WETA 1/10, and a load cell, HBM - C9B.

Fig. 1 shows the stress-strain curve and the measuring points during uniaxial tension. The internal strains for the individual lattice planes  $\{hk.l\}$  were calculated from the measured inter-planar spacing,  $d^{hk.l}$ , using the following equation

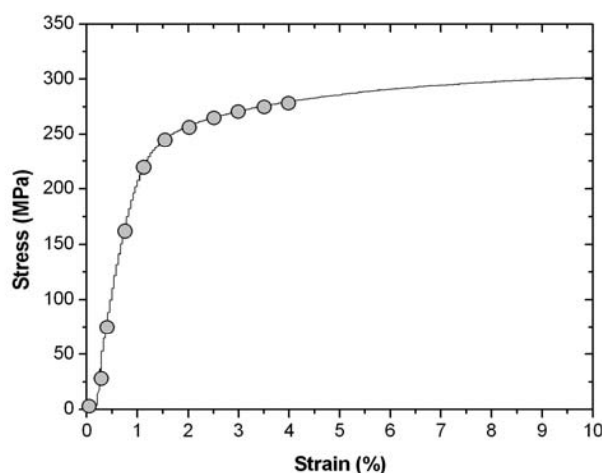


Figure 1: The flow curve during the in-situ experiment. The points on the curve indicate the measuring points for internal strain determination.

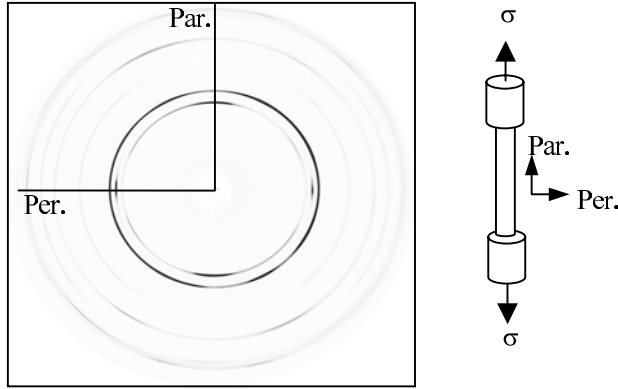


Figure 2: Image registered on the area detector and the relationship between diffraction profiles on the image and the loading direction. (Par. : parallel, Per. : perpendicular to the loading axis)

$$\varepsilon = \frac{d^{hk,l} - d_0^{hk,l}}{d_0^{hk,l}}$$

where  $d_0^{hk,l}$  represents the unstrained inter-planar spacing. A detector image from the unstrained initial sample and the geometrical relationship between the sample direction and the detector image are shown in Fig. 2. As the figure shows, the diffraction profile from the horizontal (vertical) line on the detector image represents the crystallographic planes perpendicular (parallel) to the loading axis. Fig. 3 presents the evolution of internal strains for different  $\{hk,l\}$  during tensile loading. Due to the texture of the present sample three diffraction peaks  $\{10.0\}$ ,  $\{10.1\}$  and  $\{11.0\}$  could be evaluated in the loading direction. Because the internal strains parallel to the loading axis are more constrained by external boundary conditions, the internal strains in this direction show more similarity with the stress-strain curve. The internal strains on  $\{10.1\}$  parallel to the loading axis show earlier micro yielding at 0.7% of sample strain. On the other hand the internal strains on  $\{10.0\}$  and  $\{11.0\}$  parallel to the loading axis show later micro yielding at about 1.5% of sample strain. The ratio of the internal strain on  $\{10.0\}$  and  $\{10.1\}$  is 2.4. This means the dislocation gliding on the  $\{10.1\}$  plane, the so called soft-orientation, is relatively easier than on the other planes. The crystallographic planes perpendicular to the loading axis, which are under compression, clearly show also the anisotropic response of internal strains, though the ratio of max. and min. internal strain is smaller than the case of parallel to the loading axis.  $\{00.2\}$  perpendicular to the loading axis shows the hardest behaviour, while  $\{10.1\}$  has the softest response of internal strains.

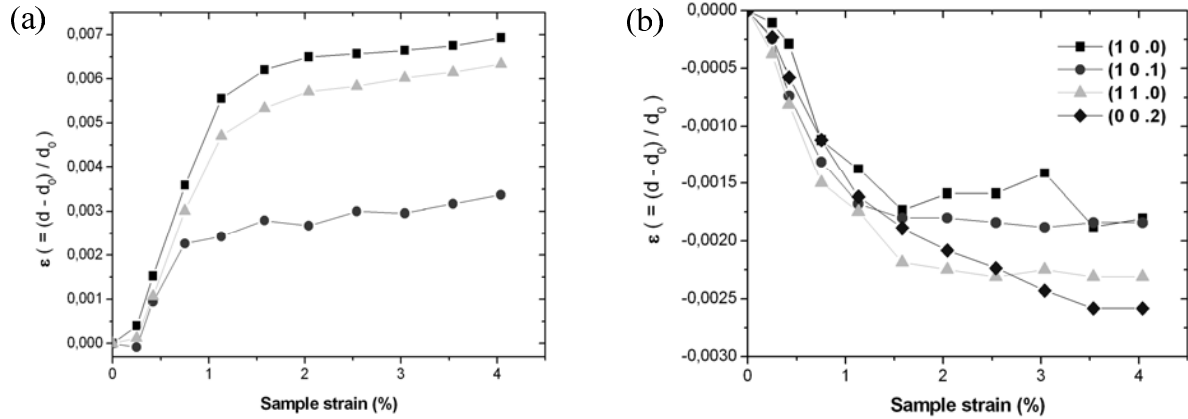


Figure 3: The evolution of internal strains for crystallographic planes as a function of the sample strain. (a) Parallel and (b) perpendicular to the loading axis.

## References

- [1] S.R. Agnew, D.W. Brown, S.C. Vogel, T.M. Holden, Mater. Sci. Forum 404-407, 747 (2002)
- [2] H.-G. Brokmeier, U. Zink, T. Reinert, W. Murach, J. Appl. Cryst. 29, 501 (1996)

# Untersuchungen an unterschiedlichen Knochenersatzmaterialien mittels Synchrotron $\mu$ -Computertomographie

D. Tadic, F. Beckmann<sup>1</sup>, T. Donath<sup>1</sup> und M. Epple\*

*Institut für Anorganische Chemie, Universität Duisburg-Essen, Campus Essen, D-45117 Essen, Deutschland*

*<sup>1</sup> GKSS, Max-Planck-Straße 1, D-21502 Geesthacht, Deutschland*

Im klinischen Alltag besteht ein großer Bedarf, Defekte durch Knochenersatzmaterialien aufzufüllen. Der menschliche Knochen weist eine enorme strukturelle Komplexität auf. Der innere Aufbau des Knochens besteht grundsätzlich aus zwei unterschiedlichen Schichten, der *Substantia compacta* und der *Substantia spongiosa*. Erstere ist eine kompakte Schicht, die die äußere Oberfläche des Knochens bildet. Letztere befindet sich innerhalb des Knochens und besteht aus kleinen Knochenbälkchen, die sich entlang der Zug- und Drucklinien ausrichten. Außen und an mechanisch besonders beanspruchten Stellen, finden sich sehr viele Knochenbälkchen (Trabekel). Die Forderung nach einem porösen Knochenersatzmaterial ergibt sich aus der Notwendigkeit, ein möglichst schnelles Einwachsen von Knochen in das Implantat zu ermöglichen. Dieses führt zur Integration mit dem umgebenden Knochen und zur mechanisch stabilen Ankopplung an das umgebende Gewebe.

Hier wurden fünf unterschiedliche kommerziell erhältliche Knochenersatzmaterialien am Messstand W2 bei einer Photonenenergie von 22-25 keV untersucht. Bei den Proben handelte es sich um:

- a) Cerabone<sup>®</sup> (Rinderknochen bei 1250°C gesintert). Deutlich sichtbar ist die porös-interkonnektierende Struktur des nativen Knochens.
- b) Cerasorb<sup>®</sup> (synthetisches beta-Tricalciumphosphat). In diesem Fall wurde die Porosität durch mechanisches Bohren erzeugt.
- c) Tutobone<sup>®</sup> J-Block (chemisch behandelter Rinderknochen). Hier sieht man die trabekuläre Knochenstruktur, in diesem Fall auch den Übergang vom kompakten zum spongiösen Knochen.
- d) Tutobone<sup>®</sup> Spongiosa bovin (chemisch behandelter Rinderknochen). Hier sieht man die poröse Struktur.
- e) Tutobone<sup>®</sup> Spongiosa human (chemisch behandelter humaner Knochen). Hier sieht man ebenfalls die poröse Struktur.

Alle gezeigten Objekte weisen Abmessungen von ca. 1 cm<sup>3</sup> auf.

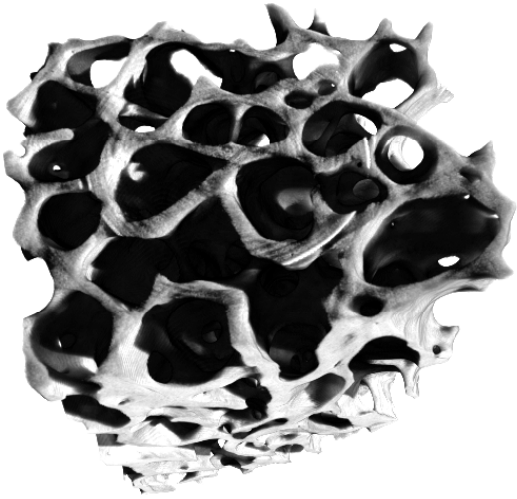


Abbildung 1 Cerabone®

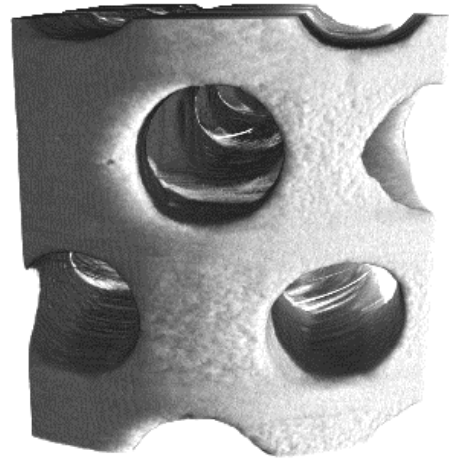


Abbildung 2: Cerasorb®

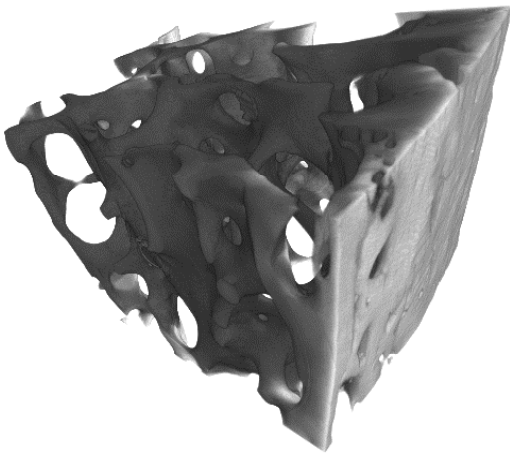


Abbildung 3: Tutobone® J-Block

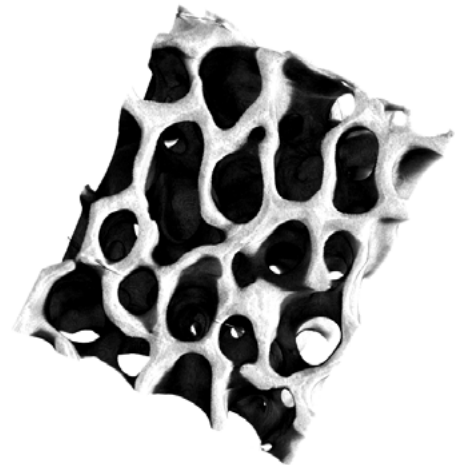


Abbildung 4: Tutobone®  
Spongiosa (bovin)

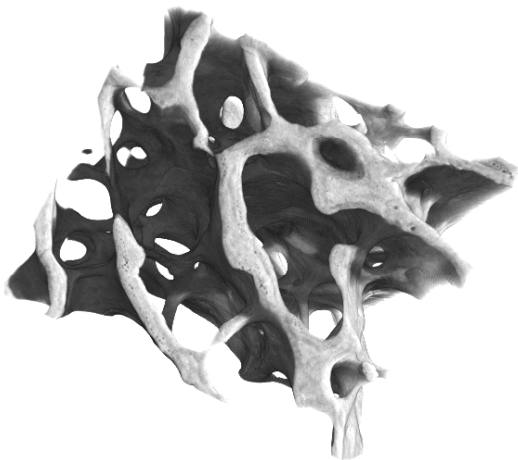


Abbildung 5: Tutobone®  
Spongiosa (human)



# Charge density study of $\text{La}_{0.5}\text{Sr}_{1.5}\text{MnO}_4$ at room temperature

T. Lippmann<sup>1</sup>, S. Kiele<sup>2,3</sup>, J. Geck<sup>3,4</sup>, P. Reutler<sup>4</sup>, M.v. Zimmermann<sup>2</sup>, B. Büchner<sup>4</sup>

<sup>1</sup>GKSS, Max-Planck-Str. 1, 21502 Geesthacht, Germany

<sup>2</sup>DESY/HASYLAB, Notkestr.85, 22603 Hamburg, Germany

<sup>3</sup>II. Physikalisches Institut A der RWTH Aachen, Huyskensweg, 52056 Aachen, Germany

<sup>4</sup>Leibniz Institute for Solid State and Materials Research Dresden at IFW Dresden, Helmholtzstraße 20, 01069 Dresden, Germany

The transition metal oxides (e.g. manganites) are featured by strong correlations of the charge, orbital and spin degrees of freedom. Their interplay leads to the formation of a charge and orbital ordered state at low temperatures. Due to the concomitant structural distortions the crystal symmetry is broken leading to the formation of superlattice reflections. They can be observed utilizing X-ray scattering techniques, e.g. [1]. The details of the charge and orbital order are still under discussion. The aim of this X-ray structure refinement experiment was to gain data that facilitate us to create charge density maps both at room temperature and at low temperatures. As an example we chose  $\text{La}_{1-x}\text{Sr}_{1+x}\text{MnO}_4$  ( $x = 0.5$ ), which is a model system for a CE-type magnetic ordering. It has relatively strong superlattice reflections and has been extensively studied using a variety of methods.

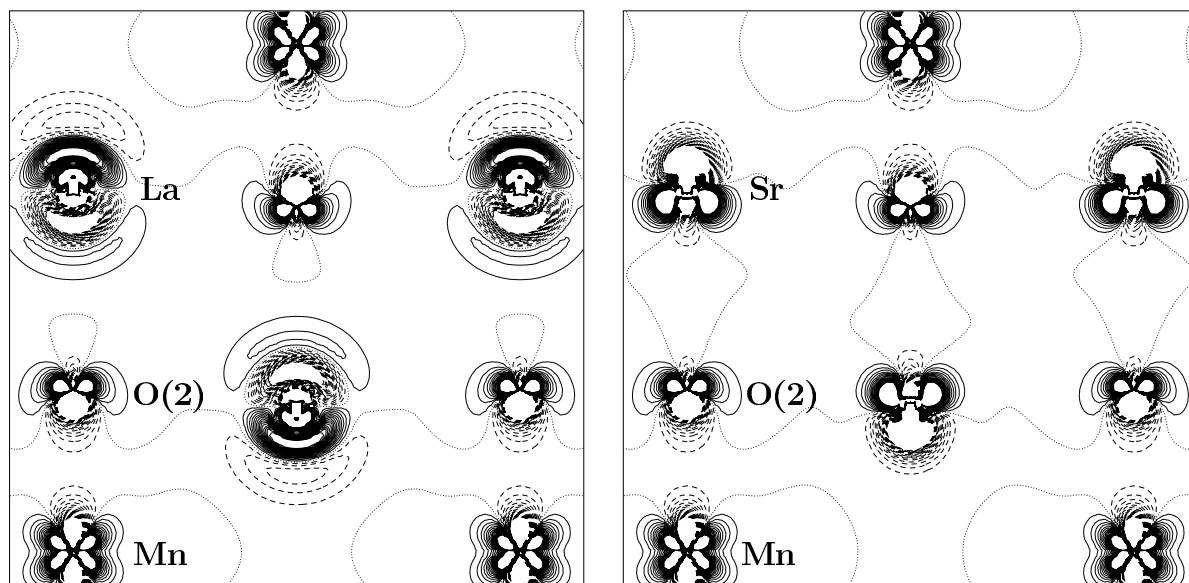


Figure 1: Static deformation density (monopoles omitted) in the (110) plane. Contours at  $0.1 \text{ e}\text{\AA}^{-3}$ , centre at  $-0.5, 0, 0.25$ . Dimensions:  $7 \times 7 \text{ \AA}^2$ , horizontal axis:  $[\bar{1}10]$ , vertical axis:  $[001]$ . La and Sr parameters constrained.

2064 reflections have been measured up to  $\sin \Theta / \lambda = 1.1$  using 100 keV radiation provided at beamline BW5 [2, 3]. Averaging yielded 340 unique reflections and an internal consistency of 0.011. First refinements were performed assuming spherical charge density distributions and results from an earlier neutron scattering experiment [4] as start parameters for the atom coordinates and the anisotropic displacement parameters. The data refined well yielding agreement indices  $R(F) = 0.009$  and  $R_w(F) = 0.013$ . For the first tests the parameters of La and Sr were constrained. In further refinements these parameters were refined independently, but in alternating cycles in order

to minimize correlations. A small difference in the atom positions  $z$  of La and Sr along the  $c$ -axis of about  $0.02 \text{ \AA}$  was found in these cases.

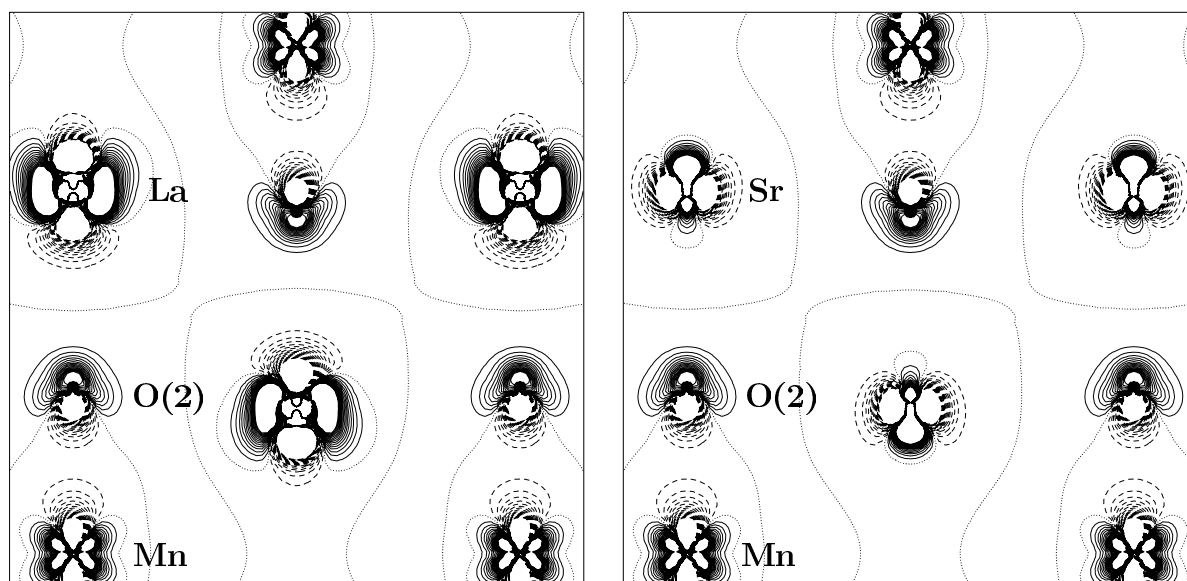


Figure 2: Static deformation density after independent refinement of La and Sr.

Next, a multipole model has been refined in order to model the aspherical parts of the charge density. Figs. 1a) and b) show the deformation density in the case of constrained La and Sr parameters and Figs. 2a) and b) after independent refinements. The density of the Mn atoms looks similar in all cases. Charge depletion was found between Mn and the neighbouring oxygen atoms, whereas accumulation lobes always point versus the empty voids of the structure. In addition, the O(2) always showed considerable charge polarization, i.e. a lone pair orbital on the opposite side of the Mn atom. Strong differences, however, are visible comparing the La and Sr densities. In the constrained case, dipole contributions always dominate the deformation density. Since a dipole is well known to correlate considerably with the atom position and the dipoles of Sr and La have different signs, the resulting density in the constrained case could be regarded as a hint for an improper refinement of the  $z$  coordinate here. In fact, the independent refinements indicate much weaker dipoles both at Sr and La. Unfortunately, the possible difference of  $0.02 \text{ \AA}$  is very small compared with the resolution of the data. Thus, further experiments are necessary to answer this open question.

The analysis of a low temperature data set of  $\text{La}_{0.5}\text{Sr}_{1.5}\text{MnO}_4$ , which was measured below the charge and orbital order transition temperature and includes superlattice reflections, is currently in progress.

## References

- [1] S. Larochelle et al., Phys. Rev. Lett. 87, 095502 (2001)
- [2] T. Lippmann, J.R. Schneider, J. Appl. Cryst. 33, 156 (2000)
- [3] T. Lippmann, N.H. Andersen, Th. Wolf, J.R. Schneider, Acta Cryst. A59, 437 (2003)
- [4] P. Reutler, Ph.D. thesis, RWTH Aachen (2003)

# Electron Density Distribution in Tephroite, $\text{Mn}_2\text{SiO}_4$ : a High-Energy Synchrotron Radiation Study

A. Kirfel<sup>1</sup>, T. Lippmann<sup>2</sup>, and W. Morgenroth<sup>1</sup>

<sup>1</sup>Mineralogisch-Petrologisches Institut, Universität Bonn, Poppelsdorfer Schloss, D-53115 Bonn, Germany

<sup>2</sup>GKSS, Max-Planck-Str., D-21502 Geesthacht, Germany

Tephroite belongs to the mineral group of olivines and is isotypic to forsterite and fayalite, the Mg- and Fe-end members, respectively of the (Mg, Fe) solid solution series. Thus, it crystallizes in the olivine structure, space group Pbnm,  $a_0 = 4.912(1) \text{ \AA}$ ,  $b_0 = 10.598(3) \text{ \AA}$ ,  $c_0 = 6.255(2) \text{ \AA}$ ,  $Z = 4$ . In continuation of our earlier forsterite [1] and fayalite [2] studies we have now carried out room temperature single-crystal diffraction experiments with the aim to complement the earlier results by adding material for a transition element with a closed half shell  $3d^5$  electron configuration. Simultaneously we want to explore the feasibility of combining data recorded from the same crystal, but on different diffraction instruments and with different synchrotron radiation energies.

For the Low-Order reflections, which carry most of the information concerning bond induced charge redistributions, but are notoriously affected by absorption and extinction effects, we have chosen synchrotron radiation of 100.3 keV in order to obtain essentially absorption and extinction free data for the electron density modelling and ensuing topological analysis. The experiment on a sample produced by the Czochalski technique and ground to an approximate sphere of 0.25 mm diameter was performed on the Triple-Crystal-Diffractometer (BW5, [3]).

For a full sphere up to  $\sin\theta/\lambda = 0.382 \text{ \AA}^{-1}$ , 1712 reflections were recorded in a Psi-Scan Mode, i. e. using  $\omega$ -scans and 3 different settings  $\Psi = 0.0^\circ$ ,  $0.5^\circ$ , and  $1.0^\circ$ . In the following full shell up to  $\sin\theta/\lambda = 0.605 \text{ \AA}^{-1}$ , 1714 reflections were recorded in the conventional bisecting mode. The data reduction including a slight drift correction, but no absorption correction resulted in a set of 309 unique observed reflections ( $I > 4\sigma$ ) with an internal agreement factor  $R(F^2) = 0.0172$ . This value is about two times larger than those in the earlier measurements are. The reason is not yet understood and thorough analysis of the raw data is in progress.

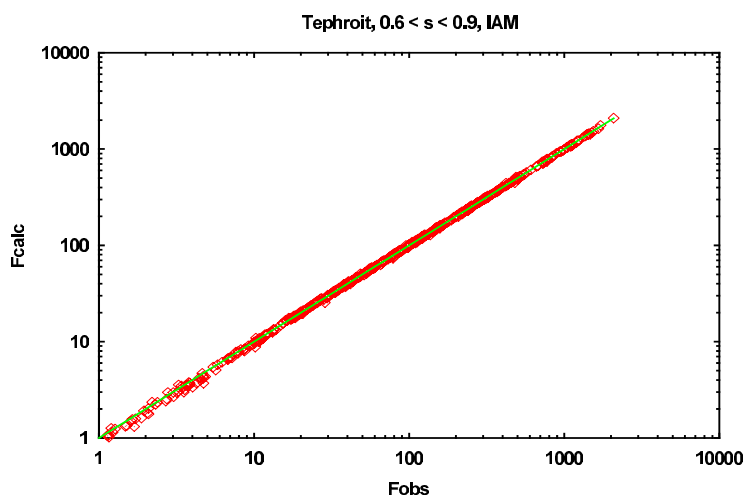


Figure 1.  $F(\text{calc})$  vs.  $F(\text{obs})$  plot of the HO-data

High-Order reflections, which are generally hardly affected by extinction and are dominated by the atomic core electrons, can be used to fix unbiased crystallographic standard parameters. To this purpose, additional data were collected at the Four-Circle-Diffractometer (D3) at a beam energy of 27.56 keV corresponding to a wavelength of  $0.50 \text{ \AA}$ . Exploring a half shell between  $0.60 \text{ \AA}^{-1}$  and

0.99 Å<sup>-1</sup>, 11310 reflections were recorded in the above quoted Psi Scan Mode yielding a set of 493 unique observed reflections with an internal agreement factor  $R(F^2) = 0.0168$ .

Up to date, structure refinements were carried out with the independent atom (IAM) model using SHELXL97 [4]. Applied to the High-Order reflections convergence was reached at  $R1 = 0.0083$ ,  $wR = 0.0214$ ,  $GoF = 1.10$ . Fig. 1 illustrates the quality of these data by a logarithmic  $F(\text{calc})$  vs.  $F(\text{obs})$  plot.

In the next step, a refinement was carried out with the Low-Order reflections alone. Fixing the previously refined atomic standard parameters considered as free from chemical bias, this refinement is expected to show the charge redistribution in terms of dynamic difference density maps. Thus, the only variable to be adjusted is the scale factor. This refinement converged at  $R = 0.0116$  after introducing a small extinction correction. Fig. 2 shows the deformation density distributions associated with the SiO<sub>4</sub>-moiety and the two Mn sites.

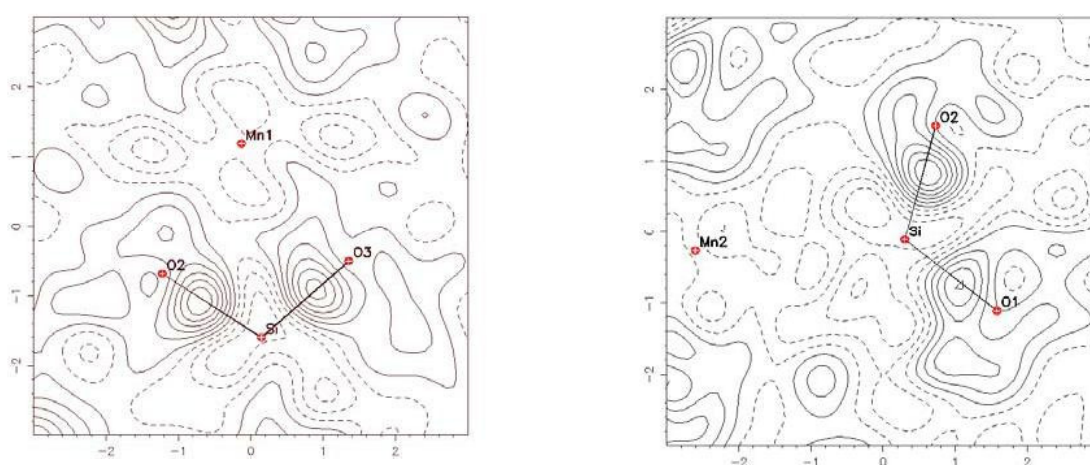


Figure 2 a, b. Deformation density distribution for the two Mn sites. contours at 0.05 e Å<sup>-3</sup>.

Both maps give clear evidence that Mn, contrary to Fe in fayalite [2], exhibits only little anisotropic 3d-electron density distribution in agreement with the chemical expectation. Modelling of the total density distribution by means of structure refinements with generalized atomic scattering factors and joint data sets is under way.

We would like to thank M. von Zimmermann for assistance with the measurements. Financial support of this project by the BMBF, contract No KS1 PDA is gratefully acknowledged.

## References

- [1] A. Kirfel, T. Lippmann, *Acta Cryst.*, **A58** (Suppl.), C165 (2002)
- [2] A. Kirfel, T. Lippmann, *HASYLAB Jahresbericht*, 515 (2002)
- [3] R. Bouchard et al., *J. Synchrotron Rad.* **5**, 90 (1998)
- [4] G. M. Sheldrick, SHELXL-97 – A program for crystal structure refinement. University of Göttingen, Germany (1997)

# Comparison of Conventional and Synchrotron-Based Microtomography of Bone around Dental Implants

*P.M. Cattaneo, M. Dalstra, F. Beckmann<sup>1,2</sup>, T. Donath<sup>2</sup> and B. Melsen*

*Dept. of Orthodontics, Royal Dental College, Aarhus University, Vennelyst Boulevard 9, 8000 Aarhus C, Denmark*

*<sup>1</sup>HASYLAB at DESY, Notkestrasse 85, 22603 Hamburg, Germany*

*<sup>2</sup>GKSS-Forschungszentrum, Max-Planck-Strasse 1, 21402 Geesthacht, Germany*

This study is a continuation of the previous two years' investigation of bone around implants and is part of a larger project (II-00-064 EC) and compares the application of a conventional microtomography ( $\mu$ CT) scanner and a synchrotron radiation (SR) based  $\mu$ CT scanner to evaluate the bone structure around titanium dental implants.

Microtomography as applied in the present study has become a well-established tool in the field of bone mechanics since it is a non-destructive technique and may provide unique 3D images of the bony architecture [1]. It is predominantly used to reconstruct the structure of trabecular bone, more seldom for cortical bone, and just recently to investigate bone around dental implants [2] [3]. The reasons for this are to be found in the fact that due to beam hardening and scattering effects, bone morphology around implant cannot be properly identified. Both problems can be solved using a monochromatic X-ray source produced by synchrotron radiation instead of a traditional X-ray tube for the  $\mu$ CT-scanning.

The bone specimen used in this study was part of a larger animal study in which titanium dental implants were inserted in the extraction sites of the second premolars and first molars in the upper and lower jaws of adult male *Macaca fascicularis* monkeys. The implants were loaded by a pair of superelastic Sentalloy® springs. Following sacrifice, the segments of the jaws containing the implants were harvested, dehydrated in a graded series of alcohol and then embedded in methyl methacrylate following a standard procedure for the generation of undecalcified sections. The blocks were then cut to a final dimension of 20x21x11 mm<sup>3</sup>. Subsequently one of the specimens was scanned with both a conventional  $\mu$ CT-scanner ( $\mu$ CT-40, Scanco Medical, Bassersdorf, Switzerland) and a SR-based scanner. (beamline W2 at DORIS, HASYLAB at DESY, Hamburg, Germany) [4].

Scanning was performed at an energy level of 70 keV when using the conventional  $\mu$ CT scanner, while at an energy level of 50 keV for the SR-based  $\mu$ CT microtomograph. In both cases reconstructions of the 3D data-sets were made starting from the sinograms using a filtered back-projection algorithm (Fig. 1). Afterwards the sample was cut for quantitative histological analysis.

The results from the two different microtomographic techniques were qualitatively compared with conventional histological sections examined under light microscopy (Fig. 2). The SR-based  $\mu$ CT produced images that, especially at the bone-implant interface, are less noisy and sharper than the ones obtained with conventional  $\mu$ CT, and are in their amount of detail comparable to the histological sections. For the proper evaluation of the

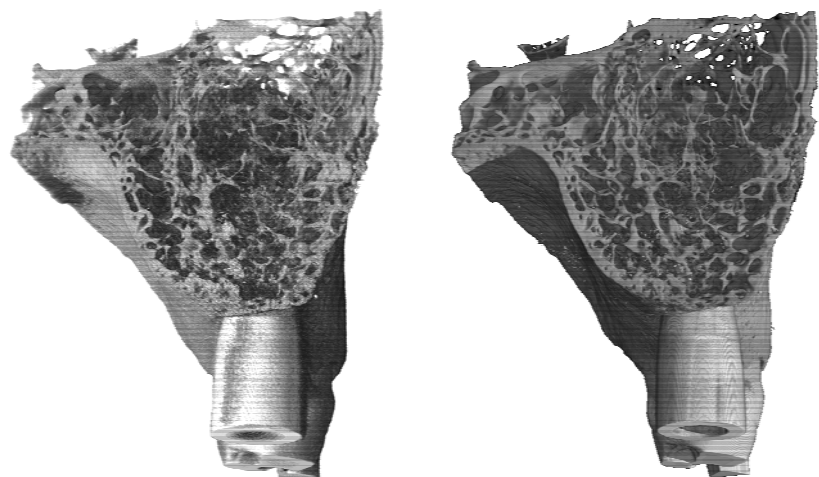


Figure 1: Volume renderings of the voxel data set from the conventional  $\mu$ CT-scanner (left) and the SR-based tomograph (right).

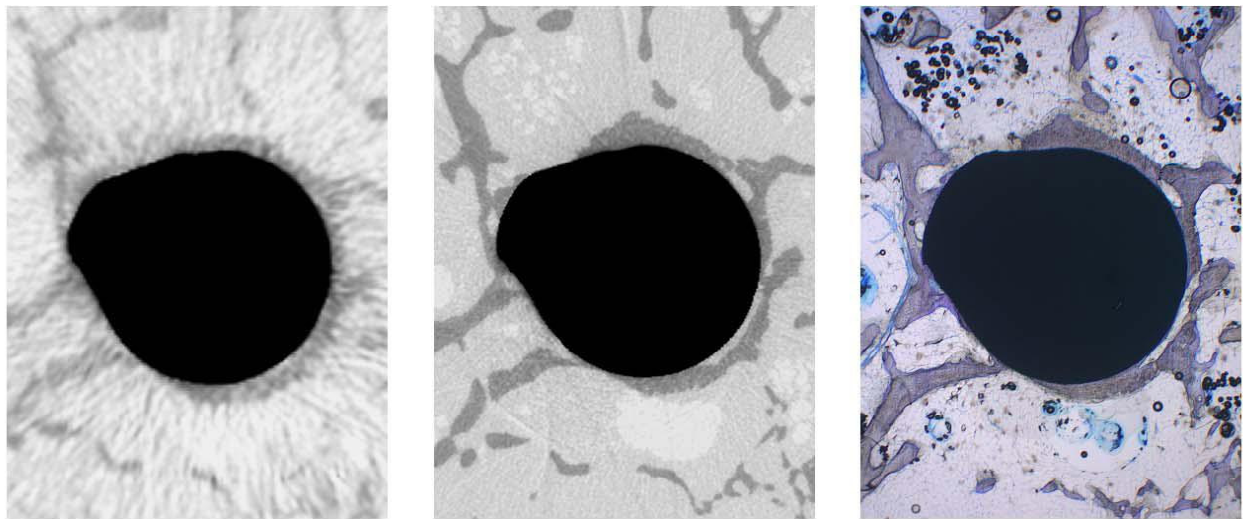


Figure 2: Detail from a single slice image obtained from the conventional  $\mu$ CT scanner (left), the SR-based tomograph (middle) and the corresponding histological section (right).

implant-bone interface, only the SR-based  $\mu$ CT technique is able to display the areas of bony contact and visualise the true 3D structure of bone around dental implants correctly. The difference in the two scanning methods is expressed in their ability to represent the implant-bone interface. Looking at two close-up images of the same section, it is evident that an accurate discrimination between the implant boundary and the true extension of bone in direct contact with the implant is only possible using the SR-based scanning method. On conventional  $\mu$ CT-scans it is very difficult to identify the bone in contact with the implant (Fig. 2, left) and in fact the amount of bony contact is overestimated. From a qualitative comparison of the histological sections with the corresponding SR-based tomographic scans it is clear that the level of detail is similar and that the bone at the implant interface in the SR-based  $\mu$ CT image fully matches the real morphology (Fig. 2 middle & right). Studies are currently being performed to test the accuracy of the SR-based  $\mu$ CT-scanning technique in retrieving the morphometric parameters conventionally used in histomorphometry (e.g. bone volume fraction, surface to volume ratio, the extent of bone/implant contact). With conventional histology it is only possible to obtain cross sections in one particular plane and, because much material is lost in the cutting procedure for samples containing metal implants, the tissue quantification is normally restricted to a few 2D sections. On the other hand, the  $\mu$ CT technique produces 3D data-sets that are equally detailed in all dimensions and therefore the possibility exists to reconstruct images in any arbitrary plane.

The results of this investigation show that both conventional and SR-based  $\mu$  CT scanning techniques are non-destructive methods that provide detailed images of bone. However with the SR-based  $\mu$ CT scanning it is possible to generate better images of bone surrounding titanium dental implant even in the close vicinity of the bone-implant interface. Therefore SR-based  $\mu$ CT scanning represents a valid and, in some aspects, better *in vitro* alternative to the serial sectioning method to evaluate the osseointegration of dental implants.

Acknowledgment: This work was financially supported by contract II 00-064-EC of the European Commission.

## References

- [1] Müller, R. & Rügsegger, P. Stud Health Technol Inform 40: 61-79 (1997).
- [2] Sennerby, L., Wennerberg, A. and Pasop, F. Clinical Oral Implants Research 12: 91 (2001).
- [3] Van Oosterwyck, H. Ph.D.-thesis. Katholieke Universiteit Leuven, Belgium. (2000).
- [4] Bonse, U., Busch, F., Günnewig, O., Beckmann, F., Pahl, R., Delling, G., Hahn, M. and Graeff, W. Bone Miner 25: 25-38 (1994).

# Comparison of Synchrotron-Based Microtomography and Scanning Acoustic Microscopy of Cortical Bone

*M. Dalstra, E. Karaj<sup>1</sup>, T. Andersen<sup>2</sup>, P.M. Cattaneo and F. Beckmann<sup>3,4</sup>*

*Dept. of Orthodontics, Royal Dental College, Aarhus University, Vennelyst Boulevard 9, 8000 Aarhus C, Denmark*

*<sup>1</sup>Fachbereich Physik,, University of Siegen, Walter-Flex-Strasse 3, 57068 Siegen, Germany*

*<sup>2</sup>Institute of Experimental Clinical Research, University Hospital, Brendstrupgaardsvej, 8200 Aarhus N, Denmark*

*<sup>3</sup>HASYLAB at DESY, Notkestrasse 85, 22603 Hamburg, Germany*

*<sup>4</sup>GKSS-Forschungszentrum, Max-Planck-Strasse 1, 21402 Geesthacht, Germany*

This study is a continuation of the previous two years' investigation of the structure of cortical bone and is part of a larger project (II-00-064 EC). The focus in this sub-project lies on the differences in mineralisation, which can be found in the individual osteons in the cortical bone. Osteons are longitudinally arranged cylindrical structures centered around a so-called haversian canal, which form the building blocks of cortical bone. Cortical bone remodeling is closely related to this osteonal organization as newly formed osteons continuously replace older ones. The degree of mineralisation in these new osteons is initially lower than in the existing bone and it takes time before the osteons mature. For this process a period of 90 days has been mentioned [1].

Synchrotron-based microtomography and scanning acoustic microscopy (SAM) are at present the two techniques, which have both sufficient spatial resolution and sensitivity to detect local variations in mineralisation in cortical bone tissue. The aim of this sub-study was therefore to use both techniques to examine osteonal mineralisation patterns and compare the outcome.

A 5-cm long segment was cut from the mid-shaft of a femur of a 54-year old, male donor and subsequently embedded in methyl metacrylate. Two matchstick-sized samples (2x2x40 mm<sup>3</sup>) were cut from the lateral, anterior, medial and posterior sides of this segment each, whereby their long axis coincided with the longitudinal axis of the femur.

The eight cortical samples were scanned with a microtomography system at beamlines BW2 and W2 at the DORIS-ring at HASYLAB/DESY [2]. Due to the synchrotron X-ray source, the samples could be scanned at a spatial resolution of 4  $\mu$ m. The samples were scanned perpendicular to their long axis and therefor had to be scanned in several sessions, as each session could only cover about 5 mm in height. The single slice images were finally stacked and a three-dimensional reconstruction was made.

After  $\mu$ CT-scanning the samples were re-embedded in epoxy resin. Using a special polishing technique, which ensured reliefs less than 0.75  $\mu$ m, the samples were prepared for SAM analysis. For this a SAM2000 (KSI GmbH, Herborn, Germany) was used with a 400 MHz lens providing a spatial resolution of 2  $\mu$ m. Single samples were scanned at several heights by cutting 5 mm material away at a time.

As SAM-scanning was performed in the same plane as the  $\mu$ CT-scanning, the SAM images could be matched to the corresponding slices from the  $\mu$ CT data-sets. Finally, for a number of characteristic osteons in the corresponding images the distribution of the gray values was determined.

Due to the monochromatic radiation, synchrotron-based  $\mu$ CT is not affected by beam hardening and the gray values (attenuation coefficients) in the reconstructed images are directly related to the local density of the material. For cortical bone this means that the more immature osteons appear darker than the surrounding bone. In SAM-images the gray values are a measure of the material's acoustic



impedance, which is a function of the local Young's modulus and density. Comparison of the  $\mu$ CT and the SAM images of the cortical samples showed a very good correspondence in the gray values of the individual osteons (Fig. 1).

At present the comparison of the acoustic impedance and the attenuation coefficients of the individual osteons are still being performed and are expected to be finished in the first quarter of 2004.

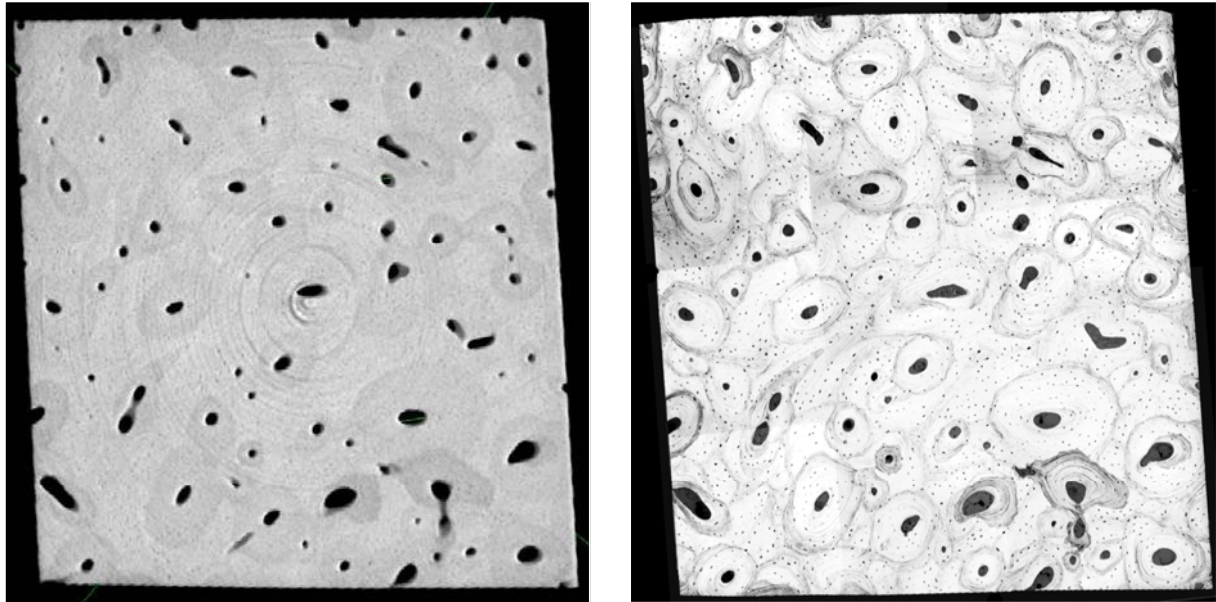


Figure 1: Comparison of the  $\mu$ CT image of a cortical sample (left) and the corresponding SAM image (right).

**Acknowledgment:** This study has been financially support by the Aarhus University Research Fund and IHP-contract II-00-064 EC of the European Commission.

## References

- [1] Eriksen, E.F., Axelrod, D.W. and Melsen, F. Bone Histomorphometry, New York, Raven Press (1994).
- [2] Bonse, U., Busch, F., Günnewig, O., Beckmann, F., Pahl, R., Delling, G., Hahn, M. and Graeff, W. Bone Miner 25: 25-38 (1994).



# Differentiation in the mineral content of trabecular bone

H. Scherf<sup>1,2</sup>, F. Beckmann<sup>3</sup> and J. Habersetzer<sup>1</sup>

<sup>1</sup> Research Institute Senckenberg, Senckenberganlage 25, 60325 Frankfurt, Germany

<sup>2</sup> Institute for Applied Geosciences TU Darmstadt, Schnittspahnstr. 9, 64287 Darmstadt, Germany

<sup>3</sup> Institute for Materials Research GKSS-Research Center, c/o HASYLAB at DESY, Notkestr. 85, 22607 Hamburg, Germany

The capacity of bone to adjust to applied loads has already been described in the 19<sup>th</sup> century. The alignment of the cancellous bone to the main stress trajectories is since then known as ‘Wolff’s law’. However, only recently has this property of cancellous bone been recognised empirically using in vivo experiments and computational studies [1, 2, 3]. Therefore, different kinds of habitual locomotion are able to leave a clear signatures in long bones by their specific load cases. In consequence, the architecture of the trabecular network is a reflection of the loading style. For biomechanical studies it is also necessary to take the material properties of bone into account. These material properties depend on structural organisation and composition of bone [4]. Especially alterations in the mineral content of the bone influence its material properties [5]. High resolution computed tomographic imaging techniques with synchrotron radiation now enable us to obtain better differentiation of the mineral density of bone due to the monochromatic x-ray source. On this base locality sensitive estimations of material properties are possible.

In a first attempt to verify the differences which may consist in the mineral content of single trabeculae parts of two *Alouatta seniculus* femora were investigated. A lower mineral content was observed as expected in the corticalis around haversian canals and at the surface of the trabecular bone. In these regions a reduced mineral density appears in newly apposed bone substance which evolves in consequence of remodeling activities. Such regions will slowly increase their degree of mineralisation. However, we also observed canal structures inside the trabeculae with a lower mineral density (Fig. 1). The latter feature is not fully understood. Postmortem changes due to fatty acids can be excluded because low density structures are only present in particular areas. In the case of postmortem acid effects lower mineral densities should be present at all bone surfaces. Therefore, it may be a sign of innertrabecular remodeling. The origin and function of the trabecular canals will be subject of further research using the presented technique.

## References

- [1] L.E. Lanyon, J. Bone Jt. Surg. 56B, 160 (1974)
- [2] R.E. Guldberg, N.J. Caldwell, X.E. Guo, R.W. Goulet, S.J. Hollister, and S.A. Goldstein, J. Bone Miner. Res. 12, 1295 (1997)
- [3] K. Tsubota, T. Adachi, and Y. Tomita, J. Biomechanics 35, 1541 (2002)
- [4] P.K. Zysset, X.E. Guo, C.E. Hoffler, K.E. Moore, and S.A. Goldstein, J. Biomechanics 32, 1005 (1999)
- [5] J.C. van der Linden, D.H. Birkenhäger-Frenkel, J.A.N. Verhaar, and H. Weinans, J. Biomechanics 34, 1573 (2001)

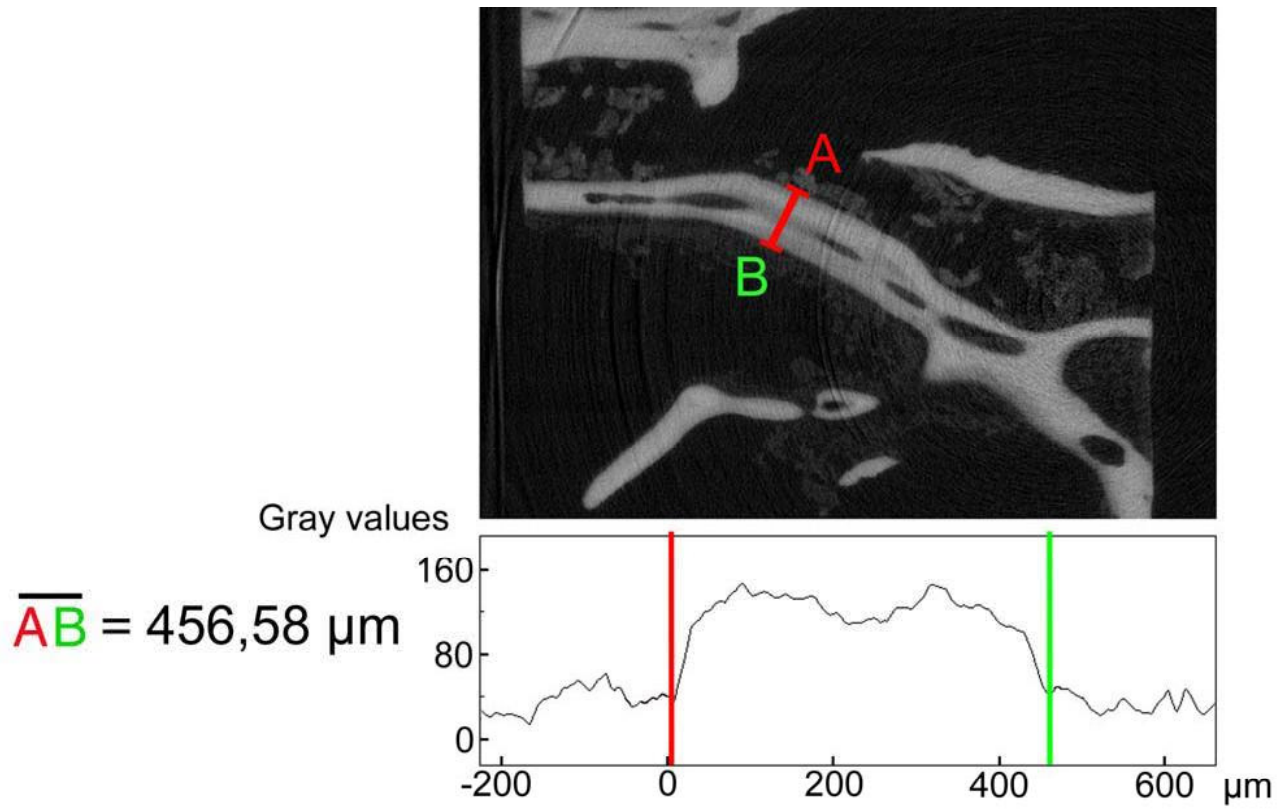


Figure 1: Trabecular canal with recently accumulated bone inside,  
Trochanter minor region of *Alouatta seniculus*

# Micro CT of polyurethane scaffolds for meniscus replacement

*R.G.J.C. Heijkants<sup>1</sup>, F. Beckmann<sup>3</sup>, T. Donath<sup>3</sup>, R.V. van Calck<sup>1</sup>, T.G. van Tienen<sup>2</sup>, N. Ramrattan<sup>2</sup>, P. Buma<sup>2</sup>, J.H. de Groot<sup>1</sup>, A.J. Pennings<sup>1</sup>, R.P.H. Veth<sup>2</sup> and A.J. Schouten<sup>1</sup>*

*<sup>1</sup>Department of Polymer Chemistry, Faculty of Mathematics & Natural Sciences,  
Rijksuniversiteit Groningen, Nijenborgh 4, 9747AG, The Netherlands*

*<sup>2</sup>Orthopaedic Research Laboratory, University Medical Center, P.O. Box 9101, 6500HB,  
Nijmegen, The Netherlands*

*<sup>3</sup>GKSS-Forschungszentrum Geesthacht, Max-Planck-Straße 1, 21502 Geesthacht, Germany*

Biomedical polyurethanes have been used for a wide range of applications. Examples include nerve guides, meniscal reconstruction materials, artificial veins and artificial skin. For these applications usually commercially available polyurethanes are used. These materials frequently exhibit good mechanical properties but an important disadvantage is that they contain aromatic diphenylmethane diisocyanate (MDI). MDI based polyurethanes are known to release carcinogenic and mutagenic products on degradation. Furthermore, they often show low resistances to tearing. A high resistance to tearing is important to prevent structures from tearing out of the biomaterial. The development of new medical grade polyurethanes with good mechanical properties is therefore highly desirable.

New high molecular weight biomedical polyurethanes and polyurethane ureas have been synthesized by chain extending  $\epsilon$ -caprolactone and lactide based macrodiisocyanates with diols and diamines. The polymers show high tensile strengths, high moduli and high resistances to tearing. On degradation, only non-toxic products will be released [1,2]. One of the degradation products will be 1,4-butanediamine (putrescine), a growth factor essential for the cell division in mammals.

It turned out to be possible to process the polyurethanes into various biomedical materials like porous meniscal reconstruction implants and nerve-guides. Furthermore, an in-situ foaming process has been developed, in which the use of organic solvents has been eliminated. This method also has the advantage of producing porous structures exhibiting a very high degree of interconnectivity

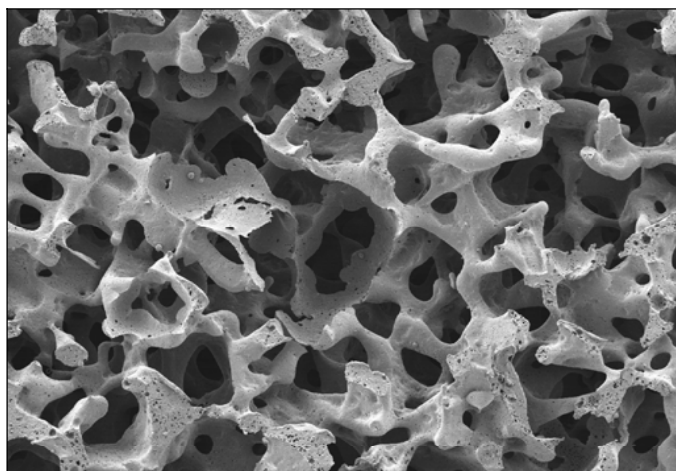


Figure 1: Scanning electron microscope picture of a polyurethane scaffold

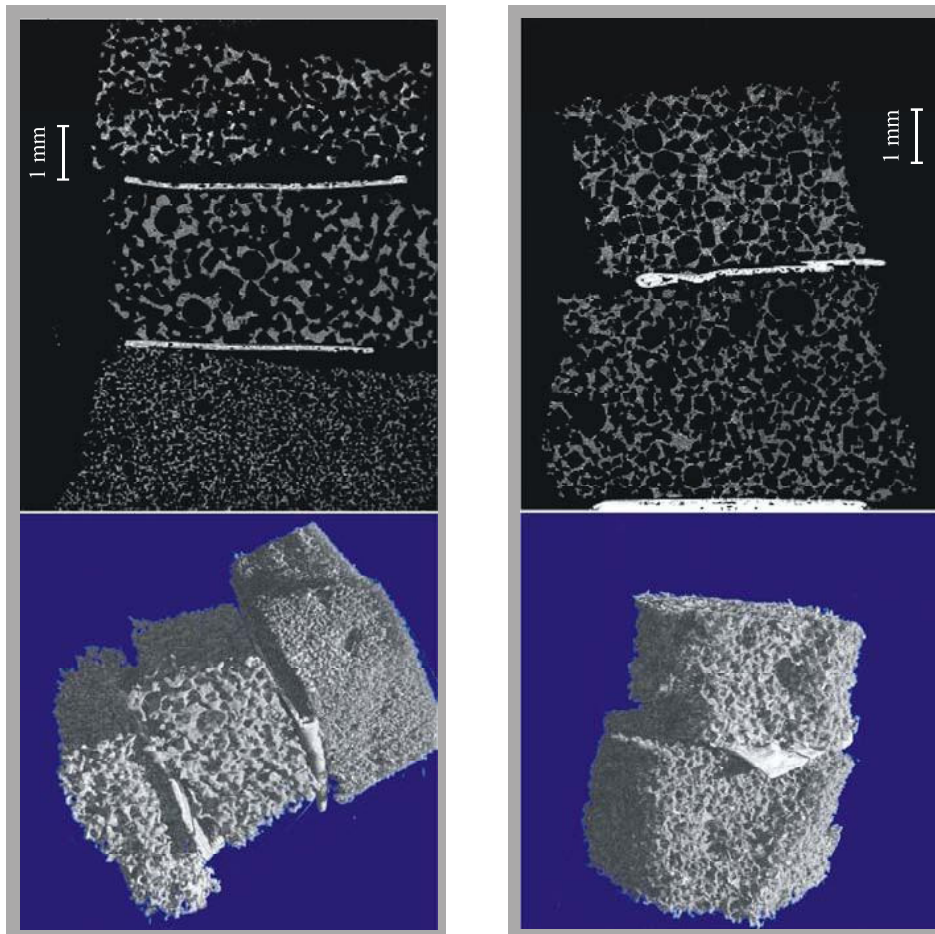


Figure 2: Microtomography of 5 different polyurethane scaffolds. The experiment was performed at beamline W2 using a photon energy of 18 keV. On the left side stack of three (left) and two (right) samples are investigated. A volume rendering (bottom) and a cross section (top) of the reconstructed volume is given.

between the pores. This enables cells, nutrients and waste products to diffuse rapidly through the scaffold which allows for cells deep inside the scaffold.

Up until now these porous structures are mainly analyzed by scanning electron microscopy. This gives an indication of pore size and structure. Accurate values are very difficult to obtain via this method. The use of high resolution micro-CT images will allow us to determine a much broader range of parameters like porosity and pore size which are very important factors that influence the incorporation of tissue in the scaffold and thus the effectiveness of the scaffold [3,4].

## References

- [1] C. Spaans, de Groot, J. H., Dekens, F. G. and A. Pennings., *Pol. Bull.* 41, 131 (1998)
- [2] C. Spaans, J. de Groot, V. Belgraver. and A. Pennings., *J. Mat. Sci. Mat. Med.* 9, 675 (1998)
- [3] T. van Tienen, R. Heijkants, P. Buma, J. de Groot, A. Pennings. and R. Veth, *Biomat.* 23, 1731 (2002)
- [4] T. van Tienen, R. Heijkants, P. Buma, J. de Groot, A. Pennings. and R. Veth, *Biomat.* 24, 2541 (2003)

# Microtomography of human and animal tendons, first results

*F. Beckmann<sup>1</sup>, C. Hurschler<sup>2</sup> and F. Witte<sup>2</sup>*

<sup>1</sup>GKSS-Forschungszentrum Geesthacht, Max-Planck-Straße 1, 21502 Geesthacht, Germany

<sup>2</sup>Department of Orthopaedic Surgery, Medical School Hannover, Anna-von-Borries-Str. 1-7, 30625 Hannover, Germany

Ligaments and tendons are the flexible collagen structures that bind together the musculoskeletal system. They are extraordinarily strong in resisting tensile loads. The hierarchical structure of tendons can be listed as:

TYPE	TYPICAL DIAMETER
collagen molecule	1.3 nm
collagen fibril	50-500 nm
fascicle	50-300 $\mu\text{m}$
tendon fibre	100-500 $\mu\text{m}$

The mechanical properties are based on the microstructure of the tendons especially the crimp pattern of the fascicles. This microstructure is of interest for the basic understanding of the pathological stress-strain behaviour which can result in acute ruptures. The 3-dimensional arrangement is by now not fully clarified [1,2]. Furthermore the 3-dimensional behaviour of this complicated system to introduced strain and stress in a tendon fibre is still unclear. Therefore, it is important to find a technique which allows for the 3-dim. mapping of the fascicle structure in a tendon fibre.

In a first test experiment we perform absorption-contrast microtomography on a human and animal tendon in different sample environment. Both were introduced into a PMMA tube, but the animal tendon was investigated in a liquid cell filled with Ringer-Lactat solution to provide for a more natural environment. Furthermore by performing a differential measurement allows for lowering the energy. This should result in an increase of the density resolution in the tomogram.

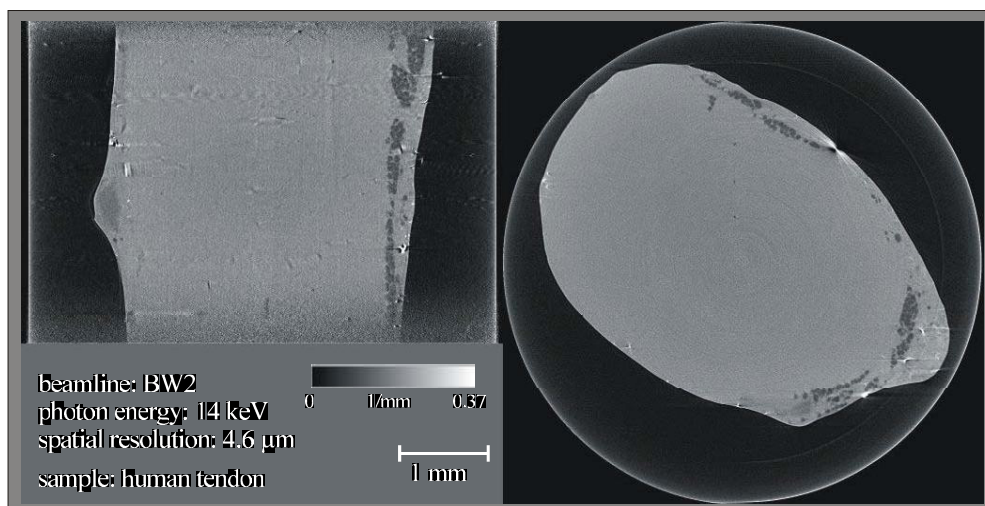


Figure 1:  $\mu\text{CT}$  of a human tendon stitched into a PMMA tube. The diameter of the tube is larger than the field of view. This results in increased intensity on a circle in the reconstructed slice (right). The interface tendon - air can very well be investigated. But the internal structure of the tendon remains invisible. The cross section on the left side is perpendicular to the reconstructed slice.

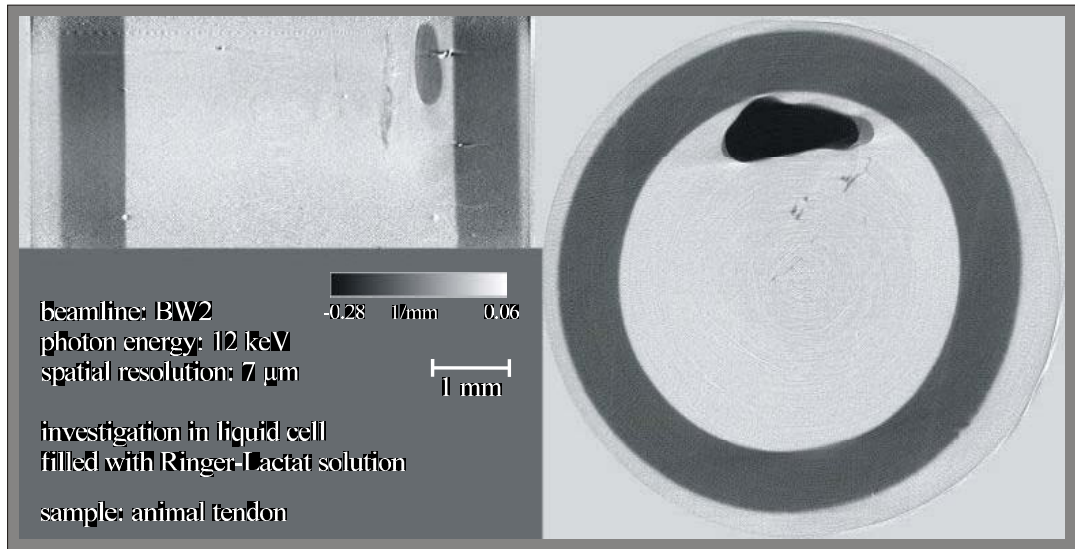


Figure 2:  $\mu$ CT of an animal tendon stitched into a PMMA tube. The scan is performed against Ringer-Lactat solution. Therefore air-bubbles result in a negative absorption (the black area in the reconstructed slice on the right). The cross section on the left is perpendicular to the reconstructed slice. Due the surrounding liquid the surface of the tendon vanished. Also the inner structure of the tendon cannot be detected.

The results shown in figure 1 and figure 2 make clear that pure absorption contrast microtomography is not sufficient to access the internal structure of human or animal tendons. Furthermore if measured in the natural environment, which is simulated by the Ringer-Lactat solution, also the surface information of the specimen vanishes.

Therefore it is necessary to perform phase contrast  $\mu$ CT and phase-outline  $\mu$ CT to test if these techniques allow for the visualization of the fascicle structure of tendons. The measurement for one phase projection using interferometric phase contrast is shown in figure 3.

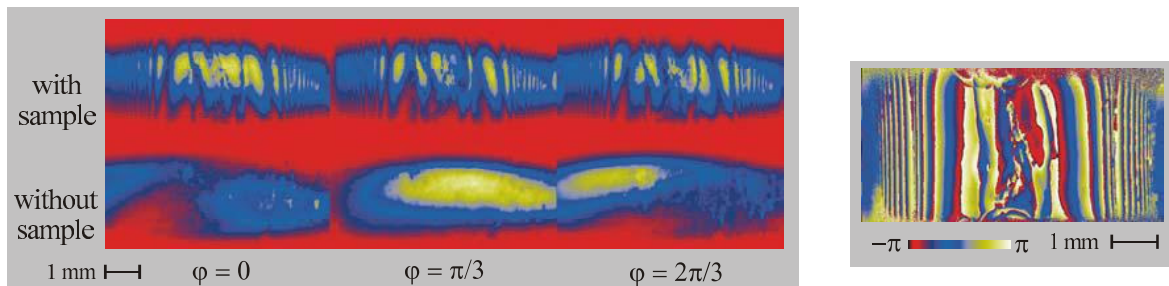


Figure 3: Measurement of interference patterns with and without the sample at different overall phase shift for one phase projection (left) and the calculated phase projection modulo  $2\pi$  (right). The animal tendon was stitched into a PMMA tube and the measurement was performed in a liquid cell filled with Ringer-Lactat solution using a photon energy of about 20 keV at beamline BW2.

## References

- [1] D.J.S. Hulmes et al. Biophys. J. 68, 1661-1670, (1995).
- [2] T.J. Wess, J. ASME. 124, 72-77, (2002).
- [3] F. Beckmann et al., SPIE Vol. 3772, 170-187, (1999).

# In-vivo Degradation Kinetic of Magnesium Implants

*F. Witte, H.-A. Crostack<sup>1</sup>, J. Nellesen<sup>1</sup>, J. Fischer and F. Beckmann<sup>2,3</sup>*

*Dept.. of Orthopaedic Surgery of Medical School Hannover, Anna-von-Borries-Str. 1-7, 30625 Hannover, Germany*

*<sup>1</sup>Lehrstuhl für Qualitätswesen of University Dortmund, Joseph-von-Fraunhofer Str. 20, 44227 Dortmund, Germany*

*<sup>2</sup>GKSS-Forschungszentrum Geesthacht, Max-Planck-Straße 1, 21502 Geesthacht, Germany*

*<sup>3</sup>Hamburger Synchrotronstrahlungslabor at Deutschen Elektronensynchrotron, Notkestr. 85, 22603 Hamburg, Germany*

Temporary bone implants made of magnesium alloys degrade in bone [1]. This degradation is predicted to be a corrosion process. The corrosion of magnesium alloys is depending on its environment, the elemental composition of the magnesium alloy and its processing treatment. The corrosion can also be controlled by surface coating. Basic principles of magnesium corrosion in bone could be demonstrated in animal studies [2].

In preliminary studies casted magnesium alloys were used that were chilled to pins and were applied as bone implants [2]. These implants showed a local and high corrosion attack at the implant surface. In a new approach to more corrosion resistant magnesium alloys the base material was extruded and chilled to little cylinders. The extrusion process provide a more homogenous magnesium alloy.

To observe the corrosion process in the bone histological sections are commonly used to determine the bone-implant interphase. These destructive methods effect the magnesium alloys because of its soluble nature. Therefore, the bone-implant interphase was studied by microcomputed tomography as a non-destructive method with a high spatial resolution.

In order to get an degradation kinetic of the magnesium alloy we had to determine magnesium samples postoperatively after various time intervals. Magnesium implant degradation was observed over a total postoperative time of 12 weeks, scanned in intervals of 2, 4, 6 and 12 weeks.

Bone healing and bone remodelling processes provide a high interindividual variety. Therefore, at least 5 animals at each time interval had to be studied. The magnesium cylinders were implanted in the femur condyls of the rabbits (New Zealand White Rabbits).

The micro-tomography measurements (XTM) were carried out at beamline W2 using a photon energy of 31.0 keV. The projection data contain radiosopic images consisting of 1536x692 pixels acquired at 720 rotation angles for one sample. The observation area was kept to the center of the bone specimen.

In total, 40 bone-implant samples were scanned each in two different levels. So, 80 tomograms were performed and have to be reconstructed and analyzed. The tomograms of each level were stacked together after reconstruction to observe the whole implantation site.

First results of the reconstructed data show that extruded magnesium alloys corrode at a slower rate and more homogeneously than casted magnesium alloys. Extruded magnesium alloys corrode in direct contact to the surrounding bone.

Further evaluation and complete reconstructed data are going to provide the first detailed information about the *in-vivo* degradation rate of magnesium alloys in bone.



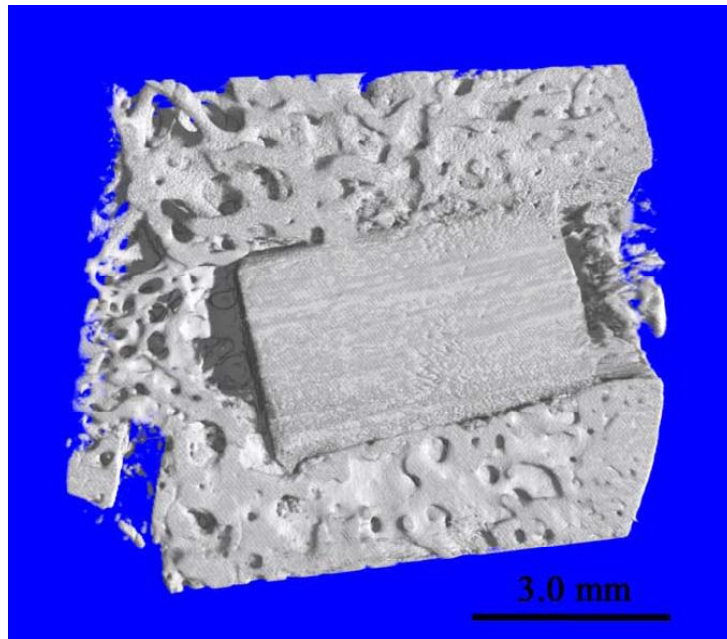


Figure 1: Magnesium implant corrodes in direct contact to surrounded bone (upper part of implant) four weeks after operation.

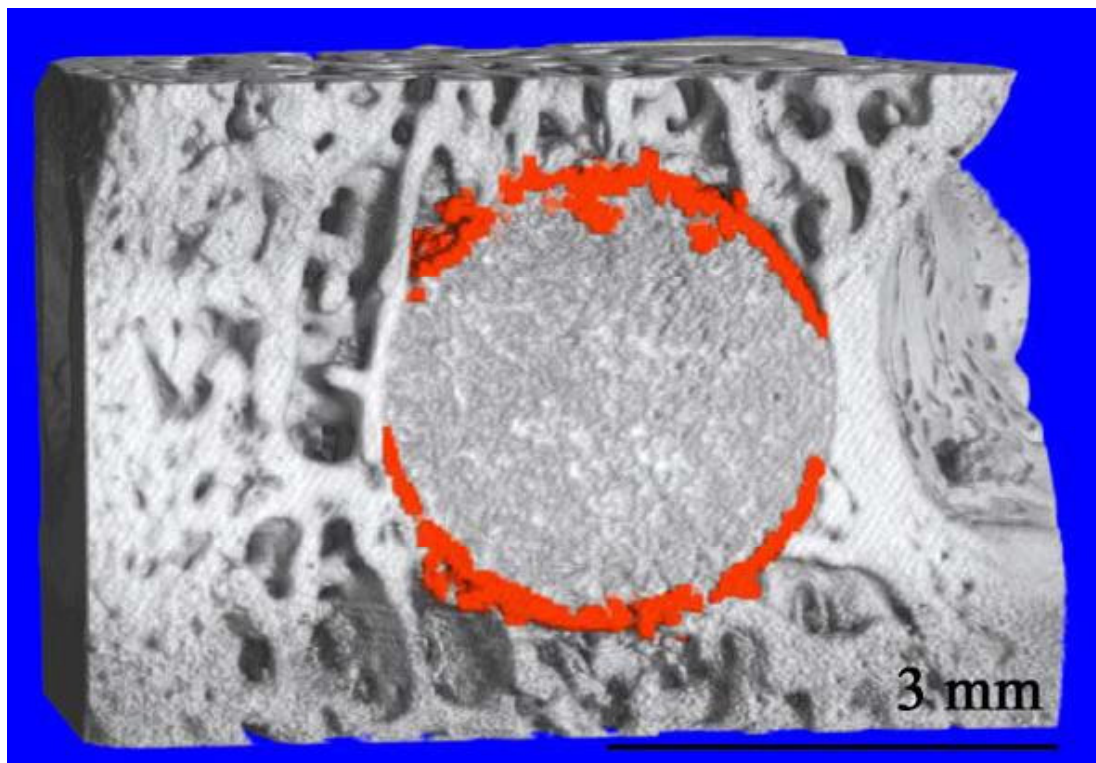


Figure 2: 3D view of corroding magnesium implant in rabbit condyl 12 weeks after operation. Red dyed grey values represent corroded magnesium alloy.

The authors acknowledge the financial support of Medical School Hannover, DFG Sonderforschungsbereich 599 and HASYLAB (II-01-078).

## References

- [1] McBride, JAMA, Vol. 111: 508-515 (1938)
- [2] F. Witte, H.-A. Crostack, J. Nellesen and F. Beckmann, Hasylab Annual Report, 954-6 (2002)